

# TECHNISCHE UNIVERSITÄT MÜNCHEN

Fakultät für Maschinenwesen  
Lehrstuhl für Werkstoffkunde und Werkstoffmechanik  
mit Materialprüfamt für den Maschinenbau

## **TRIP-assisted Thin Sheet Steel with a Bainitic and/or Martensitic Matrix**

Effects of Alloying Elements and Heat Treatment on  
Phase Transformations, Microstructures, and Mechanical Properties

Katharina Maria Angelika Hausmann

Vollständiger Abdruck der von der Fakultät für Maschinenwesen der Technischen Universität  
München zur Erlangung des akademischen Grades eines

Doktor-Ingenieurs (Dr.-Ing.)

genehmigten Dissertation.

Vorsitzender: Univ.-Prof. Dr.-Ing. Markus Lienkamp

Prüfer: 1. Univ.-Prof. Dr. mont. habil. Dr. h. c. Ewald Werner  
2. Univ.-Prof. Dr.-Ing. Wolfgang Bleck, RWTH Aachen

Die Dissertation wurde am 15.10.2014 bei der Technischen Universität München eingereicht und  
durch die Fakultät für Maschinenwesen am 13.03.2015 angenommen.

*Meiner Familie gewidmet...*  
*To my family...*

# Danksagung

Zuallererst danke ich Herrn Prof. Dr. Ewald Werner, Inhaber des Lehrstuhls für Werkstoffkunde und Werkstoffmechanik an der Technischen Universität München, für die Unterstützung und Förderung dieser Arbeit und die Übernahme des Hauptreferats. Herrn Prof. Dr. Wolfgang Bleck, Leiter des Instituts für Eisenhüttenkunde an der Rheinisch-Westfälischen Technischen Hochschule Aachen, danke ich für die Übernahme des Koreferats.

Mein besonderer Dank gilt Herrn Dr. Andreas Pichler, Leiter der Forschung und Entwicklung Business Unit Band der voestalpine Stahl GmbH, für die Möglichkeit, an diesem Thema arbeiten und durch viele interessante Diskussionen und Anregungen von ihm lernen zu dürfen. Ich danke Herrn Dr. Daniel Krizan, Projektleiter der Werkstoffentwicklung Kaltband voestalpine Stahl GmbH, besonders für die Einführung in das Thema und die Erfahrungsweitergabe.

Für die finanzielle Unterstützung und die Möglichkeit, in Forschung, Entwicklung und Produktion zu arbeiten, danke ich der voestalpine Stahl GmbH. Der gesamten Forschungsgruppe gilt mein Dank für das ausgezeichnete Arbeitsklima und die ständige Bereitschaft zu Diskussionen und Erfahrungsaustausch. Ich danke den engagierten Mitarbeitern der Werkstoffentwicklung, der Prüftechnik und Analytik sowie der Umformtechnik der voestalpine Stahl GmbH für die Hilfsbereitschaft, die qualitativ hochwertigen Untersuchungen und die fachlichen Diskussionen. Allen Beteiligten danke ich für die konstruktive Zusammenarbeit bei der Produktion der Stahlgüten. Schließlich danke ich der Alloy Development Group Seibersdorf für die Unterstützung bei den TEM-Untersuchungen.

# Zusammenfassung

Stahlfeinblech mit bainitischem und/oder martensitischem Gefüge und Restaustenit gewinnt in der Automobilindustrie auf Grund seines Potentials zur Verringerung des Treibstoffverbrauchs von Fahrzeugen zunehmend an Bedeutung. Die hohe Festigkeit dieser Stähle der dritten Generation der advanced high strength steels (AHSS) ermöglichen die Massereduzierung von Fahrzeugen bei Erhaltung oder Verbesserung der Sicherheitsstandards. Ein wesentlicher Vorteil von Stahl mit bainitischem und/oder martensitischem gegenüber polygonal-ferritischem Gefüge ist die geringere Kantenrissempfindlichkeit und das dadurch verbesserte Crashverhalten. Der Restaustenit erhöht die Dehnung und verbessert somit die Tiefziehbarkeit des Stahls. Viele bisher entwickelten TRIP-assisted bainitic-ferritic (TBF) und Quench- und Partitioning (Q&P)-Stähle enthalten 1,5 Massenprozent Silizium zur Verhinderung der Zementitausscheidung insbesondere während der Auslagerung. Bei der Produktion von Stählen mit diesem Siliziumgehalt wurde jedoch eine Oxidschicht auf den Walzen und den nachfolgenden Stahlbändern beobachtet.

Ziel der vorliegenden Arbeit war die Entwicklung und die industrielle Herstellung bainitischer und/oder martensitischer Stähle mit Restaustenit der dritten Generation der AHSS und einem Siliziumgehalt von weniger als 1 Massenprozent. Dazu wurde der Einfluss des Legierungskonzepts und der Wärmebehandlung auf das Gefüge und die mechanischen Eigenschaften von TBF und Q&P-Stählen untersucht.

Die Ergebnisse dieser Arbeit zeigen, dass TBF und Q&P-Stähle mit geringeren Siliziumgehalten als bisher üblich bei geschickter Wahl der restlichen Zusammensetzung und der Wärmebehandlung ähnliche Kombinationen an Festigkeit, Dehnung und Lochaufweitung aufweisen können. Durch die Zugabe von Mangan wird für niedrige Auslagerungstemperaturen ein höherer Restaustenitanteil erzielt. Durch die Zugabe von Niob wird das Gefüge verfeinert, die Umwandlung beschleunigt und die Morphologie des Bainit geändert. Das Absenken der Abschrecktemperatur führt zu größerer Lochaufweitung. Mit geringen Mengen polygonalen Ferrits kann der Restaustenitanteil und die Dehnung bei gleicher Festigkeit erhöht werden, ohne dabei die Lochaufweitung wesentlich zu verringern. Die im Rahmen dieser Arbeit gewonnenen Erkenntnisse flossen in die industrielle Produktion von TBF und Q&P-Stählen einer Zugfestigkeit von 980 und 1180 MPa ein.

# Abstract

As part of the third generation of advanced high-strength steels (AHSS) TRIP-assisted steels have been developed to improve vehicle fuel economy and passenger safety. In 2013, TRIP-assisted steels with bainitic and/or martensitic matrix with a tensile strength of 1180 MPa were adopted by a Japanese automobile manufacturer. The main advantage of the new steel grades is their excellent stretch-flangeability and improved crash performance compared to TRIP-assisted steels with polygonal ferritic matrix. The commercialized TRIP-assisted bainitic-ferritic (TBF) and Quench and Partitioning (Q&P) steels comprise a silicon content of 1.5 mass % to avoid cementite formation during overaging. This silicon content results in a silicon oxide layer that is picked up by the rolls on the production line and causes undesirable indentations on the following sheet surface.

In the present work, TBF and Q&P steels with a silicon content below 1 mass % and a tensile strength of 980 MPa and 1180 MPa were systematically investigated. The effect of alloying concepts and heat treatments on phase transformations, microstructures, and mechanical properties was studied in detail. The results of this work show that for specific alloying concepts and heat treatments, TBF and Q&P steels with reduced silicon contents can exhibit combinations of strength, elongation, and hole expansion strain which are similar to those of the steels with conventional silicon contents. Higher amounts of manganese result in higher amounts of retained austenite for low overaging temperatures. The addition of niobium refines the microstructure, accelerates the phase transformations, and changes the morphology of the bainite. A lower quench temperature results in higher hole expansion strain. The introduction of small amounts of polygonal ferrite into the microstructure can enhance the amount of retained austenite and elongation for the same strength level without affecting the hole expansion strain. On the basis of laboratory investigations, new alloying and processing strategies for TBF and Q&P steels were developed in order to yield enhanced combinations of strength, elongation, and stretch-flangeability. The newly designed 980 and 1180 MPa grades were successfully produced in the industrial line.



# Contents

<b>1</b>	<b>Introduction</b>	<b>1</b>
<b>2</b>	<b>Literature</b>	<b>5</b>
2.1	TBF and Q&P steels . . . . .	5
2.2	Alloying elements in TBF and Q&P steels . . . . .	8
2.2.1	Carbon . . . . .	8
2.2.2	Silicon . . . . .	9
2.2.3	Manganese . . . . .	9
2.2.4	Chromium . . . . .	10
2.2.5	Niobium . . . . .	10
2.3	Microstructure and mechanical properties . . . . .	11
2.3.1	Strength and strengthening mechanisms . . . . .	11
2.3.2	Strain-hardening behaviour . . . . .	12
2.3.3	Failure mechanism . . . . .	16
<b>3</b>	<b>Experimental Procedure</b>	<b>19</b>
3.1	Laboratory production of annealed sheets . . . . .	19
3.1.1	Material . . . . .	19
3.1.2	Production of cold-rolled sheets . . . . .	19
3.1.3	Annealing cycles . . . . .	21
3.1.4	Laboratory annealing of industrially cold-rolled sheets . . . . .	21
3.2	Industrial production of annealed sheets . . . . .	22
3.2.1	Material . . . . .	22
3.2.2	Production of cold-rolled sheets . . . . .	23
3.2.3	Annealing cycles . . . . .	23
3.3	Microstructure characterization and mechanical testing . . . . .	23
3.3.1	Metallography . . . . .	23
3.3.2	Magnetic measurements . . . . .	25
3.3.3	X-ray diffraction . . . . .	26
3.3.4	Dilatometry . . . . .	26
3.3.5	Mechanical testing . . . . .	27
<b>4</b>	<b>Results</b>	<b>29</b>
4.1	Influence of alloying elements on TBF and Q&P sheet steel . . . . .	29
4.1.1	Silicon in the 980 grade . . . . .	29
4.1.2	Silicon in the 1180 grade . . . . .	33
4.1.3	Manganese in the 980 grade . . . . .	36
4.1.4	Manganese in the 1180 grade . . . . .	39
4.1.5	Chromium in the 980 grade . . . . .	43

4.1.6	Chromium in the 1180 grade . . . . .	46
4.1.7	Niobium in the 980 grade . . . . .	50
4.1.8	Niobium in the 1180 grade . . . . .	59
4.2	Influence of annealing cycle on TBF and Q&P sheet steel . . . . .	62
4.2.1	Quench temperature . . . . .	62
4.2.2	Time at quench temperature . . . . .	65
4.2.3	Intermediate holding . . . . .	67
4.2.4	Intercritical annealing . . . . .	68
4.3	Failure mechanisms . . . . .	70
4.3.1	Void nucleation and growth . . . . .	70
4.3.2	Fracture surface characterization . . . . .	72
4.4	Industrial trials on 1180 MPa Q&P sheet steel . . . . .	76
<b>5</b>	<b>Discussion</b>	<b>81</b>
5.1	Phase transformations, microstructures, and mechanical properties: A general overview . . . . .	81
5.1.1	Phase transformation kinetics . . . . .	81
5.1.2	Microstructure and the amount of retained austenite . . . . .	82
5.1.3	Mechanical properties . . . . .	86
5.2	Influence of alloying elements on TBF and Q&P sheet steel . . . . .	88
5.2.1	Silicon . . . . .	88
5.2.2	Manganese . . . . .	92
5.2.3	Chromium . . . . .	99
5.2.4	Niobium . . . . .	102
5.3	Influence of annealing cycle on TBF and Q&P sheet steel . . . . .	107
5.3.1	Quenching . . . . .	107
5.3.2	Impact of polygonal ferrite . . . . .	109
5.4	Failure mechanisms . . . . .	110
5.5	Industrial trials on 1180 MPa Q&P sheet steel . . . . .	112
<b>6</b>	<b>Summary</b>	<b>115</b>
	<b>Bibliography</b>	<b>119</b>

# Chapter 1

## Introduction

The growing interest in vehicle safety, fuel economy and performance standards gives rise to the development of new materials. Sheet steel remains the first choice of new light-weight materials for automotive applications, as it offers the advantages of excellent formability, high strength, outstanding crash performance, and reasonable costs. To stay ahead of the mounting economic challenges in the automotive industry, steel research and development experts have made great effort to improve the mechanical properties of sheet steel. As a result, the introduction of so-called advanced high-strength steels (AHSS) began in the late 1990s [1]. Since this time various AHSS grades have been successfully produced and adopted by automobile manufacturers, and their use has increased considerably in recent years. The share of AHSS in newly designed cars averages approximately 18 to 20 % and is expected to grow significantly in the near future.

Conventional high-strength steel (HSS), including bake hardening steel, high-strength IF steels, and microalloyed steel enable tensile strengths of up to approximately 600 MPa. Solid solution hardening, precipitation strengthening, and grain refinement are strengthening mechanisms of these steels. To achieve higher strength levels it is necessary to change the microstructure constituents. This was accomplished by the implementation of dual phase (DP) steels [2, 3]. The combination of hard martensitic inclusions embedded in a soft ferritic matrix enables significantly higher strength levels compared to conventional HSS.

However, a strength increase is accompanied by a loss in elongation as long as no new physical mechanism comes into play. With the exploitation of transformation-induced plasticity (TRIP) this natural reciprocal correlation is broken by adding elongation through strain-induced martensite transformation (SIMT) [4].

At the beginning of development of the first AHSS, attention was focused on high elongations in combination with high strength. However, the comparably low edge crack resistance of DP steels can result in cracks during the forming of automotive parts [5]. In addition, reduced edge formability can impair the crash performance of specific car components [6]. Investigations on the crash behaviour have shown that advanced bending and hole expansion properties are highly important for crash performance of AHSS [3, 7, 8]. As attention was shifted from deep drawability and stretch formability towards edge crack susceptibility and crash performance, complex phase (CP) steels began to emerge. With a microstructure of small amounts of martensite, retained austenite and sometimes ferrite/pearlite embedded in a bainitic matrix, much higher yield strengths and hole expansion values can be achieved. DP, TRIP, and CP steels are often referred to as the first generation AHSS [1, 9].

Further improvement in favourable strength-ductility combinations were achieved by fully austenitic microstructures, which can be achieved by a high manganese content of 12 to 35 mass %. Twinning-induced plasticity (TWIP), Duplex, and Triplex steels, known as the so-called second generation

AHSS, offer mechanical properties superior to those of the first generation AHSS [10, 11]. In addition, some second generation AHSS grades contain high aluminum content, which can reduce the vehicle mass through lower steel density. The stacking fault energy of the austenite, which depends on the composition of the steel, decides the transformation mechanism. TWIP steels exhibit outstanding combinations of strength and elongation, as a result of their plasticity-induced twinning [11]. Duplex steels transform from austenite to hexagonal martensite to near cubic martensite [12]. In Triplex steels the austenite hardens via shear-band-induced plasticity, however, no strain-induced  $\epsilon$ -martensite is formed, since the austenite is very stable [10]. However, second generation AHSS are unfavourable for the automotive industry primarily because of their high alloying and processing costs.

Most recently, evolution in AHSS has brought about a third generation, including TRIP-assisted bainitic ferrite (TBF) and quench and partitioning (Q&P) steels. These steels contain retained austenite to utilize the TRIP effect embedded in a harder matrix compared to their predecessors [13–16]. The microstructure of these steels consists of retained austenite inclusions embedded in a bainitic and/or (tempered) martensitic matrix. Variations in alloying elements and heat treatment can be used to adjust the strength of the matrix and the amount of retained austenite to obtain the desired mechanical properties. High quench and overaging temperatures, for instance, result in a strength reduction of the matrix and can promote the amount of retained austenite enhancing strain hardening and elongations. Quenching and/or overaging at lower temperatures leads to a harder matrix that improves the toughness of the steel.

In the past decade, TBF and Q&P steels were the object of extensive research [17–21]. However, fundamental questions regarding the influence of alloying elements and heat treatment on microstructure and mechanical properties remained unanswered. Even though manganese has long been used to stabilize the austenite, lower the austenitizing ( $A_3$ ) temperature, and enhance solid solution strengthening, the effects of manganese on the transformation kinetics and therefore the morphology of bainite are not fully understood [2, 22–25]. Furthermore, since polygonal ferrite is avoided in TBF and Q&P steels, the influence of small amounts of polygonal ferrite in a mainly bainitic and/or (tempered) martensitic microstructure containing retained austenite has not been studied. Fracture mechanics and damage of DP steels have been thoroughly investigated, while an in-depth understanding of the mechanisms occurring during plastic deformation of TBF or Q&P steels is still missing. The effect of microalloying in TBF steels has been addressed by Sugimoto *et al.* [26, 27]. However, several questions remained. A high silicon content of 1.5 mass % was established early on in TBF and Q&P steels due to its highly relevant role in stabilizing the austenite by preventing carbon precipitation [13, 28]. High silicon content, however, results in detrimental silicon-oxides on the strip surface.

The goal of this work is to gain fundamental understanding of industrially produced TBF and Q&P sheet steels designed for a tensile strength of 980 and 1180 MPa. A major challenge of these third-generation AHSS steels is the prevention or reduction of the silicon-oxide layer on the strip surface. This study aims to reduce the silicon content of these steels to below 1.0 mass % and chromium is used to partially substitute silicon in its function to prevent carbon precipitation.

To achieve a cost-effective production of cold-rolled TBF and Q&P steels, this study is specifically aimed at adapting the chemical composition to the specific setup and equipment of the industrial production line. A key challenge of the present work is to develop a better understanding of the effect of carbon, silicon, manganese, chromium, molybdenum and niobium on phase transformations, microstructures, and mechanical properties via systematic laboratory studies. The goal of this study is to achieve the industrial realization of the sheet steel by developing an alloying concept based on the influence of selected variations in the annealing cycle. The quenching and overaging parameters are varied in order to evaluate the capability of the steel to form desirable amounts of retained austenite with favourable stability. To characterize the microstructure the

steels are investigated using optical microscopy and scanning electron microscopy. Transmission electron microscopy experiments are conducted to reveal more detailed insight into bainite morphology as well as carbide size and distribution. This work aims to gain an in-depth understanding of phase transformation kinetics from continuous and isothermal dilatometer experiments supported by thermodynamic calculations on the phase stability in para-equilibrium condition.

Tensile tests and hole expansion tests are conducted in order to correlate microstructures, phase transformations, and mechanical properties. Since high impact on edge formability is expected due to polygonal ferrite in the microstructure and phase transformations, the influence of annealing and intermediate holding experiments on hole expansion properties is investigated. It is envisioned that gaining an in-depth understanding of the fracture mechanics and damage behaviour of the steel provided by quantitative and qualitative void analysis will ultimately help steel producers to further improve the mechanical properties of the sheet steel.

The goal of this work was to choose the most advanced alloying concept and annealing cycle for the industrial achievement of 980 and 1180 MPa grades based on the results from fine tuning in the laboratory. This study aims to adopt the newly designed TBF and Q&P steels to the industrial production line.



# Chapter 2

## Literature

### 2.1 TBF and Q&P steels

TRIP-assisted steels have been under development since 1985 in an effort to significantly reduce vehicle mass using materials with high strength and elongation [29–33]. The excellent stretch-formability of these steels facilitated the deep drawing and press forming of the automotive parts. However, it was found that the stretch-flangeability of TRIP steels with ferritic matrix is insufficient and requires improvement for some car components [13, 34, 35]. Bainitic steels, by contrast were known for their outstanding edge formability as a result of their fine uniform lath structure [36]. In order to overcome the drawback in stretch-flangeability of TRIP-assisted steels, Sugimoto *et al.* proposed in 2000 a replacement of the ferrite matrix with bainite, thus introducing a new steel type, the TRIP-assisted Bainitic-Ferritic sheet steel [13, 35].

In 2003, Speer *et al.* introduced a new process route termed Quenching and Partitioning to produce a new type of advanced high-strength steel grade [37]. This process route involves full austenitization of the cold-rolled sheets, quenching between martensite start ( $M_s$ ) and martensite finish ( $M_f$ ) and overaging either at this quench temperature or at a higher temperature. The final microstructure consists of at least tempered martensite from the initial quenching, retained austenite enriched in carbon during overaging, and small amounts of fresh martensite formed during final cooling. In addition, cementite can precipitate and bainite can form during overaging. A model was established based on constrained para-equilibrium describing the amount of retained austenite as a function of quench temperature. The model accounts for carbon partitioning from the as-quenched supersaturated martensite to the retained austenite [37–40]. The amount of bainite is neglected in this model because of the large martensite fraction. On the basis of this model the potential of the mechanical properties of Q&P steels for the automotive industry was evaluated with respect to strength and elongation [21, 41–43].

Q&P steels were developed under different circumstances and motives, in spite of their similarity to TBF steels. Research on Q&P steel focused on the understanding of the Quench and Partitioning process on a scientific level [37–40]. In TBF steel research, a great deal of attention has been given to the properties of the bainitic matrix, as implied by the denomination TBF, TRIP-assisted Bainitic Ferrite, as a consequence of efforts to improve stretch-flangeability and later on crash performance, while maintaining the TRIP effect [13, 34, 35]. The intention in Q&P steel development, on the other hand, was to maximize the TRIP effect. Due to its significant strain-hardening potential, the TRIP effect was subject to growing interest. In Q&P steel research, the retained austenite inclusions themselves and the enhancement of their stability through carbon enrichment were at the center of interest rather than the matrix properties and the interplay between matrix and inclusions [39–41].

TBF and Q&P steels comprise 0.15 to 0.3 mass % carbon, 1.5 mass % silicon, and 1.5 to 2.5 mass %

manganese. The strength of martensite is proportional to the carbon content [44, 45]. Lower bainite exhibits a higher strength than upper bainite due to its finer lath structure and its greater dislocation density, but also because finely dispersed cementite particles are located within the bainite laths of lower bainite, whereas coarser cementite particles are precipitated between the upper bainite laths [46]. Further, carbon is of great importance for the amount and stability of the retained austenite [28, 39, 47]. Silicon plays a crucial role in preventing carbon from precipitating in the form of carbides [48–52]. The addition of manganese is valuable for TBF and Q&P steels to decelerate phase transformations and in particular to avoid the formation of polygonal ferrite [2, 53]. The following section, Section 2.2, provides a more detailed description of the alloying elements' influence on phase transformations, microstructures, and mechanical properties.

Figure 2.1 shows the time-temperature schedules of TBF, one-step and two-step Q&P steels. To obtain a microstructure without polygonal ferrite, TBF and Q&P steels are fully austenitized and cooled with a cooling rate below the critical cooling rate to avoid ferrite formation [35, 37]. TBF steels are quenched to the overaging temperature between bainite start ( $B_s$ ) and martensite start ( $M_s$ ) temperature. During overaging, bainite forms and austenite is enriched and stabilized by carbon. Higher overaging temperatures result in a more globular and blocky bainitic matrix, whereas a more lath-like, finer matrix results from lower overaging temperatures. As a consequence of an insufficient driving force, the bainite transformation stops as soon as a given carbon content for a specific overaging temperature is reached [54]. However, the carbon content of the austenite can decrease due to carbon precipitation during overaging. Depending on the stability of the austenite at the end of the overaging step, some of the austenite can transform to martensite during the final cooling [18, 34, 35].

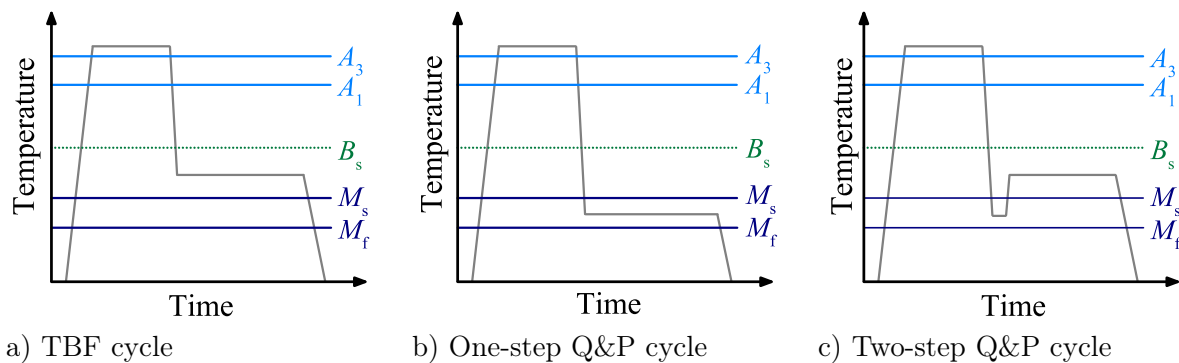


Figure 2.1: Time-temperature schedules of TBF, one-step and two-step Q&P steels.

Q&P steels are quenched between  $M_s$  and  $M_f$  temperature to adjust a certain amount of martensite followed by overaging (Figure 2.1b and 2.1c). Since martensite transformation is displacive, the amount of martensite solely depends on the undercooling [20]. The more the quench temperature is below the  $M_s$  temperature, the higher is the amount of martensite prior to the overaging step. Depending on the quench temperature and the amount of martensite, a fraction of the remaining austenite transforms during overaging. Bohemen *et al.* reported that below  $M_s$  temperature the transformation kinetics of the austenite is in agreement with that of bainite formation above  $M_s$  temperature [55, 56]. Carbon partitions from the martensite and possibly also from the transformation product formed during overaging into the austenite. This additional carbon helps to stabilize the remaining austenite. For industrially used and developed steel grades, the transformation stops after reasonable industrial holding times. Carbon possibly begins to precipitate, which can trigger further transformation due to the reduction of the carbon content of the austenite, until the steel is quenched to room temperature. The one-step Q&P process involves overaging at quench

temperature, while in the two-step Q&P process the steel is reheated and held at a temperature above quench temperature. According to TBF steels, matrix morphology as well as the amount and stability of the retained austenite of Q&P steels can be influenced by choosing corresponding overaging time and temperature parameters.

It has been shown that isothermal decomposition of austenite below  $M_s$  temperature after athermal martensite formation is in agreement with the kinetics of bainite formation above  $M_s$  temperature [55, 57]. Bainite in the form of extremely thin platelets was obtained by isothermal transformation at temperatures of approximately 200 °C, where diffusional transformation in a given time is not possible [58].

Figure 2.2 shows an overview of the total elongation and tensile strength relationship of third-generation AHSS as reported by De Moor *et al.* [59]. The tendency of decreasing total elongation with increasing tensile strength exhibits a large scatter. However, the maximum values indicate an upper limit for the considered steels. Rather high carbon content such as 0.4 mass % of the TBF/Q&P steels investigated by Matsumura *et al.* can result in comparably high strength-elongation combinations [29, 60]. TRIP-assisted steels with carbon contents of approximately 0.2 mass % show total elongations of up to 22% for a minimum tensile strength of 980 MPa according to the ASTM E-8 geometry [15]. For Q&P steels with a minimum tensile strength of 1180 MPa total elongations of approximately 16% are possible [42]. The high elongation levels obtained for TBF steels by Matsumura *et al.* are due to a high carbon content of 0.4 mass %.

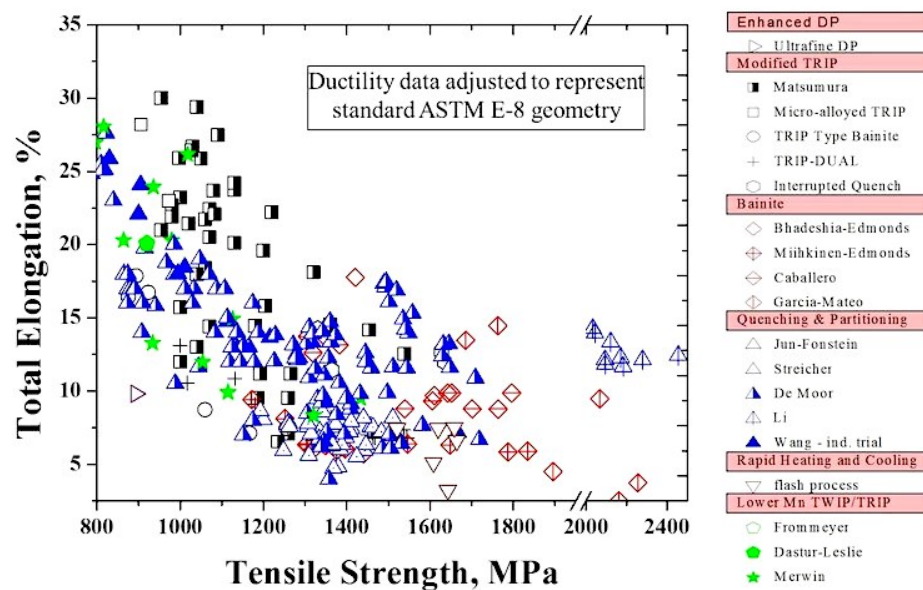


Figure 2.2: Overview of total elongation and tensile strength combinations obtained by different approaches with data adjusted to ASTM E8 standard specimen geometry [59].

Stretch-flangeability of TBF and Q&P steels shows the same decreasing tendency with increasing tensile strength as elongation for the same group of steels, for instance TRIP steels with polygonal ferritic matrix [61, 62]. However, significantly higher hole expansion strains are possible for steels with a bainitic and/or tempered martensitic matrix compared to TRIP-assisted steels with a matrix of polygonal ferrite [27].

Table 2.1 shows the mechanical properties of a TBF, a one-step Q&P, and four TRIP-assisted steels with polygonal ferrite matrix (TPF) reported by Nagasaka *et al.* [62]. The steels contain

1.5 mass % silicon, 1.5 mass % manganese and varying amounts of carbon. Increased carbon content results in considerably increased strength when the TPF steels are compared at the same overaging temperature. Interestingly, uniform and total elongation of all four TPF steels are nearly the same. This can be explained by the increase in the amount of retained austenite resulting from the higher carbon content. The expected loss in elongation as a consequence of higher strength is compensated by a gain in elongation from the TRIP effect. Hole expansion strains of the TPF steels, in contrast, decrease with increasing carbon content. The one-step Q&P steel with a tensile strength of 1154 MPa shows a strongly enhanced hole expansion strain of 40 % compared to 18 % of steel TPF4 with 50 MPa lower tensile strength. Even though held at a much higher overaging temperature of 450 °C, the hole expansion strain of the TBF steel with 0.2 mass % carbon is comparable to the hole expansion strain of TPF3, which exhibits a 20 MPa lower tensile strength, contains 0.3 mass % carbon, and was held at 400 °C overaging temperature. This evidently manifests the contribution of a harder martensitic and/or bainitic matrix to the improvement of stretch-flangeability compared to the steel grades with a ferritic matrix.

Table 2.1: Carbon content, overaging temperature, and mechanical properties including hole expansion strains of TBF/one-step Q&P, and TPF steels, reported by Nagasaka *et al.* [62].

Steel	C [mass %]	$T_{oa}$ [°C]	$R_{p02}$ [MPa]	$R_m$ [MPa]	$A_u$ [%]	$A_{25}$ [%]	$\lambda$ [%]
One-step Q&P	0.2	375	971	1154	4.4	7.8	40
TBF	0.2	450	617	918	14.2	18.2	23
TPF1	0.1	400	429	651	27.8	37.2	58
TPF2	0.2	400	526	825	31.7	36	40
TPF3	0.3	400	562	895	28.6	32.2	24
TPF4	0.4	400	728	1103	29.6	32.8	18

## 2.2 Alloying elements in TBF and Q&P steels

### 2.2.1 Carbon

As an austenite stabilizer, carbon enlarges the austenite region in CCT and TTT diagrams in particular to lower transformation temperatures [63]. The driving force for diffusive and displacive fcc-bcc transformations is reduced. As a result, kinetics of these transformations is decelerated by the addition of carbon [64]. Carbon diffuses faster in ferrite than in austenite by orders of magnitude [46]. Since the solubility of carbon in fcc is greater than in bcc, the carbon diffuses into, enriches, and stabilizes austenite against transforming into martensite during overaging or final cooling [37]. This partitioning process makes it possible to obtain higher amounts of retained austenite in TBF and Q&P steels with greater stability against martensite transformation.

In addition to the deceleration of bainite transformation kinetics, carbon influences the bainite and martensite morphology. Pickering reported that the transition temperature between upper and lower bainite transformation first increases, then decreases until it remains constant with increasing carbon content [65]. Plates tend to form in both martensite and bainite at large carbon concentrations [46].

The hardness of a bainitic or martensitic matrix increases with increasing carbon content [45]. Therefore, carbon is used to increase hardness and strength of TBF and Q&P steels. Higher carbon content in the retained austenite results in its stabilization and thereby improves the strain-hardening behaviour resulting in elevated elongation and  $n$ -values (Section 2.3.2).

### 2.2.2 Silicon

Silicon partitions to and stabilizes ferrite [66, 67]. As a result, the  $A_3$  temperature is increased by silicon additions [49]. The ferrite-stabilizing effect refers to ortho-equilibrium at high temperature, where all elements can diffuse relevant distances. The same tendency was observed in weaker form for overaging temperatures, at which the diffusion of substitutional elements such as silicon is negligible [52].

Silicon prevents carbon from precipitating in the form of iron carbides, most commonly cementite [48–52]. This role is of critical importance for TBF and Q&P steels, since the carbon stabilizes the austenite during overaging, which results in favourable amounts of retained austenite of desirable stability [16, 64, 68]. For instance during the formation of upper bainite, the formation of interlath cementite can be suppressed by addition of silicon in a way that high-carbon interlath retained austenite is obtained instead [69]. Furthermore, Owen *et al.* [49] reported, that three decomposition stages are present during overaging of steels with 0.5 to 1.2 mass % carbon. During the first stage, martensite decomposes to  $\epsilon$ -carbide in pseudo-equilibrium with low carbon martensite. The second stage involves the formation of bainite and the third stage is characterized by the formation of cementite and ferrite. A silicon content of up to 2.2 mass % was investigated. It was found that much higher overaging temperatures are required to trigger third-stage decomposition in the presence of silicon. [49].

Jacques *et al.* found that silicon addition of 1.5 mass % retards cementite formation during bainite transformation at 350 to 400 °C [64]. 0.38 mass % Si was insufficient for carbon enrichment of the austenite [64]. However, it has been proven possible to achieve nearly 10 vol. % retained austenite with this silicon content in combination with 0.18 mass % carbon and 1.3 mass % manganese for an overaging temperature of 370 °C and a short overaging time of 15 s. The suppression of carbon precipitation by silicon additions decelerates bainite transformation [64]. Previous research on the effect of silicon in para- and ortho-equilibrium conditions showed that para-equilibrium is one condition for the retardation of cementite such that silicon must be trapped in cementite [52]. However, this criterion is insufficient, and lattice defects are required to reduce the amount of carbon available for precipitation [52].

Despite the important positive effects of silicon on TBF and Q&P steels mentioned above, great effort has been put into the reduction of the silicon content because a high silicon content results in silicon-oxides on the strip surface. These oxides can be picked up by the rolls of the production line and leave traces on the subsequent steel strips [70, 71].

### 2.2.3 Manganese

Manganese stabilizes the austenite [2]. All transformation temperatures in thermodynamic equilibrium are decreased through the addition of manganese [72]. Concerning kinetics, manganese decreases the diffusivity of carbon in the austenite [53]. Increased manganese content drags the ferrite-austenite interface mobility [22, 73]. Cementite formation is decelerated by the addition of manganese [50, 74–76]. Once formed, however, manganese partitions to cementite easily [77–81].

Manganese strongly tends to macrosegregation [82–84]. For instance, high manganese contents can result in unfavourable band formation in TRIP steels [24, 85]. To avoid longitudinal manganese sulfides, which are particularly detrimental for edge formability, calcium is used to bind sulfur to form spherical particles.

TRIP, Q&P, and TBF steels in the literature are usually comprised of approximately 1.5 to 1.6 mass % manganese [13, 27, 86–88]. It was found that a manganese content of approximately 2.5 mass % is more useful for TRIP-assisted steels without polygonal ferrite than for steels with primarily bainitic and/or martensitic matrix due to its potential to stabilize austenite [89].

### 2.2.4 Chromium

While chromium thermodynamically stabilizes ferrite, it significantly slows all diffusion-controlled phase transformation kinetics, in particular at high temperatures [90, 91]. A shift of all isothermal phase transformations to longer times has been reported in the literature [92]. As a result, the amount of low-temperature transformation products such as martensite and lower bainite is higher for higher chromium contents.

Although chromium retards cementite formation [50, 74–76], it enriches in cementite [77, 78, 80, 81, 93–98]. The decomposition of martensite is inhibited by chromium additions providing enhanced tempering resistance, which enables to sustain the strength of the matrix during overaging. Chromium can be used to replace silicon in its function of preventing carbon precipitation, which indirectly contributes to increase the amount of retained austenite [99]. This helps to avoid detrimental silicon oxides on the sheet surface (Section 2.2.2).

### 2.2.5 Niobium

As one of the most important microalloying elements, niobium strongly contributes to grain refinement and precipitation hardening [100]. As described by the Hall-Petch relationship shown in Equation 2.6, grain refinement significantly increases a steel's strength [101–103]. In addition to microalloyed HSLA steels, this increase in strength as a result of niobium microalloying has also been observed in DP and TRIP steels [87, 104–107]. Grain refinement, furthermore, improves manufacturability, final properties, and performance of microalloyed steels [87, 107]. A higher amount of retained austenite was found in niobium-alloyed TRIP steels as a result of the grain refinement caused by niobium additions [104, 105]. This was explained by the formation of ferrite during cooling, which promotes carbon enrichment of the austenite.

The grain refinement through niobium additions is achieved by the pinning effect of secondary phase particles and/or the solute drag effect. The solute drag effect refers to the effect of solute atoms on grain boundaries. Finely dispersed precipitates such as niobium carbides and/or nitrides can also significantly pin the grain boundary [108]. When a grain boundary intersects a particle, a portion of the boundary is eliminated. A force is required to pull the boundary away from the particle, which lowers the grain boundary mobility [108].

The solubility of niobium monocarbides, mononitrides, and carbonitrides in austenite in equilibrium can be described by the solubility product [109]:

$$\log[\text{Nb}][\text{C}]^{C_1}[\text{N}]^{C_2} = C_3 - \frac{C_4}{T}, \quad (2.1)$$

where Nb, C, and N are the amounts of niobium, carbon, and nitrogen,  $C_{1-4}$  are fit parameters depending on the matrix composition, and  $T$  is the temperature. The main difference between the many existing solubility products is the method used to obtain a given solubility product, i.e. thermodynamic calculations or experimental separation of precipitates [100]. The actual amount and size of niobium precipitates during steel production in an industrial environment, however, can significantly deviate from equilibrium calculations and depend on formation kinetics, which can be described by sigmoidal phase transformation curves, such as the Johnson-Mehl-Avrami-Kolmogorov equation [110] (Section 5.2.2).

In the right amount and size niobium carbides provide important precipitation hardening [26, 111, 112]. The magnitude of precipitation strengthening is determined by size, shape, and volume fraction of the carbides or nitrides formed [113, 114]. Gladman introduced a model based on the Ashby-Orowan relationship, which allows estimation of particle size and volume fraction effects on precipitation strengthening [113]. An increase in strength by precipitation hardening of 240 MPa by 0.09 mass % niobium is predicted by the model. Experimental work shows that the full hardening

potential of niobium precipitation on strength is not achieved, because in practice some of the niobium precipitates in austenite at high temperatures and coarse niobium carbides do not contribute to precipitation hardening as opposed to finely dispersed niobium carbides [100, 115].

Finally, Sugimoto *et al.* reported, that grain refinement triggered by niobium additions can accelerate the bainite transformation [26]. Bainite morphology appeared much more globular in the TBF steels with niobium additions compared to the rather lath-like bainite of the TBF steels without niobium. Furthermore, an increase in non-martensitic fraction at low overaging temperatures due to niobium additions has been observed [26]. These changes in microstructure of the investigated TBF steels, result in enhanced total elongation through niobium addition, while tensile strength remains unaffected. stretch-flangeability can be significantly improved by niobium addition, especially for overaging at low temperatures of 300 to 350 °C [26].

## 2.3 Microstructure and mechanical properties of TBF and Q&P steels

The description of the mechanical properties of TBF and Q&P steels requires fundamental understanding of their microstructure. The following section provides an overview of the strength, the strain-hardening behaviour, and the failure mechanisms as a consequence of the microstructure of TBF and Q&P sheet steels.

### 2.3.1 Strength and strengthening mechanisms

Crystalline materials can be deformed plastically by the movement and formation of new dislocations [116]. To move a dislocation a critical shear stress needs to be applied. The required normal force to reach this critical shear stress depends on the orientation of the slip system. Due to the different orientations of the grains, the beginning of plastic deformation in polycrystalline materials, i.e. the yield strength, is reached as soon as the critical shear stress is exceeded in every grain [117].

The strength of a material can be increased by increasing the required stress to move or form new dislocations by the addition of lattice defects. It is therefore the superposition of the internal friction, also called Peierls-Nabarro stress to move a dislocation within the defect free lattice  $\sigma_0$  and the strengthening mechanisms taking place. A frequently used approach to calculating the strength is the assumption that the total strength is the sum of each strength contribution  $\Delta\sigma_i$  from different strengthening mechanisms [65]:

$$\sigma = \sigma_0 + \sum_i \Delta\sigma_i. \quad (2.2)$$

An important mechanism to increase the strength is solid solution strengthening. Praelastic, dielastic, and chemical interactions between the lattice and the substitutional element impair the dislocation glide resulting in higher strength of the material [118–120]. Solid solution strengthening via chemical interaction can be expressed by the so-called Suzuki effect [120]. Substitutional elements can lower the stacking fault energy by causing dislocations to move and increasing the distance between partial dislocations. This results in a higher stress required to move the dislocation increasing the overall strength of the material proportional to the square root of the alloying element concentration  $c_a$  [120]:

$$\Delta\sigma_c \propto \sqrt{c_a}. \quad (2.3)$$

At low alloy concentrations, the contribution of each alloying element to solid solution strengthening is typically estimated by an empirical approach of linear superposition:

$$\Delta\sigma_{\text{cl}} \propto \sum_a S_a c_a, \quad (2.4)$$

where  $S_a$  is a strengthening constant describing the extent of the contribution of each alloying element  $a$  to solid solution strengthening.

Further, the increase in dislocation density through plastic deformation contributes to impaired dislocation mobility. The strength is proportional to the dislocation density  $\rho$  as follows:

$$\Delta\sigma_\rho \propto \sqrt{\rho}. \quad (2.5)$$

The dislocation density of bainite is commonly higher than in polygonal ferrite, except for the dislocation density in highly deformed ferrite. In lower bainite the dislocation density is higher than in upper bainite, and martensite exhibits the highest dislocation density.

A smaller grain size results in a shorter mean free path for dislocation slip and dislocation pile up at grain boundaries. The increase in the strength of a material through grain refinement can be described by the Hall-Petch equation [102, 103]:

$$\Delta\sigma_{\text{HP}} \propto \frac{1}{\sqrt{d}}, \quad (2.6)$$

where  $d$  is the diameter of a sphere with equivalent volume to the volume of the grain. The Hall-Petch equation applies to polygonal ferrite. The strength of bainite, and martensite also increases with decreasing lath thickness down to very small lath thicknesses.

Non-metallic inclusions and precipitates can result in precipitation-strengthening. The additional strength necessary for a dislocation to bow around a particle is proportional to the particle volume fraction  $f$  and inversely proportional to the particle radius  $r$ , as described by the Orowan strengthening [101]:

$$\Delta\sigma_{\text{O}} \propto \frac{\sqrt{f}}{r}. \quad (2.7)$$

If the radius of the particle is smaller than a critical radius, and depending on whether it is a coherent or incoherent particle, the stress required to cut the particle can be smaller than to bow around it. The stress to cut a particle is proportional to the square root of its equivalent radius [121]:

$$\Delta\sigma_{\text{K}} \propto \sqrt{f} \cdot \sqrt{r}. \quad (2.8)$$

Since different phases in multiphase steels feature specific arrangements, the critical stress to move or form new dislocations varies from phase to phase. The empirical rule of mixture can be used to estimate the tensile strength of multiphase steels based on volume fraction  $f_i$  and strength  $\sigma_i$  of the respective phase  $p$ :

$$R_m = \sum_p f_i \sigma_i. \quad (2.9)$$

### 2.3.2 Strain-hardening behaviour

Strain-hardening is the increase in strength as a result of increasing formation of new dislocations, as described by Equation 2.5. Thus, the stress  $\sigma$  is a function of the dislocation density  $\rho$ . It can be quantified by applying the shear modulus  $G$ , the Burgers vector  $b$ , the dislocation density, and a geometry factor  $\alpha$  as follows:

$$\sigma = \sigma_0 + \alpha Gb\sqrt{\rho}. \quad (2.10)$$

The response of a material to stress is an increase in strain. The extent to which the stress increases with the strain can be expressed by strain-hardening rate  $\theta$ . The strain-hardening rate is the slope of the stress-strain curve defined by the increment of strength  $d\sigma$  divided by a given strain increment  $d\varphi$  [122]:

$$\theta = \frac{d\sigma}{d\varphi}, \quad (2.11)$$

In 1909, Ludwik postulated an equation, which is frequently used as one of the simplest empirical equations to describe the relationship between stress and logarithmic strain  $\varphi$  [123]:

$$\sigma = C\varphi^n, \quad (2.12)$$

where the  $n$ -value is the strain-hardening exponent typically given for a specific strain range. For instance,  $n_{4-6}$  represents the strain-hardening exponent for the strain range of 4 to 6%. The differential  $n$ -value  $n'$  can be derived from the strain-hardening exponent as follows:

$$n' = \frac{d \ln \sigma}{d \ln \varphi} = \theta \cdot \frac{\varphi}{\sigma}. \quad (2.13)$$

Plasticity and strain-hardening behaviour of multiphase materials can be described by dislocation models, continuum mechanics, and continuum dislocation mechanics. Ashby introduced a dislocation model based on geometrically necessary dislocations  $\rho_g$  [124, 125]. In this model, the dislocation density  $\rho$  is composed of statistically stored dislocations  $\rho_s$  and geometrically necessary dislocations:  $\rho = \rho_s + \rho_g$ . Statistically stored dislocations trap each other randomly. Geometrically necessary dislocations are required to accommodate the plastic shear gradients and to allow compatible deformation of two phases. Rigid cubic particles are assumed to be embedded in a deformable two-phase material. The density of geometrically necessary dislocations is proportional to the mean macroscopy shear strain. For cubic particles of the length  $a$  and the volume fraction  $f$ , the density  $\rho_g$  of geometrically necessary dislocations can be calculated as follows:

$$\rho_g = \frac{6\gamma f}{a \cdot b}. \quad (2.14)$$

This approach has been extended by Fischmeister and Karlsson to a case of coarse plastically deformable inclusions in a soft crystalline matrix [126, 127]. In this case, the density of geometrically necessary dislocations is composed of dislocations at the grain boundary  $\rho_{gb}$  and those caused by the deformation difference between inclusions and matrix  $\rho_i$ . The dislocation density at the grain boundary is proportional to the macroscopic mean deformation and inversely proportional to the mean free path of dislocation slip  $\lambda_{mf}$ :

$$\rho_{gb} \propto \frac{\gamma}{\lambda_{mf}}. \quad (2.15)$$

The dislocation density as a result of deformation difference between the inclusions of the volume fraction  $f$  and the matrix can be calculated as follows:

$$\rho_i = C_1 \cdot \frac{f}{1-f} \cdot \frac{\gamma - \gamma_i}{b\lambda_{mf}}, \quad (2.16)$$

where  $C_1$  is a constant and  $\gamma_i$  the shear deformation of the inclusions. The strength increase can be calculated by deploying the sum of both dislocation densities to Equation 2.5.

The second approach to describing plasticity and strain-hardening in multiphase materials is continuum mechanics. This approach exhibits some remarkable distinctions to dislocation models. Fischmeister and Karlsson state that the load transfer between two phases of different hardness is of higher importance for the strengthening of multiphase steels than the contribution of geometrically necessary dislocations [128]. Continuum mechanics accounts for this load transfer as opposed to dislocation models [129]. The most important difference between the approaches introduced herein is that dislocation based models by Ashby depend on the size of the particle or inclusion, while the continuum model introduced by Fischmeister and Karlsson is independent of the particle size. For the load transfer between two phases exposed to parallel loading in the elastic region, the strain  $\epsilon_\alpha$  in the elastically deformed phase  $\alpha$  is equal to the strain  $\epsilon_\beta$  in the elastically deformed phase  $\beta$  and equal to total strain  $\epsilon$  [128]:  $\epsilon_\alpha = \epsilon_\beta = \epsilon$ . As a result, the ratio between the stresses of the two elastically deformed phases  $\sigma_\alpha$  and  $\sigma_\beta$  is equal to the ratio between their elastic moduli  $E_\alpha$  and  $E_\beta$ :

$$\frac{\sigma_\beta}{\sigma_\alpha} = \frac{E_\beta}{E_\alpha}. \quad (2.17)$$

In the case of serial loading, the stresses in the two elastically deformed phases are equal to the total stress  $\sigma$ :  $\sigma_\alpha = \sigma_\beta = \sigma$ . Thus, in analogy to the parallel loading, the ratio between the strains of the two elastically deformed phases is equal to the ratio between their elastic moduli for the serial loading:

$$\frac{\epsilon_\beta}{\epsilon_\alpha} = \frac{E_\beta}{E_\alpha}, \quad (2.18)$$

where  $\epsilon_\alpha$  and  $\epsilon_\beta$  are the strains in phase  $\alpha$  and  $\beta$ , respectively. The following equations formulated by Tamura *et al.* [130] are empirical approaches to calculating total strain  $\bar{\epsilon}$  and total stress  $\bar{\sigma}$  applying the rule of mixture:

$$\bar{\sigma} = f_\alpha \sigma_\alpha + f_\beta \sigma_\beta, \quad (2.19)$$

$$\bar{\epsilon} = f_\alpha \epsilon_\alpha + f_\beta \epsilon_\beta. \quad (2.20)$$

These equations are in good agreement with empirical data [128]. However, both equations cannot be true in the elastic region. In the plastic region, the equations match empirical data more accurately, but are not justifiable. The stress and strain transfer between the two phases for any case between parallel and serial loading can be determined by the slope coefficient  $q$ :

$$q = \frac{\sigma_\beta - \sigma_\alpha}{\epsilon_\beta - \epsilon_\alpha}. \quad (2.21)$$

Figure 2.3 shows the stress-strain curves in each of the two phases as a function of volume fraction of each phase and the total stress-strain curve of both phases [128]. The size of the slope coefficient is determined by the relation between stress and strain transfer. A higher slope coefficient indicates a closer result to the parallel loading case. The lower the slope coefficient, the closer the situation to serial loading. In addition to the parameters given by Equation 2.21 such as volume fraction and flow stress, the slope coefficient depends on the geometry and the strain-hardening of the two phases.

In addition to Ashby's model, where the inclusion is rigid, the strength of matrix as well as inclusion can be varied employing the approach by Fischmeister and Karlsson [128], as illustrated by Figure 2.3.

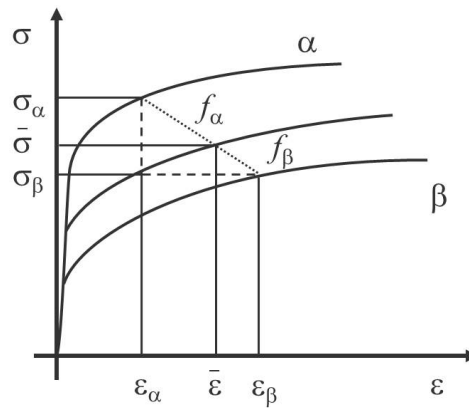


Figure 2.3: Stress and strain distribution between two phases according to Equation 2.19 and Equation 2.20 [128].

During SIMT of TRIP-assisted steels, the volume fraction of the hard martensite phase in the inclusion increases at the cost of the volume fraction of the softer austenite phase during straining. As demonstrated by Reisner and Fischer *et al.* [131, 132], the continuum mechanics approach allows to quantify the plastic deformation using finite element calculations accounting for the varying phase fractions during SIMT.

TBF and Q&P steels are multiphase steels containing retained austenite. As mentioned above, retained austenite transforms via SIMT during straining [47, 131, 133]. The strain-induced transformation from austenite to martensite involves a volume increase of the retained austenite/martensite inclusion. Geometrically necessary dislocations are required to compensate the misfit due to the volume change [124]. The additional increase in dislocation density results in particularly high strain-hardening and higher strength (Equation 2.10). As a result, the strength increment is higher for the corresponding strain increment, which is equivalent to an increase in strain-hardening rate (Equation 2.11). Since the required strain to initiate SIMT depends on the stability of the retained austenite, the impact of the TRIP effect on the strain-hardening behaviour depends on the retained austenite stability. The retained austenite stability is influenced by the amount of austenite stabilizing elements [68], in particular the carbon content [134, 135]. At very low carbon levels, the austenite transforms at very low strain levels, which was found to detrimentally affect total elongation of the steel [131]. For carbon concentrations over 1.8 mass %, some of the retained austenite can remain untransformed, thus, the TRIP effect is not entirely made use of [32].

The retained austenite stability is furthermore affected by the size of the retained austenite grains [68, 133, 134, 136, 137]. The influence of grain size on retained austenite stability results from the dependency of interfacial energy on the ratio between surface area and surface volume. The inclusion/matrix interface can pin dislocations in their movement. A critical stress has to be overcome to cut or surround the particle (Equation 2.3.1). The stress necessary to form new dislocations is frequently lower than to move existing pinned dislocations. Therefore, a higher surface area to volume ratio results in higher dislocation density per volume decreasing the interfacial energy for SIMT [68, 136, 137].

Finally, the shape or phase morphology of retained austenite as well as its location within the matrix has a significant impact on resistance of retained austenite to SIMT with the global strain applied to the steel. Lamellar retained austenite structure is more stable than equiaxed retained austenite grains [138], and retained austenite surrounded by a strong bainitic matrix is more resistant to martensite transformation than retained austenite surrounded by a weaker ferritic matrix [139].

### 2.3.3 Failure mechanism

#### Void formation at inclusions or precipitates

Ductile failure in steel consists of void nucleation, growth, and coalescence [140]. In multiphase steels in particular DP steels micro-voids are generated either by hard martensite cracking, also called cleavage, and/or by intergranular fracture, i.e. decohesion of the interfaces of the second phases [141, 142]. To initiate decohesion between a particle and its matrix, the elastic strain energy of the particle has to be greater or equal to the surface energy of the void that will be created [143–146]. This condition is necessary but insufficient. In addition, the maximum shear and/or normal stress at the particle interface has to exceed the critical stress at the inclusion/matrix interface to initiate void nucleation.

The maximum stress on a particle  $\sigma_{\max}$  in a matrix at the particle interface can be calculated as the sum of the maximum deviatoric stress  $s$ , the macroscopic mean-normal stress  $\sigma_m$ , and the elevated local stress  $\sigma_1$  [140, 143, 144]:

$$\sigma_{\max} = s + \sigma_m + \sigma_1. \quad (2.22)$$

This maximum stress on the particle needs to be at least equal to the surface energy of the void that will be created, in order for a void to nucleate [143, 144, 146].

Brown and Stobbs introduced a model based on geometrically necessary dislocations, which describes the elevated local stress on the particle interface as proportional to the square root of strain divided by the particle radius  $r$  [140]:

$$\sigma_1 \propto \sqrt{\frac{\epsilon b}{r}}. \quad (2.23)$$

Argon *et al.* reported an analysis of both non-hardening and linear-hardening plastic flow around a circular-cylindrical inclusion in a pure-shear deformation field. According to their model, a void can nucleate, if the maximum stress  $\sigma_{\max}$  at the inclusion/matrix interface is equal to a critical stress  $\sigma_c$  [145]:

$$\sigma_{\max} = \sigma_c. \quad (2.24)$$

The maximum stress  $\sigma_{\max}$  on the inclusion interface is given by the sum of the equivalent stress  $\sigma_e$  on the inclusion interface and the mean-normal stress:

$$\sigma_{\max} = \sigma_e + \sigma_m. \quad (2.25)$$

The equivalent stress can be calculated by the von Mises equation with the principal stresses  $\sigma_1$ ,  $\sigma_2$ , and  $\sigma_3$ , as follows [140, 147]:

$$\sigma_e = \frac{1}{2} [(\sigma_1 - \sigma_2)^2 + (\sigma_1 - \sigma_3)^2 + (\sigma_2 - \sigma_3)^2]^{1/2}. \quad (2.26)$$

#### Failure at phase boundaries in multiphase steels

Failure in multiphase steels can initiate at boundaries between phases of strong hardness differences or by cracking within the hard phase [148–150]. Employing continuum mechanics by means of finite element based micromechanical models is valuable to describe and understand plasticity and failure in particular regarding steels with high phase contrasts such as dual phase steels [141, 142, 148, 151]. Kremaszky *et al.* developed a micromechanical model to describe the deformation behaviour of DP steels [148]. The flow behaviour described by this model is assumed as elastoplastic with isotropic

hardening [152], and the onset of necking is defined by the classical Considère instability criterion [153]. The contiguity was used to describe the neighboring relationship of the phases [154]. It was found that a lower strength ratio between ferrite and the second phase, for instance by replacing the hard martensite by tempered martensite, reduces the strained region and the strain level in the ferrite [148]. Furthermore, the arrangement of the second phase is highly important for the strain distribution in the ferrite. More heterogeneous banding-like distribution of the second phase, i.e. retained austenite and/or martensite, results in a larger strained region and higher maximal strains [148].

In further studies a computer model based on continuum mechanics was developed to systematically study the microdamage behaviour of different dual or complex phase microstructures [142]. The complete microstructure simulation involves a parameter-controlled difference quotient-based colouring algorithm, Voronoi tessellation, geometry generation, meshing, finite element discretization, and postprocessing. The failure criterion implemented into the model's post processing routine anticipates failure when a critical stress is exceeded by the stress density function at the ferrite/martensite and martensite/martensite interfaces.

All results obtained from the models are in full agreement with correlation between microstructure, which was identified by optical and scanning electron microscopy, and failure mechanism characterized by tensile testing and hole expansion [141, 142]. The comparison of experimental results with the predictions from the simulation allowed to draw the following conclusions: First, the mechanical heterogeneity of a multiphase steel shows the highest impact on the hole expansion strain [141]. Mechanical heterogeneity depends on the hard phase fraction and the phase strength contrast [141, 142]. Low mechanical heterogeneity causes high hole expansion strains [141]. A strong banded structure also results in lower hole expansion values [142]. Second, for phase fraction of martensite of less than 40 % the model predicts higher hole expansion for lower contiguities [141]. Strong clustering of martensite for more than 40 % martensite furthermore causes high hole expansion strains. Almost fully martensitic or tempered martensitic structures result in excellent hole expansion [141, 142]. Third, the model predicts a decrease in hole expansion strains for elevated prestrain [141, 142]. Finally, the hole expansion strain was found to depend on the overall strength level of the material. Microstructures with higher overall strength levels show higher hole expansion strains [141, 142].

### Void growth

The stress-free surface of the void after nucleation causes elevated localized stress and strain concentrations in the surrounding plastic field. These stress and strain concentrations cause the growth of voids upon continuing plastic deformation. Rice *et al.* [155] report a model to calculate the growth rate  $\dot{r}$  of a spherical void with the radius  $r$ ,

$$\dot{r} = r \cdot \left[ C_2 \dot{\epsilon}_x + \sqrt{\frac{2}{3}} \dot{\epsilon}_y f \left( \frac{\sigma_m}{Y} \right) \right], \quad (2.27)$$

where  $C_2$  is a constant depending on the size of  $\sigma_m$  and the hardening type, linear or non-linear hardening,  $\epsilon_x$  and  $\epsilon_y$  are strains in  $x$  and  $y$  direction,  $f(\frac{\sigma_m}{Y})$  is a function of  $\frac{\sigma_m}{Y}$  also depending on the hardening type,  $\sigma_m$  is the mean-normal stress, as introduced in Section 2.3.3, and  $Y$  is the yield stress [155]. In this model, the interaction between voids is assumed to be negligible. Since the voids are highly elongated with elliptical cross-sections and the elongation of the voids increases with increasing total strain, it is useful to introduce the Lode constant  $\nu = -\frac{3\epsilon_y}{\epsilon_x - \epsilon_z}$  as well as the incompressibility equation  $\dot{\epsilon}_x + \dot{\epsilon}_y + \dot{\epsilon}_z = 0$ . With the Lode constant and the incompressibility equation, the three principal radii and the mean radius of the voids can be derived from the integration of Equation 2.27 [155]. Applying a specific  $\frac{\sigma_m}{Y}$  to the non-linear and linear-hardening states, the

model shows good agreement with experimental results [156]. For higher strains the results from a dual-population void nucleation model match even better with the experimental values [155].

### Void coalescence

Void coalescence is characterized by a sudden catastrophic coalescence of microvoids that nucleate and grow at the sites of inclusions [140]. During this internal necking process, the fracture surface is mathematically equivalent to a stationary discontinuity in the plastic velocity-field [157].

The onset of internal necking can be identified by a critical condition for microvoid coalescence. Thomason *et al.* [158] report a dependency of the plastic limit-load failure of the intervoid matrix on the volume fraction of voids  $f_v$  given as follows:

$$\sigma_n (1 - \sqrt{f_v}) = \sigma, \quad (2.28)$$

where  $\sigma_n$  is critical mean stress for the initiation of internal necking and  $\sigma$  is the total stress.

# Chapter 3

## Experimental Procedure

### 3.1 Laboratory production of annealed sheets

#### 3.1.1 Material

In this work, TBF and Q&P steels with silicon contents below 1 mass % and chromium additions of approximately 0.3 mass % were investigated, since literature on this subject is missing to this date, despite the critical importance to reduce the silicon content of these steels. To investigate the influence of alloying elements on phase transformations, microstructure and mechanical properties, laboratory melts for TBF and Q&P sheet steels with two different strength levels were planned. One group was designed for a minimum tensile strength of 980 MPa, termed 980 grade in the following, and the other was chosen for 1180 MPa minimum tensile strength, named 1180 grade. For each of these groups a base composition was developed, as shown in Table 3.1. The composition of each laboratory melt for the 980 grade and the 1180 grade is given in Table 3.2 and Table 3.3, respectively. To achieve the elevated strength level, a higher carbon content and a slightly higher manganese content was chosen for the 1180 grade. Carbon, silicon, manganese, and chromium were varied within the following ranges: 0.16 to 0.2 mass % carbon, 0.7 to 1.0 mass % silicon, 2.2 to 2.6 mass % manganese, 0.01 to 0.4 mass % chromium. A niobium content of 0.02 to 0.09 mass % was added to the niobium-free base compositions. To avoid deviations within the composition of each group, three or four melts were cast from the main melt, subsequently increasing the content of the investigated element.

Table 3.1: Base composition of the investigated steel grades [mass %].

Steel	C	Si + Cr	Mn + Mo	Nb	P	S	N
980 grade	0.15 - 0.20	0.9 - 1.3	2.1 - 2.5	< 0.05	< 0.01	< 0.01	< 0.007
1180 grade	0.17 - 0.22	1.0 - 1.4	2.3 - 2.7	< 0.05	< 0.01	< 0.01	< 0.007

#### 3.1.2 Production of cold-rolled sheets

To obtain material for mechanical testing, air-cast ingots were hot-rolled in a two-step procedure. In the first step 400 mm x 150 mm x 150 mm cuboids were hot-rolled to 38 mm thickness. The strips were reheated to 1180 °C and hot-rolled to 4 mm thickness in the second step. A finish rolling temperature of around 900 °C and a coiling temperature of 650 °C were chosen for the hot rolling process. The steels were then cold-rolled with forward tension to a thickness of 1 mm. Samples for chemical analysis, dilatometer samples, and samples for laboratory annealing simulations were cut from the as-cold-rolled strips.

Table 3.2: Composition of the investigated laboratory TBF and Q&amp;P steels designed for a minimum tensile strength of 980 MPa [mass %].

Steel	C	Si	Cr	Mn + Mo	Nb	P	S	N
0.7Si980	0.15 - 0.20	0.7	< 0.5	2.1 - 2.5	< 0.05	< 0.01	< 0.01	< 0.007
0.8Si980	0.15 - 0.20	0.8	< 0.5	2.1 - 2.5	< 0.05	< 0.01	< 0.01	< 0.007
0.9Si980	0.15 - 0.20	0.9	< 0.5	2.1 - 2.5	< 0.05	< 0.01	< 0.01	< 0.007
1.0Si980	0.15 - 0.20	1	< 0.5	2.1 - 2.5	< 0.05	< 0.01	< 0.01	< 0.007
Steel	C	Si + Cr	Mn	Mo	Nb	P	S	N
2.2Mn980	0.15 - 0.20	0.9 - 1.3	2.2	< 0.3	< 0.05	< 0.01	< 0.01	< 0.007
2.4Mn980	0.15 - 0.20	0.9 - 1.3	2.4	< 0.3	< 0.05	< 0.01	< 0.01	< 0.007
2.5Mn980	0.15 - 0.20	0.9 - 1.3	2.5	< 0.3	< 0.05	< 0.01	< 0.01	< 0.007
Steel	C	Si	Cr	Mn + Mo	Nb	P	S	N
0.01Cr980	0.15 - 0.20	0.6 - 1.0	0.01	2.1 - 2.5	< 0.05	< 0.01	< 0.01	< 0.007
0.2Cr980	0.15 - 0.20	0.6 - 1.0	0.2	2.1 - 2.5	< 0.05	< 0.01	< 0.01	< 0.007
0.4Cr980	0.15 - 0.20	0.6 - 1.0	0.4	2.1 - 2.5	< 0.05	< 0.01	< 0.01	< 0.007
Steel	C	Si + Cr	Mn + Mo	Nb	P	S	N	
0Nb980	0.15 - 0.20	0.9 - 1.3	2.1 - 2.5	< 0.002	< 0.01	< 0.01	< 0.007	
0.025Nb980	0.15 - 0.20	0.9 - 1.3	2.1 - 2.5	0.025	< 0.01	< 0.01	< 0.007	
0.045Nb980	0.15 - 0.20	0.9 - 1.3	2.1 - 2.5	0.045	< 0.01	< 0.01	< 0.007	
0.09Nb980	0.15 - 0.20	0.9 - 1.3	2.1 - 2.5	0.090	< 0.01	< 0.01	< 0.007	

Table 3.3: Composition of the investigated laboratory TBF and Q&amp;P steels designed for a minimum tensile strength of 1180 MPa [mass %].

Steel	C	Si + Cr	Mn + Mo	Nb	P	S	N	
0.16C1180	0.16	1.0 - 1.4	2.1 - 2.5	< 0.05	< 0.01	< 0.01	< 0.007	
0.18C1180	0.18	1.0 - 1.4	2.1 - 2.5	< 0.05	< 0.01	< 0.01	< 0.007	
0.21C1180	0.2	1.0 - 1.4	2.1 - 2.5	< 0.05	< 0.01	< 0.01	< 0.007	
Steel	C	Si	Cr	Mn + Mo	Nb	P	S	N
0.8Si1180	0.17 - 0.22	0.8	< 0.5	2.3 - 2.7	< 0.05	< 0.01	< 0.01	< 0.007
0.9Si1180	0.17 - 0.22	0.9	< 0.5	2.3 - 2.7	< 0.05	< 0.01	< 0.01	< 0.007
1.0Si1180	0.17 - 0.22	1	< 0.5	2.3 - 2.7	< 0.05	< 0.01	< 0.01	< 0.007
Steel	C	Si + Cr	Mn	Mo	Nb	P	S	N
2.2Mn1180	0.17 - 0.22	1.0 - 1.4	2.2	< 0.3	< 0.05	< 0.01	< 0.01	< 0.007
2.4Mn1180	0.17 - 0.22	1.0 - 1.4	2.4	< 0.3	< 0.05	< 0.01	< 0.01	< 0.007
2.6Mn1180	0.17 - 0.22	1.0 - 1.4	2.6	< 0.3	< 0.05	< 0.01	< 0.01	< 0.007
Steel	C	Si	Cr	Mn + Mo	Nb	P	S	N
0.01Cr1180	0.17 - 0.22	0.6 - 1.0	0.01	2.3 - 2.7	< 0.05	< 0.01	< 0.01	< 0.007
0.1Cr1180	0.17 - 0.22	0.6 - 1.0	0.1	2.3 - 2.7	< 0.05	< 0.01	< 0.01	< 0.007
0.2Cr1180	0.17 - 0.22	0.6 - 1.0	0.2	2.3 - 2.7	< 0.05	< 0.01	< 0.01	< 0.007
0.4Cr1180	0.17 - 0.22	0.6 - 1.0	0.4	2.3 - 2.7	< 0.05	< 0.01	< 0.01	< 0.007
Steel	C	Si + Cr	Mn + Mo	Nb	P	S	N	
0Nb1180	0.17 - 0.22	1.0 - 1.4	2.3 - 2.7	< 0.002	< 0.01	< 0.01	< 0.007	
0.02Nb1180	0.17 - 0.22	1.0 - 1.4	2.3 - 2.7	0.02	< 0.01	< 0.01	< 0.007	
0.04Nb1180	0.17 - 0.22	1.0 - 1.4	2.3 - 2.7	0.04	< 0.01	< 0.01	< 0.007	
0.08Nb1180	0.17 - 0.22	1.0 - 1.4	2.3 - 2.7	0.08	< 0.01	< 0.01	< 0.007	

### 3.1.3 Annealing cycles

The cold-rolled heavily deformed ferritic-pearlitic microstructure of TBF and Q&P steels was fully austenitized followed by the quenching and overaging step. As-cold-rolled samples of all 980 and 1180 grade TBF laboratory melts were heated with 25 K/s, fully austenitized at 900 °C, cooled at 50 K/s to overaging temperature  $T_{oa}$ . Further, the samples were held at various temperatures in the bainitic region and below  $M_s$  temperature between 350 and 475 °C applying overaging times  $t_{oa}$  from 30 to 600 s and finally quenched to room temperature with 50 K/s (Figure 3.1).

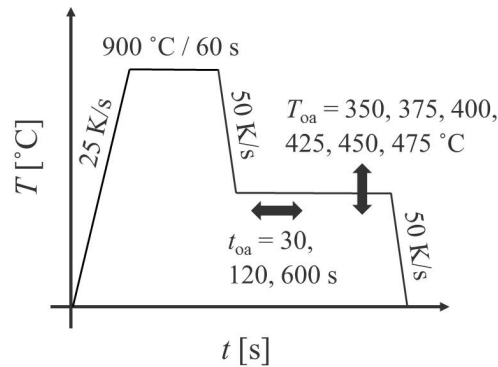


Figure 3.1: Laboratory annealing cycles for the investigated TBF and one-step Q&P steels.

### 3.1.4 Laboratory annealing of industrially cold-rolled sheets

Detailed investigations on the influence of alloying elements on microstructure and mechanical properties provided the base for the industrial production of a selected 980 grade with the most promising mechanical properties. The industrial manufacturability of this 980 grade was demonstrated by the successful production of steel IN980 (Table 3.4). In this work, selected laboratory annealing cycles were carried out on the industrially produced IN980.

Table 3.4: Composition of the industrially produced 980 grade [mass %].

Steel	C	Si + Cr	Mn + Mo	Nb	P	S	N
IN980	0.15 - 0.20	0.9 - 1.3	2.1 - 2.5	< 0.05	< 0.01	< 0.01	< 0.007

The influence of quench temperature and time at quench temperature on microstructure and mechanical properties of two-step Q&P heat-treated steels was studied applying the annealing cycle given in Figure 3.2. The cold-rolled sheets were fully austenitized, rapidly cooled to quench temperature with a cooling rate of 80 K/s, followed by reheating, overaging, and finally quenching to room temperature. Quench temperatures of 260, 280, 300, 320, 340, 360, and 380 °C were applied to steel IN980 for a time at quench temperature of 3 s. In further trials, this steel was held at selected times at quench temperature of 0, 2, 4, 8, 20, and 40 s at a quench temperature of 350 °C.

A polygonal ferritic matrix is commonly known to be less attractive for edge crack formability than a bainitic and/or martensitic matrix. In this study, the influence of polygonal ferrite on mechanical properties of TRIP-aided steels with primarily bainitic and/or martensitic matrix has been investigated. The importance of avoiding polygonal ferrite as a microstructure component of these steels was evaluated. The influence of the amount of polygonal ferrite on mechanical properties of these steels was quantified. Two different ways were applied to introduce polygonal ferrite into the microstructure, see Figure 3.3. The first approach involves an additional holding step at a

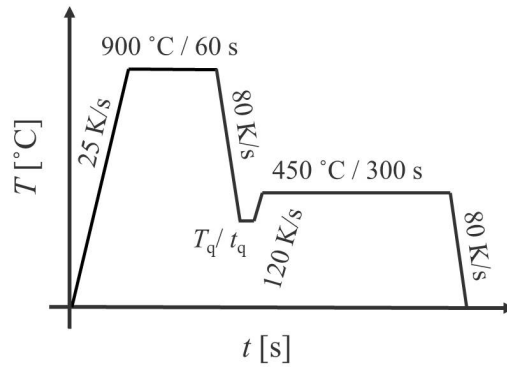


Figure 3.2: Two-step Q&P cycles with varying quench temperature  $T_q$  and time at quench temperature  $t_q$ .

temperature  $T_f$ , where polygonal ferrite forms, that is between  $A_3$  and bainite start temperature  $B_s$  (Figure 3.3a). Holding temperatures of  $T_f = 525^\circ\text{C}$  and  $625^\circ\text{C}$  and holding times of  $t_f = 2, 6, 10,$  and  $40\text{ s}$  were chosen to adjust the desired amount of polygonal ferrite. In further trials, the annealing temperature ( $T_{an}$ ) was set close to and below the  $A_3$  temperature to provoke polygonal ferrite by intercritical annealing (Figure 3.3b). For this purpose, cold-rolled sheets of grade IN980 were annealed at  $T_{an} = 780, 790, 800, 810, 820,$  and  $900^\circ\text{C}$  for  $120\text{ s}$ . The sheets were then quenched to overaging temperature  $T_{oa} = 400^\circ\text{C}$  with a cooling rate of  $80\text{ K/s}$ , isothermally held for  $600\text{ s}$  and quenched to room temperature at  $50\text{ K/s}$ .

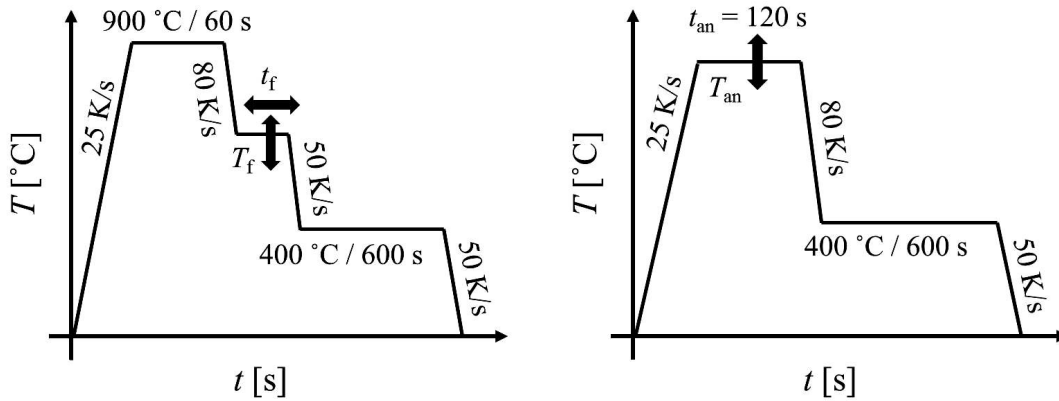


Figure 3.3: Annealing cycles (time-temperature schedules) applied to introduce polygonal ferrite into the matrix a) via an additional holding step upon continuous cooling at holding temperature  $T_f$  for holding time  $t_f$  and b) via intercritical annealing at annealing temperature ( $T_{an}$ ).

## 3.2 Industrial production of annealed sheets

### 3.2.1 Material

A key challenge in the present work is the industrial realization of a grade with a minimum tensile strength of  $1180\text{ MPa}$  and reduced silicon content offering both excellent deep drawability as well as outstanding edge formability. Based on the results from the laboratory experiments, a composition

was chosen which provides the most preferable mechanical properties and supports a cost-effective industrial production of the grade. Microstructure and mechanical properties of the benchmark grade, IN1.5Si1180, containing 1.5 mass % silicon and the newly developed grade, IN0.9Si1180, with chromium additions and a silicon content  $< 1$  mass %, were compared and their advantages were carefully evaluated. The chemical compositions of the industrially produced 1180 sheet steel grades used in this work are shown in Table 3.5.

Table 3.5: Composition of the industrial steel grades in mass %.

Steel	C	Si	Cr	Mn + Mo	Nb	P	S	N
IN1.5Si1180	0.17 - 0.22	1.5	$< 0.2$	2.3 - 2.7	$< 0.05$	$< 0.01$	$< 0.01$	$< 0.007$
IN0.9Si1180	0.17 - 0.22	0.9	$< 0.6$	2.3 - 2.7	$< 0.05$	$< 0.01$	$< 0.01$	$< 0.007$

### 3.2.2 Production of cold-rolled sheets

Slabs of the compositions given in Table 3.5 were produced in a continuous caster. The slabs were reheated followed by hot rolling in a one-stand roughing mill with five reverse strokes and a seven stand finishing mill. The final hot rolling temperature was approximately  $900^{\circ}\text{C}$  and the coiling temperature approximately  $600^{\circ}\text{C}$ . To reduce the required cold rolling forces, the hot-rolled bands were batch annealed at a temperature of  $600$  or  $650^{\circ}\text{C}$ . The tensile strengths before and after batch annealing were approximately  $1200$  to  $1250$  MPa and  $650$  to  $700$  MPa, respectively. The batch annealed bands were cold-rolled in a five stand cold rolling mill to the final thicknesses  $s_t$  of  $1$ ,  $1.2$ , and  $1.4$  mm. Finally, the cold-rolled strips were annealed in a continuous annealing line.

### 3.2.3 Annealing cycles

The cold-rolled strips were annealed in the continuous annealing line of voestalpine Stahl. In this line the strips were electrolytically cleaned and annealed in a protective atmosphere of  $95\%$   $\text{N}_2$  and  $5\%$   $\text{H}_2$ . The annealing process consists of heating, soaking, slow jet gas cooling, rapid jet gas cooling, overaging, and final cooling. The time-temperature schedules of the annealing cycles are shown in Figure 3.4a. An annealing temperature of  $850^{\circ}\text{C}$ , a slow jet cooling temperature of  $720^{\circ}\text{C}$ , and a strip speed of  $80$  m/min were chosen. Three overaging temperatures,  $360$ ,  $380$ , and  $400^{\circ}\text{C}$  were applied, and a quench temperature range of  $280$  to  $380^{\circ}\text{C}$  was investigated. Within one coil the quench temperature was lowered up to five times in steps of  $10$  to  $20$  K (Figure 3.4b). The annealed sheets were finished in a skin-pass mill.

## 3.3 Microstructure characterization and mechanical testing

### 3.3.1 Metallography

Microstructures were evaluated by optical microscopy (OM), field emission gun-scanning electron microscopy, and transmission electron microscopy (TEM). The OM samples were etched using LePera's etchant, one half of which consists of  $1\%$   $\text{Na}_2\text{S}_2\text{O}_5$  in aqueous solution and the other half of  $4\%$  picric acid in ethanol [159]. This etching technique enables to distinguish between the bainitic and/or (tempered) martensitic matrix, the polygonal ferrite, and the retained austenite/martensite inclusions. The examinations were conducted on a Zeiss Observer Z1m Axio with  $500\times$  and  $1600\times$  magnification.

For scanning electron microscopy observations, the samples were mechanically polished using first silicon oxide paper (STRUERS OPS) with different grain sizes of grits  $320$ ,  $800$ ,  $1200$ , and  $2400$ ,

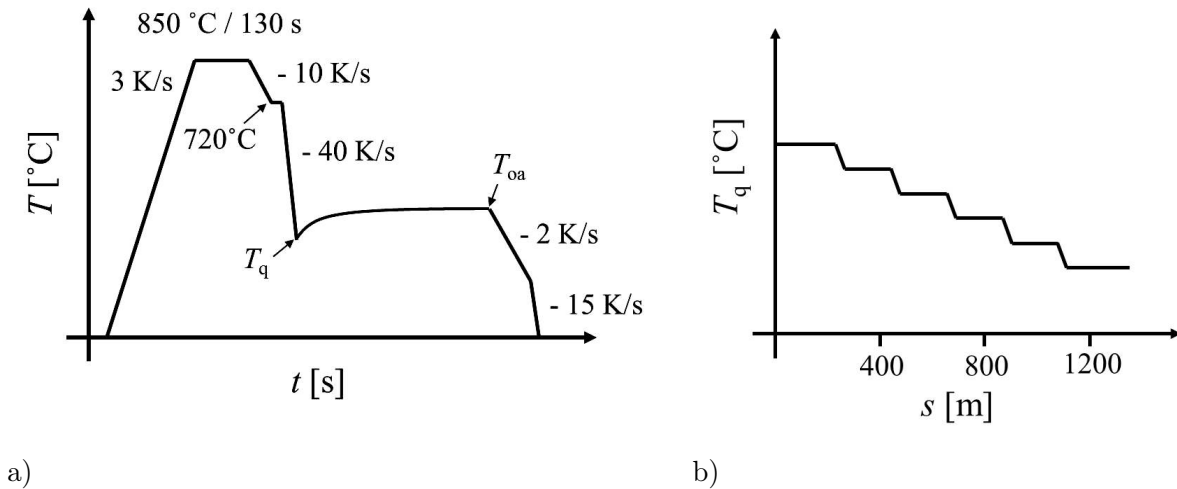


Figure 3.4: a) Industrial annealing cycle (time-temperature schedule) of the continuous annealing line, b) scheme of the quench temperature as a function of strip position  $s$ .

then water rinsed followed by air pressure cleaning the surface in between the different grit steps. Subsequently, mechanical polishing on a Struers Rotoforce was conducted using Struers MOL  $3 \mu\text{m}$  diamant spray and ethanol for 4 minutes in the first step and Struers MOL  $1 \mu\text{m}$  diamant spray and ethanol for 4 min in a second step. After intermediate etching with 5% Nital, i.e. ethanol with 5 vol. %  $\text{HNO}_3$ , for 10 s, a final mechanical polishing step was conducted using Struers MOL  $1 \mu\text{m}$  diamant spray and ethanol for 4 min. Finally, the samples were electropolished with the Struers LectroPol using 750 ml ethanol (96 vol. %), 50 ml distilled water, 80 ml perchloric acid and 5 g citric acid monohydrate at a temperature of  $5 \text{ }^{\circ}\text{C}$ .

A field emission scanning electron microscope, Zeiss SUPRA 25, equipped with both in-lens and secondary electron detector was used for scanning electron microscopy (SEM). Electrons with rather small emission angle to the sample surface were collected by applying high voltages of up to 10 keV. In this study, the in-lens detector has been used for SEM images, if not indicated otherwise.

In preparation for TEM the samples were produced by mechanical grinding up to a graining of 2400 using 3 mm diameter disks followed by electropolishing in acetic acid with 5-10% perchloric acid. TEM examinations were carried out with a voltage of 200 kV on a STEM Philips CM20 and a high resolution TEM Tecnai F20.

Finally, energy-dispersive X-ray spectroscopy (EDX) was employed to characterize the chemical composition of selected areas of the observed sample surface, in particular to determine the type of inclusions.

### Quantitative void analysis

The quantitative void analysis was conducted by applying the secondary detector of the Zeiss SUPRA 25, which runs on only 300 eV barely accelerating the electrons towards the detector. This detector is recommended for void detection as it reduces the contrast between the microstructural components and between matrix and inclusions, while the voids remain clearly visible. Figure 3.5 shows examples of SEM images used for quantitative void analysis and taken by applying the secondary electron detector.

For qualitative and quantitative void analysis, the tested tensile samples were cut in the middle of the width of the sample and the surface of the cut was examined within the necking area in the

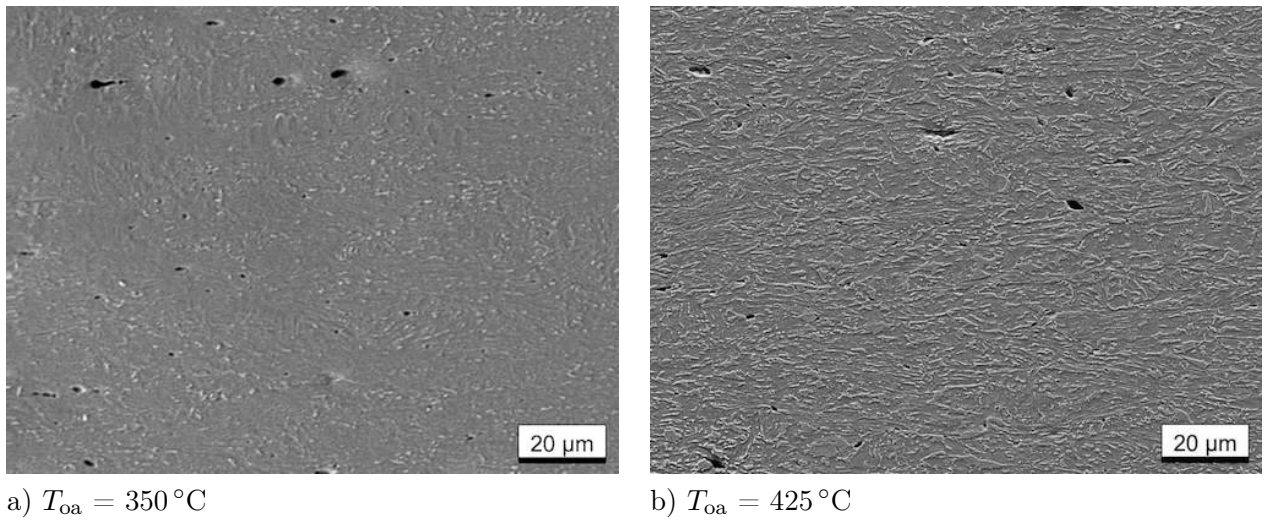


Figure 3.5: Scanning electron micrographs as used for quantitative void analysis of steel 0Nb1180 for selected distances to the fracture surface and overaging temperatures  $T_{\text{oa}} = 350\text{ °C}$  and  $425\text{ °C}$  (SE2 detector, Zeiss SUPRA 25).

middle of the thickness. SEM images were taken of the cross section in the middle of the thickness in  $200\text{ }\mu\text{m}$  steps to the fracture surface. The size of each void and the number of voids in each micrograph was determined using the software ImageJ [160]. The void density was determined from the number of voids within each SEM image divided by its area of  $0.2\text{ mm}$  by  $0.15\text{ mm}$ .

### 3.3.2 Magnetic measurements

The amount of retained austenite was measured by means of saturation magnetization method (SMM), also called Joch-Isthmus method [161, 162]. In this method a flux sensing measurement coil is exposed to a high homogeneous magnetic field. When a magnetic specimen is pushed through the surrounding coaxial measurement coil, the integral of the voltage pulse  $U_{\text{ind}}$  is induced in the coil. The magnetization  $J$  can be calculated from this voltage pulse in the following way:

$$J = \frac{\int U_{\text{ind}} dt}{\frac{N}{l} V}, \quad (3.1)$$

where  $N$  is a device and calibration constant,  $l$  is the length of the measurement coil and  $V$  is the volume of the specimen. To calculate the actual amount of retained austenite, a reference magnetization is required. The reference magnetization is the magnetization of a specimen with the same composition and without retained austenite in the microstructure. It can either be obtained from a measurement or a calculation based on fittings from measurements. In this work, the following equation was applied to calculate the reference magnetization  $J_{\text{ref}}$ :

$$J_{\text{ref}} = J_{\text{Fe}} - \sum_i \alpha_i \cdot A_i. \quad (3.2)$$

$J_{\text{Fe}}$  is the magnetization of pure iron ( $2.158\text{ T}$ ),  $\alpha_i$  is the reference factor of element  $i$  given in Table 3.6 and  $A_i$  is the amount of the alloying element in volume percent.

Applying equations 3.1 and 3.2 it is possible to determine the amount of retained austenite  $f_\gamma$  by measuring the voltage pulse of a specimen pushed through the yoke:

$$f_{\gamma} = \frac{J_{\text{ref}} - J}{J_{\text{ref}}} \cdot 100\%. \quad (3.3)$$

Table 3.6: Austenite reference element factors  $\alpha_i$  in T/% for the calculation of the reference magnetization (Equation 3.2).

Alloying Element	C	Si	Mn	Al	Cr	Mo
Reference Factor	0.15	0.048	0.0244	0.057	0.0305	0.600

### 3.3.3 X-ray diffraction

Carbon content of the retained austenite and phase fractions were determined by employing the X'Pert Pro PANalytic X-ray diffractometer. After polishing with silicon oxide paper, the same procedure as already described for the SEM samples was used, with the exception of electropolishing. Four peaks each of austenite and ferrite were monitored. The intensity and the position of each peak were determined by peak fitting software. The phase fractions were determined by applying the Rietveld method to the peak intensity [163, 164]. The peak position provides the lattice parameter, which was used to determine the carbon content of the retained austenite. The carbon content can be determined directly using various empirically fitted equations. In this work, the thermodynamic calculation tool Thermo-Calc© TCFE6 [165], which is also based on empirical fitting, was used for this purpose. The carbon content was varied to match the lattice constant of the fcc lattice extrapolated to room temperature.

### 3.3.4 Dilatometry

Continuous and isothermal dilatometer experiments were conducted on as-cold-rolled material (1 x 3.5 x 10 mm) using a Bähr dilatometer DIL 805 A/D. The samples were exposed to conductive heating and subsequent cooling using nitrogen gas. The purpose of this study was to characterize the transformation behaviour for sheet steels with the compositions listed in Table 3.2 to 3.5. The samples for the isothermal and the continuous dilatometer experiments were heated with 25 K/s and fully austenitized at 900 °C for 60 s. The austenitization step was followed by quenching with a cooling rate of 50 K/s to overaging temperature for the isothermal heat treatment (Figure 3.7a). For continuous cooling experiments, the cooling rate was varied between 3 and 80 K/s according to Figure 3.7b. Isothermal heat treatment was varied in a temperature range of 250 to 600 °C in 50 K steps and additionally 375 °C and 425 °C with an overaging time of 1200 s (Figure 3.7a). The austenitization behaviour was studied by heating with a heating rate of 3 K/s, annealing at 900 °C for 60 s and quenching with a cooling rate of 30 K/s, as shown in Figure 3.7c.

As a measure of the transformation progress, the normalized length of the dilatometer sample was determined according to the following equation:

$$\Delta l_{\text{norm}} = (l - l_0) / l_{\text{max}} \cdot 100\%, \quad (3.4)$$

where  $l$  is the current,  $l_0$  the initial, and  $l_{\text{max}}$  the total sample length after quenching to room temperature. Figure 3.6c illustrates how these lengths of the dilatometer analysis are determined by a fit of the ferrite and the austenite curve as well as a shift of the ferrite curve by the amount of retained austenite. The thermal expansion of the specimen at a given temperature is taken into account for both fits. The initial length refers to the beginning of the overaging step for the isothermal experiments and to the sample length before quenching for continuous cooling experiments.

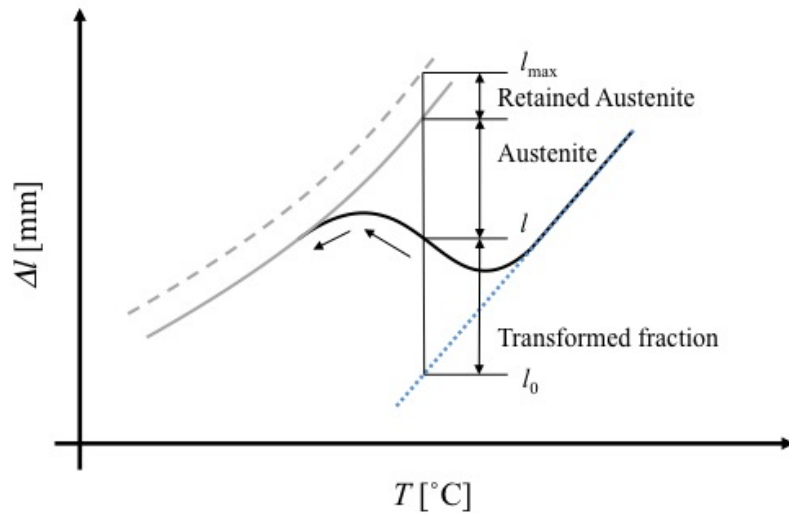


Figure 3.6: Scheme of the dilatometer analysis including the difference  $\Delta l$  between the current length of the sample and the sample length at room temperature, austenite fraction, ferrite fraction, and retained austenite correction. The grey quadratic fit of the curve from room temperature to  $A_{c3}$  temperature is the difference between the length of the untransformed ferritic specimen and the sample length at room temperature. The blue dotted linear fit of the curve above  $A_{r3}$  temperature is the difference between length of the fully austenitized specimen and the sample length at room temperature.

Table 3.7: Tensile test geometries of tested F07 and F01.

Sample	F07	F01
gauge length [mm]	$80 \pm 0.1$	$35 \pm 0.05$
sample length [mm]	$250 \pm 0.1$	$100 \pm 0.025$
sample width [mm]	$20 \pm 0.1$	$12.5 \pm 0.025$
tolerance [mm]	0.05	0.05

### 3.3.5 Mechanical testing

#### Tensile test

Flat tensile tests have been performed according to the international standard ISO 6892-1. Strength values such as yield strength and tensile strength as well as elongation, in particular uniform and total elongation, under exposure of a monotone momentum-free quasi-static increasing uniaxial tensile load were determined from the conducted tensile tests.

Industrially produced tensile samples were tested with a gauge length of 80 mm, while laboratory annealed tensile samples had been machined to a gauge length of 35 mm before tensile testing. Sample geometries are listed in Table 3.7.

In addition to basic values such as yield strength, tensile strength and uniform elongation, the strain-hardening behaviour can be deduced from the stress strain-curve by calculating strain-hardening values such as strain-hardening exponent  $n$ , the strain-hardening rate  $\theta$ , and the differential  $n$ -value, as described in Section 2.3.2.

The stability of retained austenite against SIMT was investigated by means of interrupted tensile tests. For this, tensile strains between 1 and 10% were applied in steps of 1%. An additional specimen was strained to 0.5% tensile strain.

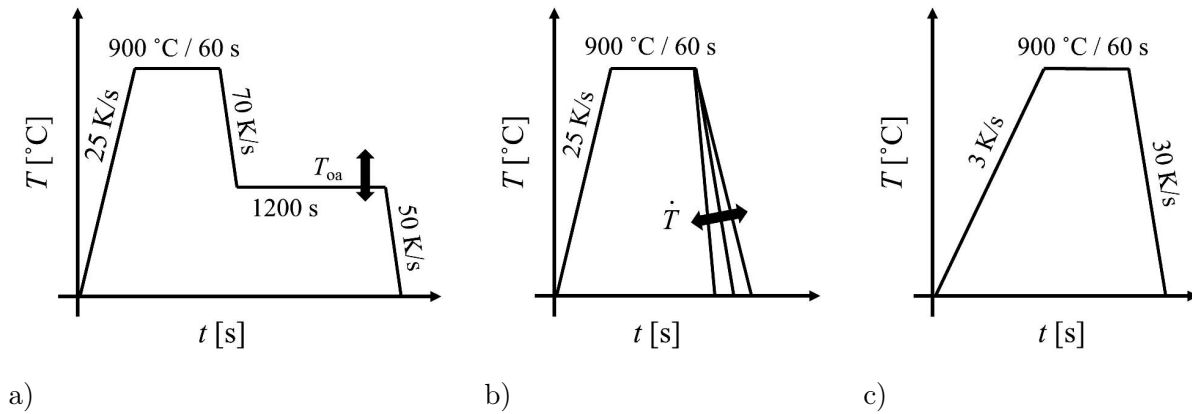


Figure 3.7: Dilatometer annealing cycles: a) Overaging ( $T_{oa} = 250, 300, 350, 375, 400, 425, 450, 500, 550,$  and  $600\text{ }^{\circ}\text{C}$ ), b) continuous cooling (cooling rate  $\dot{T} = 3, 10, 20, 30, 40, 50,$  and  $80\text{ K/s}$ ), and c) austenitization.

### Hole expansion test

Hole expansion tests (HET) have been conducted for selected samples according to the hole expanding test method of ISO/TS 16630:2009(E), metallic materials. Figure 3.8 shows a sketch of the axis-symmetrical hole expansion test setup with die, matrix and sample.  $D_0$  denote the initial diameter,  $D_h$  the final diameter, and  $D_d$  the die diameter.

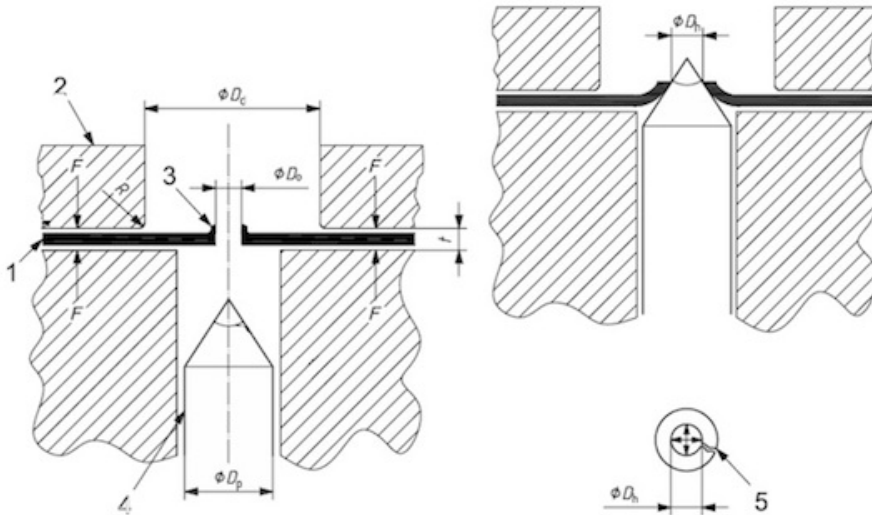


Figure 3.8: Hole expansion test sketch. 1: Sample, 2: Matrix, 3: Rim, 4: Punch, 5: Crack.

The hole expansion value is calculated as follows:

$$\lambda = \frac{D_f - D_0}{D_0} * 100 \quad (3.5)$$

Hole expansion tests on samples with punched holes are widely used in industry. In the present work, all hole expansion data will refer to specimens with punched holes if not indicated otherwise.

# Chapter 4

## Results

### 4.1 Influence of alloying elements on TBF and Q&P sheet steel

#### 4.1.1 Silicon in the 980 grade

Silicon plays an important role as an alloying element for TRIP-assisted steels such as TBF and Q&P steels. As described in Section 2.2.2, its function in suppressing cementite precipitation is of critical importance for austenite stabilization through carbon partitioning during the overaging step. However, significant effort has been put into reducing the amount of silicon caused by the mentioned shortcomings such as Si-oxides on the surface. It is therefore important to evaluate the effect of silicon additions to the investigated steel grades. It will be shown that small variations in silicon content can largely affect phase transformation, microstructure and, thus, mechanical properties of the herein presented base composition designed for 980 MPa minimum tensile strength. Parts of the results presented in this section were previously published [166].

Dilatometer experiments were conducted to use information about phase transformation to explain changes in mechanical properties caused by the addition of silicon. The transformed phase fractions as a function of temperature during continuous cooling at 3, 10, and 80 K/s of the 980 grade are shown in Figure 4.1a for a silicon content of 0.8, 0.9, and 1.0 mass %. The addition of silicon results in slight acceleration of diffusion-controlled phase transformations. Above  $M_s$  temperature of approximately 370 °C, the higher the silicon content, the higher the transformed fraction for a given temperature irrespective of cooling rate. Thus, polygonal as well as bainitic ferrite forms faster due to the addition of silicon. It is worth noting, that  $M_s$  temperature appears to be higher for higher silicon contents, which is possibly a consequence of the mentioned promoted diffusion-controlled phase transformation.

Figure 4.1b shows the isothermal time temperature transformation (TTT) diagram of the 980 grade silicon variants. There are minor changes of phase transformation behaviour during overaging as a result of changes in silicon content within the observed range of 0.8 to 1.0 mass %. In the complete observed range from 350 to 600 °C, phase transformation is slightly shifted to longer overaging times with increasing silicon content. The acceleration in transformation kinetics during continuous cooling appears to be in contradiction to the deceleration during overaging. This can be explained by the fact that silicon acts both as accelerator and decelerator of transformation kinetics. On the one hand, as a ferrite stabilizer, silicon increases the  $A_3$  temperature and silicon additions lead to higher driving forces for ferrite formation. On the other hand, silicon additions reduce the diffusivity of elements such as carbon lowering the velocity of diffusion-controlled phase transformations.

Figure 4.2 shows LePera etched optical micrographs of steels 0.8Si980, 0.9Si980, and 1.0Si980 for overaging temperatures 350 °C and 425 °C. Brown areas are tempered martensite (TM) or lower

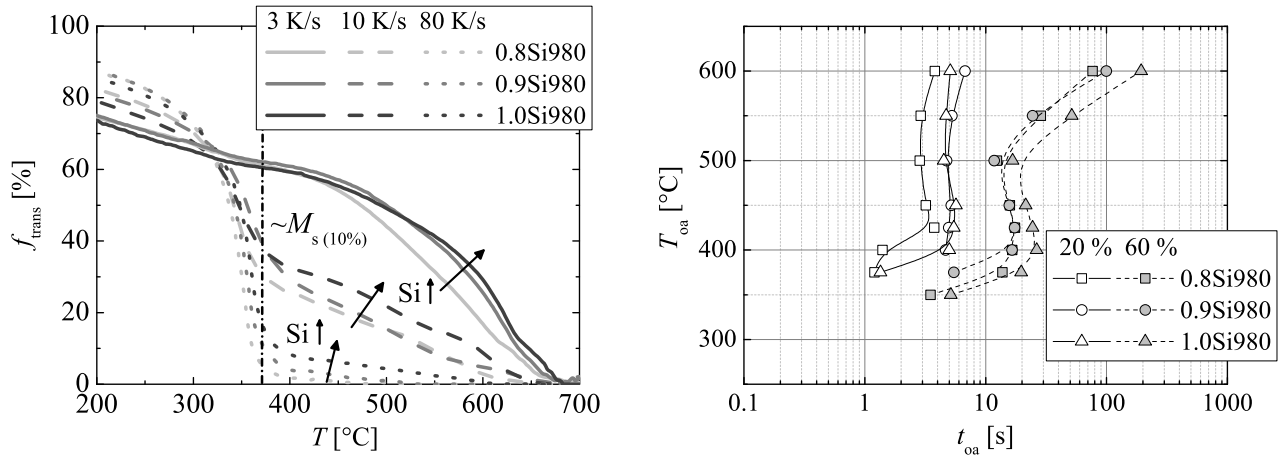


Figure 4.1: a) Transformed phase fraction during continuous cooling ( $\dot{T} = 3 \text{ K/s}$ ,  $10 \text{ K/s}$ ,  $80 \text{ K/s}$ ) and b) isothermal TTT diagram of 20% and 60% transformed phase fraction of steels 0.8Si980, 0.9Si980 and 1.0Si980 ( $T_{\text{an}} = 900 \text{ }^\circ\text{C}$ ,  $\dot{T} \approx 70 \text{ K/s}$ ).

bainite (LB). (Upper) bainite (UB) can be brownish or blue. The lath size of the bainite increases from low to high overaging temperatures. At high overaging temperatures, bainite can become globular and carbide-free. Black dots indicate carbide precipitates, usually cementite. Carbides preferably precipitate at grain boundaries or laths, which helps to visualize them and distinguish between the microstructure components. Purely white areas indicate retained austenite. There are different types of retained austenite with different shapes such as globular grains or lath-like films. Large white regions can be a mixture of retained austenite and martensite MA. Polygonal ferrite is represented by light plain blue regions without carbides.

Some polygonal ferrite is visible in particular in the microstructure with the highest silicon content (Figure 4.2c). The brownish tempered martensite as well as the brown-blue lower bainite areas become more structured and lath-like with increasing silicon content at  $350 \text{ }^\circ\text{C}$  overaging temperature. For this overaging temperature, the number and size of the white retained austenite grains increases with increasing silicon content, resulting in a higher total amount of retained austenite. At the higher overaging temperature of  $425 \text{ }^\circ\text{C}$ , the size of the retained austenite/martensite island and the number of cementite particles slightly decrease with increasing silicon content. A decrease in the number of carbides with increasing silicon content is visible for this overaging temperature.

Figures 4.3a shows yield strength, tensile strength, uniform elongation, and amount of retained austenite as a function of overaging time for overaging temperatures  $350 \text{ }^\circ\text{C}$  and  $425 \text{ }^\circ\text{C}$ . For  $350 \text{ }^\circ\text{C}$ , the yield strengths first drop at low overaging times and subsequently increase to a large extent of up to more than  $100 \text{ MPa}$  with increasing overaging time, whereas for  $425 \text{ }^\circ\text{C}$  overaging temperature yield strengths remain constant throughout the entire range of overaging temperatures. Tensile strength decreases first strongly then less pronounced with increasing overaging time until it reaches a plateau at high overaging times above  $300 \text{ s}$ . The uniform elongation remains fairly constant within the whole overaging time range at low overaging temperature of  $350 \text{ }^\circ\text{C}$ . At the high overaging temperature of  $425 \text{ }^\circ\text{C}$ , a strong increase in uniform elongation is present with overaging time up to  $180 \text{ s}$  followed by a slight drop and a plateau from  $300 \text{ s}$  to  $600 \text{ s}$ . The amount of retained austenite shows a similar behaviour with overaging temperature compared to uniform elongation. It remains almost constant with variations in overaging time for  $350 \text{ }^\circ\text{C}$ . However, the amount of retained austenite slightly increases from  $60 \text{ s}$  to  $120 \text{ s}$  overaging temperature and then slightly decreases within  $120 \text{ s}$  to  $600 \text{ s}$  overaging time for both overaging temperatures.

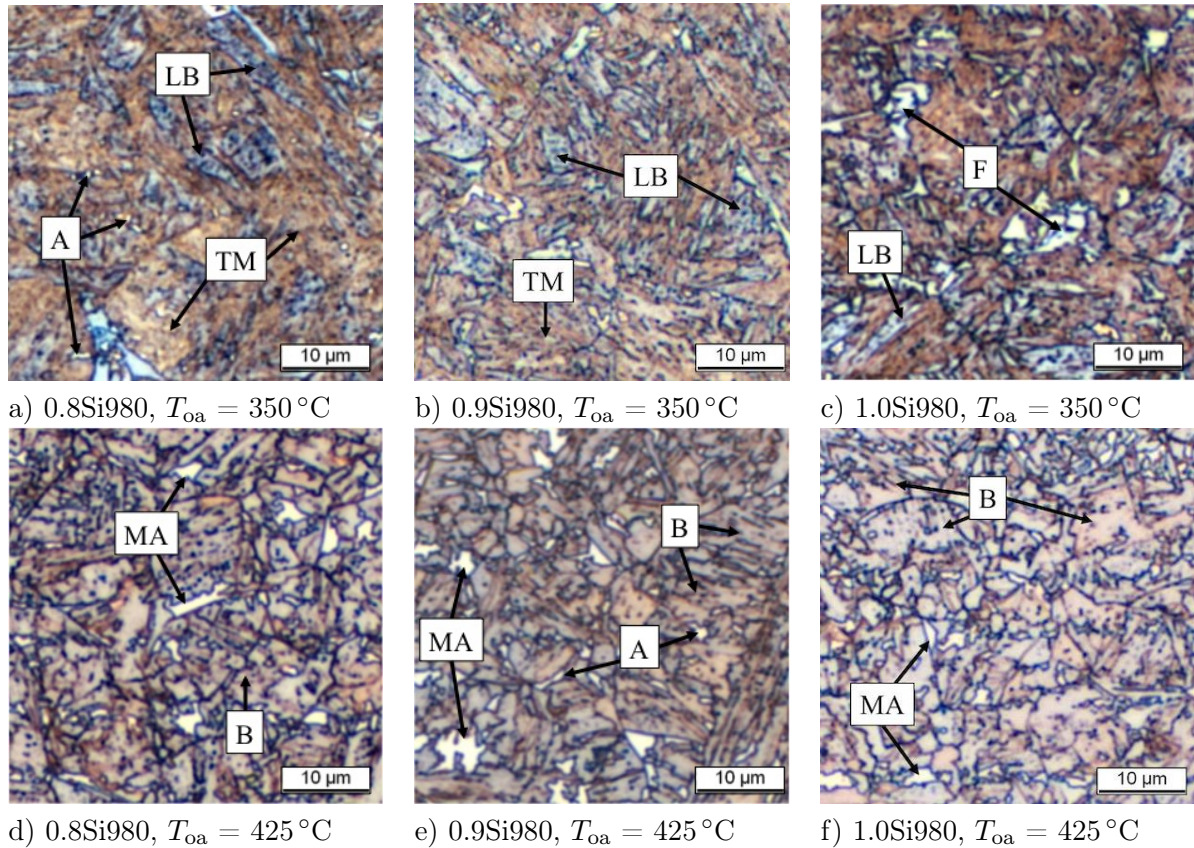


Figure 4.2: LePera etched optical micrographs of Q&P and TBF 980 grade silicon variants 0.8Si980, 0.9Si980, and 1.0Si980 for fixed overaging temperatures of 350 °C and 425 °C comprising polygonal ferrite (F), bainite (B), lower bainite (LB), tempered martensite (TM), retained austenite (A) and retained austenite/martensite islands (MA) ( $t_{oa} = 600\text{ s}$ ,  $\dot{T} \approx 50\text{ K/s}$ ).

In comparing the different silicon contents, yield strength slightly decreases for an overaging temperature of 350 °C and then increases with increasing silicon content, whereas this trend is present but negligible at 425 °C overaging temperature. The slight increase in tensile strength for the high overaging temperature and the decrease in tensile strength with increasing silicon content at low overaging temperature slightly exceeds the scatter band of 20 MPa. In contrast to the minor changes in yield and tensile strength, higher silicon content results in a slight increase in uniform elongation and the amount of retained austenite in the entire range of overaging times. In particular for 425 °C overaging temperature, uniform elongation is higher for higher silicon contents. There is an absolute increase in uniform elongation of 1 %, which is equivalent to 20 % with increasing silicon content from 0.8Si980 to 0.9Si980, whereas the additional increase in uniform elongation from grade 0.9Si980 to 1.0Si980 is negligible. The amount of retained austenite, in contrast, shows the greatest increase from steel 0.9Si980 to 1.0Si980.

Yield strength, tensile strength, uniform elongation, and amount of retained austenite as a function of overaging temperature are shown in Figures 4.3b for an overaging time of 600 s. The general tendency of yield strength with overaging temperature is a strong decrease up to an overaging temperature of 450 °C. The yield strength for an overaging temperature of 475 °C lies within the scatter band of that for 450 °C overaging temperature. Tensile strength decreases with increasing

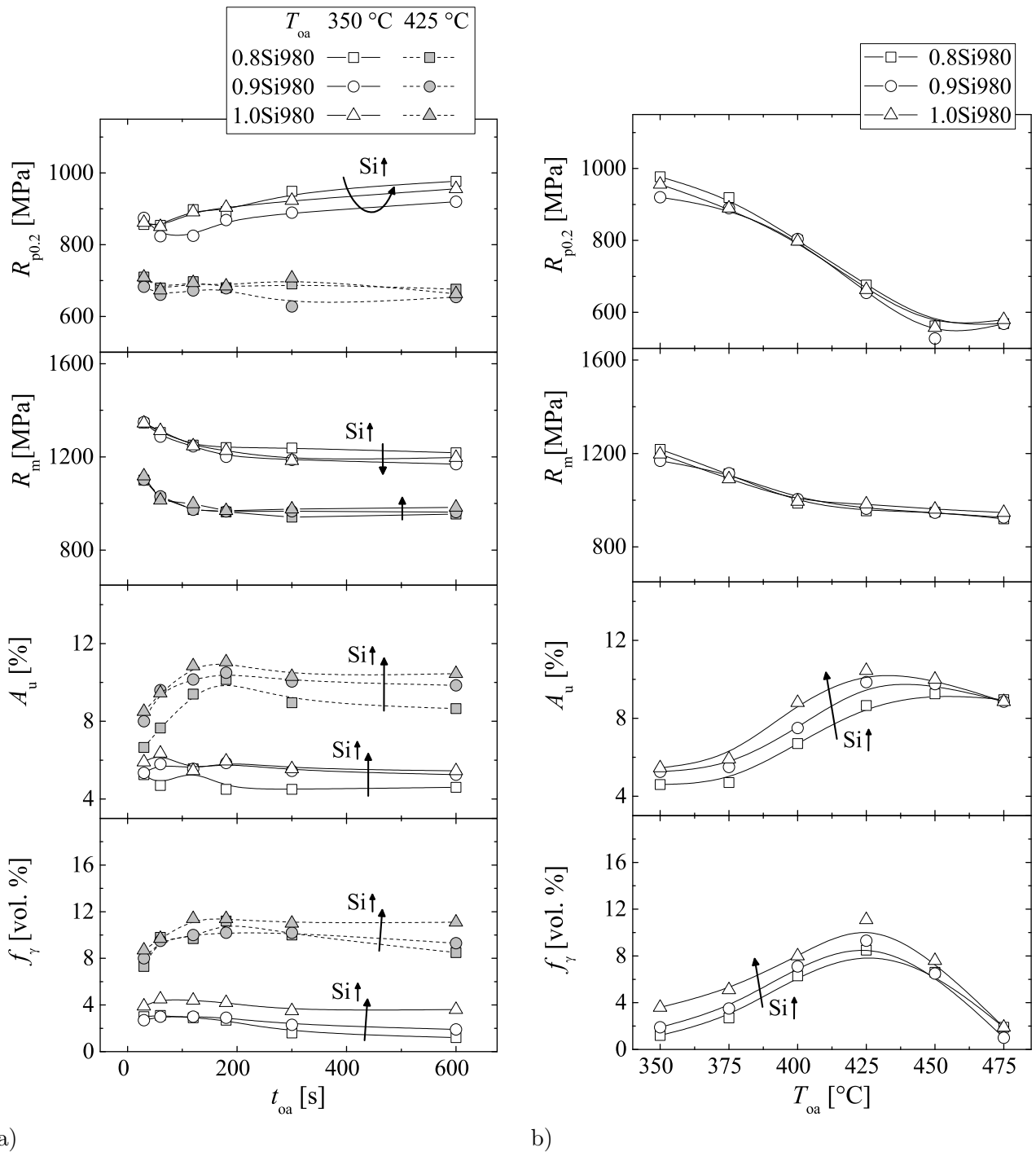


Figure 4.3: Yield strength, tensile strength, uniform elongation, and amount of retained austenite of grades 0.8Si980, 0.9Si980, and 1.0Si980 a) as a function of overaging time for overaging temperatures  $T_{oa} = 350^\circ\text{C}$  and  $T_{oa} = 425^\circ\text{C}$ , b) as a function of overaging temperature ( $t_{oa} = 600$  s).

overaging temperature in the entire observed range of 350 to 475  $^\circ\text{C}$ . The decrease is, however, less pronounced above 400  $^\circ\text{C}$ . A sigmoidal increase of uniform elongation from 350  $^\circ\text{C}$  to 425  $^\circ\text{C}$  overaging temperature is followed by a decrease. The increase of retained austenite with increasing overaging temperature is rather straight, and the drop in the amount of retained austenite above

425 °C is much more pronounced when compared to that of the uniform elongation.

The changes in yield and tensile strength with variations in silicon content mutually fall into each of their scatter bands. However, at overaging temperatures up to 375 °C, the yield strength slightly increases with increasing silicon content. As shown in Figure 4.3b, uniform elongation and amount of retained austenite increase with increasing silicon content for almost all overaging temperatures. However, the influence of silicon decreases as the overaging temperature increases, and for the TBF steels that were held at 475 °C for 600 s, uniform elongation is the same for all 980 silicon variants.

#### 4.1.2 Silicon in the 1180 grade

The transformed phase fraction during continuous cooling of the 1180 grade silicon variants is shown in Figure 4.4a. In contrast to the 980 grade variants, continuous phase transformation is slightly shifted to lower amounts of transformed fraction by the addition of silicon. As shown in Figure 4.4b, higher silicon content results in decelerated phase transformation within a range of 450 to 600 °C overaging temperature. This deceleration is more pronounced than the one observed in the 980 grade variants. However, outside this overaging temperature window, the TTT curves of the different silicon variants are very similar.

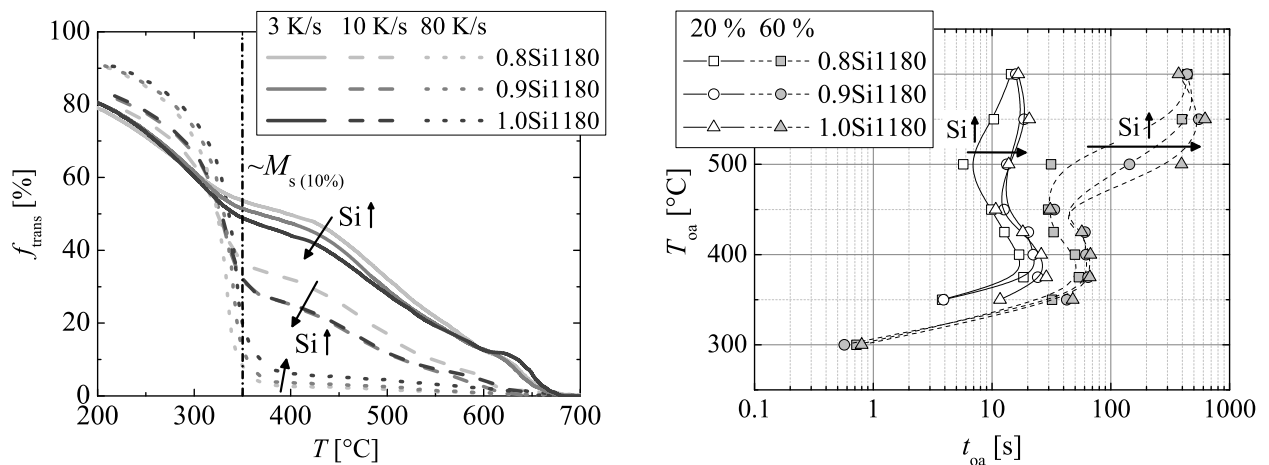


Figure 4.4: a) Transformed phase fraction during continuous cooling ( $\dot{T} = 3 \text{ K/s}$ ,  $20 \text{ K/s}$ ,  $80 \text{ K/s}$ ) and b) isothermal TTT diagram of 20 % and 60 % transformed phase fraction for steels 0.8Si1180, 0.9Si1180, and 1.0Si1180 ( $T_{\text{an}} = 900 \text{ °C}$ ,  $\dot{T} \approx 70 \text{ K/s}$ ).

LePera etched micrographs of the 1180 silicon variants are shown in Figure 4.5. For an overaging temperature of 350 °C the morphology of the tempered martensitic/bainitic matrix significantly varies between the different silicon variants. The lath structure is clearly visible in the event of higher silicon content, whereas the microstructure is much more blurry, globular and interwoven (Figure 4.5a-c) toward lower silicon content. A slight decrease in the amount of carbides and an increase in number and size of retained austenite grains with increasing silicon content is visible for 350 °C overaging temperature.

The structure of the bainitic matrix of the microstructures that were held at 425 °C overaging temperature is also coarser in the steels with lower silicon content (Figure 4.5d-f). For 425 °C overaging temperature, the amount of carbides decreases with increasing silicon content even more so than at 350 °C. The size of the retained austenite/martensite islands is very similar within the silicon variants but slightly larger for higher silicon contents.

Yield strength, tensile strength, uniform elongation, and the amount of retained austenite as a

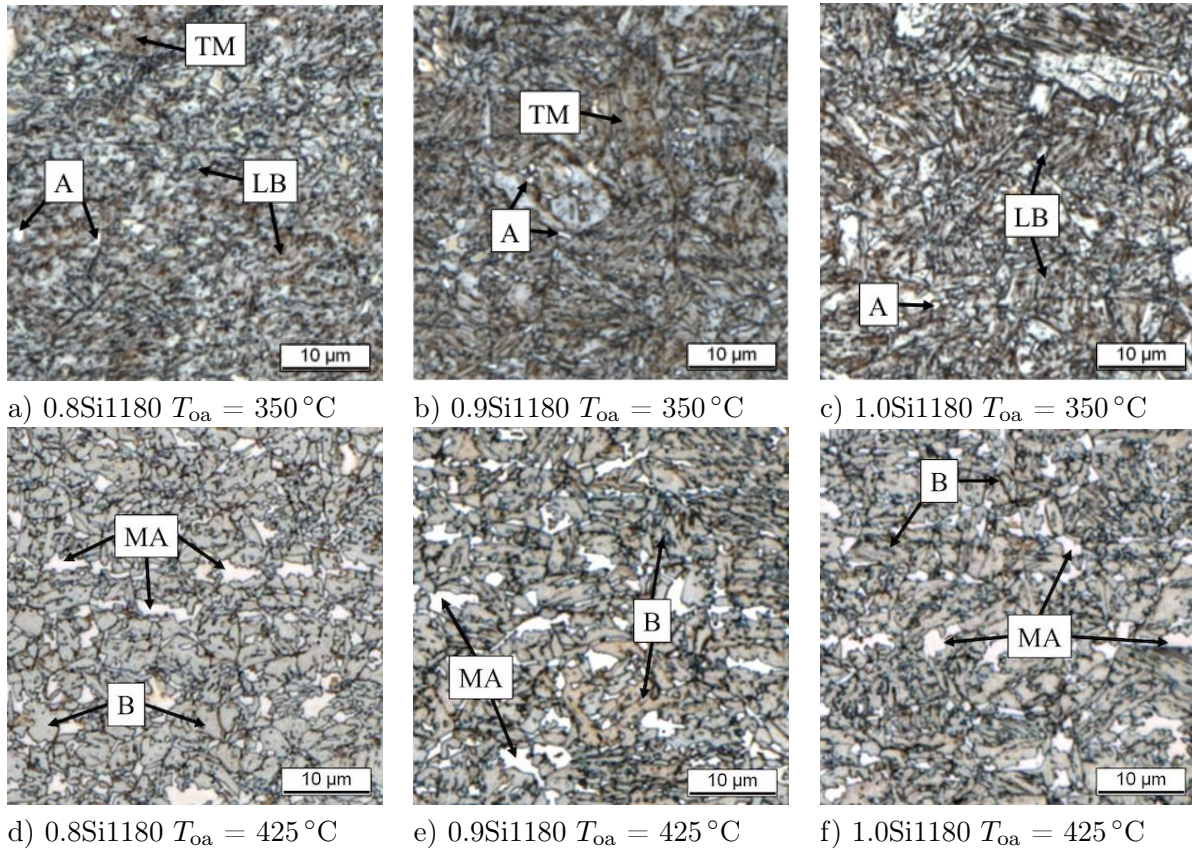


Figure 4.5: LePera etched optical micrographs of Q&P and TBF 1180 grade silicon variants 0.8Si1180, 0.9Si1180, and 1.0Si1180 for fixed overaging temperatures of 350 °C and 425 °C comprising polygonal ferrite (F), bainite (B), lower bainite (LB), tempered martensite (TM), retained austenite (A) and retained austenite/martensite islands (MA) ( $t_{oa} = 600\text{ s}$ ,  $\dot{T} \approx 50\text{ K/s}$ ).

function of overaging time and overaging temperature are shown in Figures 4.6. There are some remarkable differences between the general trends of the mechanical properties of the 980 and 1180 grade silicon variants as a function of overaging time. The decrease in yield strength with increasing overaging time is much more pronounced and lasts up to 120s overaging time. For an overaging temperature of 425 °C, the yield strength shows a strong decrease and continues to decrease, however, less pronounced with increasing overaging time. This behaviour is in strong contrast to the 980 grade, where the yield strength for elevated overaging temperatures is nearly independent of overaging temperature.

When the absolute values of the observed properties are compared at the end of the overaging step after 600s overaging, yield strength is more than 1000 MPa, which is 100 MPa higher in the 1180 than in the 980 silicon variants for an overaging temperature of 350 °C. Contrastingly at 425 °C overaging temperature, yield strength is 50 MPa lower in the 1180 silicon variants when compared to the 980 group for the same overaging time. Furthermore, the drop in yield and tensile strength at the beginning of the overaging step is much more pronounced in the 1180 group as opposed to the 980 variants, where it is almost negligible. The tensile strength of the 980 group is 980 MPa for an overaging temperature of 425 °C and  $\sim 220\text{ MPa}$  higher for 350 °C overaging temperature. In the 1180 group, tensile strength is 1150 MPa for 425 °C overaging temperature and only 150 MPa higher

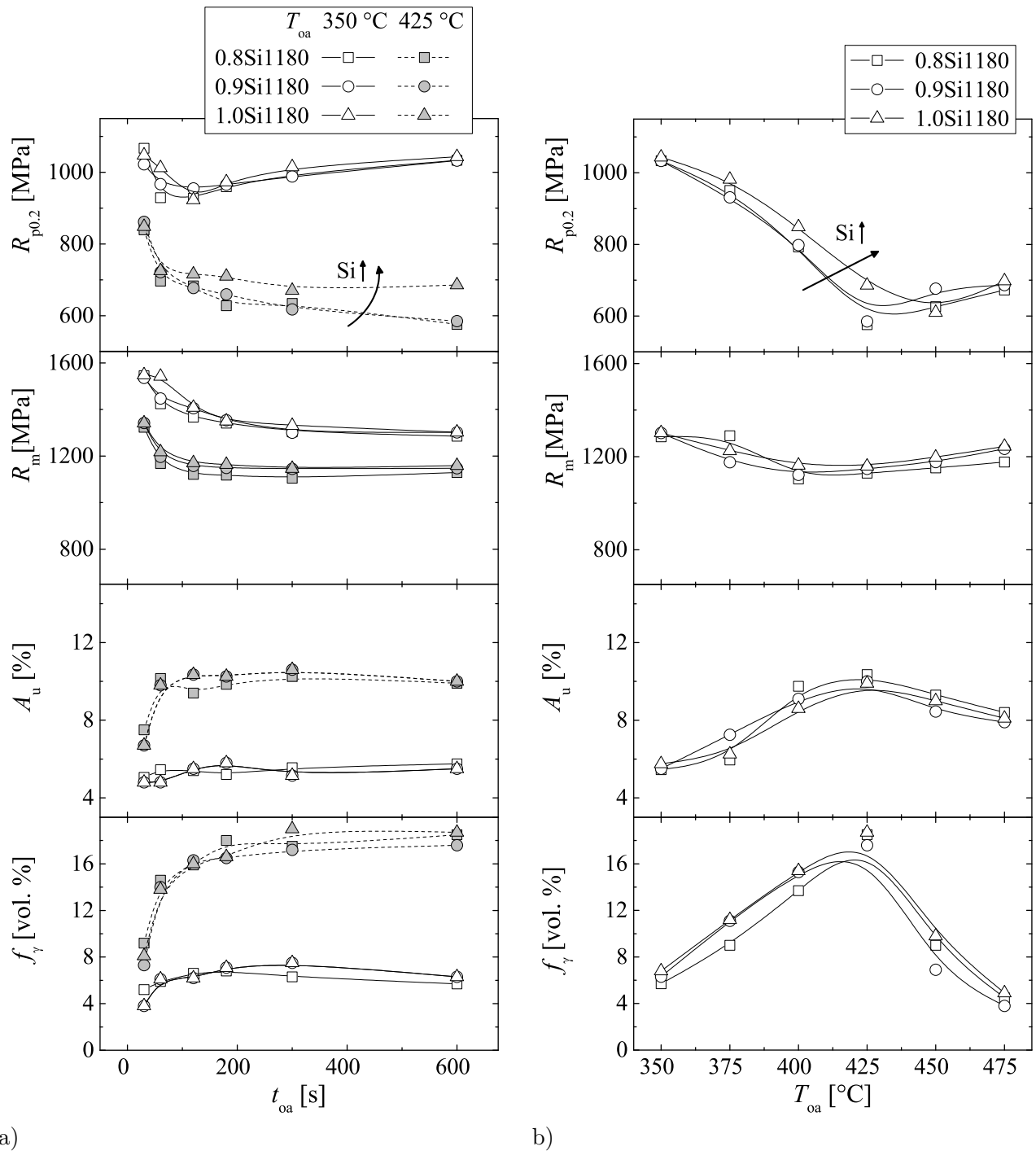


Figure 4.6: Yield strength, tensile strength, uniform elongation, and amount of retained austenite of grades 0.8Si1180, 0.9Si1180, and 1.0Si1180 a) as a function of overaging time for overaging temperatures  $T_{oa} = 350^\circ\text{C}$  and  $T_{oa} = 425^\circ\text{C}$ , b) as a function of overaging temperature ( $t_{oa} = 600$  s).

at an overaging temperature of  $350^\circ\text{C}$ . Uniform elongation of the 980 and the 1180 silicon variants are 5 and 10% for 350 and  $425^\circ\text{C}$  overaging temperature, respectively. The difference between uniform elongation of the 980 and the 1180 silicon variants is almost negligible. The low overaging temperature of  $350^\circ\text{C}$  results in amounts of retained austenite of 2 to 4 vol.%, while all silicon

variants of the 1180 grade comprise 6 vol-% at the end of the overaging step. With  $\sim 18$  vol.%, the 1180 silicon variants contain approximately twice as much retained austenite compared to the 980 group for the high overaging temperature of 425 °C. The differences between the mechanical properties and amount of retained austenite for different silicon contents within the 1180 group are much less pronounced compared to the 980 group. For the low overaging temperature, the yield strength of the steel with the highest silicon content is higher compared to the other variants. A slight increase in tensile strength with increasing silicon content can be observed in the entire investigated range of overaging times. In terms of all other observed properties the 1180 group silicon variants behave very similar to each other.

Mechanical properties and the amount of retained austenite as a function of overaging temperature are shown in Figures 4.6b. It is worth noting, that the tensile strength of the 1180 grade silicon variants increases with increasing overaging temperature above 425 °C. This is in contrast to the 980 group, where it continues to decrease.

The yield strength of steel 1.0Si1180 is distinctly higher compared to grade 0.8Si1180 and 0.9Si1180 for nearly all overaging temperatures below  $T_{oa} = 450$  °C. Tensile strength slightly increases with increasing silicon content at almost all overaging temperatures, as opposed to the 980 group, which shows negligible changes in tensile strengths with varying silicon content within the observed range. The trends of uniform elongation with increasing overaging temperature of the 980 and the 1180 grade are comparable. While the uniform elongation of the 980 silicon variants significantly increases with increasing silicon content, in the 1180 group uniform elongation even slightly decreases for higher amounts of silicon. The amount of retained austenite in the 1180 silicon variants is higher for higher silicon contents up to an overaging temperature of 425 °C.

### 4.1.3 Manganese in the 980 grade

The choice of the appropriate manganese content is crucial to many important characteristic properties such as transformation kinetics and austenite stability of TBF and Q&P steels. This chapter provides the results of investigations on the influence of 2.2 to 2.6 mass% manganese on phase transformations, microstructure, and mechanical properties of the 980 group TBF/Q&P steels.

The transformed phase fraction during continuous cooling at a rate of 3, 10, and 80 K/s of the 980 grade manganese variants is shown in Figure 4.7a. Increasing the cooling rate results in lower amounts of transformed phase fraction during cooling. Manganese significantly shifts the phase transformation to lower transformed phase fractions for a given temperature.  $M_s$  temperature is slightly lower for higher manganese contents. Isothermal phase transformation is significantly decelerated at all overaging temperatures by the addition of manganese.

Figure 4.8 shows LePera etched optical micrographs of the 980 manganese variants for overaging temperatures 350 °C and 425 °C with an overaging time of 600 s. The steels that were held at low overaging temperature exhibit a more lath-like rather than globular microstructure with a much smaller lath thickness and longer laths compared to the steels with the same composition and higher overaging temperature. The matrix of the low overaging temperature (Figure 4.8a-c) is also darker compared to the high overaging temperature (Figure 4.8d-f), which can be explained by the finer distribution of carbides within the lath structure. Retained austenite/martensite islands are larger at the higher overaging temperature. However, this difference is much more pronounced in the silicon variants of the 980 and even more so in the 1180 grade, as can be seen above (Figure 4.2 and 4.5).

The matrix of steel 2.2Mn980 is more globular compared to steels 2.4Mn980 and 2.5Mn980. In particular at an overaging temperature of 350 °C, steels 2.4Mn980 and 2.5Mn980 are much more lath-like than steel 2.2Mn980. At higher overaging temperature, the microstructures of the steels with higher manganese contents are also finer and the grains are slightly smaller as opposed to

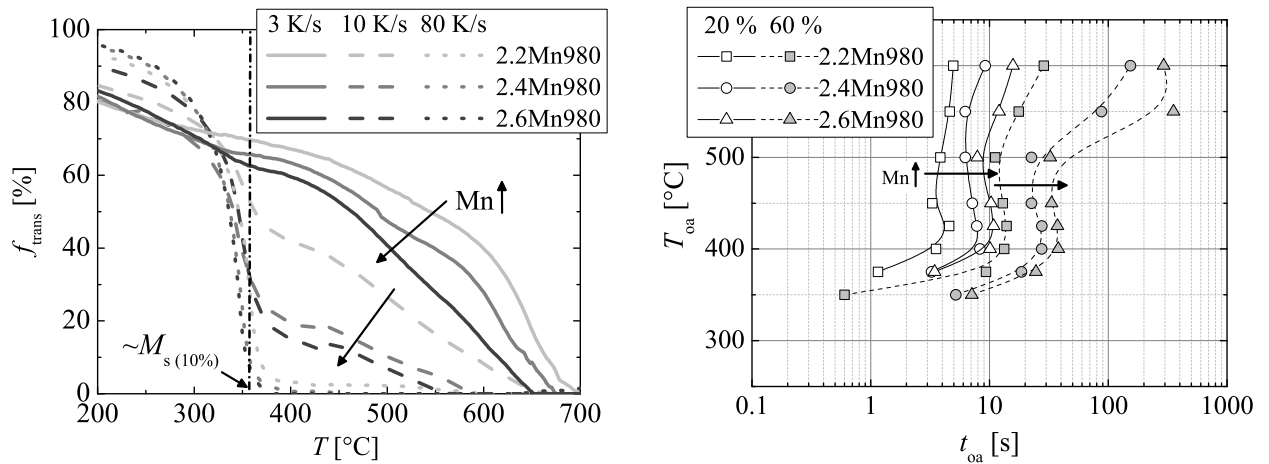


Figure 4.7: a) Transformed phase fraction during continuous cooling ( $\dot{T} = 3 \text{ K/s}, 10 \text{ K/s}, 80 \text{ K/s}$ ) and b) isothermal TTT diagram of 20% and 60% transformed phase fraction of steels 2.2Mn980, 2.4Mn980 and 2.5Mn980 ( $T_{\text{an}} = 900 \text{ °C}, \dot{T} \approx 70 \text{ K/s}$ ).

steel 2.2Mn980. Furthermore, the steel with the lowest manganese content of 2.2 mass% contains small amounts of polygonal ferrite (Figure 4.8a). The size of the retained austenite/martensite islands slightly increases with increasing manganese content in the steels that were held at 425 °C (Figure 4.8d-f). Finally, for both overaging temperatures, some carbide-depleted areas are present in the steel with the lowest manganese content, 2.2Mn980.

Figure 4.9a shows yield strength, tensile strength, uniform elongation, and the amount of retained austenite as a function of overaging time of the 980 manganese variants. The yield strength first decreases then increases with increasing overaging for an overaging temperature of 350 °C. At the high overaging temperature of 425 °C steel 2.2Mn980 and 2.4Mn980 show a strong then slight decrease in yield strength in accordance to the 1180 silicon variants. The yield strength of the steel with the lowest manganese content, however, increases with increasing overaging time after 180s overaging. The strongly decreasing trend in tensile strength of the manganese variants with increasing overaging time is also in good agreement with both the 980 and the 1180 silicon variants as well as the plateau for longer overaging times. However, the tensile strength slightly increases with increasing overaging time above an overaging time of 180s for an overaging temperature of 425 °C. Similar to the silicon variants, uniform elongation remains at 5% for all overaging times at the low overaging temperature. At an overaging temperature of 425 °C, however, uniform elongation first increases with increasing overaging time, in accordance with the silicon variants, but then decreases with increasing overaging temperature. The same trends can also be observed for the amount of retained austenite, except for the two variants with the highest manganese content, which keep their high amounts of retained austenite at long overaging times.

While the yield strength increases with increasing manganese content for an overaging temperature of 350 °C, a decrease in yield strength with increasing manganese content is observed for 425 °C overaging temperature for longer overaging times than 60s, which becomes more pronounced for prolonged overaging times. Manganese additions slightly increase the tensile strength to the same extent for all overaging times and for both overaging temperatures. While the uniform elongation of 5% is unaffected by manganese additions at the 350 °C overaging temperature, the variant with the lowest manganese content shows lower uniform elongation than the other variants for overaging times of more than 120s. The amount of retained austenite increases with increasing manganese content at both overaging temperatures, however, more pronounced for the higher overaging tem-

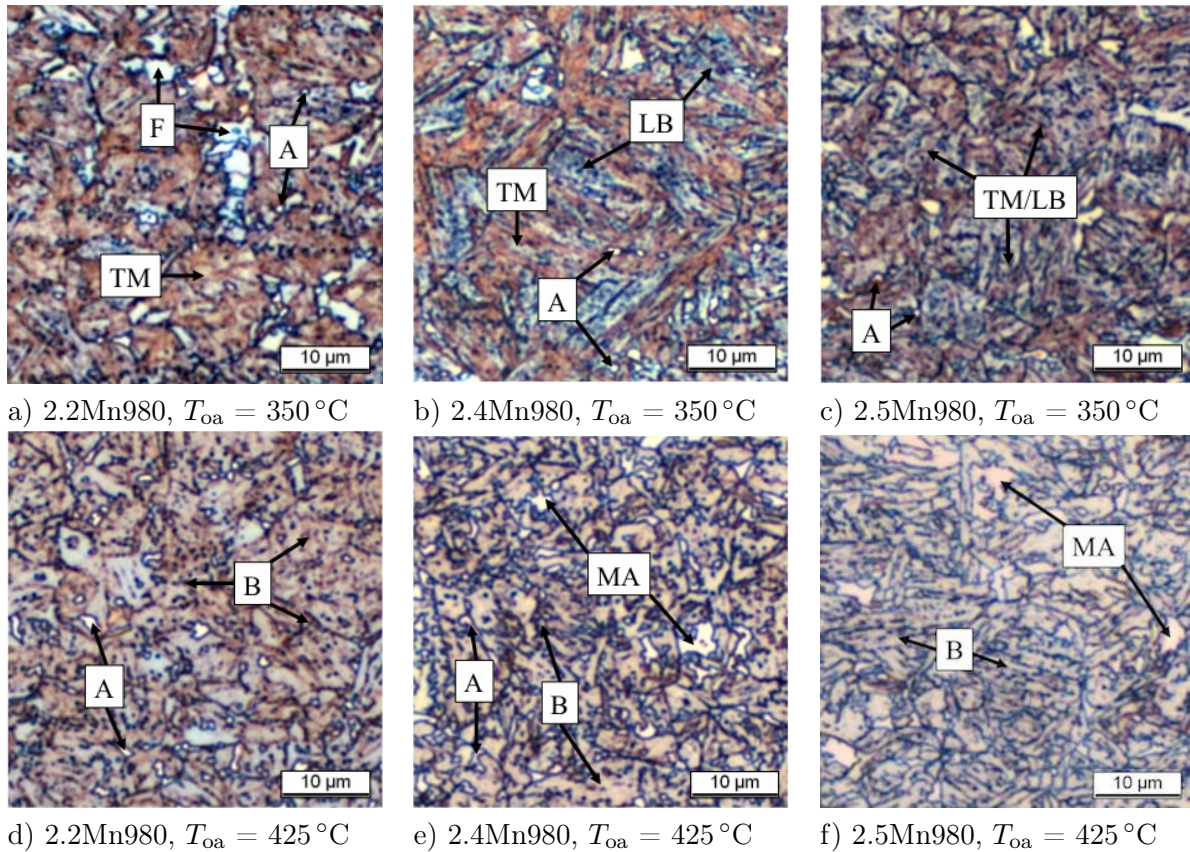


Figure 4.8: LePera etched optical micrographs of TBF heat-treated 980 grade manganese variants 2.2Mn980, 2.4Mn980, and 2.5Mn980 for overaging temperatures  $350\text{ }^{\circ}\text{C}$  and  $425\text{ }^{\circ}\text{C}$  comprising polygonal ferrite (F), bainite (B), lower bainite (LB), tempered martensite (TM), retained austenite (A) and retained austenite/martensite islands (MA) ( $t_{oa} = 600\text{ s}$ ,  $\dot{T} \approx 50\text{ K/s}$ ).

perature.

With respect to the manganese influence as a function of overaging temperature (Figure 4.9b), the yield strength decreases with increasing manganese content for overaging temperatures  $400\text{ }^{\circ}\text{C}$  and  $425\text{ }^{\circ}\text{C}$ , and is unaffected by variations in manganese content above or below these temperatures. Tensile strength increases with increasing manganese content, in particular at higher overaging temperatures. Up to  $400\text{ }^{\circ}\text{C}$  overaging temperature, uniform elongation slightly increase with increasing overaging temperature. Above this temperature, uniform elongation for higher manganese content decreases more pronounced with increasing overaging temperature. At an overaging temperature of  $475\text{ }^{\circ}\text{C}$ , the tendency is inverse compared to  $425\text{ }^{\circ}\text{C}$ , i.e. higher manganese content results in lower uniform elongation. The amount of retained austenite is higher for higher manganese content below  $450\text{ }^{\circ}\text{C}$  overaging temperature. The increase in retained austenite with increasing overaging temperature up to  $425\text{ }^{\circ}\text{C}$  is much more pronounced for steel 2.4Mn980 and 2.5Mn980 as opposed to grade 2.2Mn980. Above this temperature, the amount of retained austenite of steel 2.5Mn980 drops significantly to almost the same level as grade 2.2Mn980.

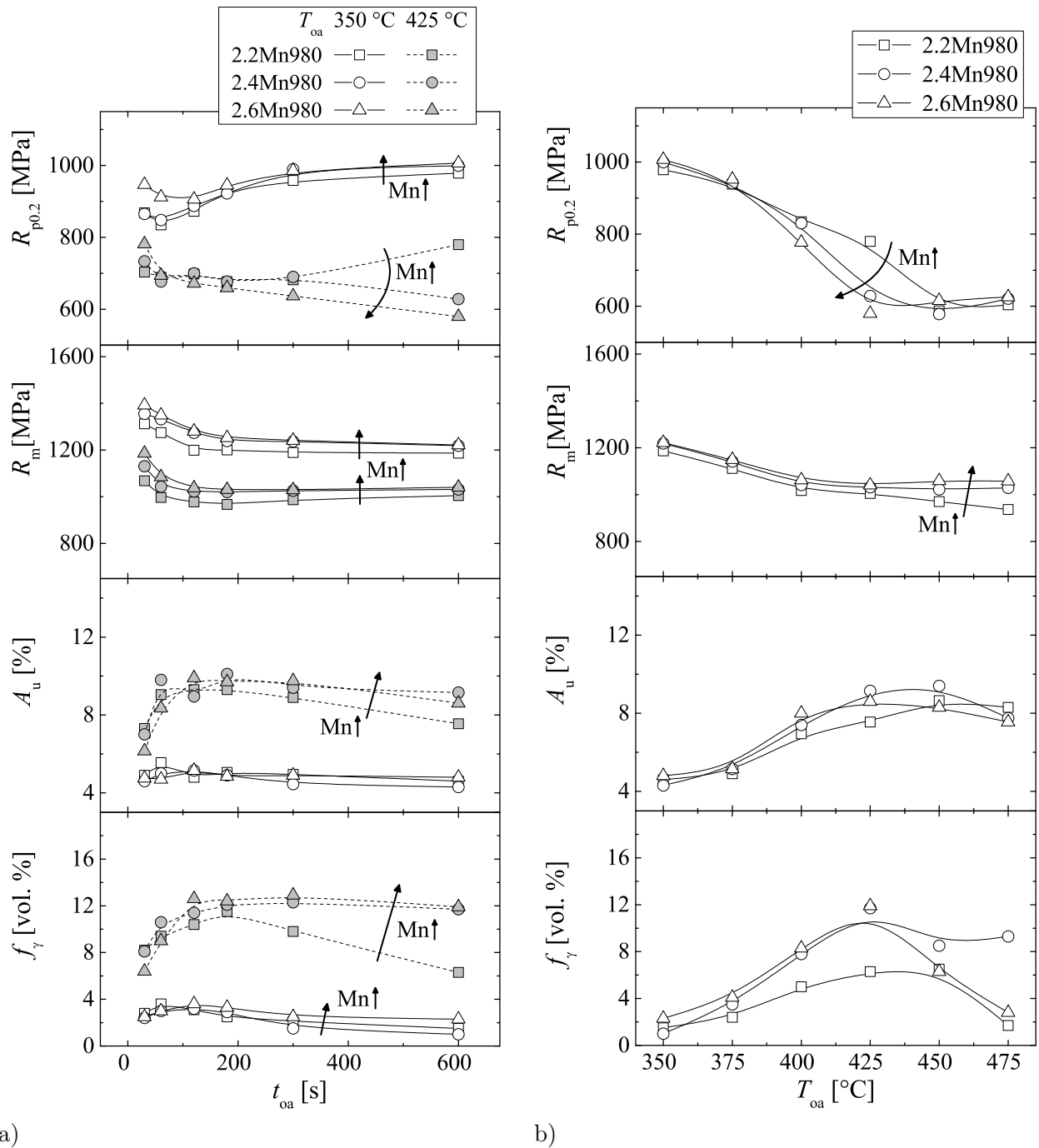


Figure 4.9: Yield strength, tensile strength, uniform elongation, and amount of retained austenite of grades 2.2Mn980, 2.4Mn980, and 2.5Mn980 a) as a function of overaging time for overaging temperatures  $T_{oa} = 350$  °C and  $T_{oa} = 425$  °C, b) as a function of overaging temperature ( $t_{oa} = 600$  s).

#### 4.1.4 Manganese in the 1180 grade

This section shows the response of phase transformation behaviour, microstructure, and mechanical properties to manganese variants in the 1180 base composition. The continuous and isothermal phase transformation behaviour is represented by Figure 4.10. An increase in manganese content

from 2.2 to 2.6 mass % results in a significant shift of transformations to lower phase fractions for a given temperature during continuous cooling. The transformed fraction of microstructure components formed at higher overaging temperature are therefore much greater for steels with lower manganese content. Further,  $M_s$  temperature is lowered by manganese additions. Manganese, furthermore, shifts the isothermal transformation to longer overaging times. From 350 to 450 °C overaging temperature the deceleration of isothermal transformation through the addition of manganese is comparable. Above 450 °C, the effect is much stronger and increases with increasing overaging temperature.

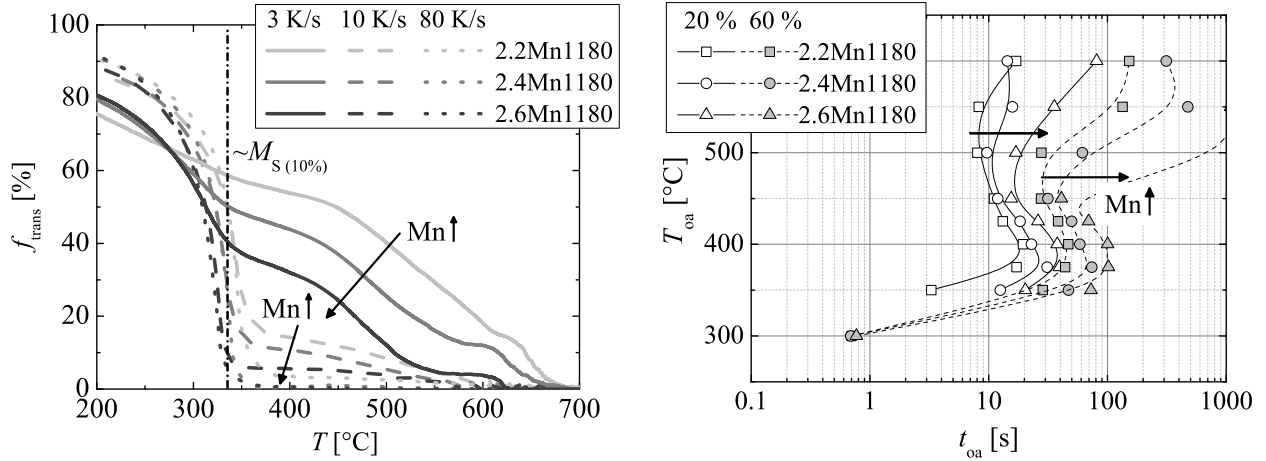


Figure 4.10: a) Transformed phase fraction during continuous cooling ( $\dot{T} = 3 \text{ K/s}$ ,  $10 \text{ K/s}$ ,  $80 \text{ K/s}$ ) and b) isothermal TTT diagram of 20 % and 60 % transformed phase fraction of steels 2.2Mn1180, 2.4Mn1180 and 2.6Mn1180 ( $T_{\text{an}} = 900 \text{ °C}$ ,  $\dot{T} \approx 70 \text{ K/s}$ ).

Figure 4.11 shows LePera etched optical micrographs of the 1180 grade manganese variants for overaging temperatures 350 °C and 425 °C with an overaging time of 600 s. The differences between the different manganese grades of the same heat treatment are even more subtle than between the 980 manganese variants. The microstructure is also generally finer for higher manganese contents at this overaging temperature.

Steels 2.4Mn1180 and 2.6Mn1180 comprise some retained austenite/martensite (MA) islands even for an overaging temperature of 350 °C, which are relatively large and are brownish in particular towards the center of the inclusion (Figure 4.11b and 4.11c). These areas indicate tempered martensite. The carbon content decreases towards the center of the MA islands, since the diffusion distance for carbon atoms during overaging is larger. Therefore, the center is more likely to transform to martensite, which is auto-tempered upon the final cooling. Auto-tempered martensite is more likely for higher manganese contents and lower overaging temperatures such as 350 °C, because of the larger austenite grains and the smaller diffusion distances at this temperature compared to higher overaging temperatures. The stabilization of the austenite by manganese additions does not necessarily result in more retained austenite, since there is less interstitially dissolved carbon available as a result of carbon precipitation, and the diffusion distances of the carbon are shorter at lower overaging temperatures.

Similar to the 980 manganese variants, the retained austenite/martensite islands of the 1180 grade for an overaging temperature of 425 °C increase in size and amount with increasing manganese content (Figure 4.11d-f). In steel 2.6Mn1180 for 425 °C overaging temperature, banding of retained austenite/martensite islands is present. Finally, in analogy to the 980 grade, some areas exist with a lower amount of carbides in the steel with the lowest manganese content (Figure 4.11a).

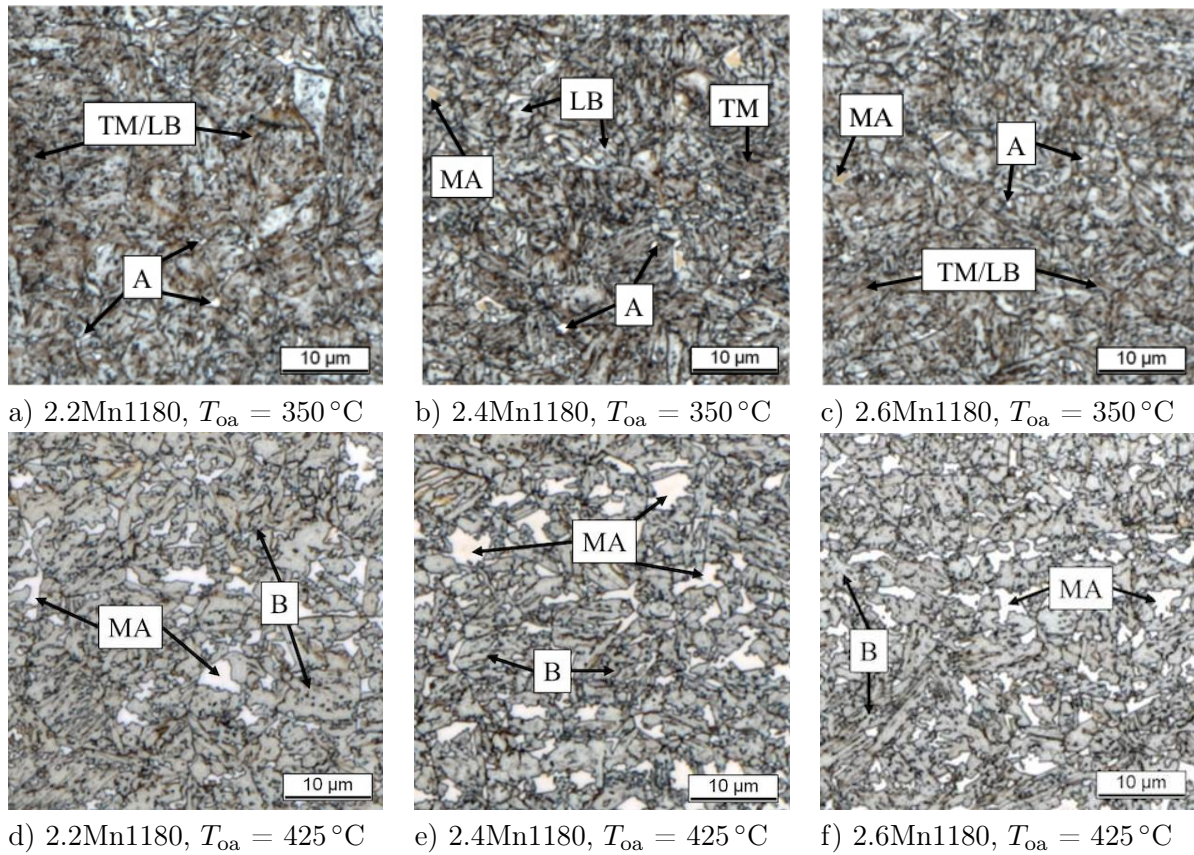


Figure 4.11: LePera etched optical micrographs of TBF heat-treated 1180 grade manganese variants 2.2Mn1180, 2.4Mn1180, and 2.6Mn1180 for overaging temperatures 350 °C and 425 °C comprising polygonal ferrite (F), bainite (B), lower bainite (LB), tempered martensite (TM), retained austenite (A) and retained austenite/martensite islands (MA) ( $t_{oa} = 600\text{ s}$ ,  $\dot{T} \approx 50\text{ K/s}$ ).

Yield strength, tensile strength, uniform elongation, and the amount of retained austenite as a function of overaging time are shown in Figure 4.12a. An increase in manganese content results in an increase of yield strength at short overaging times and a strong decrease at long overaging times. For the overaging temperature of 350 °C, this is because steel 2.4Mn1180 and even more so grade 2.2Mn1180 show a decrease and then an increase of yield strength with increasing overaging time. At the high overaging temperature, the decrease in yield strength is much stronger for higher manganese contents.

Tensile strength shows the same behaviour as yield strength at 425 °C, whereas at 350 °C higher manganese content brings about higher tensile strengths. Higher manganese contents, furthermore, result in significantly enhanced uniform elongation at both overaging temperatures. The manganese variants show the same tendency for the amount of retained austenite as a function of overaging time as for uniform elongation except for the steel with the highest manganese content, which exhibits a significant drop in the amount of retained austenite with increasing overaging time.

In contrast to the 980 group, manganese shows a very strong impact on mechanical properties and the amount of retained austenite as a function of overaging temperature (Figure 4.12b). Mechanical properties and amount of retained austenite show a switch in tendencies with manganese content at a given overaging temperature. Up to an overaging temperature of 425 °C, yield

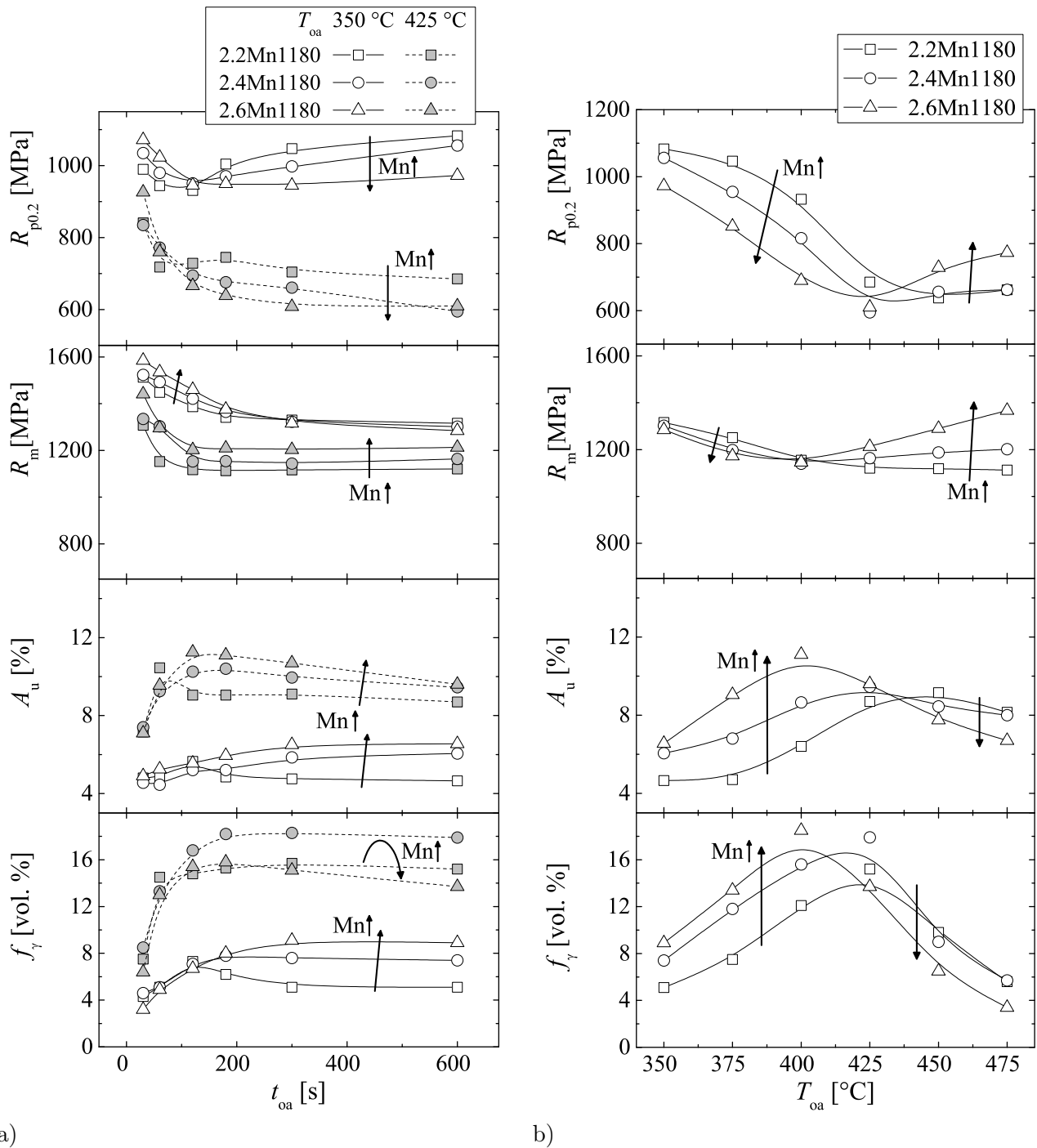


Figure 4.12: Yield strength, tensile strength, uniform elongation, and amount of retained austenite of grades 2.2Mn1180, 2.4Mn1180, and 2.6Mn1180 a) as a function of overaging time for overaging temperatures  $T_{oa} = 350^\circ\text{C}$  and  $T_{oa} = 425^\circ\text{C}$ , b) as a function of overaging temperature ( $t_{oa} = 600$  s).

strength decreases with increasing manganese content, whereas the addition of manganese above this temperature results in enhanced yield strength. The same tendencies exist in the behaviour of tensile strength for changes in the manganese content. However, these trends are less pronounced at low and more pronounced at high overaging temperature. The turning point of these tenden-

cies is shifted to a lower overaging temperature of 400 °C. Inverse behaviour is reflected in uniform elongation and the amount of retained austenite. Within the overaging temperature range of 350 to 400 °C, uniform elongation and amount of retained austenite are distinctly greater for higher manganese contents. In contrast, above this temperature range, both of these values are lower for higher manganese contents.

#### 4.1.5 Chromium in the 980 grade

Chromium has been found suitable as a partial substitute for silicon in TBF/Q&P steels [99, 167]. Cementite precipitation can successfully be delayed by the addition of chromium. Unlike aluminum, which has frequently been used to substitute silicon in TRIP steels, chromium does not increase  $A_{c3}$  temperature which is a necessary requirement to fully austenitize the steel on the industrial production line. However, chromium decelerates bainite transformation. To evaluate the overall industrial benefits and the effectiveness of chromium for the investigated TBF/Q&P steels, a chromium content of 0.01, 0.2 and 0.4 mass % was added to the base composition. This section provides insight into phase transformation behaviour, microstructure, and mechanical properties of the 980 manganese variants.

Figure 4.13a shows the transformed fraction during continuous cooling. Chromium significantly decelerates fcc-bcc transformation upon continuous cooling. A chromium content of 0.4 mass % is scarcely sufficient to prevent ferrite formation and some (upper) bainite still forms with a cooling rate of 50 K/s (Figure 4.13a). The isothermal time temperature transformation (TTT) plot of steel grade 0.01Cr980, 0.2Cr980 and 0.4Cr980 is shown in Figure 4.13b. Chromium significantly decelerates isothermal transformation for all investigated overaging temperatures above  $M_s$  temperature  $M_s \approx 378$  °C. The higher the overaging temperature, the stronger the deceleration of the phase transformation.

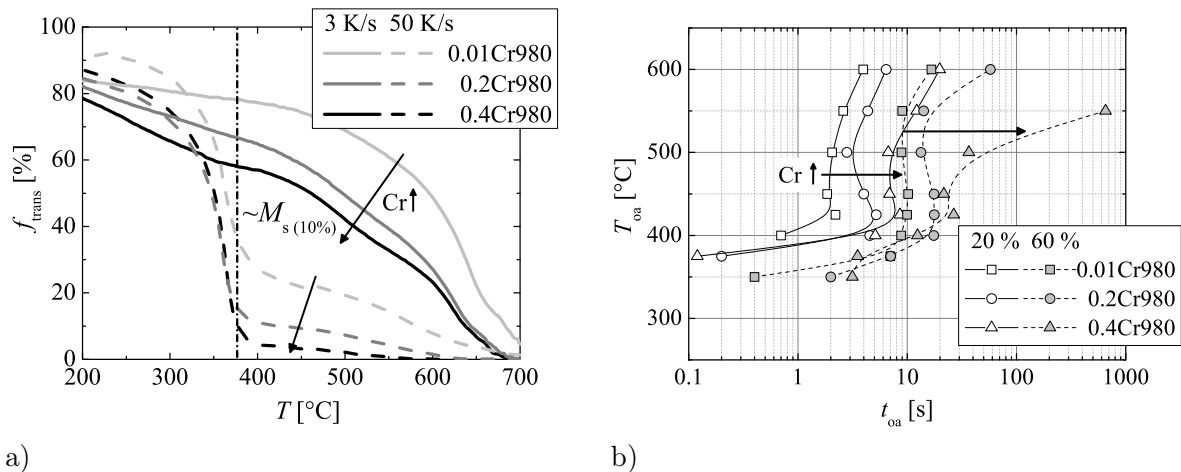


Figure 4.13: a) Transformed phase fraction during continuous cooling at rates of 3 and 50 K/s, b) isothermal TTT curve for steel grades 0.01Cr980, 0.2Cr980 and 0.4Cr980.

LePera etched optical micrographs of Q&P and TBF steels 0.01Cr980, 0.2Cr980, and 0.4Cr980 for fixed overaging temperatures of 350 °C and 425 °C are shown in Figure 4.14. Steel 0.01Cr980 comprises significant amounts of polygonal ferrite, while grade 0.2Cr980 and 0.4Cr980 contain very few small polygonal ferrite grains. This is the case for both overaging temperatures. However, it is much more obvious for an overaging temperature of 350 °C compared to 425 °C, because polygonal ferrite etches tempered martensite and lower bainite much more distinctly than upper bainite, where the transition between the microstructure components is unclear. While the bainitic/tempered

martensitic matrix of steel 0.01Cr980 is rather homogeneous, higher chromium content results in a larger variety of bainite types, lath structures, and carbide distributions (Figure 4.14a-c). The amount of retained austenite grains increases with increasing chromium content at 350 °C. The morphology of the (upper) bainite for the steels that were held at an overaging temperature of 425 °C is very similar for the different chromium variants. There are less precipitates present at higher chromium contents in particular at 425 °C. The size of the retained austenite/martensite islands is also larger for higher chromium contents (Figure 4.14d-f).

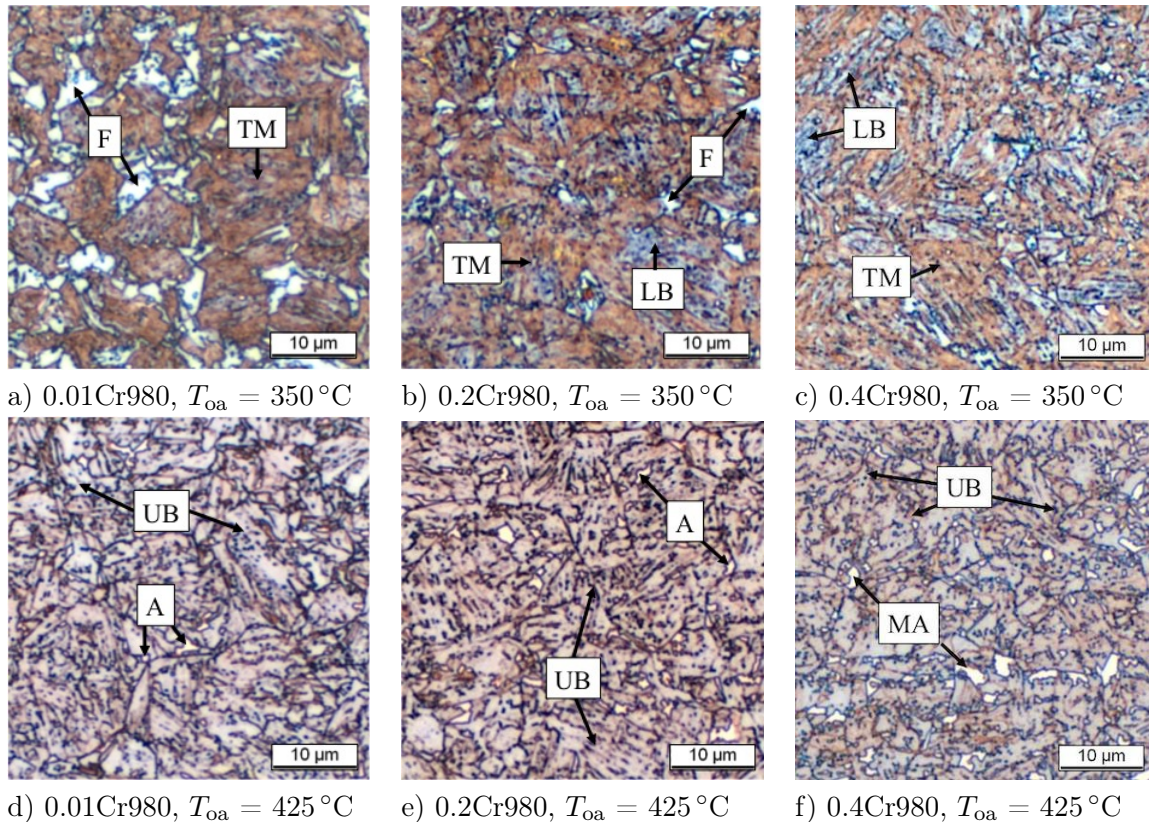


Figure 4.14: LePera etched optical micrographs of Q&P and TBF heat-treated 980 grade chromium variants 0.01Cr980, 0.2Cr980, and 0.4Cr980 for fixed overaging temperatures of 350 °C and 425 °C comprising polygonal ferrite (F), bainite (B), lower bainite (LB), tempered martensite (TM), retained austenite (A) and retained austenite/martensite islands (MA) ( $t_{oa} = 600\text{ s}$ ,  $\dot{T} \approx 50\text{ K/s}$ ).

Yield strength, tensile strength, uniform elongation, and the amount of retained austenite as a function of overaging time are shown in Figure 4.15a. All investigated properties increase with increasing chromium content. However, the increase is much more pronounced from steel 0.01Cr980 to 0.2Cr980 than from 0.2Cr980 to 0.4Cr980. Uniform elongation behaves slightly differently, as it shows similar values of all grades at low overaging temperatures and a equal increase with chromium content at high overaging temperatures.

As seen in Figure 4.15b, yield strength decreases at low and increases at high overaging temperatures with increasing chromium content. Tensile strength, in contrast, consistently shows higher values for higher chromium contents in the complete range of investigated overaging temperatures from 350 °C to 475 °C. However, this trend is more pronounced at high overaging temperatures. The amount of retained austenite is significantly higher in steels 0.2Cr980 and 0.4Cr980 than in grade 0.01Cr980, and slightly higher in steel 0.4Cr980 than in grade 0.2Cr980 at all overaging temperatures, except for 350 °C. The difference in uniform elongation between the different chromium

grades is almost negligible. The steel with the highest chromium content shows a higher uniform elongation for 425 °C and a lower uniform elongation for the highest overaging temperature of 475 °C as compared to the grades with the lower chromium content.

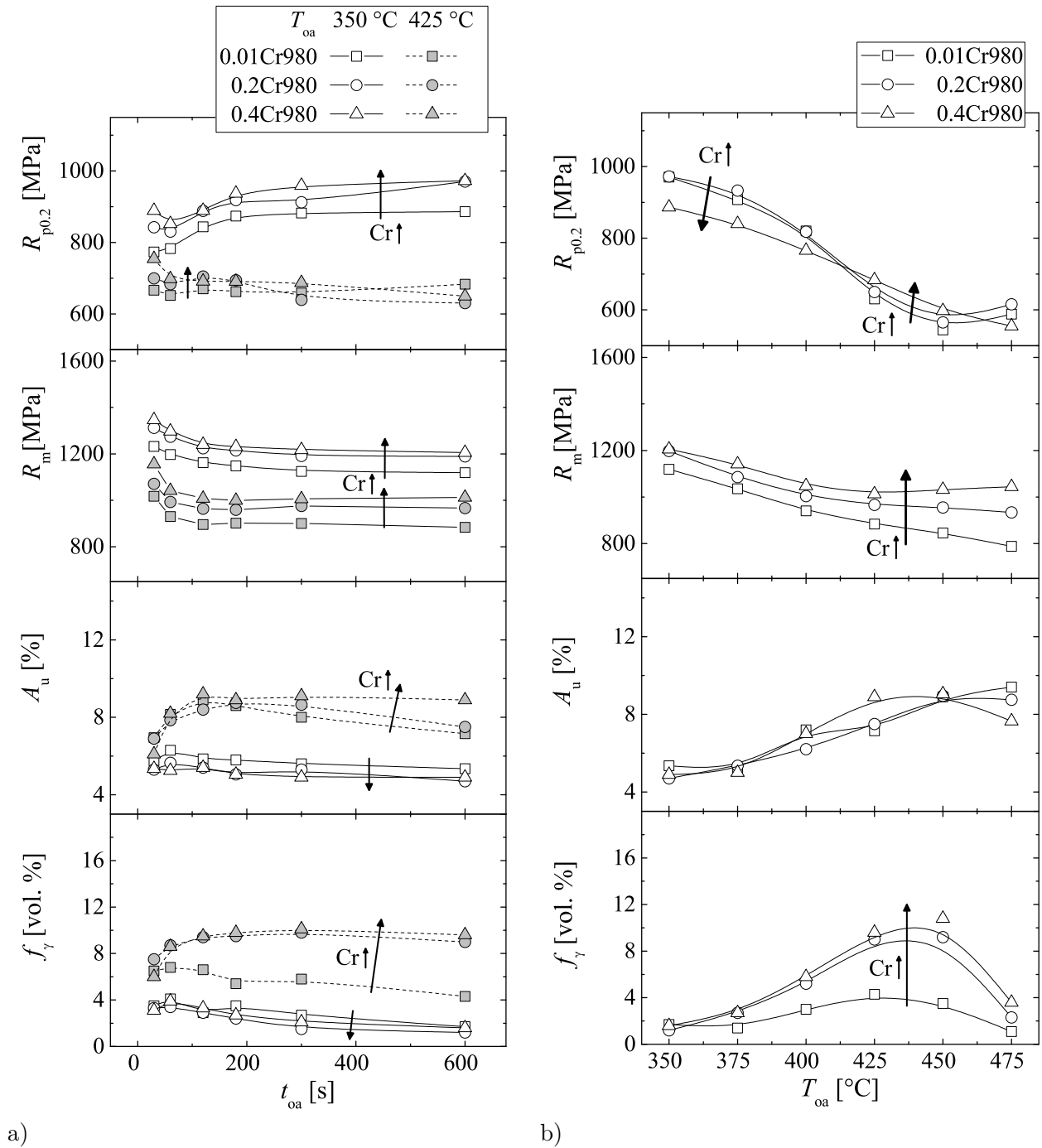


Figure 4.15: Yield strength, tensile strength, uniform elongation, and amount of retained austenite of grades 0.01Cr980, 0.2Cr980 and 0.4Cr980 a) as a function of overaging time for overaging temperatures  $T_{oa} = 350$  °C and  $T_{oa} = 425$  °C, b) as a function of overaging temperature ( $t_{oa} = 600$  s).

### 4.1.6 Chromium in the 1180 grade

The transformation behaviour during continuous cooling and overaging has been studied by selected dilatometer experiments. As seen in Figure 4.16a, the transformed fraction during cooling with a cooling rate of 3 K/s decreases with increasing chromium content. For the high cooling rate of 50 K/s, ferrite and bainite forms during cooling of the 0.01Cr1180 grade, whereas this formation is suppressed by a chromium content of 0.2 mass% Cr and above.  $M_s$  temperature is approximately 360 °C and slightly lower for higher chromium content, as indicated by the transformed fraction curves of 0.2Cr1180 and 0.4Cr1180 with a cooling rate of 50 K/s.

Figure 4.16b shows, that chromium decelerates the isothermal bainite formation at all overaging temperatures from 350 to 550 °C. The higher the overaging temperature, the stronger the deceleration of phase transformations by chromium additions. Between 400 and 550 °C overaging temperature, chromium slows down phase transformation kinetics particularly pronounced. In addition, it is worth noting that isothermal phase transformation kinetics remains essentially the same for the investigated 1180 chromium variants at an overaging temperature of 300 °C. Interestingly, at 600 °C, the isothermal phase transformation is decelerated at first and then accelerated as the chromium content increases.

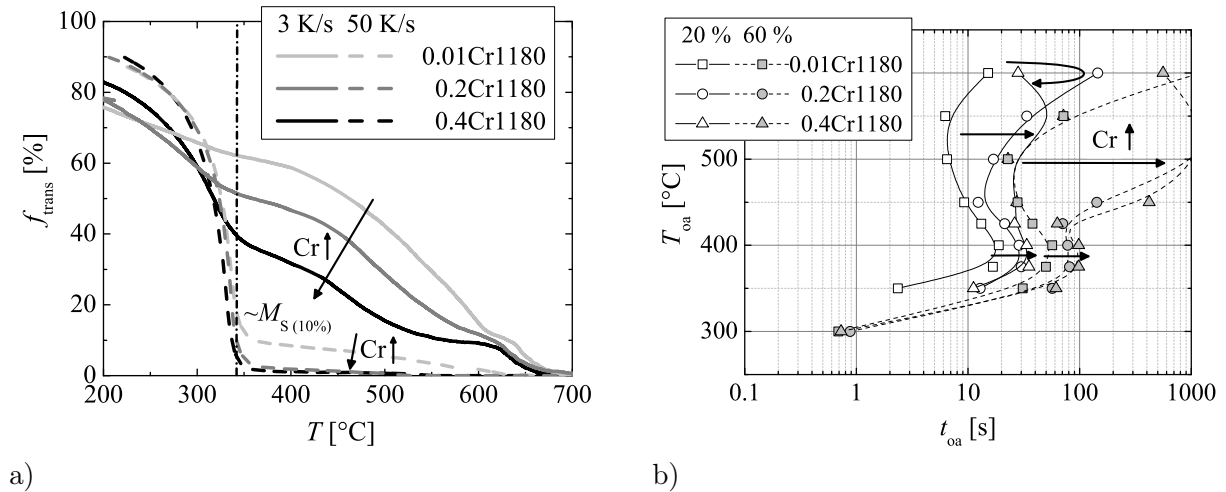


Figure 4.16: a) Transformed phase fraction during continuous cooling at rates of 3 and 50 K/s, b) isothermal TTT curve for steel grades 0.01Cr1180, 0.2Cr1180 and 0.4Cr1180.

The normalized length as a function of overaging time as shown in Figure 4.17a indicates both a deceleration of isothermal transformation and a lower amount of bainite at which the isothermal transformation proceeds at a very slow rate. The same trend has been found for all overaging temperatures.

Thermo-Calc© TCFE6 [165] calculations can be used to identify, if the reason for the lower amount of bainite formed during overaging is of thermodynamic or kinetic nature. Figure 4.17b shows the phase diagram and the  $T_0$  temperature obtained from Thermo-Calc© calculations. The  $T_0$  temperature is the temperature at which the Gibbs free energy of the fcc structure equals that of the bcc structure for a given carbon content [46]. According to the  $T_0$  concept, bainite transformation can only occur at a temperature below  $T_0$  temperature. Chromium increases the  $A_1$  temperature and very slightly decreases the  $T_0$  as well as  $A_3$  temperature. However, the influence of chromium content on  $T_0$  temperature appears almost negligible in the investigated range. Thus, the presumable stagnation of the isothermal transformation at lower amounts of bainite for higher chromium contents is not a consequence of a shift in  $T_0$  temperature. In fact, the driving force

for transformation should be higher for higher chromium contents, since  $A_1$  temperature increases with increasing chromium content. A possible explanation is that chromium strongly decelerates the diffusion in particular after a specific amount of bainite has formed. This is inversely proportional lower for higher chromium contents. This means that for infinitely long overaging times, all chromium variants would exhibit very similar amounts of bainite during overaging.

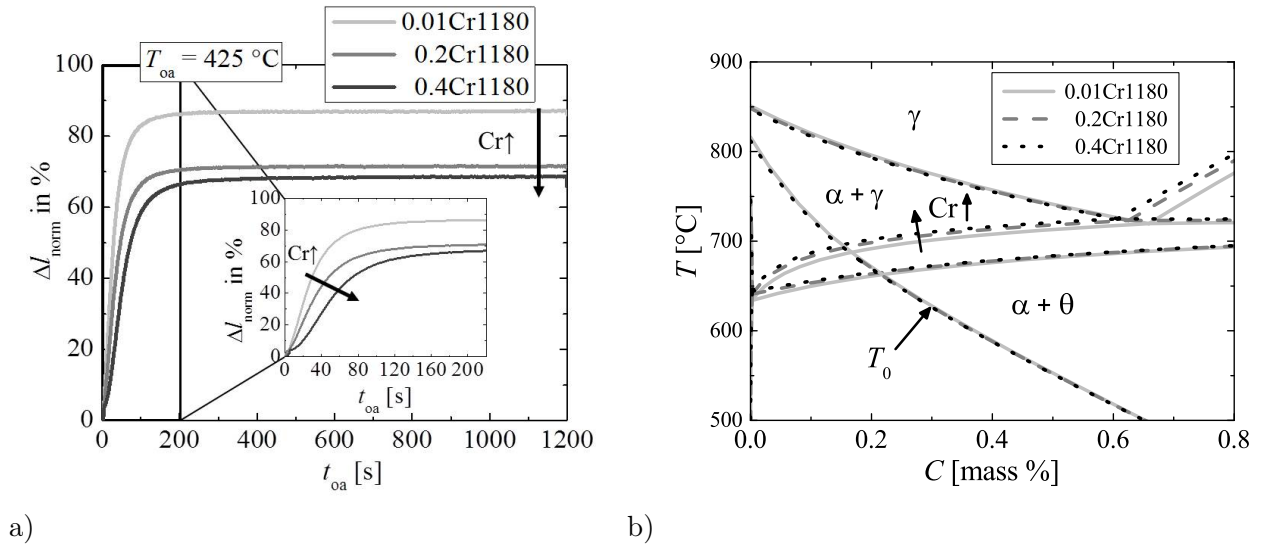


Figure 4.17: a) Normalized length during overaging at  $T_{\text{oa}} = 425 \text{ } ^\circ\text{C}$  of grades 0.01Cr1180, 0.2Cr1180 and 0.4Cr1180. b) Phase diagram and  $T_0$  temperature of grades 0.01Cr1180, 0.2Cr1180 and 0.4Cr1180 in thermodynamic equilibrium calculated using Thermo-Calc®.

LePera etched optical micrographs of the 1180 grade chromium variants are shown in Figure 4.18 for overaging temperatures  $350 \text{ } ^\circ\text{C}$  and  $425 \text{ } ^\circ\text{C}$ . The bainite morphology changes from lath-like to more globular with increasing chromium content for an overaging temperature of  $350 \text{ } ^\circ\text{C}$ , whereas there is no notable difference between the bainite morphologies of the different chromium variants at  $425 \text{ } ^\circ\text{C}$  overaging temperature. The steel with the lowest chromium content contains small amounts of polygonal ferrite, which is particularly visible for  $350 \text{ } ^\circ\text{C}$  overaging temperature due to a greater contrast to the surrounding lower bainitic/tempered martensitic matrix. The number of retained austenite grains of approximately  $1 \text{ } \mu\text{m}$  in equivalent diameter increases with increasing chromium content for an overaging temperature of  $350 \text{ } ^\circ\text{C}$ . Steel 0.4Cr1180 exhibits some relatively large retained austenite/martensite inclusions with brownish tempered martensite in the center for the overaging temperature of  $350 \text{ } ^\circ\text{C}$ . The size of the retained austenite/martensite inclusions at  $425 \text{ } ^\circ\text{C}$  overaging temperature strongly increases with increasing chromium content.

SEM images can provide more detailed insight than optical micrographs into the morphology of bainite and retained austenite as well as the presence and shape of fine inclusions in particular carbides (Figure 4.19). For an overaging temperature of  $350 \text{ } ^\circ\text{C}$ , the bainite of the grade with the lowest chromium content, 0.01Cr1180, is finer, and the laths are both thinner and longer compared to the grade 0.4Cr1180 (Figure 4.19a). Distinctly higher amounts of retained austenite are present in the grade with the high chromium content at this overaging temperature. The retained austenite of steel 0.4Cr1180 is more block-like, while most of the retained austenite of the grade with low chromium content exists in the form of small films between the bainite laths (Figure 4.19a-c). Grade 0.01Cr1180 also contains more carbides, most of which are cementite as detected by EDX measurements.

For the higher overaging temperature of  $425 \text{ } ^\circ\text{C}$ , the bainite morphology is more lath-like and the

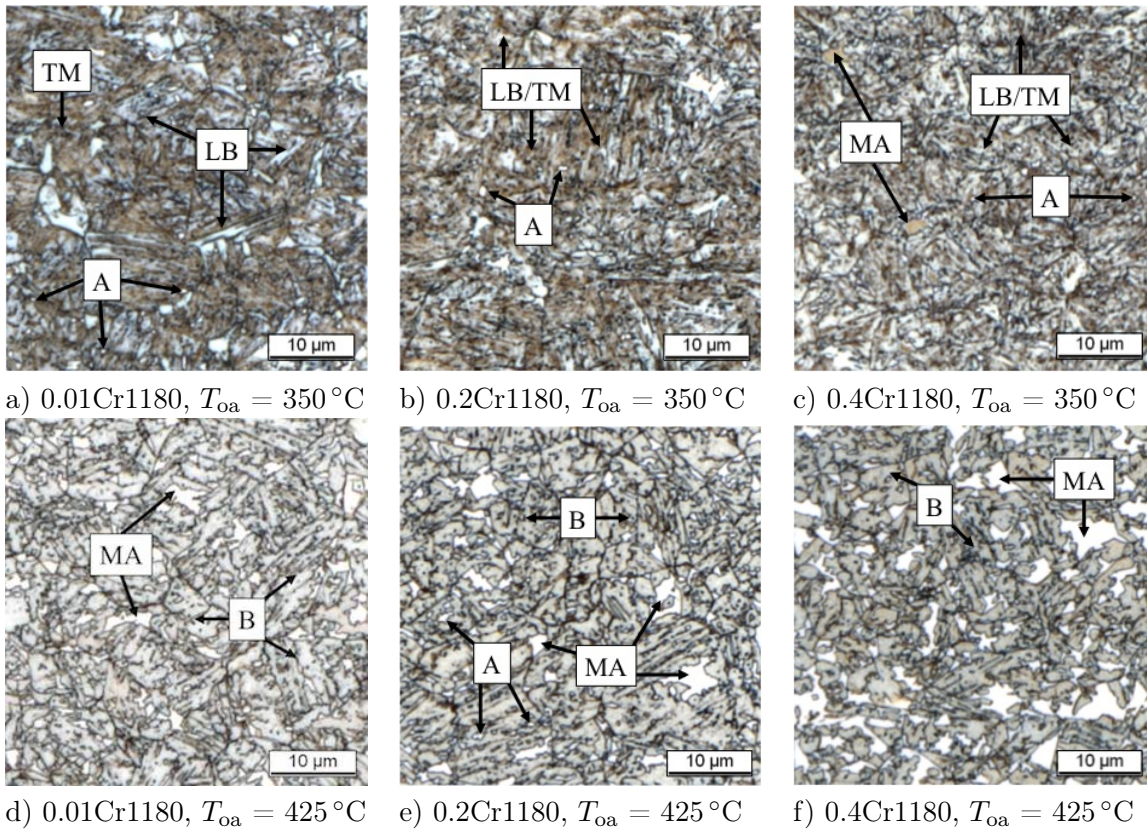


Figure 4.18: LePera etched optical micrographs of Q&P and TBF heat-treated 1180 grade chromium variants 0.01Cr1180, 0.2Cr1180, and 0.4Cr1180 for fixed overaging temperatures of  $350\text{ }^{\circ}\text{C}$  and  $425\text{ }^{\circ}\text{C}$  comprising polygonal ferrite (F), bainite (B), lower bainite (LB), tempered martensite (TM), retained austenite (A) and retained austenite/martensite islands (MA) ( $t_{oa} = 600\text{ s}$ ,  $\dot{T} \approx 50\text{ K/s}$ ).

laths are separated by thin retained austenite films for steels 0.01Cr1180 and 0.2Cr1180 as opposed to grade 0.4Cr1180 (Figure 4.19b). The bainite morphology of steel 0.4Cr1180, in contrast, is much coarser, and contains less cementite compared to the steels with the lower chromium content. The size of the retained austenite/martensite islands strongly increases with increasing chromium content for  $425\text{ }^{\circ}\text{C}$  overaging temperature.

Yield strength, tensile strength, uniform elongation, and amount of retained austenite as a function of overaging time are shown in Figure 4.20a. In principle, the trends of mechanical properties and amount of retained austenite with increasing overaging temperature are in good agreement with those of the 1180 grade manganese or silicon variants. However, the decreasing and then increasing tendency of the yield strength is not as pronounced as seen for the other 1180 variants. Furthermore, uniform elongation continues to increase for the highest chromium content and the low overaging temperature of  $350\text{ }^{\circ}\text{C}$ , while it decreases for the lowest chromium content at the higher overaging temperature. The former tendency can be observed for the 1180 manganese variant as well, whereas the later trend is typical only for this specific composition. The behaviour of the amount of retained austenite with overaging time is in good agreement with the 1180 manganese variants.

Similar to the 1180 manganese variants, the yield strength shifts from an increase to a decrease with increasing chromium content at overaging times of more than 180 s for an overaging temperature of  $350\text{ }^{\circ}\text{C}$ . At the higher overaging temperature of  $425\text{ }^{\circ}\text{C}$ , yield strength consistently increases with increasing chromium content. Higher chromium content results in higher tensile strength values within the whole range of overaging times, particularly at high overaging temperature. The

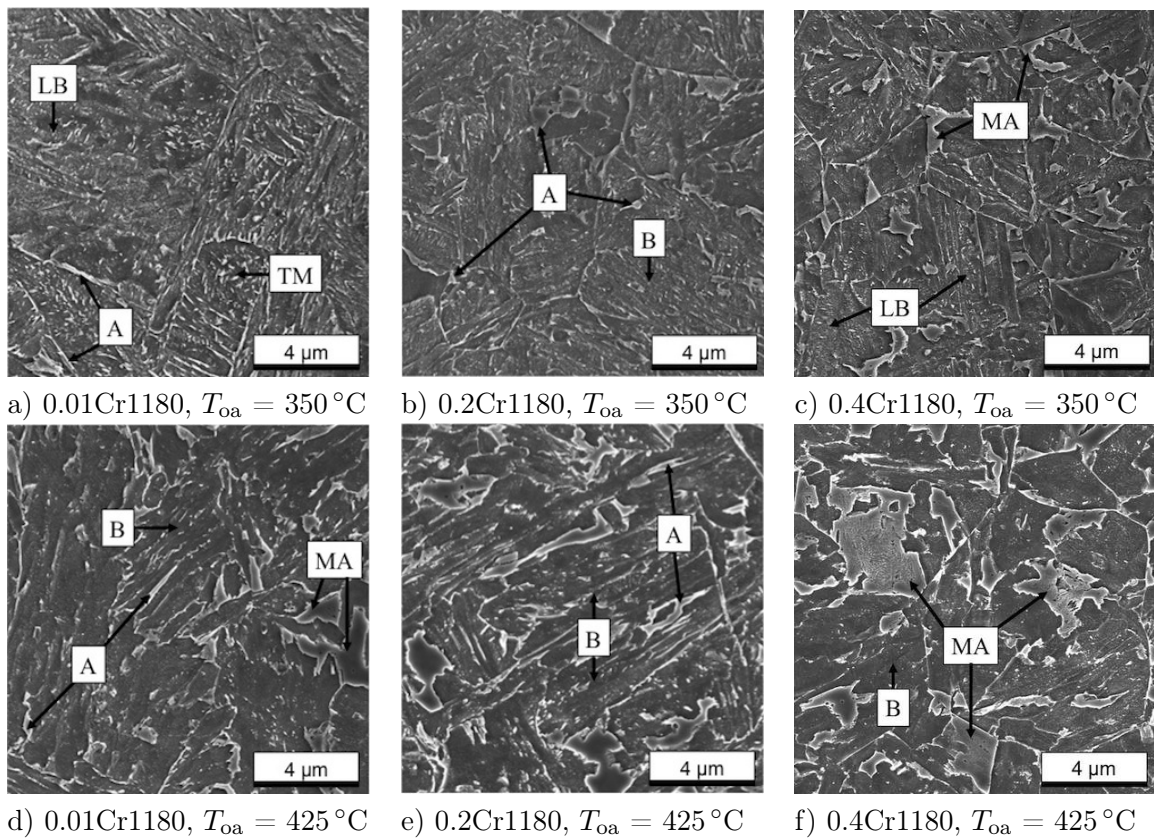


Figure 4.19: SEM images of Q&P and TBF heat-treated 1180 grade chromium variants 0.01Cr1180, 0.2Cr1180, and 0.4Cr1180 for fixed overaging temperatures of 350 °C and 425 °C comprising polygonal ferrite (F), bainite (B), lower bainite (LB), tempered martensite (TM), retained austenite (A) and retained austenite/martensite islands (MA) ( $t_{oa} = 600\text{ s}$ ,  $\dot{T} \approx 50\text{ K/s}$ ).

uniform elongation increases at low and decreases at high overaging temperatures with increasing chromium content. This behaviour is unique among the investigated alloying concepts, since an increase in an alloying element such as silicon or manganese usually results in an increase in uniform elongation, except for the 980 manganese variants at the low overaging temperature and the 1180 silicon variants, where the changes as a consequence of alloying additions are negligible. The amount of retained austenite also increases at low and decreases at high overaging temperatures with increasing chromium content. The tendency towards this behaviour is present in the 1180 manganese variants.

The results of mechanical properties and amount of retained austenite as a function of overaging temperature are shown in Figure 4.20b. The yield strength as a function of overaging time shifts from decreasing to increasing yield strength with increasing chromium content. Such a tendency was also found in the 1180 manganese variants. Higher chromium content results in higher tensile strength with a strongly increasing tendency for higher overaging temperatures. Uniform elongation slightly increases for higher chromium contents at 350 °C, and strongly decreases for overaging temperatures above 400 °C. Similar behaviour was observed in the 1180 grade manganese variants, with a stronger increase in uniform elongation with increasing manganese content at low overaging temperatures. The amount of retained austenite is significantly higher for higher chromium contents and overaging temperatures up to 400 °C, and drops to lower values which are similar among the different chromium variants for higher overaging temperatures.

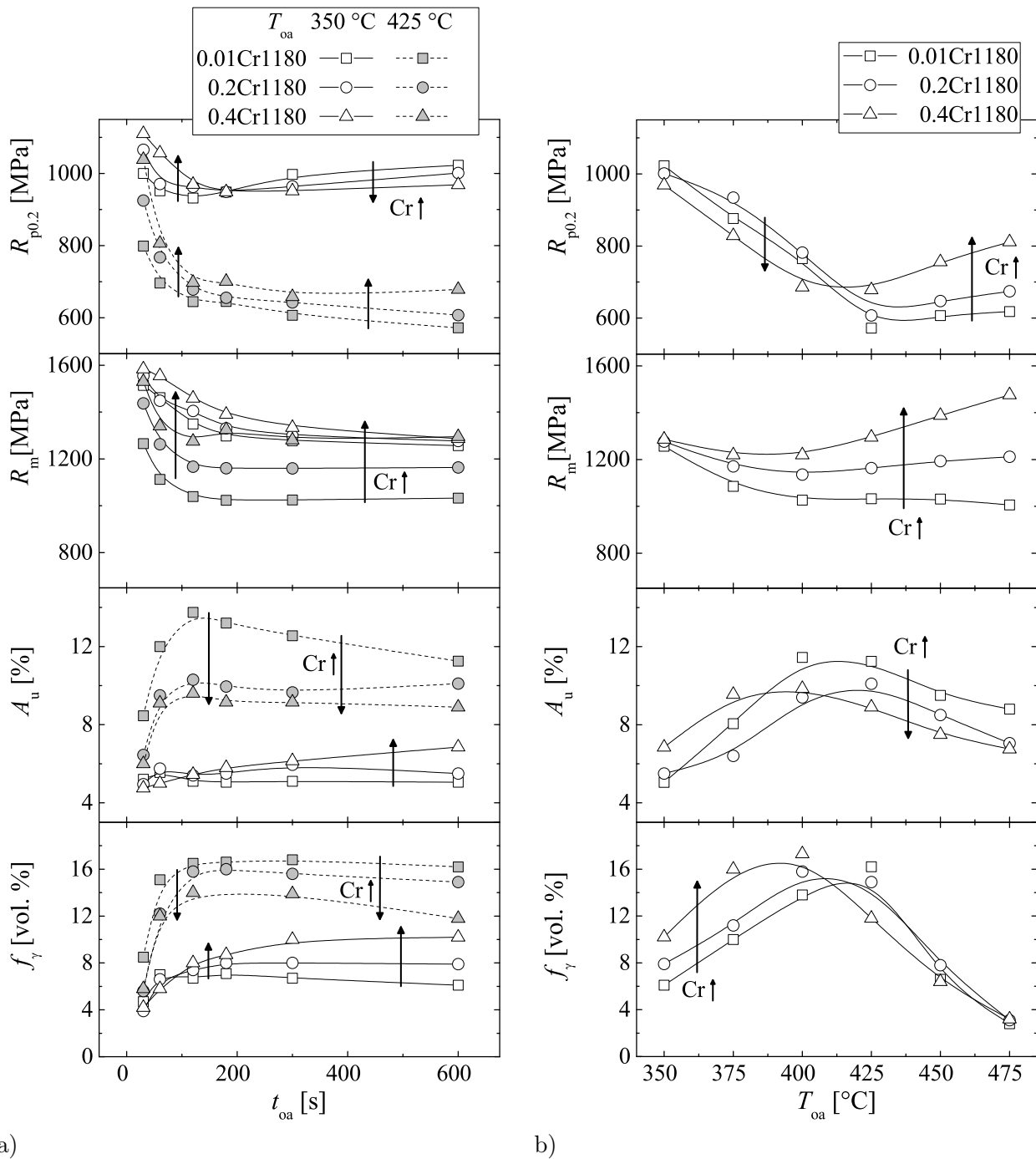


Figure 4.20: Yield strength, tensile strength, uniform elongation, and amount of retained austenite of grades 0.01Cr1180, 0.2Cr1180 and 0.4Cr1180 a) as a function of overaging time for overaging temperatures  $T_{oa} = 350^\circ\text{C}$  and  $T_{oa} = 425^\circ\text{C}$ , b) as a function of overaging temperature ( $t_{oa} = 600\text{ s}$ ).

#### 4.1.7 Niobium in the 980 grade

Niobium plays a crucial role for grain refinement and precipitation strengthening in many steel grades [87, 100, 106, 107, 168–170]. The influence of niobium on conventional TRIP steels is thoroughly documented in literature [171, 172]. The present work fills the gap of combining third-

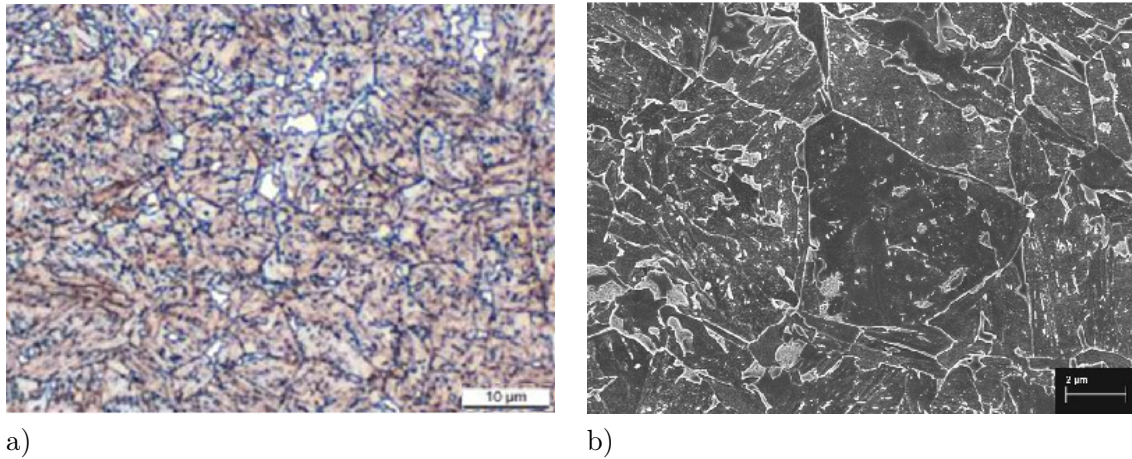


Figure 4.21: a) LePera etched optical micrograph and b) SEM of TBF steel 0.025Nb980 for a fixed overaging temperature and overaging time of  $T_{oa} = 400\text{ }^{\circ}\text{C}$  and  $t_{oa} = 600\text{ s}$ , respectively [173].

generation AHS-TBF steels of  $\text{Si} < 1.5\%$  with the concept of microalloying. Parts of the results presented in this section were previously published [173].

Bechet-Beaujard etching is used to reveal the prior austenite grain size of a reference TBF steel without niobium and three niobium microalloyed variants comprising 0.025 to 0.09 mass % niobium (Table 4.1) [174]. The prior austenite grain size of the niobium-free reference material is significantly larger than the grain size of a niobium containing steel. There are minor differences between the prior austenite for the different niobium contents of 0.025 to 0.09 mass %.

Table 4.1: Prior austenite grain size after quenching from annealing temperature expressed by the equivalent circle diameter (ECD)  $T_{an} = 900\text{ }^{\circ}\text{C}$  for the niobium free steel and the three steels alloyed with niobium [173].

Steel	0Nb980	0.025Nb980	0.045Nb980	0.09Nb980
ECD [ $\mu\text{m}$ ]	$12.1 \pm 7.3$	$6.0 \pm 3.4$	$5.3 \pm 2.9$	$5.5 \pm 3.1$

Figure 4.21 shows a typical example for the microstructure of a niobium-microalloyed TBF steel as observed in the optical microscope (Figure 4.21a) and in the scanning electron microscope (Figure 4.21b) after overaging at  $T_{oa} = 400\text{ }^{\circ}\text{C}$  for  $t_{oa} = 600\text{ s}$ . LePera's etchant colours the bainitic matrix brown/blue (Figure 4.21a). The numerous small white areas indicate retained austenite. The large white/brownish areas in the micrograph of Figure 4.21a potentially contain martensite.

The purely white areas observed in the LePera etched optical micrograph (Figure 4.21a) can be identified as dark and even elevated retained austenite grains in the SEM of Figure 4.21b. The white and brownish areas in the optical micrograph correspond to dark elevated and white structured patterns indicating retained austenite/martensite islands in the SEM, respectively (Figure 4.21b).

The microstructures of all niobium variants and the niobium-free reference material observed by SEM after overaging at a temperature of  $400\text{ }^{\circ}\text{C}$  for 600 s are shown in Figure 4.22. The bainite of the niobium-variants appears more globular as compared to the mainly lath-like bainite of the reference material. Also, the reference material contains large amounts of lath-like retained austenite, while the retained austenite of the grades with niobium addition appears more block-like.

Transmission electron microscopy is a valuable tool to confirm the SEM observations with re-

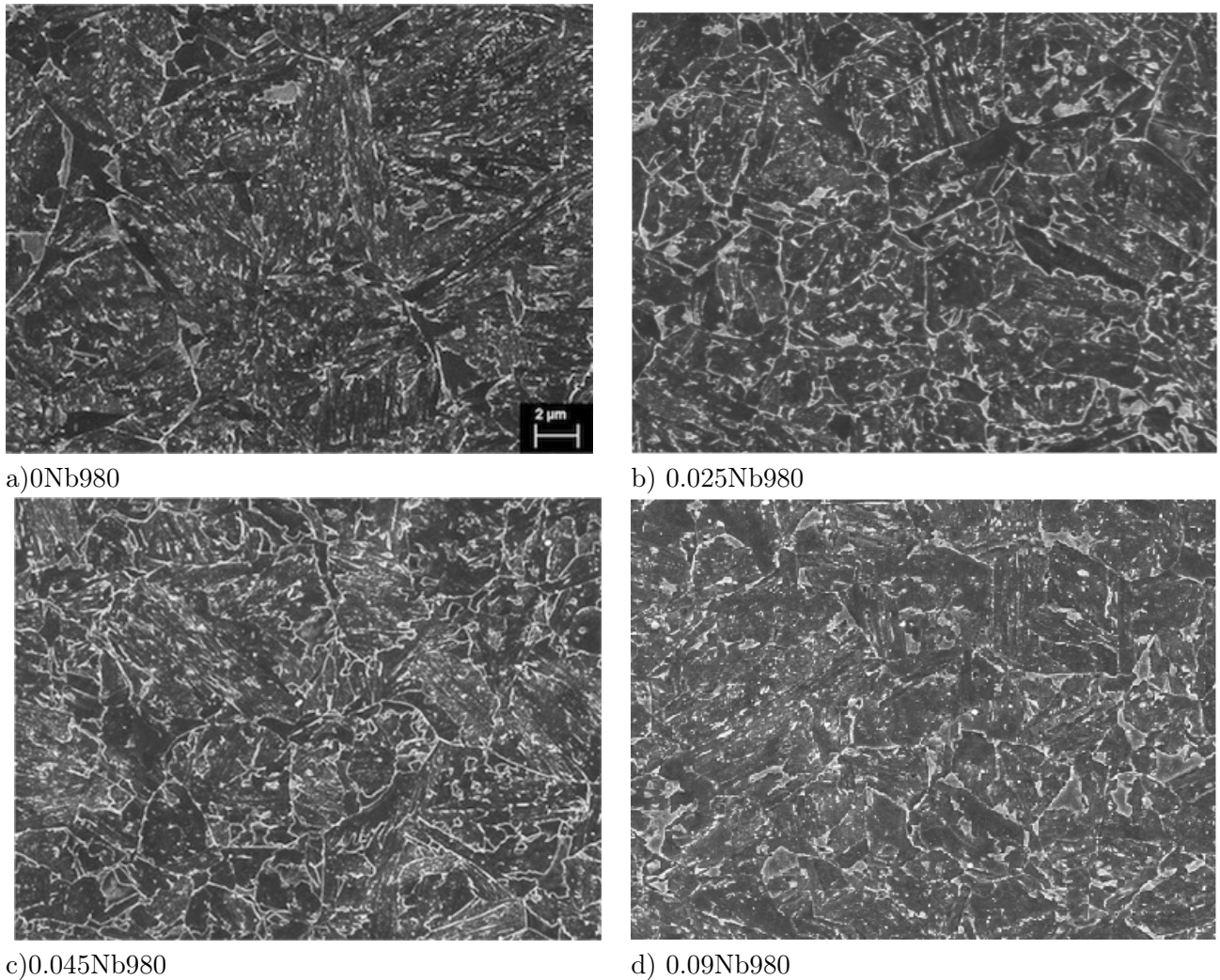


Figure 4.22: SEM images of a) 0Nb980 b) 0.025Nb980 c) 0.045Nb980 d) 0.09Nb980 heat-treated TBF steels for a fixed overaging temperature of  $T_{oa} = 400\text{ }^{\circ}\text{C}$  ( $t_{oa} = 600\text{ s}$ ,  $\dot{T} \approx 50\text{ K/s}$ ) [173].

spect to the change in bainite and retained austenite morphology as well as to gain quantitative information on carbide precipitation. The TEM analysis performed on all investigated steel grades (Figure 4.23) confirm the SEM results in terms of the above-mentioned morphology changes. Moreover, considerably less cementite is found in the bainite of the niobium microalloyed TBF steels compared to the reference material. The black round dots appearing in the grade 0.045Nb980 (Figure 4.23c) and even larger in the grade 0.09Nb980 (Figure 4.23d) were identified as niobium carbides using EDX.

The composition of the carbides was identified by selected area diffraction (SAD) in the transmission electron microscope. Figure 4.24 gives an example for the identification of a large precipitate. The Laue-Bragg indices Figure 4.24b were deduced from selected area diffraction patterns (SADP) (Figure 4.24a).

Two populations of NbC particles are present in the niobium-containing steels. Quantitative analysis (Table 4.2) reveals that all niobium variants contain both NbC particle populations. While

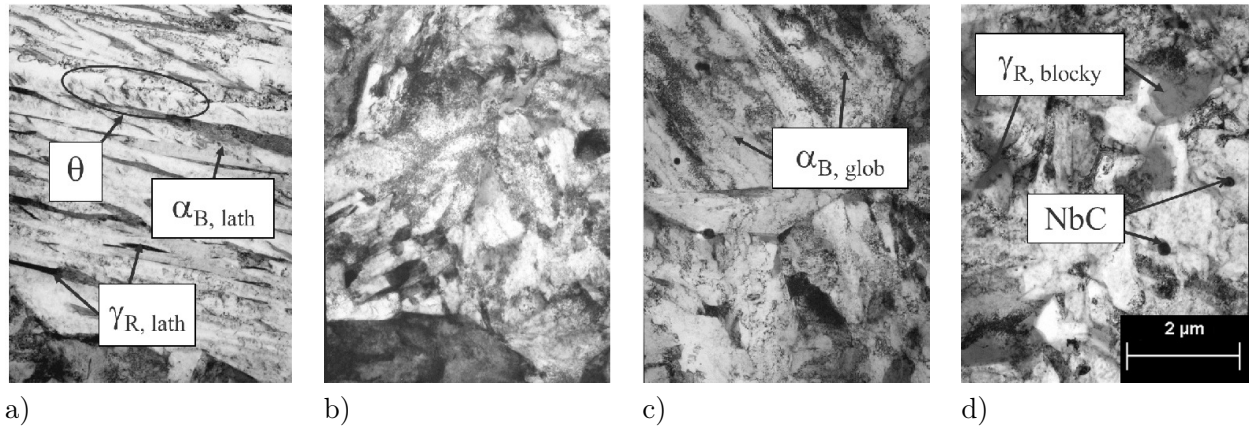


Figure 4.23: TEM images of a) 0Nb980 b) 0.025Nb980 c) 0.045Nb980 d) 0.09Nb980 heat-treated TBF steels for a fixed overaging temperature of  $T_{oa} = 400^\circ\text{C}$  ( $t_{oa} = 600\text{ s}$ ,  $\dot{T} \approx 50\text{ K/s}$ ) [173].

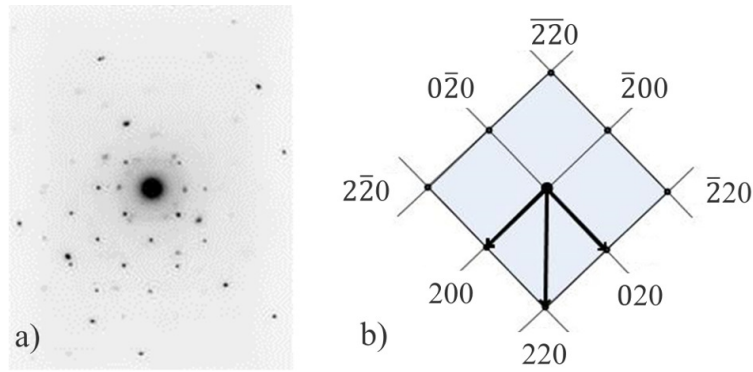


Figure 4.24: a) Selected Area Diffraction Pattern (SADP) and b) Laue-/Bragg-indices of a NbC particle shown in Figure 4.23d [173].

the density of coarse NbC particles remarkably increases with the niobium content, no significant trend was found regarding the density of fine NbC particles.

Table 4.2: Two NbC particle populations, fine and coarse, characterized by the equivalent circle diameter (ECD) and density of these precipitates in the steels 0.025Nb980, 0.045Nb980, and 0.09Nb980 [173].

	fine NbC particles		
Steel	0.025Nb980	0.045Nb980	0.09Nb980
ECD [nm]	$5.7 \pm 1.9$	$6.4 \pm 2.8$	$6.7 \pm 3.0$
Particle density [ $1/\text{m}^2$ ]	$76 \pm 13$	$65 \pm 21$	$82 \pm 28$
	coarse NbC particles		
Steel	0.025Nb980	0.045Nb980	0.09Nb980
ECD [nm]	$82 \pm 18$	$73 \pm 52$	$89 \pm 51$
Particle density [ $1/\text{m}^2$ ]	$0.10 \pm 0.06$	$0.21 \pm 0.10$	$0.41 \pm 0.18$

The amount of undissolved niobium was measured before and after annealing in order to investi-

gate the potential to dissolve the NbC particles during annealing. The greater the niobium content the more niobium precipitates were observed (Figure 4.25). Since the results for the as-cold-rolled and annealed samples mutually fall into their scatter bands, a significant dissolution or further precipitation of NbC during the austenitization step can be excluded. Due to the filtering technique employed in this analysis, fine particles are hardly detected. The amounts shown are thus minimum amounts of niobium carbides.

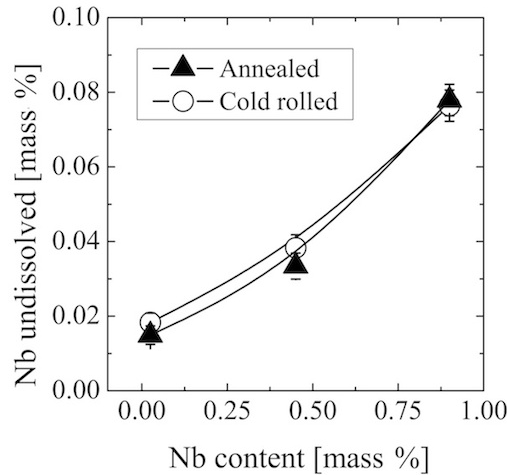


Figure 4.25: Amount of undissolved niobium as a function of the overall niobium content for steel grades 0.025Nb980, 0.045Nb980, and 0.09Nb980 measured by ICP-MS [173].

The transformed austenite fraction of continuously cooled samples ( $\dot{T} = 50 \text{ K/s}$ ) is shown in Figure 4.26a as a function of temperature. Down to a temperature of  $400^\circ\text{C}$  the reference material does not begin to transform, whereas the austenite of the niobium alloyed steels transforms starting at  $640^\circ\text{C}$  until the overaging temperature is reached where roughly 20% ferrite and upper bainite are formed. The same transformation behaviour is observed for all niobium variants.

Figure 4.26b illustrates the effect of niobium on the isothermal bainite transformation (IBT) at  $400^\circ\text{C}$ . All steel grades transform approximately with the same velocity as indicated in the insert, and IBT is completed after 120 s. The amount of isothermal bainite as shown in Figure 4.26b is less for niobium microalloyed steels. The fractions of both the isothermal bainite and the transformation product of cooling to overaging (Figure 4.26a) add up to approximately the same amount.

The amount of retained austenite as a function of overaging time for the investigated niobium microalloyed TBF steels and the reference material are shown in Figure 4.27a. It initially increases in all steel grades, followed by a saturation after approximately 200 s. The most significant increase of retained austenite as compared to the reference material was observed for the 0.025Nb980 steel. A further increase of the niobium content does not result in a further increase of the amount of retained austenite.

The stability of retained austenite against strain induced martensitic transformation was studied by measuring the amount of retained austenite as a function of tensile strain by means of interrupted tensile tests (Figure 4.27b). The amount of retained austenite decreases with increasing plastic deformation. A significant amount of retained austenite of up to 4 vol.% remains untransformed until fracture strain is reached. All steel grades show almost the same stability behaviour.

The carbon content of retained austenite for the series of TBF heat-treated samples was determined by XRD measurements based on lattice constants according to Dyson and Holmes [175]. All steels, the reference material as well as the niobium microalloyed variants, contain the same amount of carbon in the retained austenite of 0.98 mass% after an isothermal heat treatment at

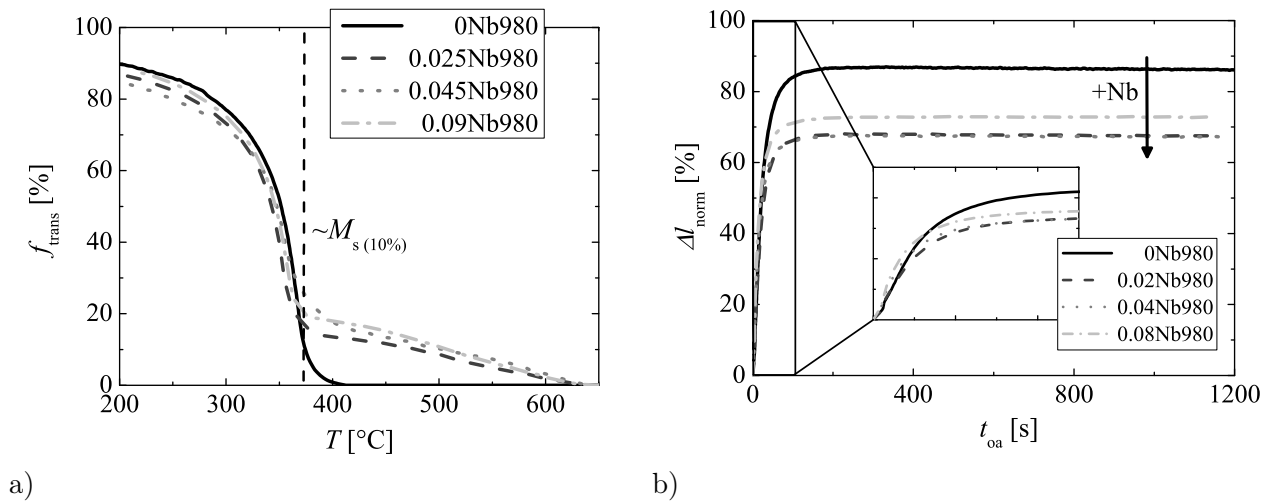


Figure 4.26: Transformation behaviour for steel grades 0Nb980, 0.025Nb980, 0.045Nb980, and 0.09Nb980: a) Transformed phase fraction of continuously cooled samples (50 K/s), b) normalized length of dilatometer samples during overaging at 400 °C ( $T_{\text{an}} = 900$  °C,  $\dot{T} \approx 70$  K/s).

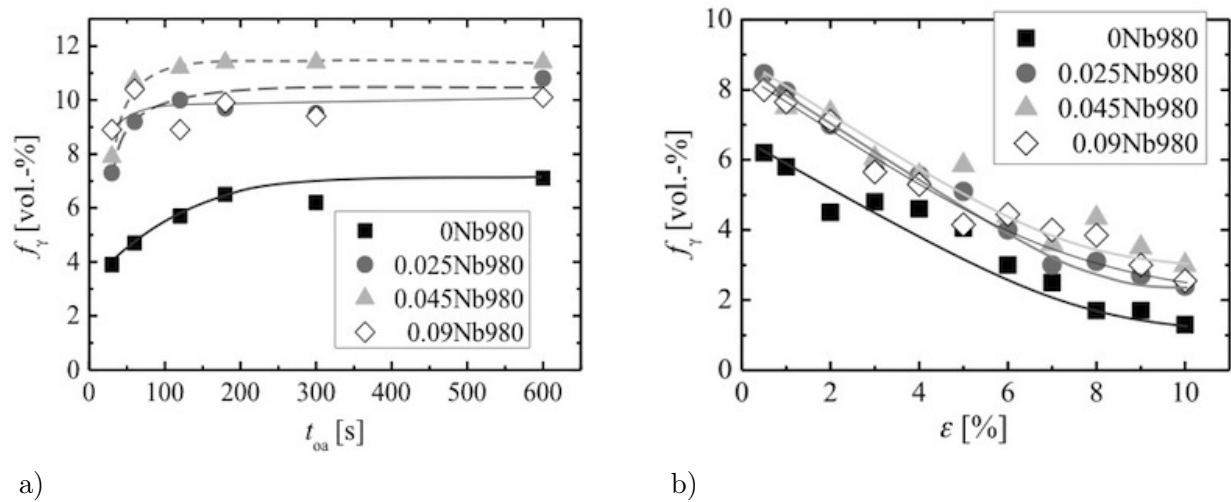


Figure 4.27: Amount of retained austenite for alloys 0Nb980, 0.025Nb980, 0.045Nb980, and 0.09Nb980 held at  $T_{\text{oa}} = 400$  °C for  $t_{\text{oa}} = 600$  s a) as a function of overaging time and b) as a function of engineering strain  $\epsilon$ .

$T_{\text{oa}} = 400$  °C and  $t_{\text{oa}} = 600$  s.

Yield strength and tensile strength as a function of overaging time are given in Figure 4.28a for all steel grades after overaging at 400 °C. Tensile strength drops by 200 MPa with increasing holding time and remains the same after 200 s in the overaging zone. Yield strength first decreases slightly then increases again and stabilizes after 300 s of overaging. Figure 4.28b shows the uniform and total elongation as a function of holding time. Apart from small deviations for the niobium alloys, the two elongation values increase with increasing holding time with a logarithmic-type behaviour. The niobium steels exhibit outstanding improvements in both uniform and total elongation compared to the reference material. However, the difference in uniform and total elongation between the different niobium variants is nearly negligible.

Figure 4.29 shows the true stress-logarithmic strain ( $\sigma_t$ - $\varphi$ ) flow curves, the strain-hardening rate

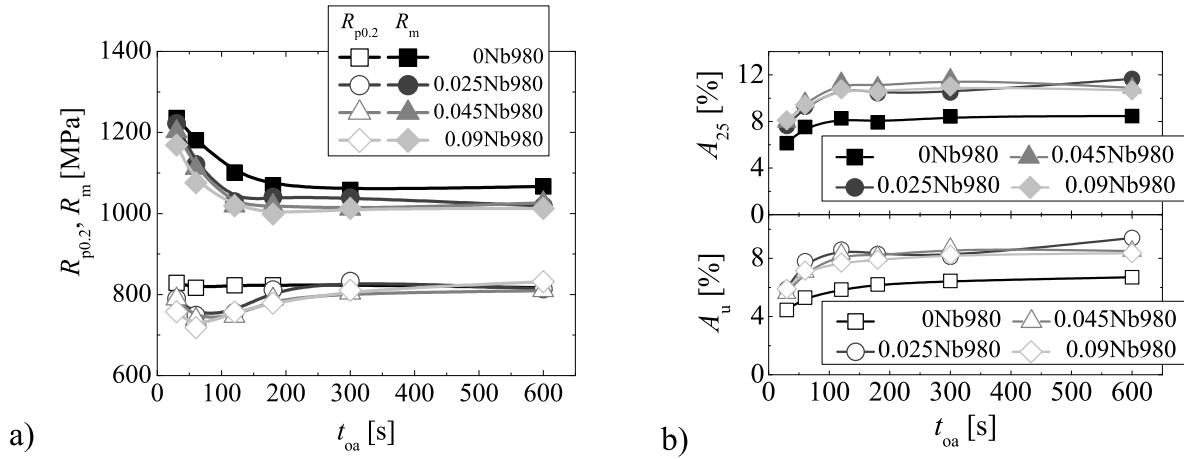


Figure 4.28: a) Yield strength  $R_{p0.2}$  and tensile strength  $R_m$ , b) uniform elongation  $A_u$ , and total elongation  $A_{25}$  as a function of overaging time at  $T_{oa} = 400^\circ\text{C}$  for steel grades 0Nb980, 0.025Nb980, 0.045Nb980, and 0.09Nb980.

$\theta$ , and the differential  $n$ -value  $n'$  as a function of logarithmic strain of the alloys that were held at  $400^\circ\text{C}$  for 600 s. The flow curve of the niobium-free reference material is steeper and its strain-hardening rate and differential  $n$ -value are distinctly higher than those of the niobium containing variants, especially up to approximately 2% of logarithmic strain. This results in higher elongation via elevated strain-hardening with increasing strain.

Mechanical properties and amount of retained austenite of the grade 0.025Nb980 as a function of overaging temperature are shown in Figure 4.30. Both yield and tensile strength decrease and elongations increase with overaging temperature. The relation between mechanical properties and overaging temperature can be divided into three stages, namely into rather flat plateaus at temperatures below  $M_s$  temperature as well as above  $450^\circ\text{C}$  and a linear range in between the plateaus. The amount of retained austenite increases with overaging temperature, decreases remarkably with overaging time at the highest overaging temperature of  $475^\circ\text{C}$  and reaches its highest values after 120 s of overaging at  $450^\circ\text{C}$ .

Hole expansion strain as a function of overaging temperature is shown in Figure 4.31. The hole expansion strain decreases with increasing holding temperature, and the addition of niobium barely affects the hole expansion strain.

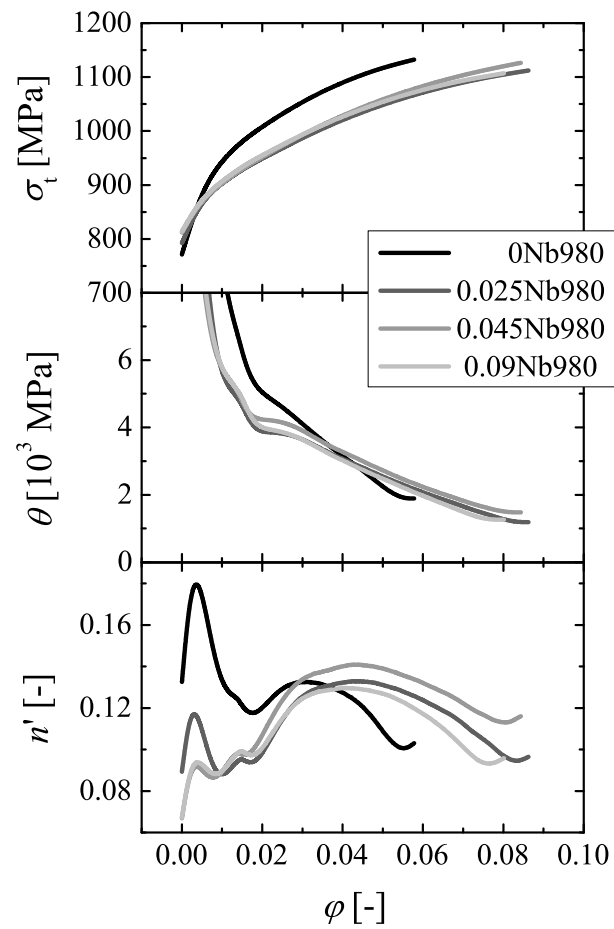


Figure 4.29: Flow curves ( $\sigma_t$  vs.  $\varphi$ ), strain-hardening rate  $\theta$  and differential  $n$ -value  $n'$  as a function of logarithmic strain  $\varphi$  for all steel grades annealed at  $T_{\text{oa}} = 400^\circ\text{C}$  for  $t_{\text{oa}} = 600$  s.

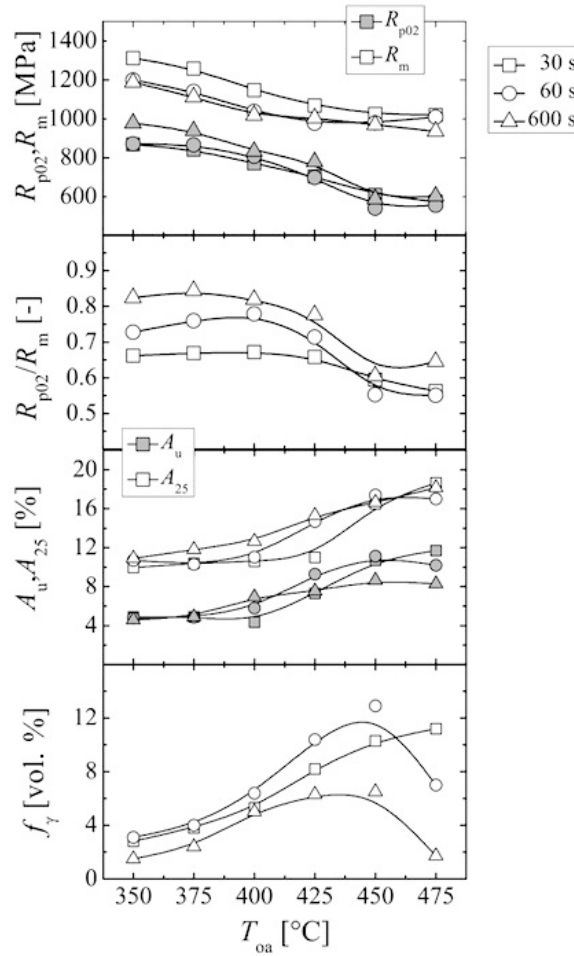


Figure 4.30: Tensile strength  $R_m$ , yield strength  $R_{p0.2}$ , yield ratio  $R_{p0.2}/R_m$ , total elongation  $A_{25}$ , uniform elongation  $A_u$ , and the amount of retained austenite  $f_\gamma$  as a function of overaging temperature for the grade 0.025Nb980.

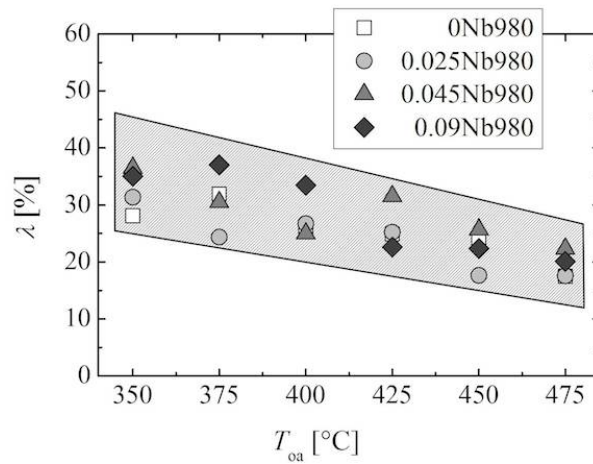


Figure 4.31: Hole expansion strain  $\lambda$  as a function of overaging temperature after  $t_{0a} = 600$  s for the reference material and all 980 niobium variants.

### 4.1.8 Niobium in the 1180 grade

In this section, the response of the 1180 grade to niobium additions of 0.02, 0.04, and 0.08 mass % Nb is evaluated. As opposed to the 980 grade, the transformation behaviour of both continuous cooling and overaging of the niobium-free reference material and each niobium variant are comparable (Figure 4.32a). That is, the reference material and all 1180 niobium variants do not change the phase transformation kinetics during continuous cooling prior to martensite transformation. Moreover, all investigated variants exhibit similar  $M_s$  temperatures. The isothermal transformation of the niobium variants proceeds marginally slower and stops at slightly lower amounts of isothermal transformation product (Figure 4.32b).

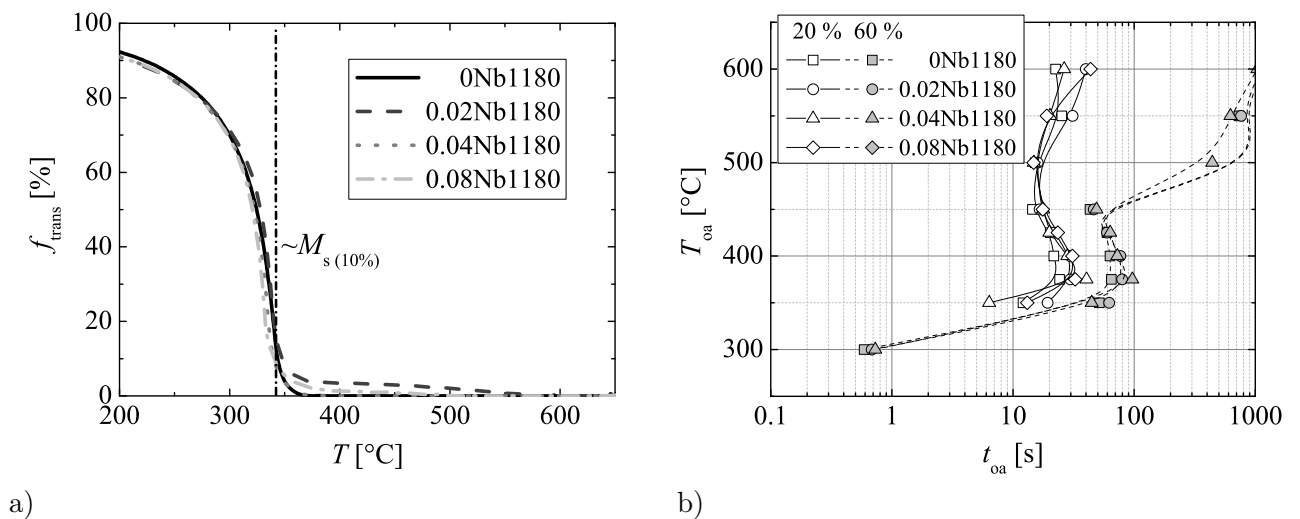


Figure 4.32: Transformation behaviour for steel grades 0Nb1180, 0.02Nb1180, 0.04Nb1180 and 0.08Nb1180: a) Transformed phase fraction during continuous cooling ( $\dot{T} \approx 50$  K/s) and b) isothermal TTT diagram of 20% and 60% transformed phase fraction for steels 0.02Nb1180, 0.04Nb1180, and 0.08Nb1180 ( $T_{\text{an}} = 900$  °C,  $\dot{T} \approx 70$  K/s).

Figure 4.33 shows the micrographs of the niobium-free reference material and the three niobium microalloyed 1180 grades. The microstructures of the niobium variants are finer, especially the one of the 0.04Nb1180 grade (Figure 4.33c). Similarly to the 980 grade, a change in bainite morphology from lath-like to globular can be observed through the addition of niobium. All grades contain comparable amounts of retained austenite, which will be verified with the following observations.

The mechanical properties and the amount of retained austenite as a function of overaging time are shown in Figure 4.34a. All values of each observed quantity are very similar among the niobium microalloyed 1180 grades. A slight increase in yield strength and tensile strength from the niobium-free steel to the niobium-containing steels is notable.

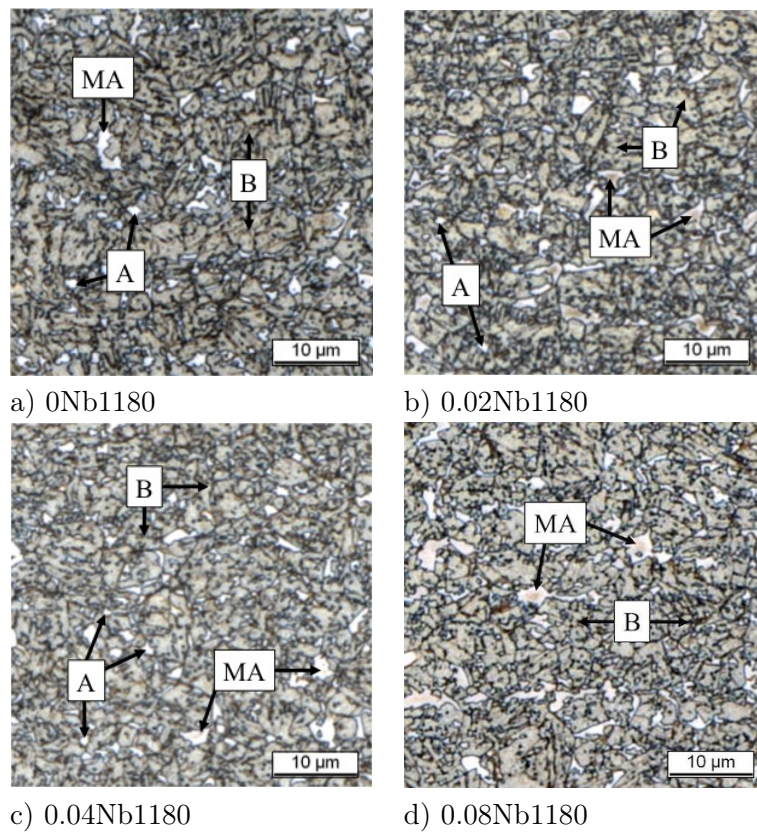


Figure 4.33: LePera etched optical micrographs of TBF heat-treated 1180 grade niobium variants a) 0Nb1180 b) 0.02Nb1180 c) 0.08Nb1180 for a fixed overaging temperature and time of  $T_{oa} = 400\text{ }^{\circ}\text{C}$  and  $t_{oa} = 600\text{ s}$ , respectively, comprising lower polygonal ferrite (F), bainite (B), lower bainite (LB), tempered martensite (TM), retained austenite (A) and retained austenite/martensite islands (MA) ( $\dot{T} \approx 50\text{ K/s}$ ).

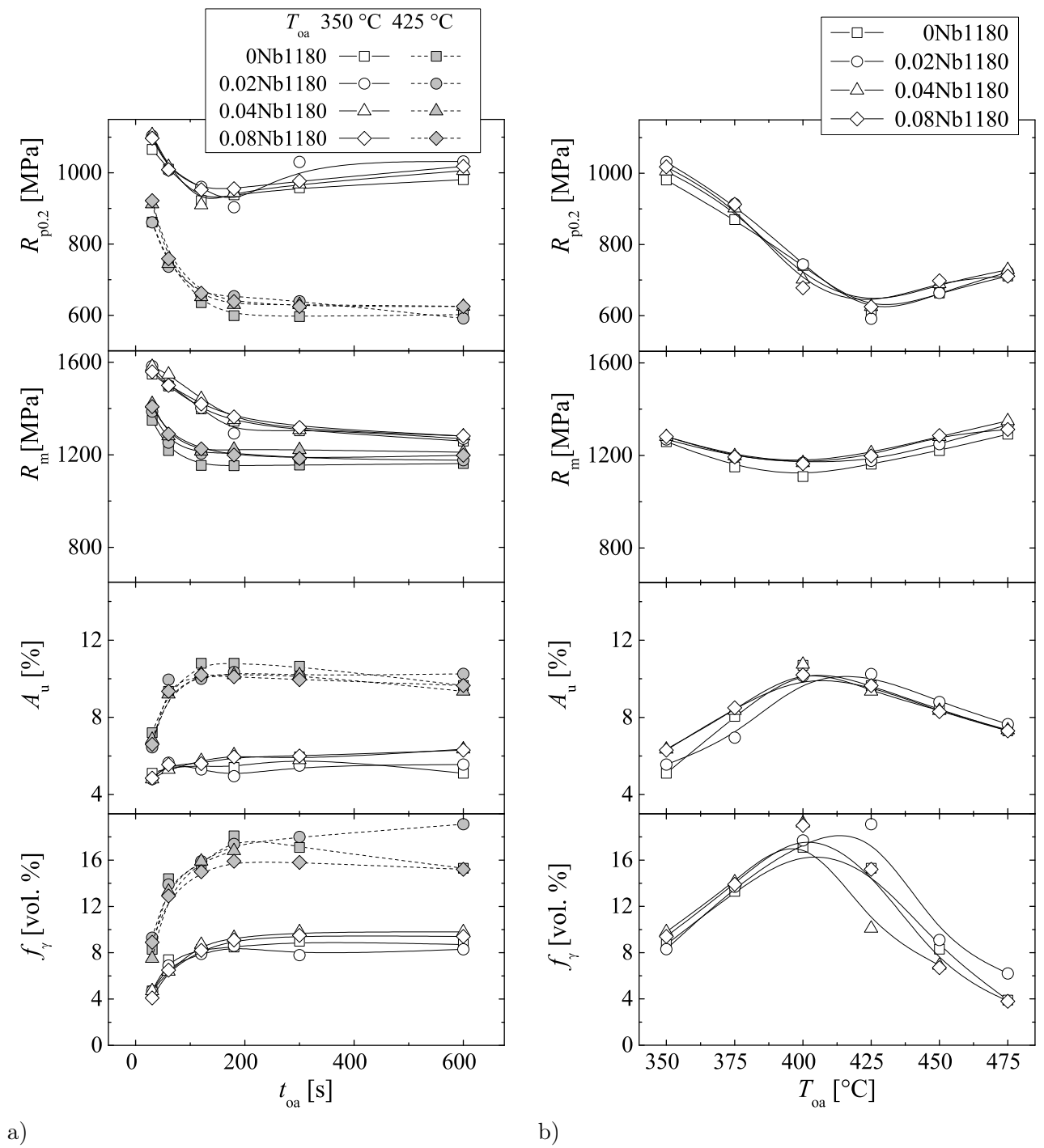


Figure 4.34: Yield strength, tensile strength, uniform elongation, and amount of retained austenite of grades 0Nb1180, 0.02Nb1180, 0.04Nb1180 and 0.08Nb1180 a) as a function of overaging time for overaging temperatures  $T_{oa} = 350$  °C and  $T_{oa} = 425$  °C, b) as a function of overaging temperature ( $t_{oa} = 600$  s).

## 4.2 Influence of annealing cycle on TBF and Q&P sheet steel

### 4.2.1 Quench temperature

This section demonstrates the influence of quench temperature on microstructure, amount of retained austenite, and mechanical properties on TRIP-assisted steels with bainitic and/or martensitic microstructure. The industrially produced steels of this work exhibit higher levels of purity in composition compared to the laboratory-produced sheets. As a result of this and other differences in production, the mechanical properties, in particular hole expansion strains, of industrially produced sheets can differ from those of laboratory-produced material. In most cases, industrially produced steels show slightly more advanced combinations of mechanical properties than those of laboratory-produced steels with similar composition and heat treatment. Figure 4.35 shows LePera etched optical micrographs of two-step Q&P heat-treated sheet steel IN980 and IN0.9Si1180 for selected quench temperatures ( $T_{oa} = 450\text{ }^{\circ}\text{C}$ ,  $t_{oa} = 300\text{ s}$  and  $T_{oa} = 400\text{ }^{\circ}\text{C}$ ,  $t_{oa} \approx 450\text{ s}$ , respectively).

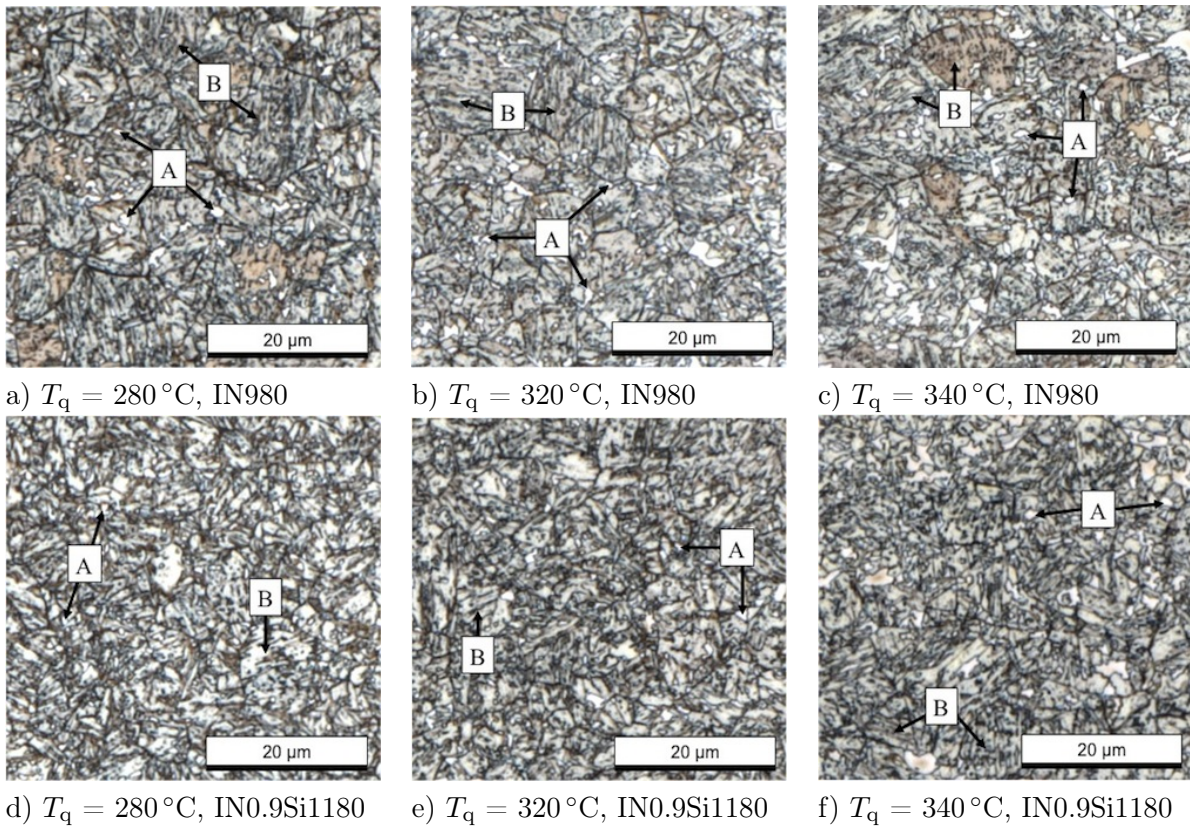


Figure 4.35: LePera etched optical micrographs of two-step Q&P heat-treated sheet steel for quench temperatures  $T_q = 280\text{ }^{\circ}\text{C}$ ,  $T_q = 320\text{ }^{\circ}\text{C}$  and  $T_q = 340\text{ }^{\circ}\text{C}$  comprising bainite (B) and retained austenite (A). Upper row: IN980, lower row: IN0.9Si1180. The cold-rolled sheets of both steels were industrially produced. Steel IN980 was annealed in the laboratory by electrical resistance ( $t_q = 3\text{ s}$ ,  $T_{oa} = 450\text{ }^{\circ}\text{C}$ ,  $t_{oa} = 300\text{ s}$ ) and grade IN0.9Si1180 was produced in the industrial annealing line ( $T_{oa} = 400\text{ }^{\circ}\text{C}$ ,  $t_{oa} \approx 450\text{ s}$ ).

The size of the retained austenite grains increases with increasing quench temperature in both grades. However, the shape of the retained austenite islands is independent of quench tempera-

ture. The lower contrast of the white retained austenite islands to the surrounding matrix indicate that less retained austenite is present in the grade IN0.9Si1180. However, magnetic measurements confirmed that both grades contain the same amount of retained austenite for a given quench temperature (Figure 4.36b). There is no visible difference in the amount and size of the carbides between different quench temperatures or between the two different grades. The former austenite grain boundary is clearly visible only in the grade IN980.

Yield strength, tensile strength, uniform elongation, and the amount of retained austenite as a function of quench temperature of steel IN980 and IN0.9Si1180 are shown in Figure 4.36. Tensile strength and even more so yield strength decrease with increasing quench temperature to the same extent in both grades, while the absolute tensile strength of the grade IN0.9Si1180 is 100 MPa and its yield strength is 200 MPa higher than that of the grade IN980 (Figure 4.36a). Uniform and total elongation are insignificantly lower for the grade IN0.9Si1180 than for grade IN980 and increase with increasing quench temperature, as the amount of retained austenite also increases in both grades (Figure 4.36b). Hole expansion strain of the grade IN0.9Si1180 remarkably decreases with increasing quench temperature (Figure 4.36a). It drops below 20% above  $T_q = 340^\circ\text{C}$ , while exceeding 50% for below  $T_q = 280^\circ\text{C}$ . Steel IN980 shows the same tendency in hole expansion strain with quench temperature. However, grade IN980 is less quench-temperature-sensitive and decreases much more slowly with increasing quench temperature resulting in significantly higher hole expansion strain of 37% vs. 23% for a quench temperature of  $T_q = 340^\circ\text{C}$ .

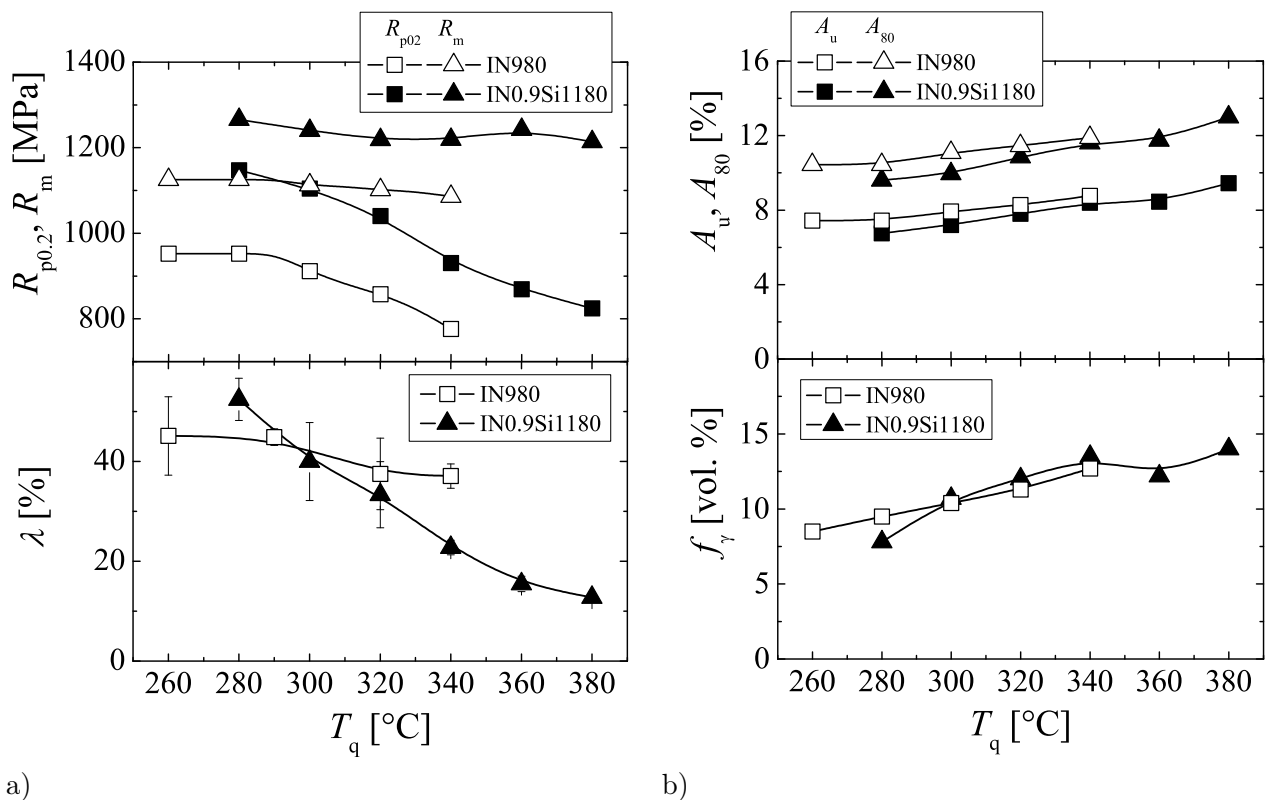


Figure 4.36: a) Hole expansion strain, yield strength, tensile strength, b) amount of retained austenite, uniform elongation, and total elongation  $A_{80}$  as a function of quench temperature of two-step Q&P heat-treated sheet steels IN980 ( $t_q = 3\text{ s}$ ,  $T_{oa} = 450^\circ\text{C}$ ,  $t_{oa} = 300\text{ s}$ ) and IN0.9Si1180 ( $T_{oa} = 400^\circ\text{C}$ ,  $t_{oa} \approx 450\text{ s}$ ) for quench temperatures  $T_q = 280^\circ\text{C}$  and  $340^\circ\text{C}$ .

Figure 4.37 shows the engineering stress-strain curves of steel grades IN980 and IN0.9Si1180. Steel grade IN980 was originally designed for a minimum tensile strength of 980 MPa, in combination with TBF heat treatments and overaging temperatures above  $M_s$  temperature. Exposed to quench temperatures as low as  $T_q = 280^\circ\text{C}$  and  $T_q = 340^\circ\text{C}$  below  $M_s$  temperature ( $M_s \approx 375^\circ\text{C}$ ) before overaging, it shows quite high tensile strength of 1085 and 1125 MPa, respectively. The strength levels and the stress-strain curves of grade IN980 are much more alike for the different quench temperatures compared to those of grade IN0.9Si1180. It is important to note that the lower quench temperature of  $T_q = 280^\circ\text{C}$  postpones yielding in both steels. The low strain-hardening rate at strains directly above the yield strength of IN980 at a quench temperature of  $T_q = 280^\circ\text{C}$  could indicate an onset of the development of a yield point elongation. The stress-strain curves can be divided into a range of strain-hardening before necking and post-uniform deformation. Interestingly, the grade IN980 shows similar strain-hardening behaviour, except for the delayed yielding, but very distinct post-uniform deformation. While the strain-hardening behaviour of steel IN980 is very similar for both quench temperatures, steel IN0.9Si1180 shows much stronger strain-hardening at a quench temperature of  $T_q = 340^\circ\text{C}$  compared to  $T_q = 280^\circ\text{C}$ .

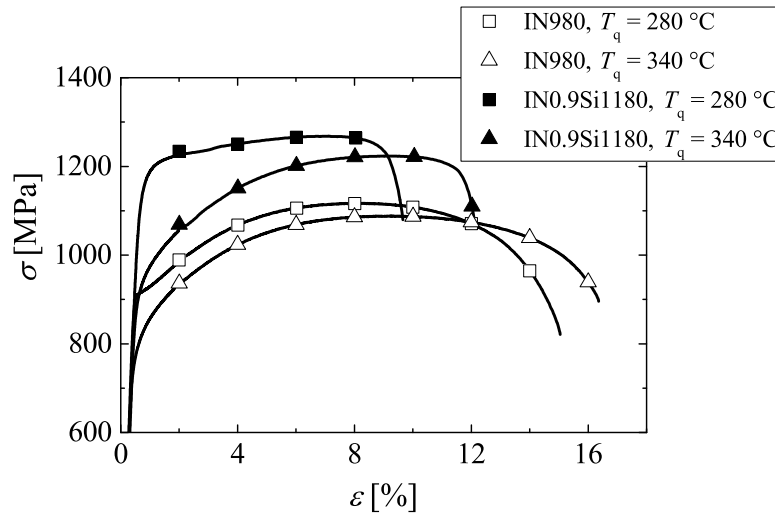


Figure 4.37: Engineering stress-strain curves of two-step Q&P heat-treated sheet steels IN980 ( $t_q = 3\text{ s}$ ,  $T_{oa} = 450^\circ\text{C}$ ,  $t_{oa} = 300\text{ s}$ ) and IN0.9Si1180 ( $T_{oa} = 400^\circ\text{C}$ ,  $t_{oa} \approx 450\text{ s}$ ) for quench temperatures  $T_q = 280^\circ\text{C}$  and  $340^\circ\text{C}$ .

Figure 4.38 shows the differential  $n$ -value and the strain-hardening rate as a function of logarithmic strain of the same steel grades and quench temperatures as in Figure 4.37. The strain-hardening rate of both steels is very similar for a quench temperature of  $340^\circ\text{C}$ . It begins at 20,000 MPa, drops strongly at low strains, and decays towards higher strains. In contrast, the strain rates of both steels are very different at a quench temperature of  $280^\circ\text{C}$ . It begins lower for steel IN0.9Si1180 and decays to values comparable to those for the higher quench temperature. The strain rate of grade IN980, however, begins with distinctly high values and drops to much lower rates. Likewise, the differential  $n$ -value of both steels is very similar for a quench temperature of  $340^\circ\text{C}$ , but slightly higher in the case of steel IN980 for a given strain. This steel also exhibits a higher maximum differential  $n$ -value, which correlates with the elevated uniform elongation (Figure 4.36). The differential  $n$ -values at the lower quench temperature of  $280^\circ\text{C}$  are generally lower and very distinct between the steels, which is in good agreement with the diverging strain-hardening rates for this heat treatment. While

the differential  $n$ -value of steel IN980 for this quench temperature is shifted to higher strains up to a logarithmic strain of 0.03 compared to both steels at the higher quench temperature, steel IN0.9Si1180 begins at similar values, but exhibits a peak at 0.001, drops to half the peak value, and does not regain values as high as those of steel IN980.

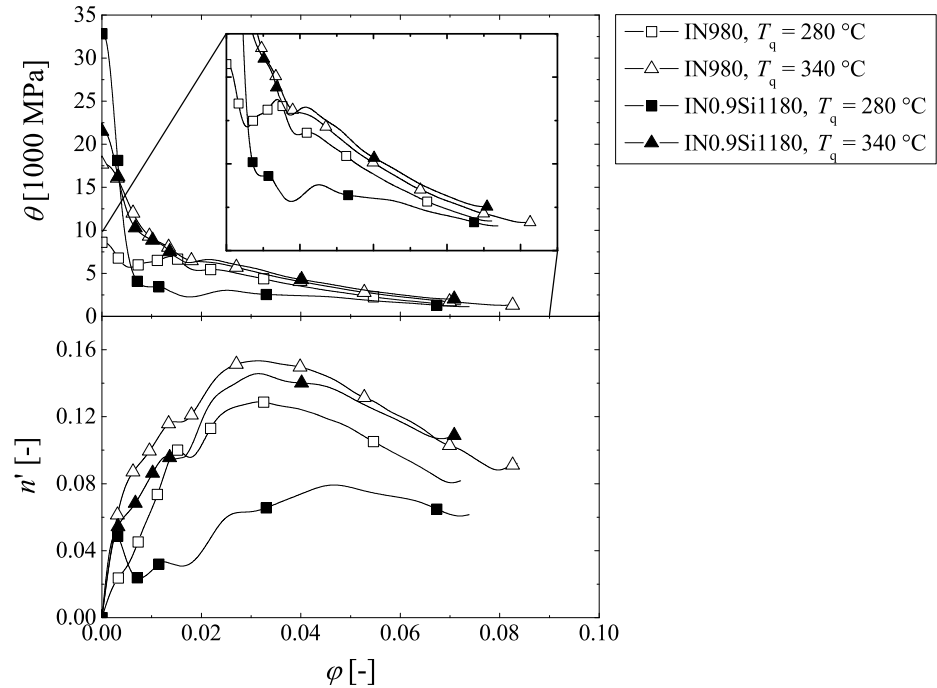


Figure 4.38: Strain-hardening rate and differential  $n$ -value as a function of logarithmic strain of two-step Q&P heat-treated sheet steels IN980 ( $t_q = 3$  s,  $T_{oa} = 450$  °C,  $t_{oa} = 300$  s) and IN0.9Si1180 ( $T_{oa} = 400$  °C,  $t_{oa} \approx 450$  s) for quench temperatures  $T_q = 280$  °C and 340 °C.

#### 4.2.2 Time at quench temperature

This section demonstrates the influence of the time at quench temperature on microstructure, amount of retained austenite, and mechanical properties of two-step Q&P heat-treated sheet steel. Time at quench temperature refers to how long the steel was held at quench temperature after quenching and before reheating to overaging temperature in a two-step Q&P annealing cycle. Figure 4.39 shows the LePera etched micrographs of steel IN980 for various times at quench temperature. The matrix appears to become much finer with increasing time at quench temperature. The size of the retained austenite/martensite islands decreases with increasing time at quench temperature. The brownish areas indicate carbon-depleted zones within the islands used to be austenite prior to the final cooling. Therefore, they commonly correspond to fresh martensite. In some cases, brownish areas within a white inclusion like these can indicate (auto-)tempered martensite. Here, however, temperatures are too low and time is too short to allow relevant tempering during the final cooling. After 8 s time at quench temperature, there are no more brownish areas of fresh martensite left (Figure 4.39d-f). The MA islands disappear completely for 40 s time at quench temperature, and only retained austenite grains are left (Figure 4.39f). For short times at quench temperature significant amounts of retained austenite appear in a film-type elongated shape (Figure 4.39a-c),

while prolonged quenching results in a larger number of small, round and finely dispersed retained austenite are present (Figure 4.39d-f). Finally, the carbide density slightly increases with increasing time at quench temperature. With the higher amount of finely dispersed carbides more subgrain boundaries and laths seem to become visible.

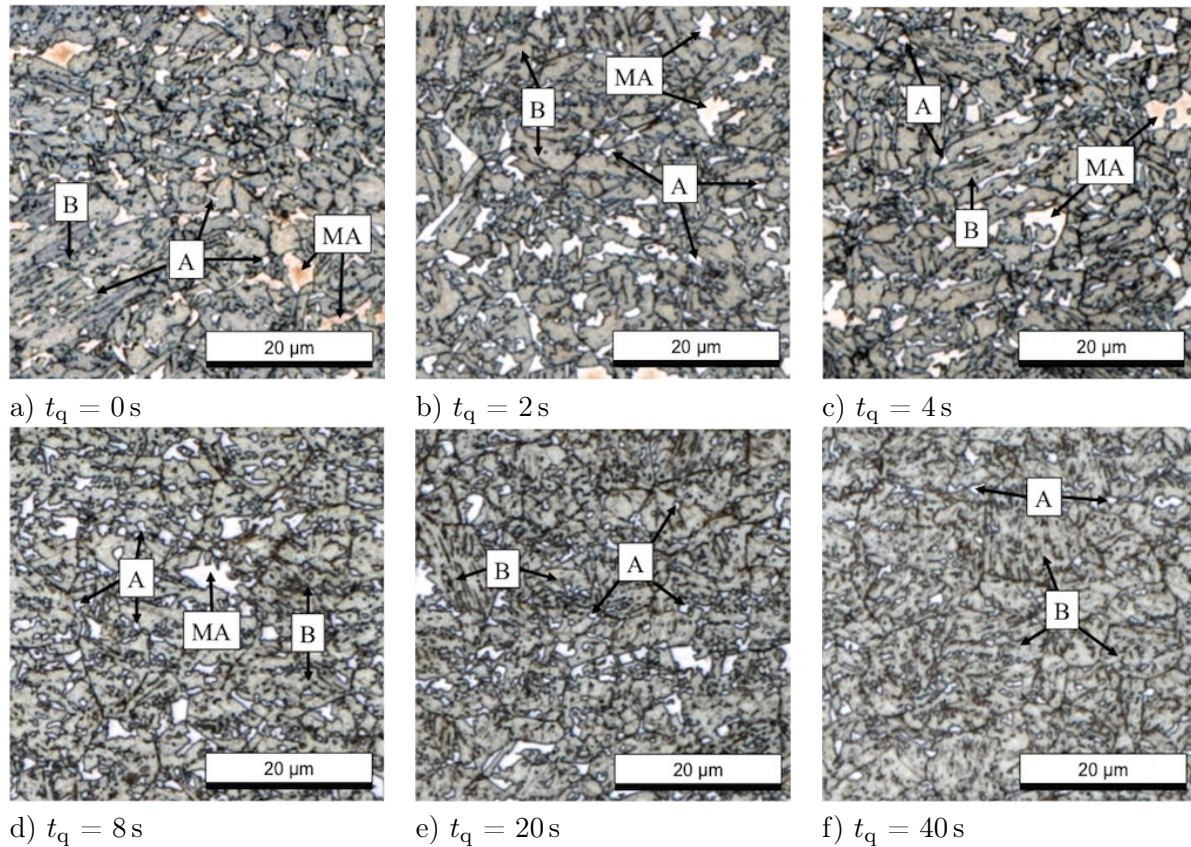


Figure 4.39: LePera etched optical micrographs of the two-step Q&P heat-treated sheet steel IN980 for various times at quench temperature comprising bainite (B), retained austenite (A), and retained austenite/martensite islands (MA) ( $\dot{T} \approx 80$  K/s,  $T_q = 350$  °C,  $T_{oa} = 450$  °C,  $t_{oa} = 300$  s).

Yield strength, tensile strength, uniform elongation, and the amount of retained austenite are shown in Figure 4.40. Interestingly, tensile strength, even more so yield strength, and in particular hole expansion strain increase strongly with increasing time at quench temperature. Uniform elongation and total elongation decrease with increasing time at quench temperature. The amounts of retained austenite are approximately at the same level within the first 20 s of quenching, while the amount of retained austenite slightly drops at the longest time of 40 s at quench temperature.

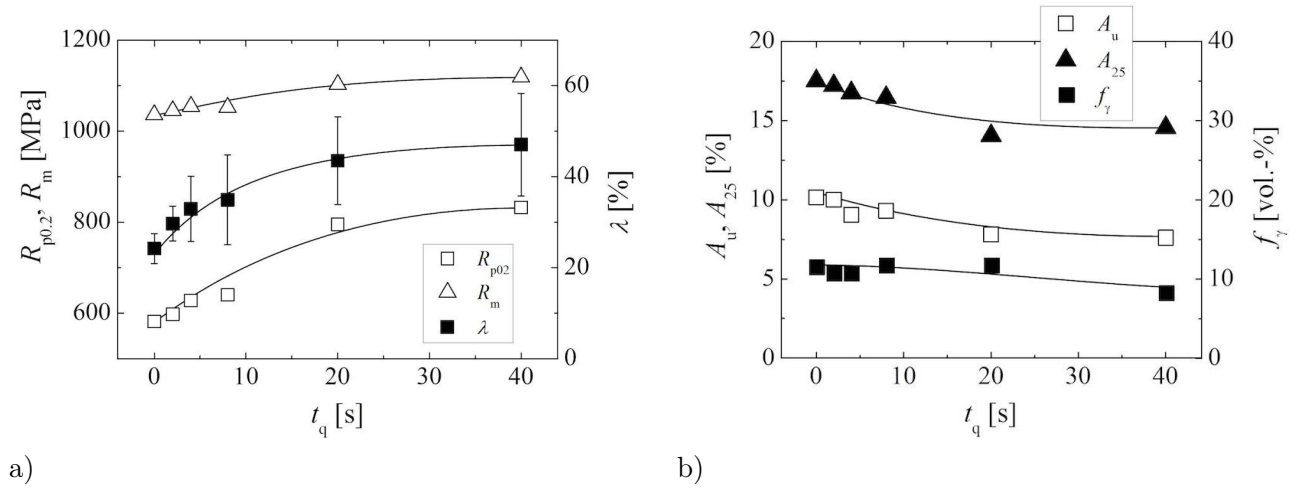


Figure 4.40: a) Yield strength, tensile strength, hole expansion strain, b) uniform elongation, total elongation  $A_{25}$  and amount of retained austenite as a function of time at quench temperature of two-step Q&P heat-treated sheet steel IN980 ( $\dot{T} \approx 80$  K/s,  $T_q = 350^\circ\text{C}$ ,  $T_{\text{oa}} = 450^\circ\text{C}$ ,  $t_{\text{oa}} = 300$  s).

### 4.2.3 Intermediate holding

To produce small amounts of polygonal ferrite, an intermediate holding step was conducted upon cooling to overaging in addition to the TBF heat treatment. The LePera etched optical micrographs of the same steel including intermediate holding are shown in Figure 4.41 for various intermediate holding temperatures and holding times. The steel that was held at  $575^\circ\text{C}$  for 2 s shows several scattered blue islands depleted of carbides and free of ferrite laths, whereas no polygonal ferrite is visible in the microstructure of  $T_f = 625^\circ\text{C}$  and  $t_f = 2$  s (Figure 4.41a and 4.41d). Considerable amounts of polygonal ferrite can be found in Figure 4.41b, while the steel of higher intermediate holding temperature (Figure 4.41e) again resembles the purely TBF heated treated reference material. However, it contains a small amount of carbide-depleted polygonal ferrite. After 40 s of intermediate holding time, the steel begins to appear like a TRIP steel with polygonal ferritic matrix for both holding temperatures. The matrix primarily consists of polygonal ferrite with embedded retained austenite/martensite islands.

Figure 4.42 shows yield strength, tensile strength, uniform elongation, total elongation, and hole expansion strain as a function of the intermediate holding time. Yield strength, tensile strength, and hole expansion strain decrease, while uniform and total elongation increase with increasing intermediate holding time particularly pronounced at short intermediate holding times decaying with an exponential type of trend.

Yield strength and tensile strength decrease by 60 MPa within the first 6 s of intermediate holding for both intermediate holding temperatures. After 80 s intermediate holding time yield strength drops to less than half its original value of 900 MPa. Tensile strength decreases from 1100 MPa to around 900 MPa within 80 s of intermediate holding. Uniform and total elongation both increase by 2% within 6 s and by 10% after 80 s of intermediate holding in absolute numbers. The later is equivalent to a doubling of uniform elongation. Short holding times significantly lower the hole expansion strain. Intermediate holding for  $t_f = 6$  s results in a relative loss of 20% in hole expansion strain. After 80 s of intermediate holding, hole expansion strain is reduced to half its original value of 56%.

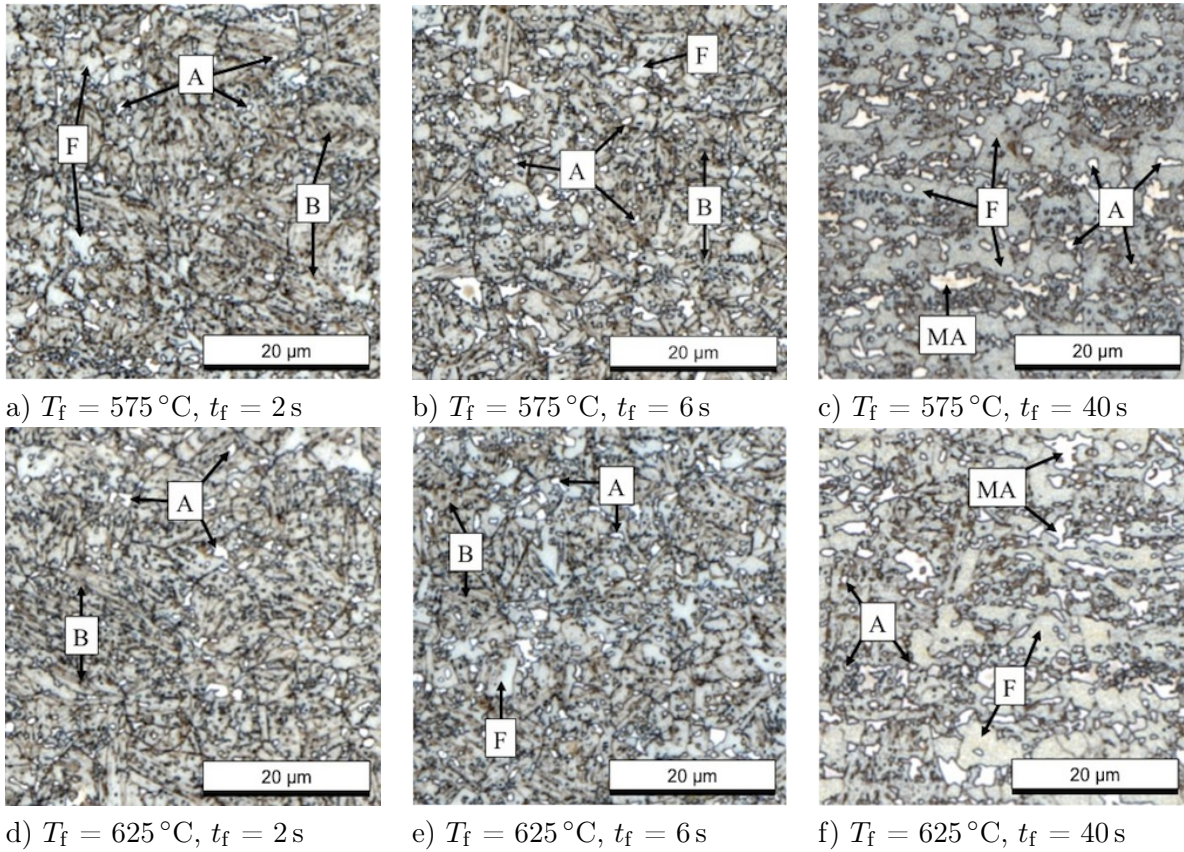


Figure 4.41: LePera etched optical micrographs of steel IN980 with varying intermediate holding temperatures  $T_f$  and intermediate holding times  $t_f$  to induce polygonal ferrite upon cooling to overaging ( $\dot{T} \approx 80\text{ K/s}$ ,  $T_{\text{oa}} = 400^\circ\text{C}$  and  $t_{\text{oa}} = 600\text{ s}$ ). The microstructures contain polygonal ferrite (F), bainite (B), retained austenite (A), and retained austenite/martensite islands (MA).

Overall differences are minor when the two intermediate holding temperatures are compared. Steels that were intermediately held at the lower temperature of  $575^\circ\text{C}$  are more sensitive to long intermediate holding times in terms of tensile strength and elongations, but less sensitive with respect to hole expansion strain. With the higher intermediate holding temperature, yield strength is slightly higher at short intermediate holding times and 30 MPa lower after intermediate holding for 80 s. Tensile strength is 25 MPa higher for  $625^\circ\text{C}$  intermediate holding temperature consistently for all intermediate holding times. In absolute terms, elongations are 1% higher for the lower intermediate holding temperature. Very short holding at  $575^\circ\text{C}$  for 2 s does not change hole expansion strain, whereas higher holding temperature of  $625^\circ\text{C}$  results in slightly reduced hole expansion. Hole expansion strain is significantly higher for the lower intermediate holding temperature in particular after 40 s of intermediate holding, where it is 38% instead of 30%. The sheet steel with nearly completely polygonal ferritic matrix of the same material, as seen in Figure 4.41c and 4.41f, still reaches rather high hole expansion strains of 30 and 25% for an intermediate holding temperature of  $575^\circ\text{C}$  and  $625^\circ\text{C}$ , respectively.

#### 4.2.4 Intercritical annealing

In further trials, polygonal ferrite was induced via intercritical annealing. The microstructures of this investigation largely differ from those of the intermediate holding step. Figure 4.43 shows optical

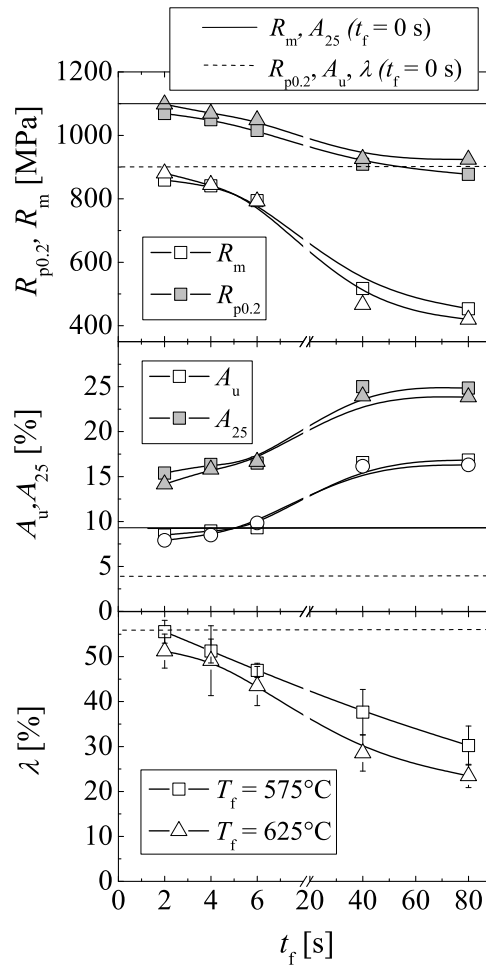


Figure 4.42: Yield strength, tensile strength, uniform elongation, total elongation, and hole expansion strain of steel grade IN980 as a function of intermediate holding time  $t_f$  at holding temperature  $T_f$  ( $\dot{T} \approx 80$  K/s,  $T_{\text{oa}} = 400^\circ\text{C}$  and  $t_{\text{oa}} = 600$  s).

micrographs of steel IN980 for different annealing temperatures  $T_{\text{an}}$  ( $A_3 \approx 820^\circ\text{C}$ ). The amount of polygonal ferrite and the size of the retained austenite islands increase with decreasing annealing temperature. The segregation bands that appear in all microstructures, though less pronounced in the reference TBF heat-treated material in Figure 4.43a, arise primarily from the strong segregation tendency of manganese, as described in Section 4.1.3. The lower the  $T_{\text{an}}$ , the more pronounced the segregation bands appear, and the larger the retained austenite/martensite islands. Finally, the carbides become less disperse with decreasing annealing temperature, which means they are smaller and more homogeneously distributed.

Figure 4.44 shows yield strength, tensile strength, uniform elongation, the amount of retained austenite, and hole expansion strain of steel grade IN980 as a function of annealing temperature. Tensile strength increases almost linearly, whereas the other properties show a sigmoidal trend where yield strength and hole expansion increase and retained austenite and elongations decrease with increasing annealing temperature. Interestingly, there is no significant difference in hole expansion strain between  $810^\circ\text{C}$ ,  $820^\circ\text{C}$  and  $900^\circ\text{C}$  annealing temperature. However, a  $30^\circ\text{C}$  drop in annealing temperature from  $810^\circ\text{C}$  to  $780^\circ\text{C}$  results in a relative loss of 50% in hole expansion strain.

Once the microstructure has turned into a classical TRIP type appearance with polygonal ma-

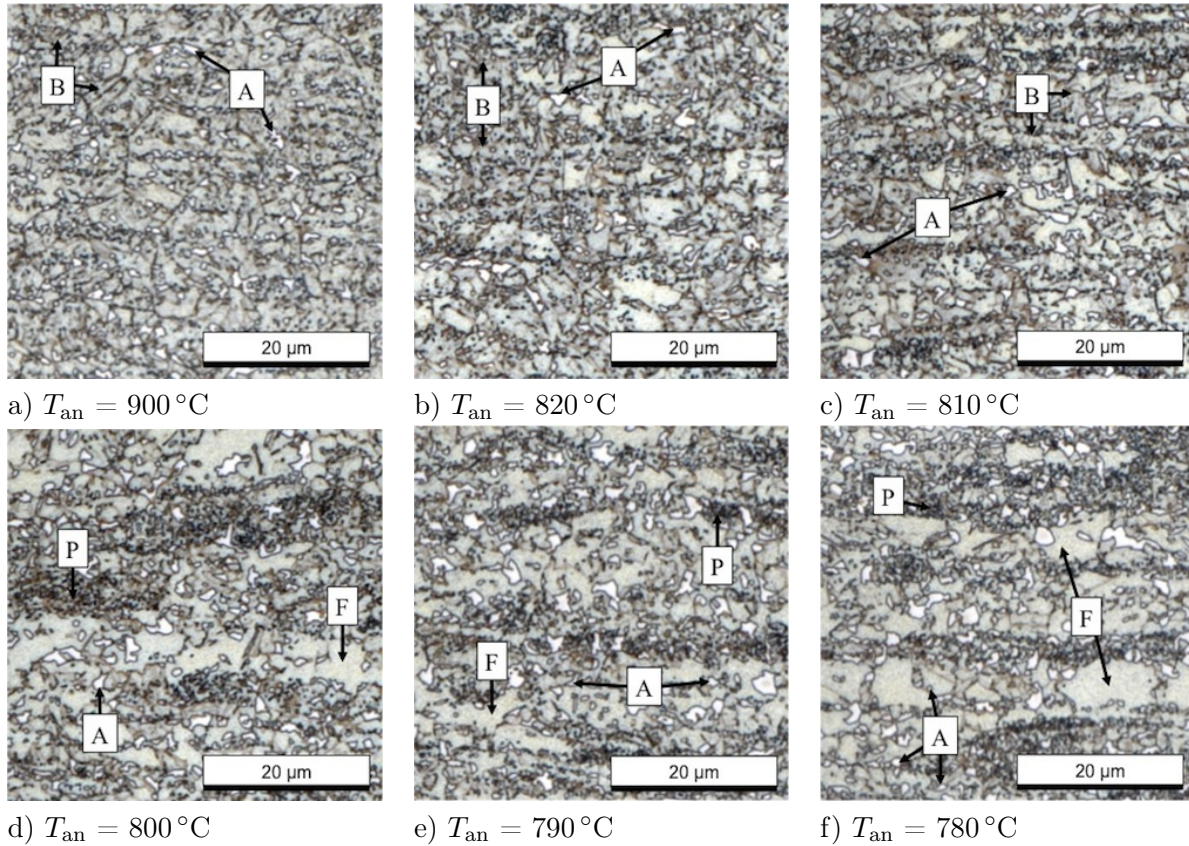


Figure 4.43: LePera etched optical micrographs of a-e) intercritical annealed and f) fully austenitized steel IN980 for varying annealing temperatures  $T_{\text{an}}$  to induce polygonal ferrite upon cooling to overaging ( $\dot{T} \approx 80\text{ K/s}$ ,  $t_{\text{an}} = 120\text{ s}$ ,  $T_{\text{oa}} = 400\text{ }^{\circ}\text{C}$  and  $t_{\text{oa}} = 600\text{ s}$ ). Denomination of the microstructure constituents: Polygonal ferrite (F), pearlite (P), bainite (B), and retained austenite (A). Pearlite is difficult to distinguish from bainite by optical microscopy, but was determined by SEM and dilatometry.

trix, the hole expansion strain is cut to half the initial value of its bainitic counterpart, irrespectively of whether the matrix was obtained via intermediate holding or intercritical annealing.

## 4.3 Failure mechanisms

### 4.3.1 Void nucleation and growth

The mechanical properties of the TBF/one-step Q&P heat-treated steels used for the following void analysis are given in Table 4.3.

Table 4.3: Mechanical properties of TBF/one-step Q&P heat-treated steel 0Nb980 used for void analysis.

Steel	$T_{\text{oa}}\text{ [}^{\circ}\text{C]}$	$R_{\text{p02}}\text{ [MPa]}$	$R_{\text{m}}\text{ [MPa]}$	$A_{\text{u}}\text{ [%]}$	$A_{25}\text{ [%]}$	$f_{\gamma}\text{ [%]}$	$n_{2-4}\text{ [-]}$
0Nb980	350	1007	1240	5	10	3.1	0.059
0Nb980	375	981	1177	5	10	3.9	0.065
0Nb980	400	817	1067	7	11	7.3	0.12
0Nb980	425	646	1015	8	13	10.4	0.1825

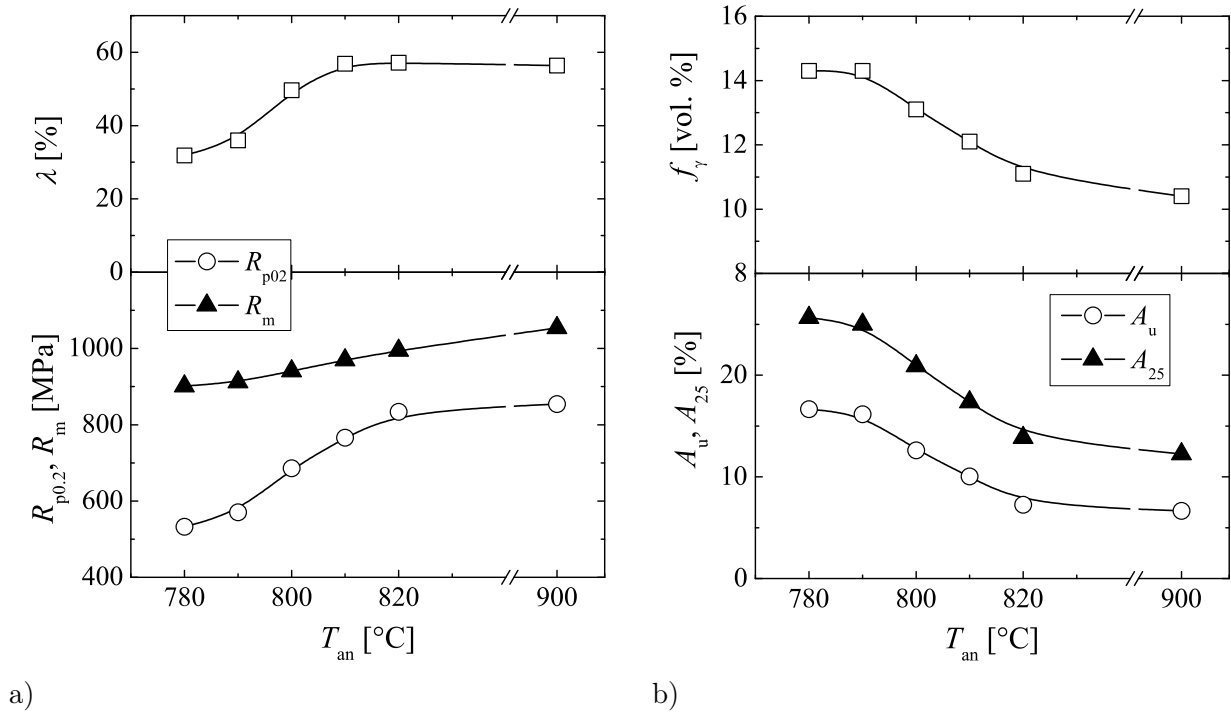


Figure 4.44: a) Hole expansion strain, yield strength and tensile strength, b) amount of retained austenite, uniform elongation and total elongation  $A_{25}$  of steel grade IN980 as a function of annealing temperature  $T_{an}$  ( $\dot{T} \approx 80$  K/s,  $t_{an} = 120$  s,  $T_{oa} = 400$  °C and  $t_{oa} = 600$  s).

Figure 4.45a shows the void density of tensile tested steel 0Nb980 as a function of distance to the fracture surface for selected overaging temperatures. The void density exponentially decays with increasing distance to the fracture surface. The higher the overaging temperature, the higher the void density. The void density of the same samples as a function of strain in thickness direction, the engineering strain in thickness direction, is shown in Figure 4.45b. When the two figures are compared, the void density increases with increasing strain in thickness direction as it increases with decreasing distance to the fracture surface. However, in relation to the strain in thickness direction the increase is less pronounced. Strains in thickness direction at uniform elongation, which are the lowest strain in thickness direction given, are higher for higher overaging temperatures. The maximum strain in thickness direction is only slightly higher for higher overaging temperatures.

The average ECD of all voids as a function of strain in thickness direction of steel 0Nb980 is shown in Figure 4.46 for selected overaging temperatures. The average ECD increases with increasing strain in thickness direction. It is important to note that the average ECDs of the different overaging temperatures exhibit quite similar values. Interestingly, even at the lowest strain in thickness direction of 0.12%, which correspond to uniform elongation, voids are still present. The void density in a strain range from 0.12% to 0.25% (Figure 4.45b), which is equivalent to a distance from the fracture surface of 1100 to 700  $\mu\text{m}$  (Figure 4.45a), is at a considerable amount of  $0.005 \mu\text{m}^{-2}$ . Particularly the ECD of these voids is remarkably high with up to 200 nm (Figure 4.46).

Figure 4.47 shows SEM images of steel 0Nb980 for a distance at 100  $\mu\text{m}$  to the fracture surface in the middle of thickness and width of the sample for overaging temperatures of  $T_{oa} = 350$  °C and 425 °C. The magnifications to the right of each overview image represent selected voids characteristic for each steel. A few voids are present within the bainitic ferritic matrix without the presence of a hard inclusion (top right image of Figure 4.47a). The majority of voids are located at the interface

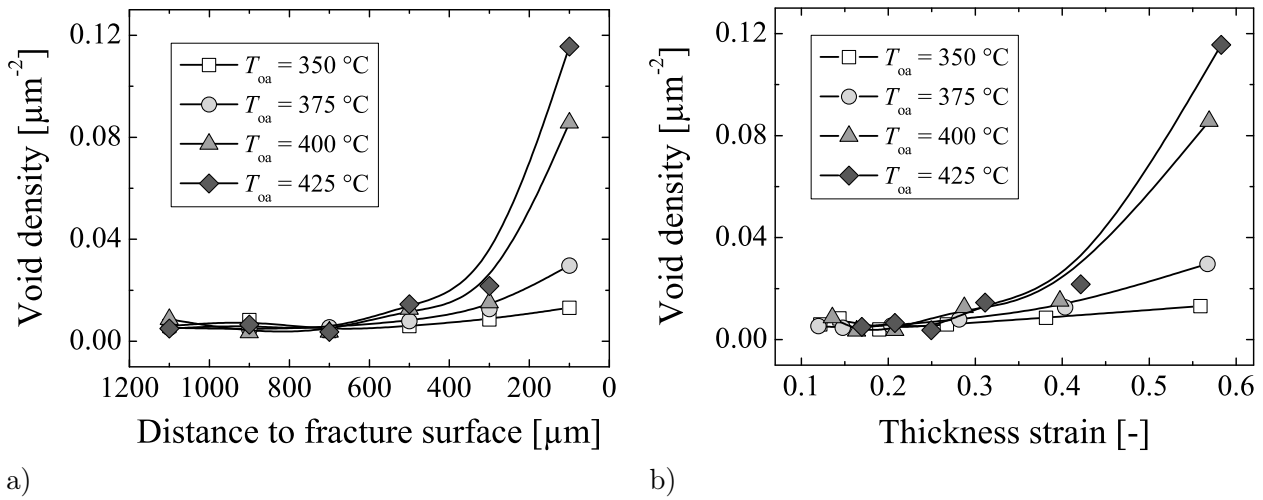


Figure 4.45: Void density of steel 0Nb980 for selected overaging temperatures: a) Void density as a function of distance to the fracture surface, b) void density as a function of strain in thickness direction.

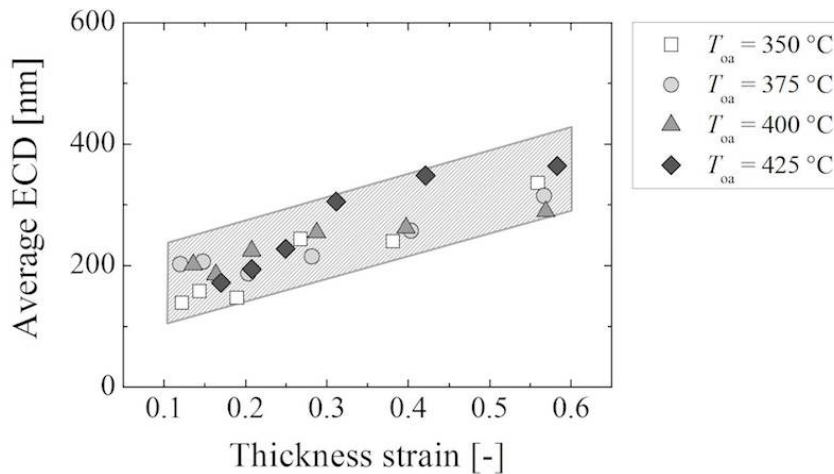


Figure 4.46: Average ECD of all voids as a function of strain in thickness direction of steel 0Nb980 for selected overaging temperatures.

of hard martensitic inclusions. Often these voids surround a sharp corner of the hard inclusion, which is typically associated with high localized strain (e.g. in the top right image of Figure 4.47b).

### 4.3.2 Fracture surface characterization

Figure 4.48 shows the fracture surfaces of two tensile tested TBF/one-step Q&P heat-treated steels, the mechanical properties of which are given in Table 4.4. Steels 2.5Mn980 and 2.6Mn1180 were exposed to the same TBF annealing cycle involving an overaging temperature of  $T_{\text{oa}} = 400^\circ\text{C}$  (Figure 4.48a-d). Both steels show one population of dimple sizes represented by log-normal distribution. While the steel 2.5Mn980 and 2.6Mn1180 are comparable with respect to dimple size and density, their shape largely varies (Figure 4.48a-d). The dimples of the fracture surface of steel 2.5Mn980 are very round and deep compared to grade 2.6Mn1180, which shows rather flat and distorted dimples that appear drawn out to a side.

The dimples are even flatter for the same steel 2.6Mn1180, when it was held at a lower overaging temperature of  $T_{\text{oa}} = 350\text{ }^{\circ}\text{C}$  (Figure 4.48e,f). It is important to note that this overaging temperature even brings about two distinct dimple populations. The density of small dimples of 0.2 to 2  $\mu\text{m}$  in ECD is very high, there are very few dimples of medium size, and there is a considerable amount of dimples with ECDs of approximately 10  $\mu\text{m}$ .

Table 4.4: Mechanical properties of TBF/one-step Q&P heat-treated steels 2.5Mn980 and 2.6Mn1180 for tensile test fracture surfaces shown in Table 4.48 ( $t_{\text{oa}} = 600\text{ s}$ ).

Steel	$T_{\text{oa}}$	$R_{\text{p}02}$	$R_{\text{m}}$	$A_{\text{u}}$	$A_{25}$
2.5Mn980	400 $^{\circ}\text{C}$	778 MPa	1063 MPa	8 %	14 %
2.6Mn1180	400 $^{\circ}\text{C}$	690 MPa	1147 MPa	11 %	18 %
2.6Mn1180	350 $^{\circ}\text{C}$	945 MPa	1317 MPa	7 %	13 %

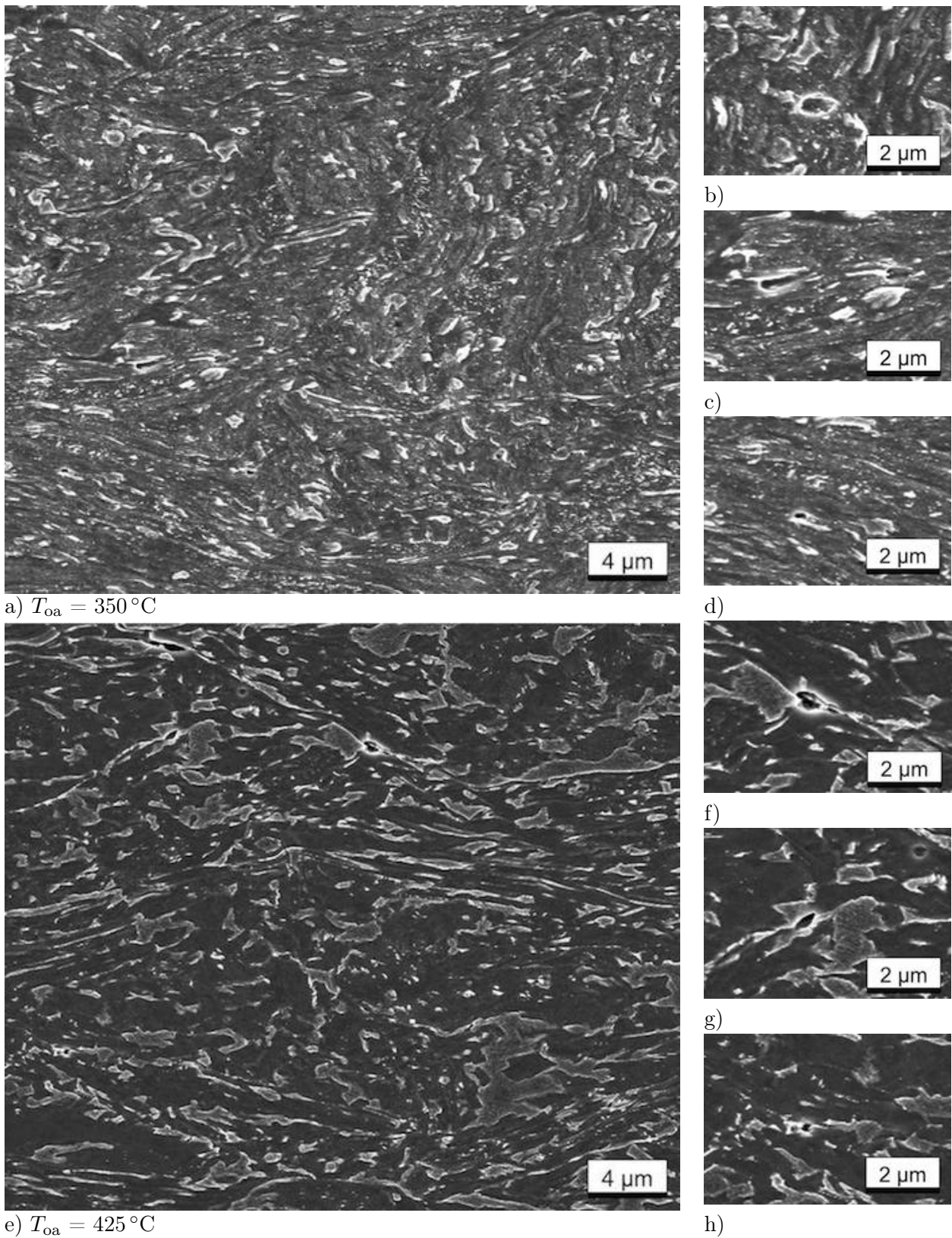


Figure 4.47: SEM images of steel 0Nb980 for a distance at  $100\text{ }\mu\text{m}$  to the fracture surface in the middle of thickness and width of the sample. The steel was TBF/Q&P heat-treated at overaging temperatures of a-d)  $T_{0a} = 350\text{ }^{\circ}\text{C}$  and e-h)  $T_{0a} = 425\text{ }^{\circ}\text{C}$ , respectively ( $t_{0a} = 600\text{ s}$ ,  $\dot{T} \approx 50\text{ K/s}$ ).

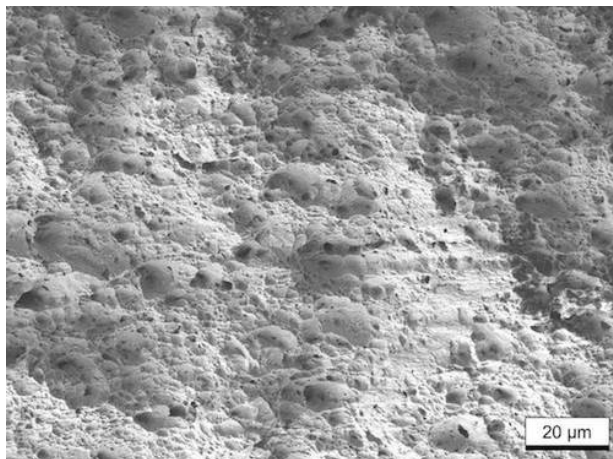
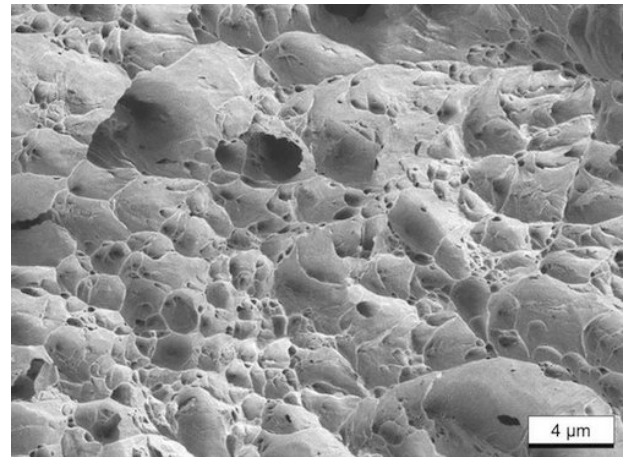
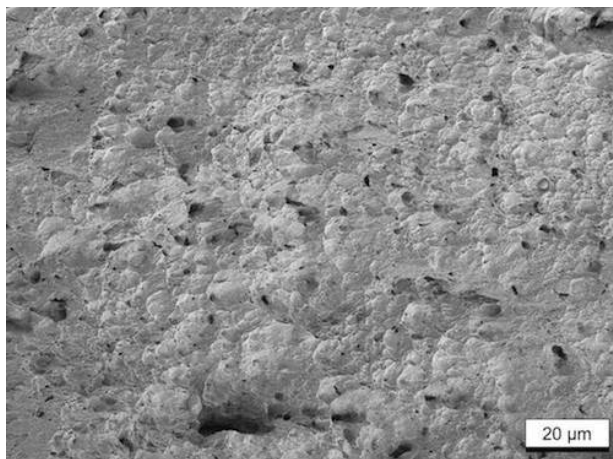
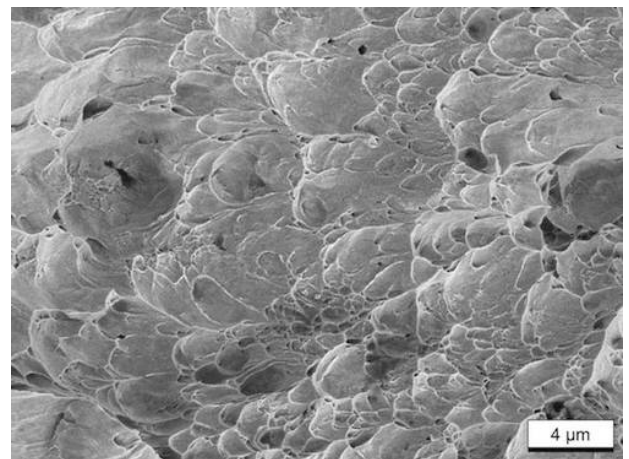
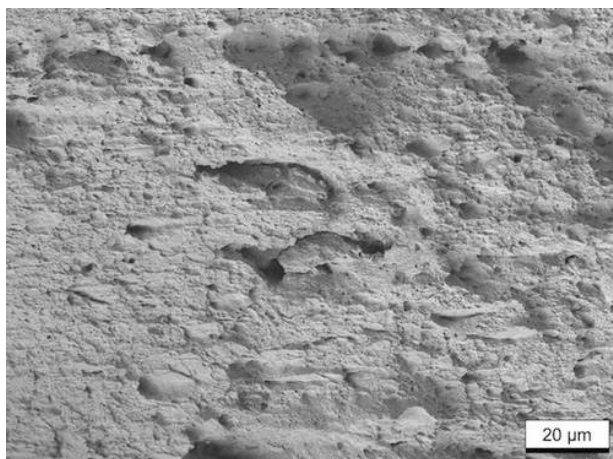
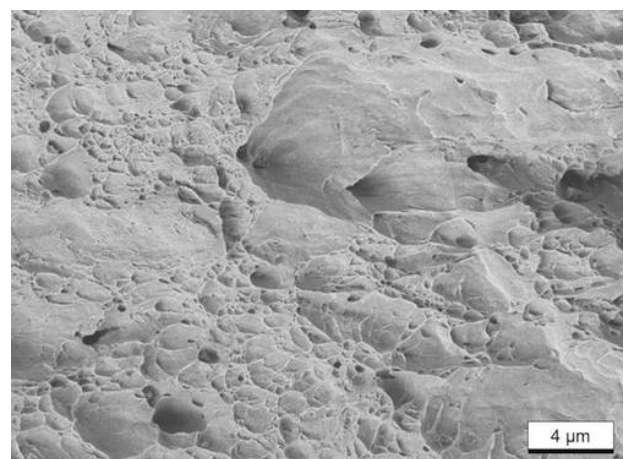
a) 2.5Mn980,  $T_{\text{oa}} = 400^\circ\text{C}$ b) 2.5Mn980,  $T_{\text{oa}} = 400^\circ\text{C}$ c) 2.6Mn1180,  $T_{\text{oa}} = 400^\circ\text{C}$ d) 2.6Mn1180,  $T_{\text{oa}} = 400^\circ\text{C}$ e) 2.6Mn1180,  $T_{\text{oa}} = 350^\circ\text{C}$ f) 2.6Mn1180,  $T_{\text{oa}} = 350^\circ\text{C}$ 

Figure 4.48: Fracture surfaces of tensile tested TBF/one-step Q&P heat-treated steels 2.5Mn980 for an overaging temperature of  $T_{\text{oa}} = 400^\circ\text{C}$  and 2.6Mn1180 for overaging temperatures of  $T_{\text{oa}} = 400^\circ\text{C}$  and  $350^\circ\text{C}$  ( $t_{\text{oa}} = 600\text{ s}$ ). The mechanical properties are shown in Table 4.4.

#### 4.4 Industrial trials on 1180 MPa Q&P sheet steel

The following results will demonstrate the effect of the changes in composition of the industrially produced 1180 MPa Q&P sheet steels on phase transformation behaviour, microstructure and mechanical properties.

Figure 4.49 shows the LePera etched micrographs of industrially produced two-step Q&P sheet steels IN1.5Si1180 and IN0.9Si1180. The steels were annealed at 850 °C, quenched to  $T_q = 340$  °C or 360 °C, and held at 380 °C. Steel IN1.5Si1180 shows a significant amount of polygonal ferrite, whereas there is no polygonal ferrite present in steel IN0.9Si1180. The microstructure of steel IN0.9Si1180 is much finer than that of steel IN1.5Si1180. When the different quench temperatures are compared, the microstructures of both IN1.5Si1180 and IN0.9Si1180 are finer and more lath-like for a quench temperature of 340 °C compared to 360 °C. There is less bainite present in IN1.5Si1180 at  $T_q = 360$  °C as opposed to 340 °C. The amount of polygonal ferrite and bainite as well as the size of the retained austenite/martensite island are considerably greater in the steel IN1.5Si1180 that was quenched to 360 °C compared to the steel of the same composition quenched to 340 °C.

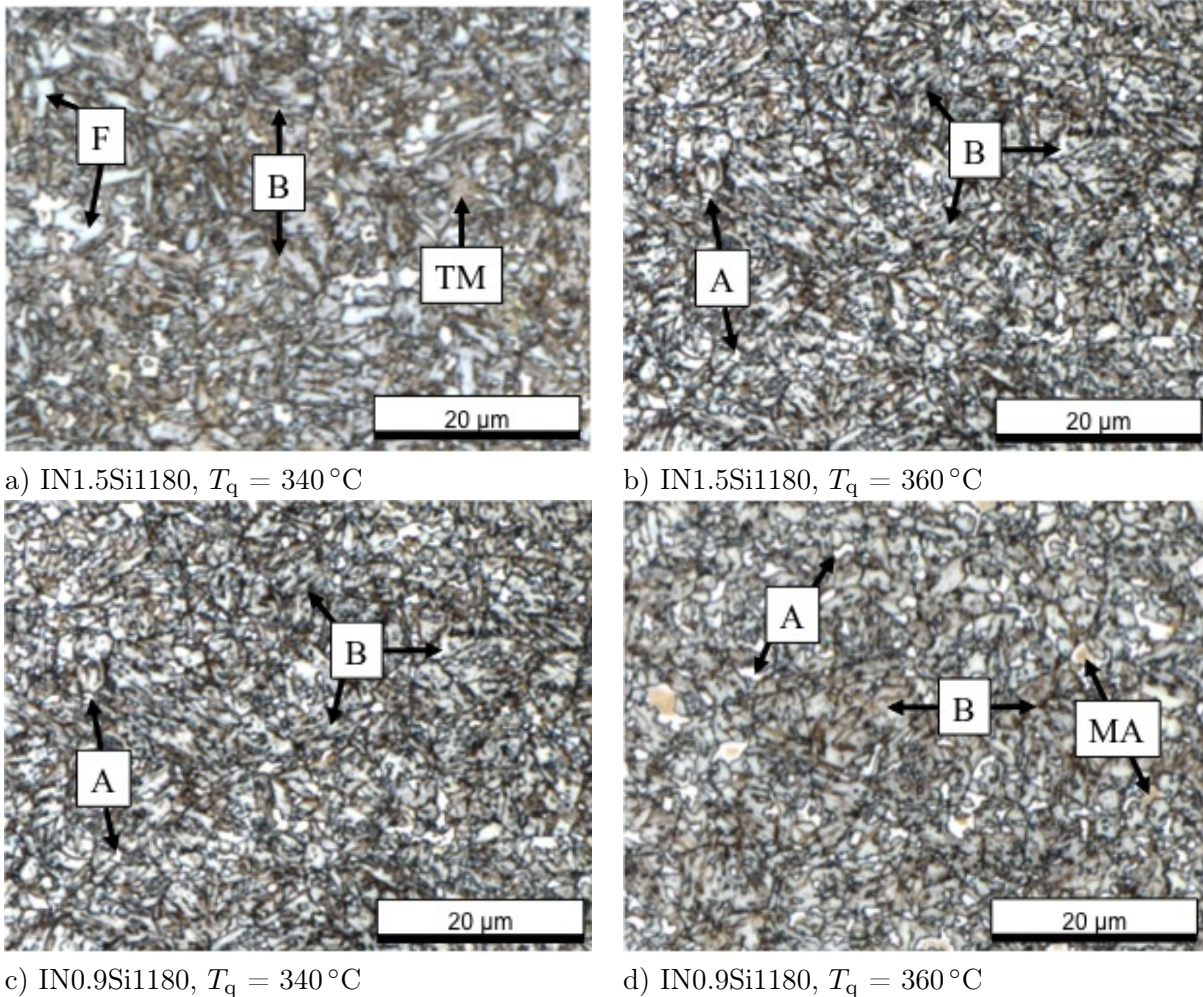


Figure 4.49: LePera etched micrographs of industrially produced two-step Q&P steels a),b) IN1.5Si1180 and c),d) IN0.9Si1180 for quench temperatures of a),c)  $T_q = 340$  °C and b),d)  $T_q = 360$  °C comprising polygonal ferrite (F), bainite (B), tempered martensite (TM), retained austenite (A), and retained austenite/martensite islands (MA) ( $T_{oa} = 380$  °C,  $T_{an} = 850$  °C).

The austenitized fraction as a function of steels IN1.5Si1180 and IN0.9Si1180 during heating at 25 K/s is shown in Figure 4.50a. The  $A_3$  temperature of grade IN1.5Si1180 is higher and its austenitization temperature range is wider than that of steel IN0.9Si1180. However, the  $A_3$  temperature depends on the heating/cooling rate. Higher heating rates or lower cooling rates result in higher  $A_3$  temperatures. At the annealing temperature  $T_{\text{an}} = 850^\circ\text{C}$ , which has been applied to all industrial trials in this thesis, steel IN0.9Si1180 is fully austenitized, while steel IN1.5Si1180 is only austenitized to 70%. In contrast to the laboratory air cooling medium frequency furnace, it is technically not possible to anneal at a much higher temperature than  $850^\circ\text{C}$  on the industrial continuous annealing line used in this thesis.

Figure 4.50b shows the transformed fraction during continuous cooling of steels IN1.5Si1180 and IN0.9Si1180 with a cooling rate of 30 K/s. None of the steels exhibit any phase transformation before  $M_s$  temperature at  $350^\circ\text{C}$  and  $360^\circ\text{C}$  of grade IN1.5Si1180 and grade IN0.9Si1180, respectively. The transformed phase fraction at  $200^\circ\text{C}$  is slightly higher in steel IN1.5Si1180.

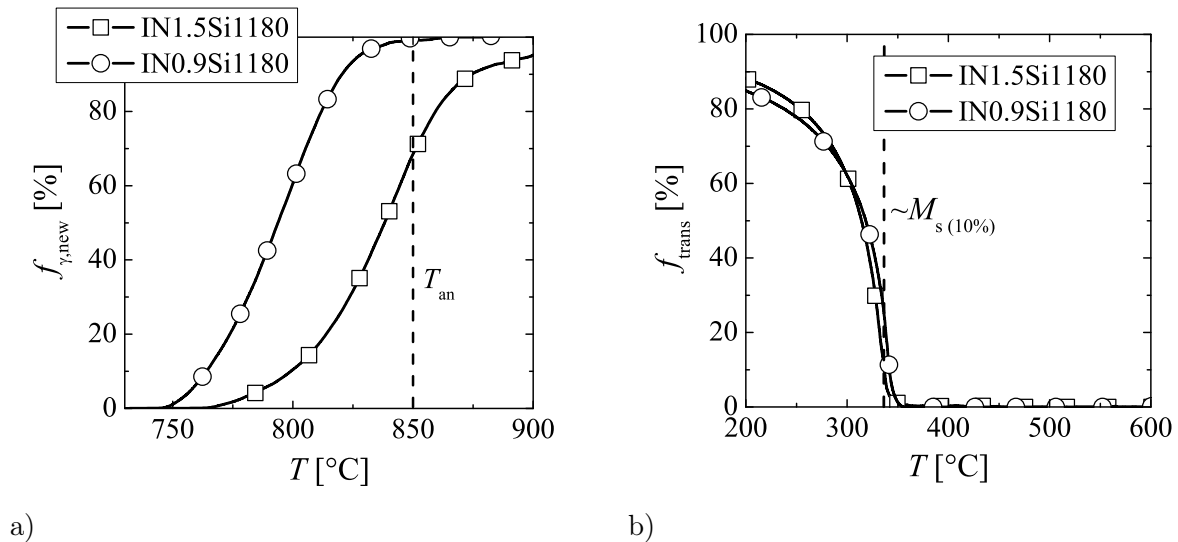


Figure 4.50: a) Austenitized phase fraction  $f_{\gamma, \text{new}}$  during heating with a heating rate of 25 K/s, b) transformed phase fraction  $f_{\text{trans}}$  during continuous cooling with a cooling rate of 30 K/s as a function of temperature of steels IN1.5Si1180 and IN0.9Si1180.

Figure 4.51 shows the normalized length of dilatometer samples during overaging at selected temperatures. At an overaging temperature of  $350^\circ\text{C}$  both steels transform with comparable transformation rates and exhibit very similar final amounts of transformation products, i.e. their transformation kinetics are alike. As the transformation temperature increases, the transformation clearly slows down for grade IN1.5Si1180, while different overaging temperatures result in the same transformation rate in the case of steel IN0.9Si1180. In addition, the transformed phase fraction of grade IN1.5Si1180 decreases in a more pronounced manner with increasing overaging temperature at a given overaging time, and the slope suggests that the transformation continues beyond the investigated time range, whereas it is saturated after 400 s in the case of steel IN0.9Si1180.

Figure 4.52 shows yield strength, tensile strength, uniform elongation, and the amount of retained austenite as a function of quench temperature. The basic tendencies of mechanical properties and amount of retained austenite with varying quench temperature are demonstrated in Section 4.2.1 and discussed in Section 5.3.1. In this section, the influence of the overaging temperature on the effect of the quench temperature is emphasized. The higher the overaging temperature, the lower the yield strength. At quench temperatures below  $T_q = 340^\circ\text{C}$ , the tensile strength negligibly

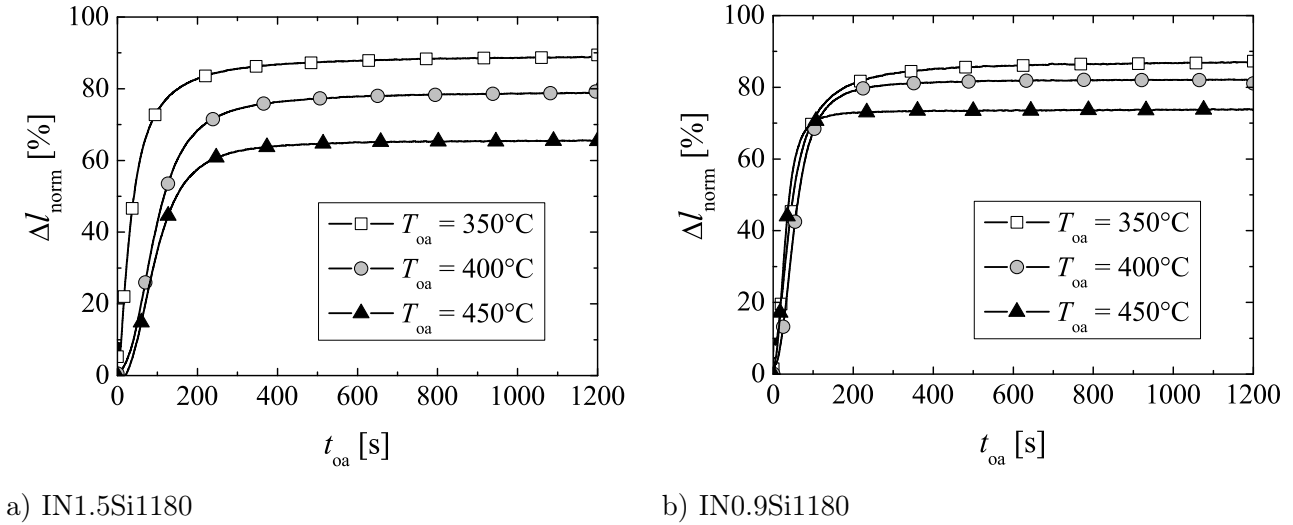


Figure 4.51: Normalized length of dilatometer samples during overaging of steels a) IN1.5Si1180, b) IN0.9Si1180 ( $T_{\text{oa}} = 350^\circ\text{C}$ ,  $400^\circ\text{C}$ , and  $450^\circ\text{C}$ ).

decreases, whereas above  $T_{\text{q}} = 340^\circ\text{C}$  it remains above 1200 MPa for an overaging temperature of  $T_{\text{oa}} = 400^\circ\text{C}$ , whereas it decreases for lower quench temperatures. An increase in overaging temperature results in a more pronounced effect of quench temperature on hole expansion strain, uniform and total elongation. Hole expansion strain is therefore lower for higher overaging temperatures for quench temperatures of  $300^\circ\text{C}$  and below, whereas a rather low quench temperature of  $T_{\text{q}} = 280^\circ\text{C}$  combined with the highest overaging temperature the highest hole expansion strain of more than 50% are reached. While at high quench temperatures above  $340^\circ\text{C}$  uniform and total elongation are slightly lower for an overaging temperature of  $T_{\text{oa}} = 400^\circ\text{C}$ . The lower the quench temperature below  $T_{\text{q}} = 340^\circ\text{C}$ , the more pronounced the differences between elongations of different overaging temperatures, where higher overaging temperatures result in higher total elongation and in particular higher uniform elongation. Interestingly, the amount of retained austenite is unaffected by changes in overaging temperatures in the range of  $360^\circ\text{C}$  to  $400^\circ\text{C}$ . Furthermore, attention should be paid to the comparison between the performance of the preceding steel grade and the newly developed 1180 MPa grade. The tensile strength of steel IN1.5Si1180 remains rather constant, while the amount of retained austenite and elongations increase and decrease again with increasing in quench temperature. In the same manner, yield strength decreases and increases again with increasing quench temperature. Hole expansion strain of steel IN1.5Si1180 shows the same tendencies with slightly higher values for the overaging temperature of  $T_{\text{oa}} = 400^\circ\text{C}$  and the given quench temperature range compared to grade IN0.9Si1180.

Tensile strength and hole expansion strain as a function of total elongation of steels IN1.5Si1180 and IN0.9Si1180 are shown in Figure 4.53a. Uniform elongation and hole expansion strain as a function of yield ratio are shown in Figure 4.53b. The graphs comprise various overaging temperatures  $T_{\text{oa}}$  of  $360$  to  $400^\circ\text{C}$  in combination with a wide range of quench temperatures  $T_{\text{q}}$  of  $280$  to  $420^\circ\text{C}$ . While the overall performance of the two grades is comparable, some considerable differences appear in particular at the high end of total elongation and tensile strength. The tensile strength level remains slightly above 1180 MPa (Figure 4.53a). Higher uniform and in particular total elongation of up to 15% are achieved by the predecessor IN1.5Si1180 compared to steel IN0.9Si1180 up to a quench temperature of  $360^\circ\text{C}$ . Interestingly, there is hardly any difference in uniform elongation of

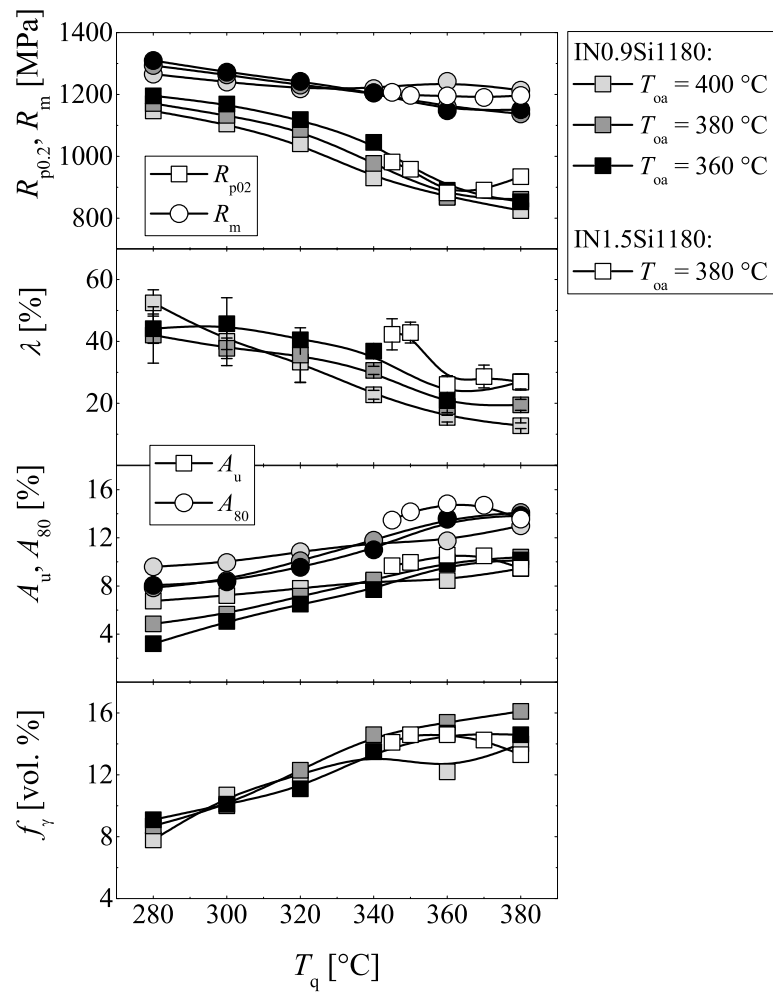
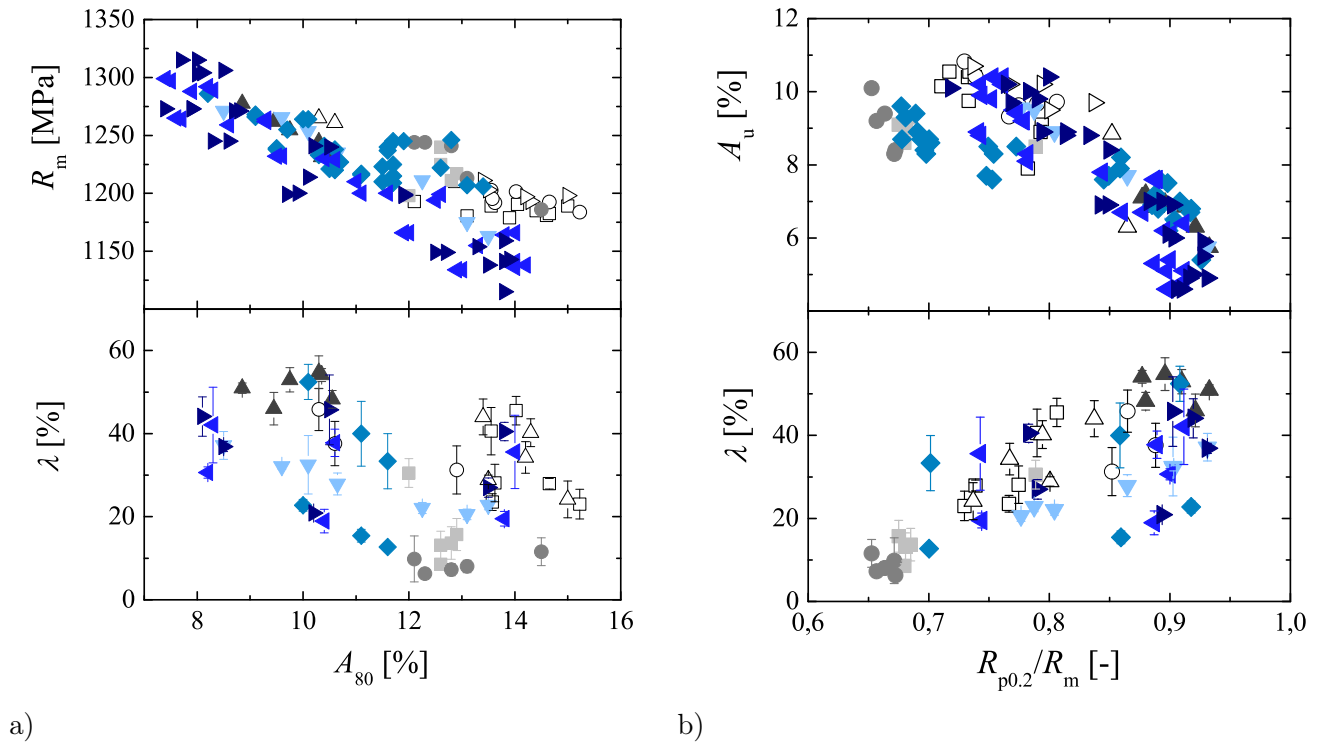


Figure 4.52: Yield strength, tensile strength, hole expansion strain, uniform elongation, total elongation, and amount of retained austenite of industrially produced two-step Q&P heat-treated steels IN1.5Si1180 and IN0.9Si1180 as a function of quench temperature, i.e. quench temperature  $T_q$ , for various overaging temperatures  $T_{oa}$  of 360, 380, and 400  $^{\circ}\text{C}$  ( $t_{oa} = 460$  s).

the two steels at a quench temperature of 380  $^{\circ}\text{C}$ . Steel IN0.9Si1180, in contrast, clearly succeeds in terms of hole expansion strain well above 50% in combination with total elongations of more than 10%. Interestingly, for an overaging temperature of  $T_{oa} = 380$   $^{\circ}\text{C}$  the decrease in hole expansion strain with increasing total elongation is not very pronounced. An increase in yield ratio is a necessary but insufficient condition for an increase in hole expansion strain (Figure 4.53b).



1.5Si1180				0.9Si1180				
	$T_q$ [°C]	$T_{oa}$ [°C]		$T_q$ [°C]	$T_{oa}$ [°C]		$T_q$ [°C]	$T_{oa}$ [°C]
□	400	380	■	380 - 340	400	▼	360 - 300	380
○	340	370	●	420 - 380	400	◆	360 - 280	400
△	380 - 340	380	▲	340 - 280	400	▶	380 - 280	380
						▶	380 - 280	360

Figure 4.53: a) Hole expansion strain and tensile strength as a function of total elongation  $A_{80}$ , b) hole expansion strain and uniform elongation as a function of yield ratio of industrially produced two-step Q&P steels of compositions IN1.5Si1180 and IN0.9Si1180 for various annealing cycles ( $T_{an} = 850$  °C).

# Chapter 5

## Discussion

### 5.1 Phase transformations, microstructures, and mechanical properties: A general overview

#### 5.1.1 Phase transformation kinetics

The investigated steels show similarities in phase transformations, microstructures, and mechanical properties, which are typical for TBF and Q&P steels. This section will present the generally observed tendencies, explain their origin, and demonstrate the scope of action to design specific properties of TBF and Q&P steels.

Phase transformation diagrams are used to estimate the time and temperature at which a phase forms. The transformed phase fraction specific time-temperature heat treatment can be determined from the dilatation measured at a given time and temperature (Section 3.3.4). Continuous cooling transformation (CCT) diagrams and time temperature transformation (TTT) diagrams show the continuous and isothermal phase transformation behaviour of TBF and Q&P steels prior to and during overaging. Figure 5.1a shows a schematic diagram of the transformed phase fraction during continuous cooling. The type of transformation product during continuous cooling depends on the cooling rate.

Above  $M_s$  temperature, higher cooling rates shift the transformation to lower temperatures (Figure 5.1a). If cooled at high cooling rates above the critical cooling rate, i.e. more than 50 to 70 K/s in the 980 grade and 30 to 50 K/s in the 1180 grade, there is insufficient time for diffusional transformation and displacive transformation takes place below  $M_s$  temperature of approximately 380 °C. Due to the higher carbon and manganese content as well as the slightly elevated silicon content, phase transformations are generally more sluggish and critical cooling rate as well as  $M_s$  temperature are lower for the 1180 compared to the 980 base composition. At low cooling rates, a slightly enhanced phase transformation rate above 600 °C at the beginning of the transformation during continuous cooling indicates ferrite and/or pearlite formation, as shown in Figure 5.1. Bainite forms below the temperature range for ferrite transformation and above the  $M_s$  temperature.

The time-temperature curve for a given transformed phase fraction during overaging is shown in the TTT diagram of Figure 5.1b. During overaging, pearlite can form in addition to (polygonal) ferrite, which is indicated by an acceleration of phase transformation at relatively high overaging temperatures for TBF steels (Figure 5.1b). In this work, pearlite was observed in some of the investigated steels that were held at the highest temperatures within the applied overaging temperature range of up to 600 °C. Bainite forms below temperatures at which polygonal ferrite and pearlite form and above  $M_s$  temperature. Upper bainite and globular or carbide-free bainite tend to form at rather high temperatures in this range. Lower bainite is more likely to form at lower overaging

temperatures.

If the steel is cooled below  $M_s$  temperature at a higher velocity than the critical cooling rate, a certain amount of the austenite transforms to martensite. The amount of martensite formed can be quantified by the empirical athermal Koistinen-Marburger equation [176]. An isothermal transformation occurs during overaging below  $M_s$  temperature. The kinetics of this transformation corresponds to those of the bainite formation above  $M_s$  temperature, as mentioned in Section 2.1 [55, 57]. Therefore, the isothermal transformation product below  $M_s$  is referred to as bainite formation in the corresponding literature references. Martensite formed upon cooling to overaging temperature serves as a nucleation site and promotes the bainite formation. Therefore, isothermal phase transformation is accelerated below  $M_s$  (Figure 5.1b). It is important to note that an acceleration of phase transformations also occurs close to and above  $M_s$  temperature. This can be explained by inhomogeneities in composition. The  $M_s$  temperature is given for the overall chemical composition, whereas the local  $M_s$  may vary due to local differences in the chemical composition. This acceleration of phase transformations below the bainite C-curve, i.e. below as well as close to and above  $M_s$ , is called swing-back [89, 177].

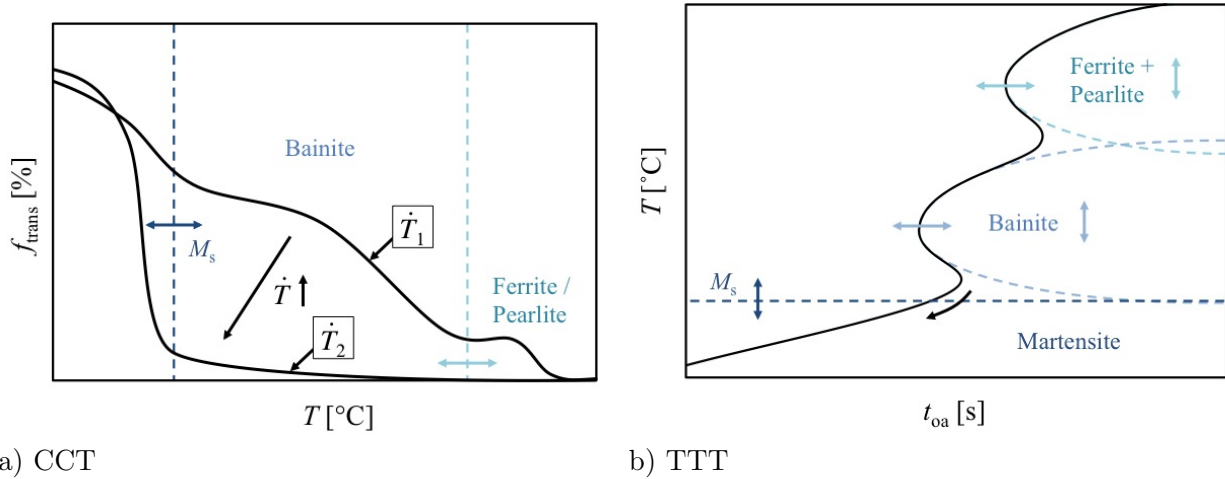


Figure 5.1: Time-temperature-transformation diagrams: a) Transformed phase fraction during continuous cooling (CCT) for two cooling rates  $\dot{T}_1 < \dot{T}_2$ . The dashed lines divide the diagram into different temperature ranges, at which ferrite, pearlite, bainite and martensite form. b) Time-temperature curve for a given transformed phase fraction (black curve) during overaging at a given temperature (TTT). The dashed C curves indicate the time-temperature range at which ferrite, pearlite, and bainite form. The dashed line indicates  $M_s$  temperature. The black arrow denotes the swing back phenomenon, i.e. the acceleration of isothermal phase transformation with decreasing overaging temperature close to and above  $M_s$  [89, 177]. The isothermal phase transformation also continues below  $M_s$  (see Section 2.1).

The influence of alloying elements on phase transformations will be discussed in detail in Section 5.2 of this chapter.

### 5.1.2 Microstructure and the amount of retained austenite

The typical trend in the amount of retained austenite with proceeding overaging time is shown in Figure 5.2a. For very short overaging times, the majority of the large austenite fraction present at the end of the overaging step is unstable at room temperature and transforms to martensite upon the final cooling. The amount of retained austenite rapidly increases at the beginning of the

overaging step. While bainite forms during overaging, interstitially dissolved carbon can diffuse and partition from the newly transformed bainite to the remaining austenite. Higher carbon content provides higher stability of the austenite against martensite transformation upon the final cooling. Furthermore, the amount of austenite is reduced by the amount of bainite formed at overaging temperature. A lower amount of austenite during overaging means that the carbon in the austenite is spread over a lower volume fraction, which results in a higher average carbon content in the austenite. Smaller austenite islands result in shorter diffusion distances in the austenite. Therefore, more carbon diffuses closer to the center of the austenite islands.

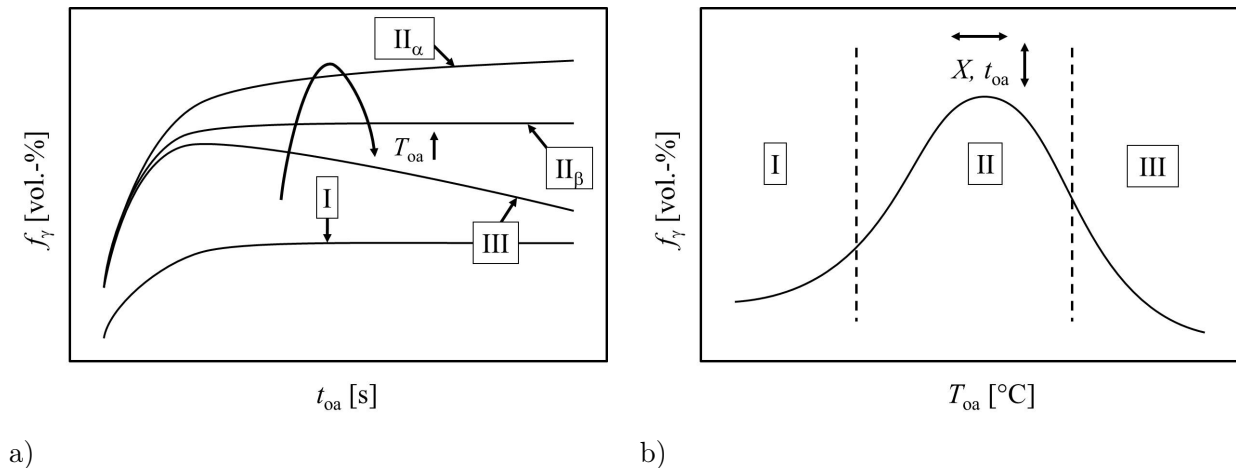


Figure 5.2: Scheme of the amount of retained austenite as a function of a) overaging time and b) overaging temperature (I: low  $T_{oa}$ , II: medium  $T_{oa}$ , III: high  $T_{oa}$ ).

The SEM images of Figures 5.3a and 5.3b show that the amount of bainite and retained austenite increases, while the fraction of fresh martensite decreases for short overaging times. The microstructure of steel 0.2Cr1180 still shows large areas of fresh martensite formed during the final quenching after holding for 30 s at an overaging temperature of 400 °C (Figure 5.3a). After 120 s of overaging, the amount of bainite is higher, the retained austenite islands are larger, and there is almost no more fresh martensite (Figure 5.3b).

After the initial increase, there are three options for the further development of the amount of retained austenite during overaging (Figure 5.2a). Each of these following scenarios occurs within a typical overaging temperature range (Figure 5.2b). As shown in Figure 5.2b, the amount of retained austenite increases up to a peak and then decreases with increasing overaging temperature (e.g. Figure 4.20). In the first option after the initial increase in the amount of retained austenite as overaging proceeds, the amount of retained austenite stays at the same level (I and II $_\beta$ , Figure 5.2a). This is typical for low and medium overaging temperatures (I and II, Figure 5.2b). Second, the amount of retained austenite slightly continues to increase (II $_\alpha$ , Figure 5.2a), which can be observed for medium overaging temperatures (II $_\alpha$ , Figure 5.2a). Third, the amount of retained austenite decreases as the overaging time proceeds (III, Figure 5.2a). This tendency is mainly found for higher overaging temperatures (III, Figure 5.2b).

In the first option after the initial increase in the amount of retained austenite with increasing overaging time, bainite transformation stops, which is indicated by a plateau in the amount of retained austenite (I and II $_\beta$  in Figure 5.2a). Figure 5.3 shows an example of case II $_\beta$ . As indicated by Figures 5.3b and 5.3c, most of the bainite has transformed after overaging for 120 s, and the partitioning of carbon resulting in the stabilization of the majority of the austenite to room temperature corresponds to II $_\alpha$ , as shown in Figure 5.2a. This is why both microstructures are

very similar. According to the  $T_0$ -concept, this scenario may happen as soon as the critical carbon content is reached in the austenite, which corresponds to  $T_0 = T_{0a}$  [46]. After the bainite formation has stopped, either no more carbon partitions to the austenite or further partitioning does not result in higher amounts of retained austenite but further stabilization of the existing austenite.

The lower amount of retained austenite at low overaging temperatures (I in Figure 5.2) compared to medium overaging temperatures can be explained as follows: Carbide precipitation during overaging is more pronounced for low overaging temperatures, as seen in (Figure 5.4a). On the one hand, transformation is faster below the swing-back phase at lower overaging temperatures. On the other hand, diffusion rates are lower at lower overaging temperatures. As a consequence, there might be not enough time and the carbon is too slow to diffuse to the austenite. In addition, the driving force for carbide precipitation is higher and the solubility of carbon in the bainitic/martensitic matrix is lower at lower overaging temperatures.

The second option after the initial increase is, that the amount of retained austenite continues to increase. As long as this is the case ( $II_\alpha$ , Figure 5.2a), there is still carbon diffusing from the bainite into the austenite during overaging and this carbon contributes to the stabilization of further amounts of austenite to room temperature. This does not necessarily have to involve further bainite formation because carbon can continue to partition from the existing bainite to the austenite.

The critical carbon content  $c_0$  at which bainite formation stops increases with decreasing temperature. Thus, higher amounts of bainite can form at medium overaging temperatures compared to high overaging temperatures until bainite formation stops. This leads to smaller austenite islands, that are comprised of higher carbon content prior to the final cooling when compared to higher overaging temperatures. Furthermore, at medium overaging temperatures less carbides are present in the bainitic matrix compared to lower overaging temperatures (Figure 5.4b vs. Figure 5.4a, respectively). Thus, more carbon remains dissolved and stabilizes the austenite, which results in higher amounts of retained austenite. As a consequence, the amount of retained austenite is highest for medium overaging temperatures (II in Figure 5.2), as confirmed by Figure 5.4b.

Finally, the third possible continuation after the initial increase is a drop in the amount of retained austenite with increasing overaging time (III in Figure 5.2a). At higher overaging temperatures, the bainite formation stops at lower amounts of bainite. This is because, according to the  $T_0$  concept, at higher overaging temperature the critical carbon concentration  $c_0$  required to stop bainite transformation is lower. For higher overaging temperatures carbon diffusion is faster and the driving force for carbide precipitation is lower. Therefore, the bainite formed at high overaging temperatures such as 475 °C contains much less carbides compared to lower overaging temperatures, as can be seen in Figure 5.4c.

However, in the case of the drop in the amount of retained austenite with proceeding overaging time, carbon precipitates from the austenite during overaging reducing the amount of austenite that can be stabilized to room temperature. One option to explain the carbon precipitation is the formation of pearlite. Another possibility is the precipitation of carbon in the form of carbides. The most common carbide in the present steels is cementite. However, transition carbides are also possible. For both of these options, carbon precipitation from the austenite reduces its carbon content and, thereby, its stability. On the one hand, austenite decomposition by carbon precipitation, e.g. in the form of cementite, directly reduces the amount of austenite. Steels that were held at high overaging temperatures such as steel 0.2Cr1180 in Figure 5.4c contain large fractions of fresh martensite and may contain pearlite formed during overaging. The longer the overaging time, the more of the austenite transforms to pearlite during overaging. On the other hand, carbon precipitation can deplete the remaining austenite of carbon. The later can lower the stability of the austenite, thereby promoting the decomposition of the austenite to martensite upon final cooling. As a result, higher overaging temperatures above the peak in the amount of retained austenite given in Figure 5.2b, lead to lower amounts of retained austenite.

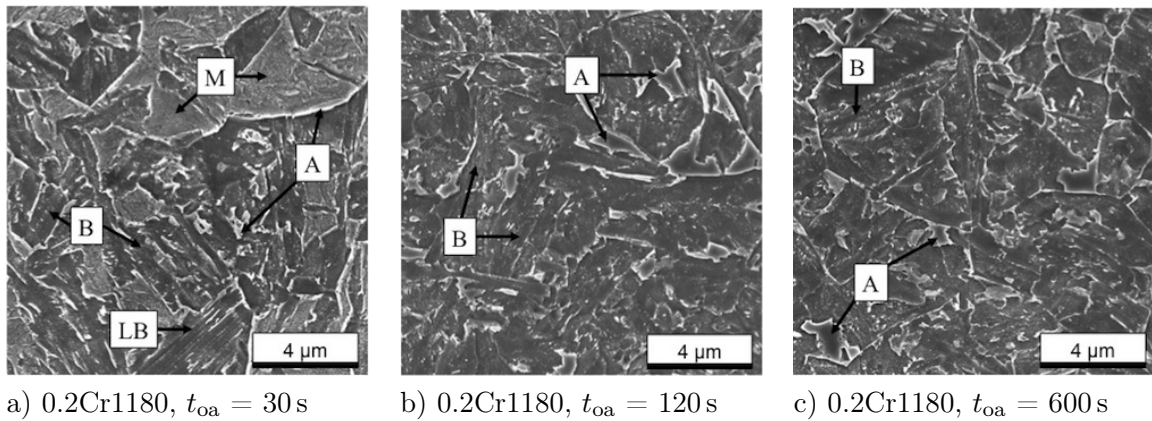


Figure 5.3: SEM images of TBF heat-treated steel 0.2Cr1180 for overaging times of a)  $t_{0a} = 30$  s, b)  $t_{0a} = 120$  s, and c)  $t_{0a} = 600$  s comprising bainite (B), lower bainite (LB), austenite (A) and martensite (M) ( $T_{0a} = 400$  s,  $\dot{T} \approx 50$  K/s).

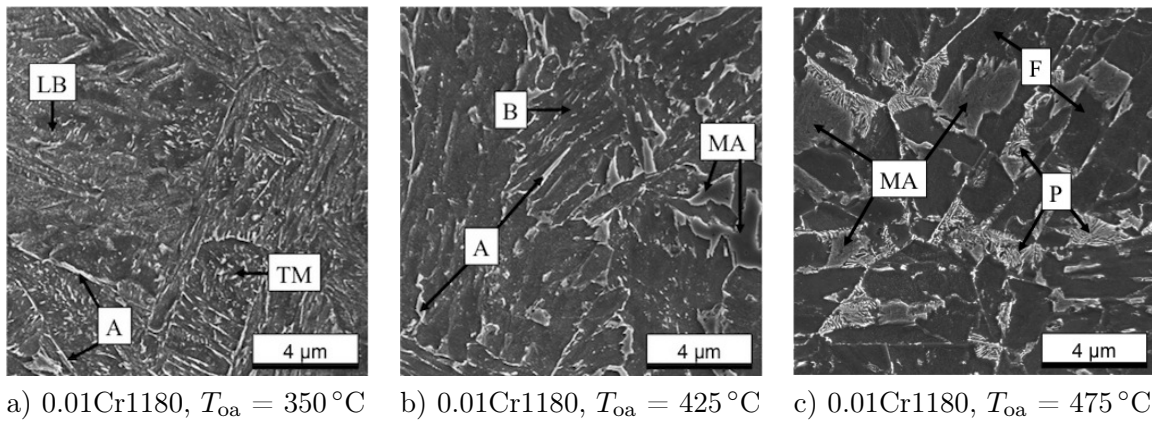


Figure 5.4: SEM images of Q&P and TBF steel 0.01Cr1180 for various overaging temperatures comprising polygonal ferrite (F), pearlite (P), bainite (B), lower bainite (LB), tempered martensite (TM), retained austenite (A) and retained austenite/martensite islands (MA) ( $t_{0a} = 600$  s,  $\dot{T} \approx 50$  K/s). a)  $T_{0a} = 350$  °C corresponding to *I* in Figure 5.2b, b)  $T_{0a} = 425$  °C (*II* in Figure 5.2b), and c)  $T_{0a} = 475$  °C (*III* in Figure 5.2b).

The stabilization procedure of the retained austenite via carbon partitioning during the overaging step is different in comparison to conventional TRIP steels [107, 172]. The most important difference between conventional TRIP steels and TRIP-assisted steels with bainitic and/or martensitic matrix is, that conventional TRIP steels comprise almost no carbides down to overaging temperatures of 350 °C. In the TRIP-assisted TBF and Q&P sheet steels presented in this work, carbide precipitations are present at most overaging temperatures, albeit less pronounced at higher overaging temperatures. Furthermore, in the presence of polygonal ferrite from intercritical annealing of conventional TRIP steels, the gain in the amount of retained austenite correlates with the overaging temperature. As long as the gain in diffusion velocity has a higher impact on phase transformation rate than the reduction of the thermodynamic driving force, higher overaging temperatures result in the faster progression of diffusion-controlled phase transformations. Therefore, the amount of retained austenite in conventional TRIP steels is higher for higher overaging temperatures after the same overaging time. In TBF steels, in contrast, the isothermal bainite transformation stops at the latest when the critical carbon content  $c_0$  of the austenite is reached for a given overaging

temperature.

Speer *et al.* [40] developed a model to describe the amount of retained austenite and assumed the amount of retained austenite to be the residual of the total amount of austenite after annealing less the initial amount of martensite formed before overaging and less the martensite formed during final cooling depending on the austenite stability. However, bainite formation is not taken into account in this approach. The present work demonstrates the significant influence of bainite formation and carbon partitioning in particular into the austenite during overaging on the amount of retained austenite of TBF and Q&P steels.

### 5.1.3 Mechanical properties

Mechanical properties are explained on the basis of the knowledge gained about the overall microstructure and especially the amount of retained austenite. Figure 5.6 shows the trend of mechanical properties as a function of overaging time and overaging temperature. Looking at the beginning of the overaging step, the yield strength of TBF or Q&P heat-treated steels rapidly decreases with increasing overaging time (Figure 5.6a). In this first step, bainite rapidly forms. As described in detail above, the amount of retained austenite also increases for the beginning of the overaging step mainly due to carbon partitioning in combination with the reduction of the size of the austenite grains before cooling. As a result, the amount of fresh martensite in the microstructure significantly decreases with progressing bainite transformation for the beginning of the overaging step (Figure 5.3a). The replacement of hard fresh martensite by softer microstructure components such as bainite leads to an increase in uniform and total elongation and a decrease in the overall strength of the material.

After the initial decrease, there are three options for the further development of the yield strength as overaging time progresses (Figure 5.6a). These different possibilities roughly correspond to overaging temperature ranges (*I*: low  $T_{oa}$ , *II*: medium  $T_{oa}$ , *III*: high  $T_{oa}$ ) marked in Figure 5.6b and Figure 5.2b. At low overaging temperature, yield strength changes its tendency to an increase with increasing overaging time. This gain in yield strength arises in particular from two different sources: first, the strongest improving effect on yield strength appears to be the continuing reduction of the size and amount of the fresh martensite islands. Second, the present work shows that yield strength benefits from lower amounts of retained austenite. The effect of tempering on yield strength is much lower than that of changes in the size and amount of fresh martensite and/or retained austenite inclusions. As overaging proceeds, yield strength only slightly increases as a result of matrix tempering.

Figure 5.5a-c in combination with yield strength and amount of retained austenite shown in Figure 4.12a confirm the importance of the amount of retained austenite for yield strength. Despite the significant decrease in the amount of fresh martensite as overaging time proceeds, yield strength remains at the same level. Here, the decrease in the amount of fresh martensite appears to be compensated by the increase in the amount of retained austenite, as shown in Figure 4.12a. Moreover, if both the amount of retained austenite as well as the amount of fresh martensite decrease, yield strength significantly increases. In both cases, tensile strength stays at similar values, and the morphology of the matrix looks similar for the different overaging times. Thus, it can be concluded that the amount of retained austenite not only largely promotes uniform elongation, but also significantly impairs yield strength (Figure 4.12a).

Tensile strength also strongly decreases with increasing overaging time considering short overaging times (Figure 5.6a). This also can be attributed to the loss in strength as a result of the replacement of fresh martensite by bainite, as explained above for yield strength. The most remarkable thing about tensile strength is that it stays at the same level after the initial drop, which can be explained as follows: most of the retained austenite transforms to martensite via SIMT

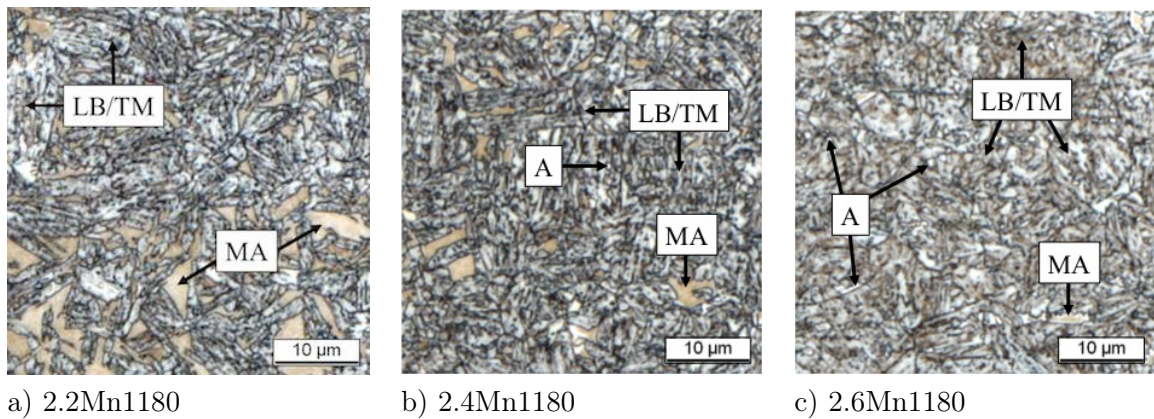


Figure 5.5: LePera etched optical micrographs of Q&P steel 2.6Mn1180 for a fixed overaging temperature of  $T_{0a} = 350\text{ }^{\circ}\text{C}$  comprising lower bainite (LB), tempered martensite (TM), retained austenite (A), and retained austenite/martensite islands (MA) ( $\dot{T} \approx 50\text{ K/s}$ ). a)  $t_{0a} = 120\text{ s}$ , b)  $t_{0a} = 180\text{ s}$ , and c)  $t_{0a} = 600\text{ s}$ .

during straining below the onset of necking. Therefore, the replacement of martensite by retained austenite through further stabilization of the austenite by carbon partitioning prior to cooling to room temperature has little effect on the microstructure present at uniform elongation.

Furthermore, tensile strength first decreases then increases with increasing overaging temperature (Figure 5.6b). The main reason for the decrease in tensile strength with increasing overaging temperature in the low overaging temperature range is a result of the change in bainitic/martensitic matrix. The lath thickness increases with increasing overaging temperature, which contributes to the reduced strength of the matrix. In addition, the strength of the matrix decreases as overaging temperature increases, because the carbides are less dispersed at higher overaging temperatures. The change in the tendency of tensile strength to an increase with increasing overaging temperature in the high overaging temperature range arises from the increase in the amount of retained austenite and martensite in the final microstructure as a consequence of the  $T_0$  effect.

Uniform elongation as a function of overaging time (Figure 5.6a) correlates very well with the amount of retained austenite overall (Figure 5.2a). This means that uniform elongation increases with increasing overaging temperature for low overaging temperatures, whereas the opposite is the case for high overaging temperatures. In analogy to the amount of retained austenite, the overaging temperature above which the tendency changes is lower for the 1180 grade than for the 980 grade. As mentioned above, this is because the additional carbon and manganese in the 1180 grade stabilize the austenite and result in higher amounts of austenite before the final cooling. Due to the larger size and the lower carbon content of the austenite, less retained austenite is stabilized to room temperature resulting in higher amounts of fresh martensite. Higher amounts of fresh martensite instead of bainite result in higher tensile strength and lower uniform elongation, as described in the first paragraph of this section. The replacement of retained austenite by fresh martensite does not necessarily result in higher tensile strength, but it considerably deteriorates uniform elongation.

At high overaging temperatures, uniform elongation does not decrease as drastically as the amount of retained austenite with increasing overaging temperature. This can be explained by the much softer, more globular and less lath-like (upper) bainitic matrix at higher overaging temperatures. It is worth noting that the uniform elongation of both the 980 and the 1180 group are at a similar level, while yield and tensile strength are on average 100 to 200 MPa higher for the 1180 steels than for the 980 grades (e.g. Figure 4.6a and 4.6b). This is a result of the significantly higher amount of retained austenite in the 1180 grade, which in many cases is almost twice that of

the 980 grade. The higher amount of retained austenite compensates the loss in uniform elongation, which is expected to arise from such a significant strength increase.

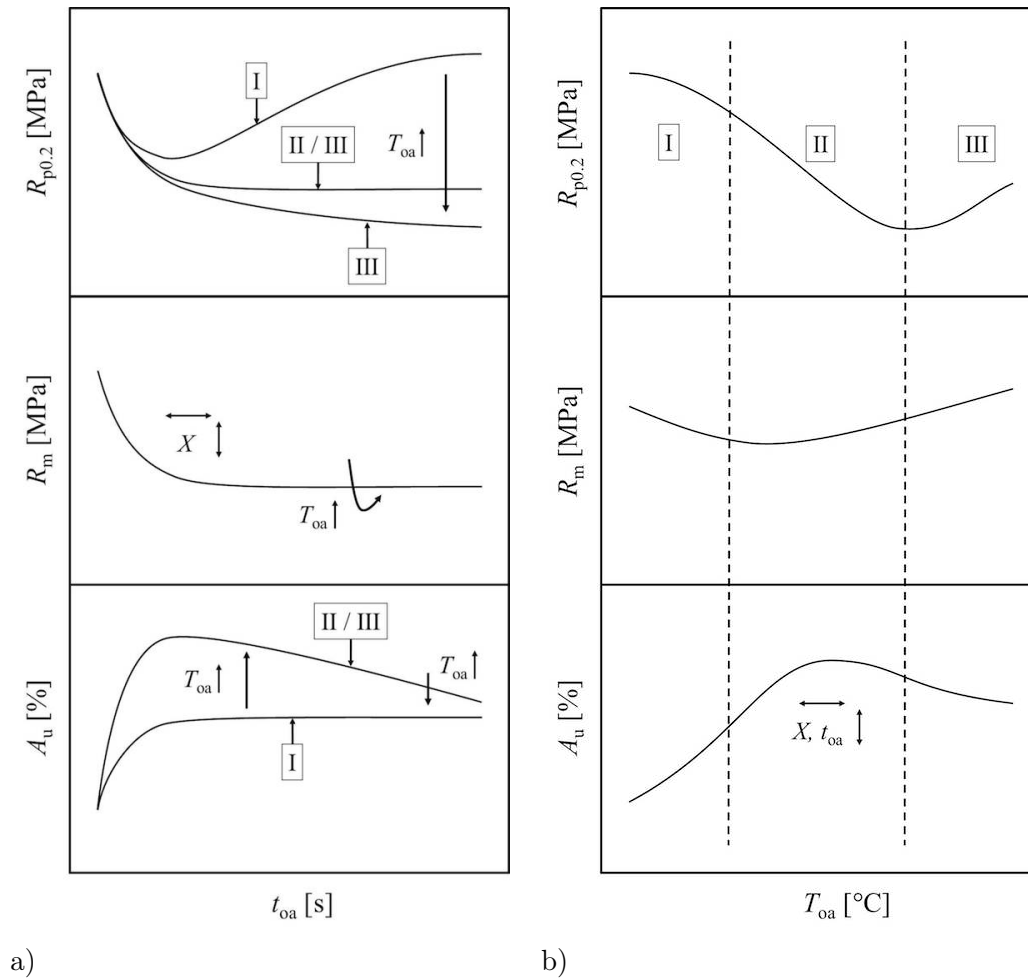


Figure 5.6: Scheme of yield strength, tensile strength, and uniform elongation as a function of a) overaging time and b) overaging temperature (*I*: low  $T_{oa}$ , *II*: medium  $T_{oa}$ , *III*: high  $T_{oa}$ ).

## 5.2 Influence of alloying elements on TBF and Q&P sheet steel

### 5.2.1 Silicon

In this chapter, the effect of silicon on phase transformation behaviour, amount of retained austenite, microstructure, and mechanical properties is discussed.

As shown in Figure 4.1a, phase transformations during continuous cooling are slightly accelerated by silicon additions to the 980 grade for almost the whole investigated temperature range. The temperature at which ferrite begins to form from austenite,  $A_{r3}$ , upon cooling at a rate of 3 K/s is also slightly higher for higher silicon contents (Figure 4.1a). The acceleration in phase transformations during continuous cooling can be explained as follows: as a ferrite stabilizer, silicon increases the  $A_{r3}$  temperature. As a result the thermodynamic driving force of phase transformations determined by the difference between the current and  $A_{r3}$  temperature is higher. The higher the transformation temperature, the stronger silicon accelerates phase transformations. The possible reason might be that at higher temperatures the temperature difference between the current and  $A_{r3}$  temperature is

smaller. Therefore, changes in the  $A_{r3}$  temperature can have a greater impact on the thermodynamic driving force at temperatures closer to  $A_{r3}$  temperature.

In contrast, silicon decelerates phase transformations in the entire investigated temperature-time window during overaging (Figure 4.4b). Both the mostly carbide-free pre-isothermal transformation product as well as the suppression of carbide precipitation by silicon can contribute to a higher carbon content in the austenite, which most probably enhances its stability. The higher stability of the austenite decreases the thermodynamic driving force and decelerates the phase transformation during overaging.

A second explanation for the deceleration of isothermal phase transformation is that a higher amount of substitutionally dissolved silicon can contribute to the solute drag effect. Silicon can impair the mobility of the grain boundary between the remaining austenite and the new transformation product. However, this influence is limited to the temperature-time window at which silicon diffusion velocity is only slightly lower than the grain boundary velocity of the phase transformation. Since silicon is a substitutional element, high overaging temperatures are required to fulfil this premise given the present industry-related overaging time range.

An important finding of the present work is that silicon decelerates phase transformations in the 1180 grade during continuous and isothermal transformation almost in the entire observed time and temperature window (Figure 4.4). The austenite stabilizing and the solute drag effect arising from the higher carbon, manganese, silicon, and chromium content apparently outweigh the ferrite stabilizing effect of silicon on phase transformations in the case of the grade 1180.

Only at very high overaging temperatures of more than 550 °C, silicon accelerates the isothermal phase transformation in this grade (Figure 4.4b). Here, pearlite is observed to form faster for higher silicon contents, even though silicon retards the precipitation of carbon from the austenite. This effect was previously reported for conventional C-Si-Mn TRIP steels [178]. The promotion of pearlite formation by silicon additions at high overaging temperatures might be a result of the stronger impact of changes in  $A_{r3}$  temperature on the thermodynamic driving force at higher overaging temperatures. Moreover, silicon diffuses much faster at these temperatures, allowing a silicon redistribution in favour of carbon precipitation. In addition, the high carbon diffusion rate at these temperatures support a more rapid accumulation of carbon to precipitate. This observation is in good agreement with literature [52]. Based on thermodynamic calculations, Kozeschnik *et al.* state that silicon decelerates cementite formation in para-equilibrium only, while in ortho-equilibrium no deceleration through silicon additions is observed [52].

Microstructure and amount of retained austenite are in good agreement with the observations on phase transformations (Figure 4.2 and 4.3). Silicon increases the amount of retained austenite up to an overaging temperature of 425 °C in particular in the 980 grade. This can be attributed to the higher stability of the austenite and its higher carbon content through the reduction of carbon precipitation resulting from silicon additions. This hypothesis is supported by the observation of reduced presence of carbides in this grade for higher silicon content. Furthermore, for the 980 grade polygonal ferrite is observed in the steel with the highest silicon content, grade 1.0Si980, as a result of the accelerated phase transformation at high temperatures during continuous cooling (Figure 4.1). Finally, a more lath-like and structured bainite can be observed for higher silicon content. This is most likely a result of the retarded bainite formation. The lath-structure of bainite or martensite tends to become blurry, and the laths tend to vanish as tempering proceeds, which can be attributed to precipitation of the formerly interstitially dissolved carbon. The formation of bainite is later in the event of higher silicon content, so its tempering time is shorter. Therefore, tempering is less progressed and the bainite is more lath-like and structured for greater silicon additions.

In the 1180 grade, there is only a very slight increase in the amount of retained austenite from the lowest to the two higher silicon contents (Figure 4.6). The amount of retained austenite is already much higher in all variants of the 1180 grade as opposed to the 980 grade. The austenite is

already closer to saturation in carbon content as a result of the higher carbon content in the base composition of the 1180 grade as opposed to the 980 grade. This can be concluded from the isothermal dilatometer experiments of both grades, which show that the amount of bainite at which the isothermal transformation stops, is lower in the 1180 grade compared to the 980 grade, in particular for higher overaging temperatures. Furthermore, the higher manganese content of the 1180 base composition contributes to a higher austenite stability compared to the 980 grade. Since the solubility of carbon in ferrite is negligible compared to that in austenite, a higher austenite fraction results in less carbon precipitation. Therefore, the effect of silicon in reducing carbon precipitation is less pronounced in microstructures that exhibit higher austenite fractions by themselves.

Tensile strength slightly decreases at low and very slightly increases at high overaging temperatures with increasing silicon content in the 980 grade (Figure 4.3a), which can be explained as follows: first, the increase in the amount of retained austenite by the addition of silicon is more pronounced at higher overaging temperatures. Second, the strength of a (tempered) martensitic and bainitic matrix formed at low overaging temperatures is higher than the strength of a bainitic matrix formed at higher overaging temperatures. This means that a partial replacement of the bainitic/martensitic matrix with retained austenite is associated with a greater loss in strength at low than at high overaging temperatures, which can be explained applying the rule of mixture introduced in Section 5.2.4. Finally, the strength decrease as a result of polygonal ferrite in the matrix is more effective in steels that were held at lower overaging temperatures. In the 1180 grade, tensile strength remains unchanged despite changes in silicon content, since changes in microstructure and the amount of retained austenite are smaller (Figure 4.6a).

The changes in yield strength caused by the addition of silicon are mainly driven by the amount of retained austenite. Yield strength decreases from lowest to next higher silicon content in the 980 grade for the low overaging temperature of 350 °C (Figure 4.3a). This can be explained by the fact that the amount of retained austenite increases, while tensile strength decreases. A higher amount of retained austenite with comparable stability is expected to result in higher strain-hardening potential, thus, a higher difference between yield and tensile strength. In addition, higher amounts of retained austenite increase the amount of softer phase fraction in the harder bainitic/(tempered) martensitic matrix resulting in a higher fraction of grain boundaries with enhanced hardness difference between the adjacent phases. Therefore, the decrease in yield strength is even more pronounced than that in tensile strength. In the 1180 grade, yield strength is rather unaffected by silicon additions. This behaviour can be explained by the quite similar microstructures and amounts of retained austenite of the different silicon variants in analogy to tensile strength, which also remain at the same level regardless of changes in silicon content (Figure 4.6a).

An increase in the amount of retained austenite is usually accompanied by an increase in uniform elongation (e.g. Section 4.1.1). Since silicon reduces carbide precipitation in particular in the 980 grade and thereby stabilizes the remaining austenite, elevated uniform elongation is expected for higher silicon content. Interestingly, uniform elongation increases in a more pronounced manner with increasing silicon content at high overaging temperatures than at low overaging temperatures (Figure 4.3a). The effect of a higher amount of retained austenite presumably superposes with that of the presence of polygonal ferrite, which both contribute to elevated uniform elongation. In the 1180 grade, uniform elongations of the different silicon contents mutually fall into their scatter bands, which is in good agreement with the amount of retained austenite and tensile strength, which consistently remain at the same level unaffected by silicon additions in the investigated range.

Figure 5.7 contains valuable insights into the relationship between the amount of retained austenite and uniform elongation. Higher overaging temperatures as well as higher silicon contents result in higher amounts of retained austenite and higher uniform elongation, as discussed in the previous paragraph. The gain in uniform elongation achieved by the additional amount of retained austenite is comparable for the four selected overaging temperatures. However, the increase of both

the amount of retained austenite and uniform elongation as a result of silicon additions is more pronounced at higher overaging temperatures. This is most probably because in the investigated range the amount of retained austenite is higher at higher overaging temperatures in the first place. Therefore, a proportional increase in the amount of retained austenite results in a stronger increase in the amount of retained austenite in absolute terms.

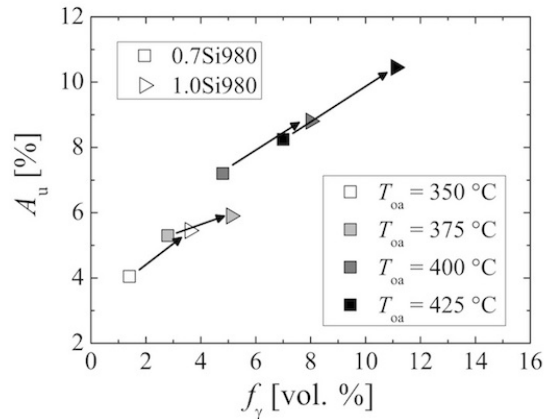


Figure 5.7: Uniform elongation as a function of the amount of retained austenite for steel grades 0.8Si980 and 1.0Si980 ( $t_{oa} = 600$  s).

Tensile strength and yield ratio as a function of uniform elongation are shown in Figures 5.8a and 5.8b, respectively. Uniform elongation increases as tensile strength decreases with increasing overaging temperature and increasing silicon content. The replacement of some of the isothermally formed bainite by martensite formed during the final cooling and tempered during overaging resulting from the addition of silicon as seen in Figure 4.2 should result at least in a slight increase in hardness and tensile strength. However, the significant increase in the amount of ferrite and retained austenite have a much stronger impact on tensile strength as can be explained by applying the rule of mixture (Equation 2.9). It is worth noting that at  $T_{oa} = 425$  °C both tensile strength and uniform elongation increase with increasing silicon content (Figure 5.8a). This is because steel 1.0Si980 contains a higher amount of fresh martensite formed during cooling. In addition, the elevated amount of retained austenite results in enhanced strain-hardening, delayed necking, and higher tensile strength due to the TRIP effect, even though plastic deformation begins at lower strength for higher silicon contents as shown in Figure 4.3a. As a result of the enhanced TRIP effect, silicon additions can result in higher combinations of tensile strength and uniform elongation, especially in the case of very high or very low overaging temperatures (Figure 5.8a).

The increase in uniform elongation due to the addition of silicon is accompanied by a loss in yield ratio (see Figure 5.8b). Enhanced stretch-formability is frequently associated with an impaired edge crack resistance. The yield ratio correlates very well with edge formability in many cases. Therefore, it might seem surprising that the yield ratio does not continuously decrease with increasing overaging temperature and increasing uniform elongation. Instead, yield ratio first increases then decreases with increasing uniform elongation. The yield ratio initially increases with increasing uniform elongation from 350 to 375 °C. This can be attributed to the distinct decrease in tensile strength. Another possible reason is the higher fraction of (annealed) martensite in relation to bainite as well as the greater hardness of the martensite and the bainite for lower overaging temperatures. Harder bainite and/or martensite results in a stronger hardness contrast between the (retained austenite) inclusions and the surrounding bainite/martensite.

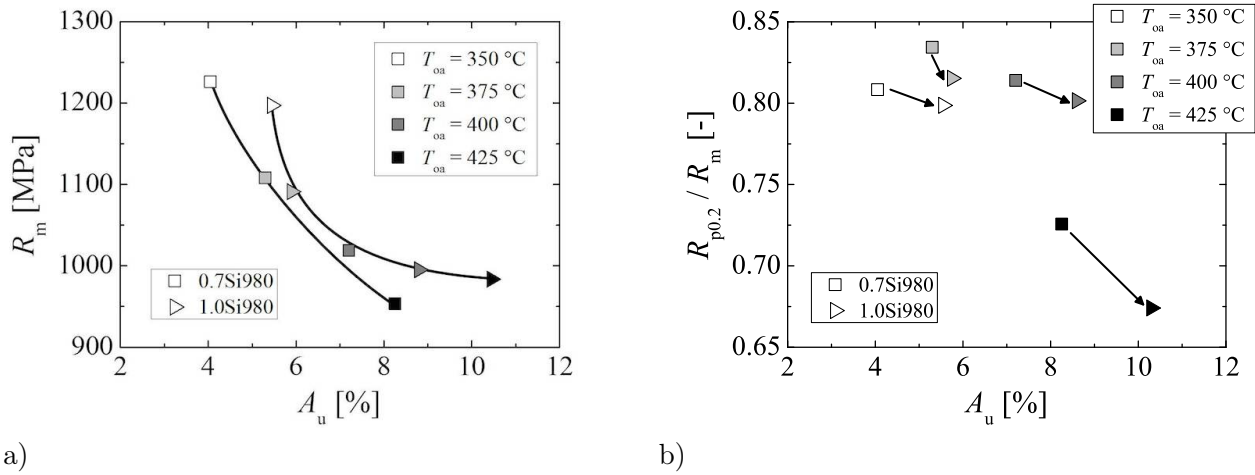


Figure 5.8: a) Tensile strength and b) yield ratio as a function of uniform elongation for steel grades 0.8Si980 and 1.0Si980 ( $t_{oa} = 600$  s).

## 5.2.2 Manganese

In this section, the influence of manganese on phase transformation behaviour, microstructure, and mechanical properties of TBF and Q&P steels is discussed. Relatively small changes in manganese content of 0.2 mass % result in significant changes in phase transformation kinetics, microstructure, and mechanical properties. The following paragraphs will show, that the impact of manganese on phase transformations, microstructures, and mechanical properties is even more pronounced in the 1180 grade compared to the 980 grade, in particular at high overaging temperatures.

As demonstrated in the Sections 4.1.3 and 4.1.4, manganese strongly decelerates both phase transformations during continuous cooling as well as the bainite transformation during overaging. Figure 5.9 confirms that the deceleration of bainite formation during overaging is more pronounced in the 1180 than in the 980 grade. It further shows, that the final transformed phase fraction after 1200 s of overaging is lower for higher manganese contents. The slight slope in the curve at the end of the overaging step indicates that bainite transformation does not stop within the first 1200 s of overaging (Figure 5.9).

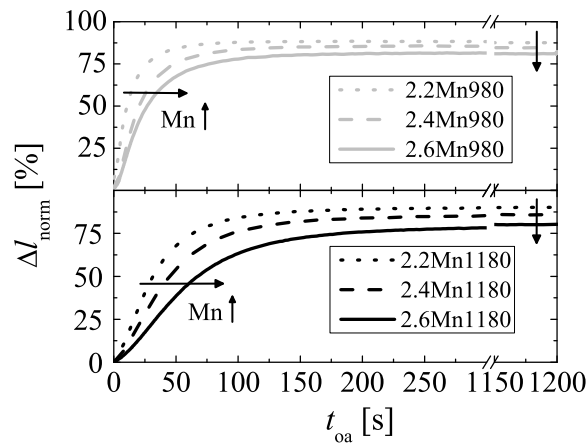


Figure 5.9: Normalized sample length of both 980 and 1180 grade manganese variants during overaging at  $T_{oa} = 400^\circ\text{C}$  ( $T_{an} = 900^\circ\text{C}$ ,  $\dot{T} \approx 70$  K/s).

The deceleration of phase transformations is in good agreement with the changes in the microstructure. Polygonal ferrite is observed in the 980 variant with the lowest manganese content (Figure 4.8a and 4.8d), 2.2Mn980, the formation of which is significantly reduced by higher manganese contents. Only very few small polygonal ferrite grains are present in steel 2.4Mn980 and no polygonal ferrite can be found in grade 2.5Mn980 (Figure 4.8b, c, e, and f). The polygonal ferrite seems to alter the morphology of the bainite that forms during overaging. As a result, the matrix is much more globular and there are no laths visible in steel 2.2Mn980 as opposed to 2.4Mn980 and 2.5Mn980 (Figure 4.8).

In both the 980 and 1180 grades, the size of the retained austenite grains for low overaging temperatures and the size of the retained austenite/martensite islands at high overaging temperatures is larger for higher manganese contents, which is a result of the decelerated phase transformation due to manganese additions. It is worth noting, that the amount of retained austenite of steel 2.2Mn980 decreases for longer overaging times of 300 and 600 s at the high overaging temperature of 425 °C, whereas it remains at the same level for the grades with higher manganese content (Figure 4.9). This is most probably a consequence of the change in bainite morphology resulting from the polygonal ferrite in the matrix. The change in morphology of the phases constituting the matrix affects the shape as well as the carbon content and distribution of the retained austenite. A replacement of thin film type austenite embedded in a lath-like matrix by globular austenite islands most probably reduces its stability and therefore the amount that is stable at room temperature.

To gain a deeper understanding of the changes in bainite morphology of the matrix caused by manganese additions, it is useful to take a closer look at the transformation kinetics. The growth mechanism of bainite is unclear to this date. In fact, the nature of bainite transformation has been subject of controversial discussion ever since the discovery of bainite [179]. The shape and morphology of bainite is similar to that of martensite. Both bainite and martensite do not grow across former austenite grain boundaries, and both martensite and bainite transformation stop prior to equilibrium [180]. However, there are fundamental differences between bainite and martensite such as different habit planes depending on transformation temperature and the limited size of less than that of the austenite grain that bainite plates grow to. There are indicators for purely diffusion-controlled, also termed reconstructive, and displacive transformation, also referred to as displace, martensitic, or military. The actual type of the transformation could possibly be a mixture of both. Since the driving force for transformation depends on the underlying transformation mechanism, there is no consistent description for it either.

Displacive transformations cause internal strains. To initiate displacive phase transformation, the applied energy must at least overcome the elastic energy caused by the additional lattice distortion and the stored energy caused by the newly generated grain boundaries and surfaces. The highest share of the stored energy in bainite arises from the invariant-plane shape deformation, whereas the interfacial energy is negligible [46]. The chemical driving force plays a crucial role in overcoming the mentioned energy barriers of displacive transformations. It can be described as  $F = \frac{k_B}{\Omega} (T - T_e) \cdot c_e \ln c_e$ , where  $k_B$  is the Boltzmann constant,  $\Omega$  is the atomic volume,  $T$  is the overaging temperature,  $T_e$  is the equilibrium temperature, and  $c_e$  is the equilibrium concentration of the alloying element. Due to their low diffusion velocities at overaging temperatures, which are typical for TBF and Q&P steels, the partitioning of substitutional elements during the bainite reaction is very limited. However, they strongly affect the relative thermodynamic stabilities of the austenite and ferrite phases [46]. A tendency is deducible when different empirical equations for transformation temperature are compared throughout the literature: The higher the difference in Gibbs free energy  $\Delta G_{m,chem} = G_{m,bcc} - G_{m,fcc}$  between the bcc and the fcc phase, the lower all transformation temperatures, that is  $A_3$  for eutectoid transformations in equilibrium,  $T_0$  for bainite transformations and  $M_s$  for purely martensitic transformations.

Figure 5.10 shows  $\Delta G_{m,chem}$  as a function of temperature for the three investigated manganese

contents of the 1180 grade obtained from Thermo-Calc© TCFE6 [165] calculations.  $\Delta G_{m,chem}$  decreases with increasing manganese content. This means that the bcc phase is energetically less favourable compared to the fcc phase for higher manganese content. As expected from literature and the present experimental observations, manganese thermodynamically stabilizes the austenite. However, it is interesting to note that rather small changes in molar Gibbs free energy due to manganese additions result in remarkable changes in phase transformations, microstructures, and mechanical properties. The lower driving force for ferrite formation from the austenite through higher manganese contents explains the observed deceleration of reconstructive phase transformations during continuous cooling and overaging. This deceleration is in good agreement with literature [22, 53, 73]. As a result, the size of the retained austenite/martensite islands increases with increasing manganese content and is even larger in the 1180 grade (Figure 4.8). Furthermore, the manganese content of the 2.2Mn980 grade is insufficient to suppress ferrite formation during cooling to overaging temperature in the 980 grade, as seen in Figure 4.8a.

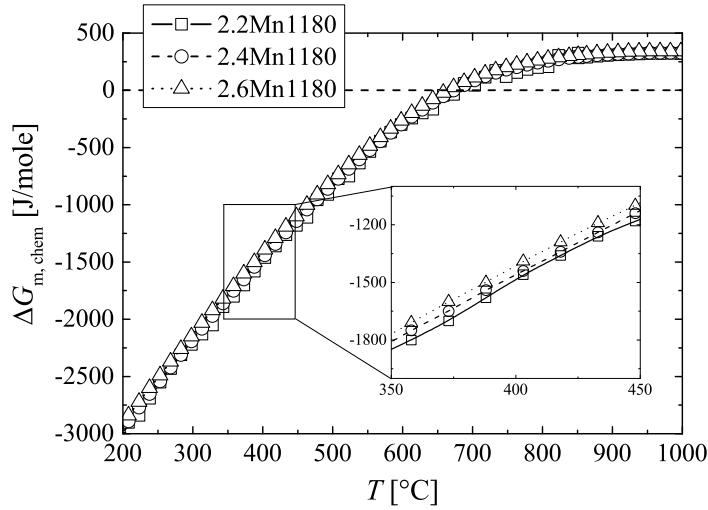


Figure 5.10: Thermo-Calc© calculations: Difference in molar Gibbs free energy of fcc and bcc phase  $\Delta G_{m,chem}$  as a function of temperature.

If bainite transformation itself or the nucleation required to initiate bainite transformation is considered as a diffusion-controlled growth process, it follows a sigmoid function of transformed fraction over time. This transformation behaviour can be described by the Johnson-Mehl-Avrami-Kolmogorov equation [110, 181]:

$$f_{trans} = \sum_i x_i [1 - \exp(-k_i \cdot t^{\eta_i})]. \quad (5.1)$$

Here,  $f_{trans}$  corresponds to the transformed fraction,  $k$  is the reaction rate, and  $\eta$  is the Avrami exponent of the transformed phase  $i$ . The reaction rate is a function of temperature  $T$  and activation energy  $Q$  and can be described by the Arrhenius relation:

$$k = k_0 \exp(-Q/RT), \quad (5.2)$$

with  $k_0$  being a constant and  $R$  the universal gas constant. To determine the values of  $k$  and  $\eta$ , it is convenient to linearize Equation 5.1 [110]:

$$\ln(-\ln[1 - f_{trans}]) = \ln k + \eta \ln t \quad (5.3)$$

Figure 5.11 shows this approach applied to the dilatometer data of the manganese variants of the 980 and 1180 grade presented in this section. This plot enables to draw conclusions about the nature of nucleation and growth kinetics of the bainitic reaction. In fact, the plot does not show straight lines, but a slight decrease in the slope of the curves with increasing time. Thus, the character of the bainite reaction changes over time or is superposed by another reaction such as cementite precipitation. The Avrami exponent  $\eta$  equals the slope of the curve and depends on shape, nucleation, and growth rate. Since nucleation and growth rate are not necessarily constant,  $\eta$  may be time dependent as it obviously is in this case. The higher the manganese content the steeper the slope, thus, according to Equation 5.3 the higher the Avrami exponent  $\eta$  in both the 980 and 1180 grades. A higher Avrami exponent is associated with a higher volume to surface ratio. Therefore, with increasing  $\eta$  the shape of the bainite crystals can change from needle, to plate, to spherical growth. This explains why the bainite morphology slightly changes from more lath-like to rather globular with increasing manganese content (Figure 4.11). The variable  $k$  is the activation energy for nucleation, as seen in Equation 5.2. It can be determined by exponentiating the axis of ordinate,  $\ln k$  in Equations 5.3, where  $\ln t = 0$ . The higher  $\ln k$  the lower the activation energy. The  $\ln k$  is lower for higher manganese contents in both the 980 and the 1180 grade. Thus, the more manganese the more sluggish nucleation. Just as manganese slows down both nucleation and growth, so do the additional carbon and silicon in grade 1180 as compared to grade 980.

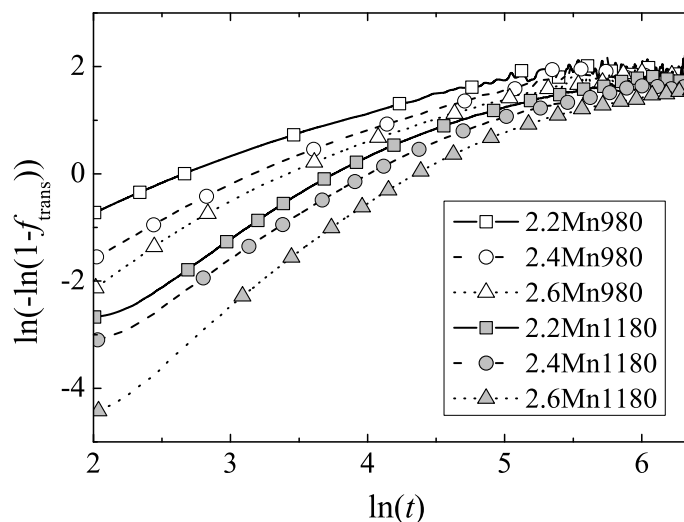


Figure 5.11: Phase transformation kinetics for the manganese variants of both 980 and 1180 grades expressed by the Johnson-Mehl-Avrami-Kolmogorov approach given in Equation 5.3 applied on dilatometer results depicted in Figure 5.9b ( $T_{oa} = 400\text{ }^{\circ}\text{C}$ ).

As mentioned in Section 2.2.3, manganese strongly segregates and thereby causes banding. Figure 5.12 illustrates the extent to which manganese segregates in the present steels, calculated using the Scheil module of Thermo-Calc© TCFE6 [165]. The manganese content in the liquid and the solid phases grow exponentially with the mass fraction of the solid, and the solid phase contains approximately two thirds as much dissolved manganese as the liquid phase during solidification. Thus, manganese strongly segregates with a tendency to remain in the liquid phase. The inhomogeneous manganese distribution results in inhomogeneous size distribution of the retained austenite inclusions. While the retained austenite grains look fine and disperse in the grade 2.2Mn980 and 2.4Mn980, large retained austenite inclusions appear in the grade 2.5Mn980 (Figure 4.8a-c). Manganese segregation is even more detrimental in the 1180 grade, where large retained austenite/martensite islands appear already in the grade with the lowest manganese content of 2.2Mn1180,

and the grade 2.6Mn1180 clearly shows bands of retained austenite/martensite islands (Figure 4.8d and 4.8f). Inhomogeneous manganese distribution does not only impair the desired fine dispersion of the retained austenite grains, however, as demonstrated above, a change in manganese content affects growth kinetics, thus, the morphology of the primarily bainitic matrix (Figure 5.11). Therefore, some regions in the microstructure appear more granular and others more needle-like or plate-like. For instance, in the immediate vicinity of the large retained austenite/martensite islands, the bainite is carbon-depleted and is thus carbide-free.

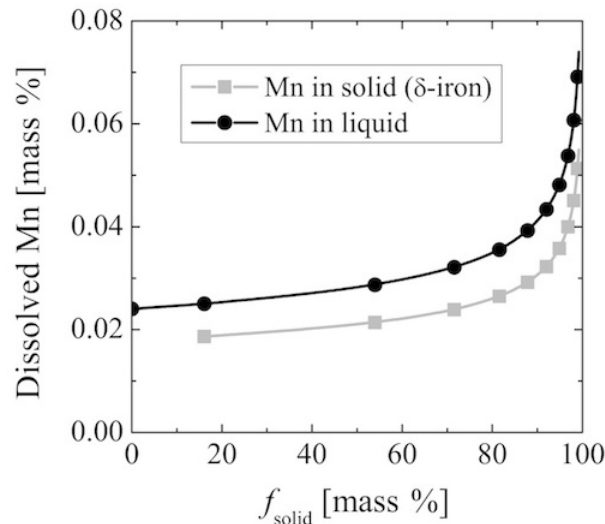


Figure 5.12: Manganese dissolved in liquid and solid phase as a function of mass fraction of solid of the grade 2.4Mn980 according to the Scheil module of Thermo-Calc©.

The mechanical properties resulting from the phase transformation behaviour, the amount of retained austenite and the microstructure will be analyzed in more detail in order to gain further understanding of the influence of manganese on TBF and Q&P steels. As explained in the previous paragraphs of this section, an increase in the amount of retained austenite is usually accompanied by a decrease in yield strength, which is also the case for the 980 grade manganese variants. As the amount of retained austenite and/or martensite fraction increases, yield strength decreases with increasing manganese content in particular for higher overaging temperatures.

Tensile strength increases with increasing manganese content in particular at high overaging temperatures. This is a result of the higher amount of retained austenite and/or fresh martensite. Furthermore, the deceleration of bainite formation could result in a harder bainitic matrix as a result of a shorter tempering time, as discussed above.

Uniform elongation is independent of manganese additions at low overaging temperatures and increase with increasing manganese content for high overaging temperatures in the 980 grade as well as for all overaging temperatures in the 1180 grade (Figure 4.9 and 4.12). The increase in uniform elongation with increasing manganese content correlates very well with the amount of retained austenite. Since this increase is not as pronounced for a low overaging temperature in the 980 grade, it shows no relevant effect in these steels. Further, uniform elongation slightly decreases for prolonged overaging times in both the 980 as well as the 1180 grade for high overaging temperatures, as the amount of retained austenite also slightly decreases most probably due to carbide precipitation as overaging progresses.

Most remarkable about the amount of retained austenite and mechanical properties as a function of overaging temperature is the (parallel) shift of the curves towards lower overaging temperatures (Figure 4.12b). This trend is in excellent agreement with the deceleration of phase transformations,

which results in lower amounts of transformed phase fraction during continuous cooling as well as overaging (Figure 4.10).

It is important to note that the changes in amount of retained austenite and mechanical properties caused by the same amount of manganese additions are much greater in the 1180 grade with the higher carbon and slightly higher silicon content compared to the 980 grade. The drop in yield and tensile strength as well as the increase in the amount of retained austenite and uniform elongation at low overaging temperatures and roughly *vice versa* at high overaging temperatures are much more pronounced in the 1180 grade than in the 980 grade.

Yield ratio and the difference between tensile strength and fracture stress as a function of overaging temperature in the 980 and the 1180 manganese variants are shown in Figures 5.13a and 5.13b, respectively. Similar to yield strength, yield ratio decreases with increasing overaging temperature and slightly increases above  $T_{oa} = 425^\circ\text{C}$ . In a certain overaging temperature range, which includes higher overaging temperatures for the 980 grade compared to the 1180 grade, a significant drop in yield ratio with increasing manganese content is visible (Figure 5.13a). This behaviour can be explained as follows: Both the significant decrease in yield strength as well as the increase in tensile strength with increasing manganese content contribute to significantly lower yield ratio in the mentioned overaging temperature window. Both effects are a result of the austenite stabilizing effect of manganese. As mentioned above, yield strength decreases due to the increasing size and presumably also increasing number of retained austenite islands. If quenched to very low temperatures before overaging, most carbon precipitates and very low amounts of retained austenite are stabilized to room temperature. The less carbon precipitates before overaging, which is the case for increasing overaging temperature, the higher the additional amount of austenite through the austenite stabilizing effect of manganese. Tensile strength primarily increases with increasing amount of martensite due to manganese additions. This is only relevant for overaging temperatures of above  $400^\circ\text{C}$  for the 1180 grade. However, there is a lower limit in yield ratio, which indicates that a further increase in the amount of fresh martensite at the cost of retained austenite and bainite does not result in further decrease in yield strength. This means that the damage mechanism presumably switches from void formation at inclusion/matrix boundaries to decohesion within or between martensitic areas.

The difference between tensile strength and fracture stress  $R_m - R_b$  decreases with increasing overaging temperature in a similar but less pronounced sigmoidal manner compared to yield strength and yield ratio (Figure 5.13b). The decrease slows down, however, the difference between tensile strength and fracture stress does not begin to increase with increasing overaging temperature like yield strength and yield ratio. While the different manganese contents of the 980 grade show very similar values amongst each other, the difference in tensile strength and fracture stress is slightly lower for higher manganese contents in the 1180 grade to the same extent for all investigated overaging temperatures. The key finding of these tendencies is, that the changes in the difference between tensile strength and fracture stress caused by manganese additions are much less pronounced and very similar for different overaging temperatures as compared to the changes in yield ratio due to the addition of manganese. That is, significant changes in the mechanical behaviour of TBF and Q&P steels at strains below uniform elongation, which mainly arise from an increasing amount of retained austenite for increasing manganese content, have a minor effect on the post-uniform strength decrease and fracture strength.

Figure 5.14 shows the engineering stress-strain curves of the 980 and the 1180 grades. The graphs demonstrate the significant TRIP potential of both grades and how the TRIP effect acts in both grades at an overaging temperature of  $400^\circ\text{C}$ . In the 980 grade, engineering stress significantly increases as a result of manganese additions, while uniform and total elongation remain almost unchanged. As mentioned above, manganese reduces the formation of polygonal ferrite, which itself is a softer matrix constituent than bainite. The polygonal ferrite, furthermore, serves as a

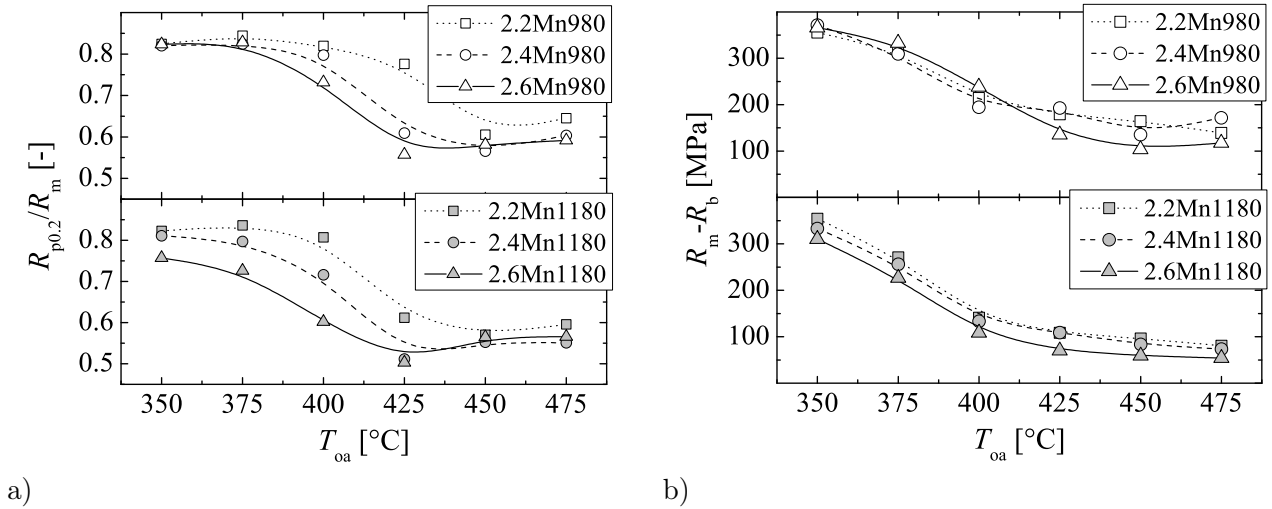


Figure 5.13: a) Yield ratio and b) difference between tensile strength and fracture stress  $R_m - R_b$  as a function of overaging temperature of both 980 and 1180 manganese variants ( $t_{oa} = 600$  s).

nucleation site, presumably causing the more globular bainitic matrix for lower manganese contents. In addition, manganese only slightly increases the amount of retained austenite in the 980 grade, in particular compared to the significantly more pronounced increase in the amount of retained austenite as a consequence of manganese additions to the 1180 grade. Therefore, it can be concluded that the deceleration of diffusional phase transformations results in a significantly higher hardness of the matrix through manganese additions in the 980 grade. In addition to the strength increase, uniform elongation also slightly increases with manganese content, which can be attributed to the slightly higher amount of retained austenite (Figure 4.12b).

Grade 1180, in contrast, shows significant increase in total elongation with increasing manganese content, while tensile strength remains almost at the same level. Since the difference between total and uniform elongation is negligible in this grade, the gain in total elongation can exclusively be attributed to superior pre-uniform strain-hardening behaviour, which significantly promotes uniform elongation. This gain in uniform elongation correlates very well with the significant increase in the amount of retained austenite with increasing manganese content shown in Figure 4.12b. Therefore, it can be concluded that most of the retained austenite transforms until uniform elongation is reached. In addition, the amount of microstructure components and their morphology, in particular bainite morphology, are fairly similar amongst the different manganese variants of the 1180 grade as opposed to the 980 grade. Thus, an increase in the amount of retained austenite does not result in higher tensile strength in the 1180 grade, even though it causes quite a significant increase in uniform elongation.

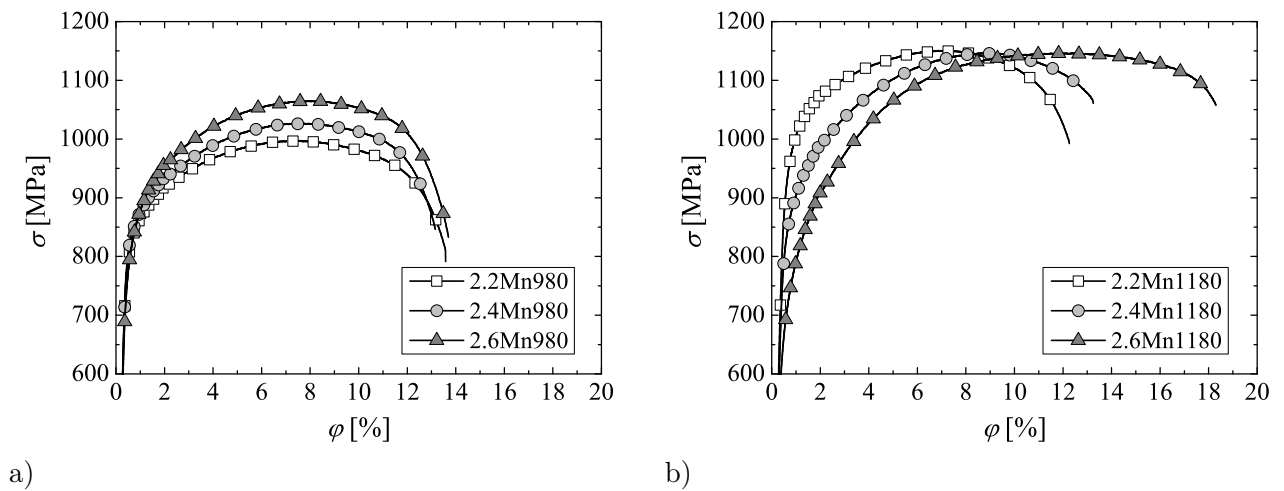


Figure 5.14: Engineering stress-strain curves of a) the 980 and b) the 1180 grade manganese variants for an overaging temperature of 400 °C and an overaging time of 600 s.

### 5.2.3 Chromium

The influence of chromium on phase transformations, microstructures, and mechanical properties shows some similarities to the influence of manganese described in the previous section. Chromium also significantly decelerates all diffusion-controlled phase transformations during continuous cooling and overaging, except for pearlite formation in both the 980 and 1180 grades (Figures 4.13 and 4.16). While the deceleration is similar for different temperatures during continuous cooling, chromium decelerates isothermal phase transformations in a more pronounced manner at higher overaging temperatures, in contrast to manganese, where phase transformations are only slightly slower at higher overaging temperatures. Similar to the manganese variants, the isothermal TTT curve of the 1180 grade is shifted to lower overaging times and lower overaging temperatures as compared to the 980 grade. At an overaging temperature of 600 °C, chromium accelerates the isothermal phase transformation in the 1180 grade, which is an indicator for pearlite formation (Figure 4.16). The observed acceleration at high overaging temperatures and a deceleration as well as a shift to lower temperatures of the isothermal phase transformation through chromium additions for lower overaging temperatures has previously been reported to cause a "bay" between these transformations of different microstructure components such as pearlite and (upper) bainite [92].

Chromium additions result in a significant increase of the size of the retained austenite/martensite islands as a result of austenite stabilization. The effect of chromium additions on the size of the retained austenite/martensite islands is much greater when compared to manganese. Steel 0.01Cr980 comprises small but considerable amounts of polygonal ferrite, as seen in Figure 4.14. The additional chromium suppresses the formation of polygonal ferrite during cooling to overaging temperature mainly in the 980 but also in the 1180 grade (Figure 4.14 and 4.18). Finally, the bainitic matrix is also more globular in the presence of large polygonal ferrite grains, particularly in steel 0.01Cr980 (Figure 4.14a).

In addition to the strong deceleration of continuous and isothermal phase transformations, a significant decrease in the amount of cementite has been observed (Figure 4.18-4.19). These two findings are connected with each other, since the unprecipitated carbon is available for partitioning and the stabilization of the austenite. The isothermal transformation, furthermore, saturates in the event of lower amounts of bainite with higher chromium content.

Since the temperature  $T_0$  is unaffected by chromium variants in the investigated range (Fig-

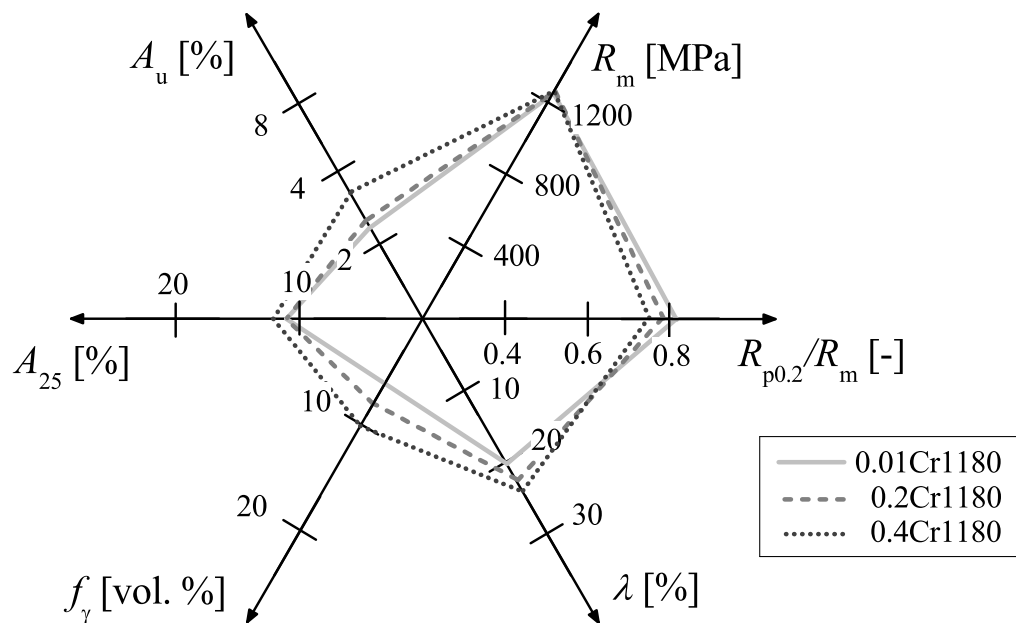
ure 4.17b), the reduced amount of bainite can be explained as follows: The diffusion of substitutional elements in para-equilibrium is negligibly small compared to interstitial elements such as carbon. The difference between the amount of austenite which is stable at room temperature, i.e. retained austenite, and the transformed fraction at overaging temperature transforms to martensite upon final cooling. Chromium promotes the austenite stability in para-equilibrium during overaging. Above a certain threshold in overaging temperature, part of the austenite that is stabilized by chromium additions at overaging temperature, transforms to martensite during the final cooling. The fraction of austenite which transforms to martensite upon final cooling depends on the size, the shape, and the composition of the retained austenite islands, as explained in Section 2.3.2. As a consequence of its austenite stabilizing effect, the addition of chromium results in higher amounts of retained austenite below the mentioned threshold temperature (between  $T_{oa} = 350^\circ\text{C}$  and  $T_{oa} = 425^\circ\text{C}$ ) and reduced amounts of retained austenite above this temperature.

The influence of chromium on mechanical properties correlates very well with its influence on phase transformations, microstructures, and amount of retained austenite. Mechanical properties of the 980 grade and the 1180 grade react differently to chromium additions (Figure 4.15). Yield and tensile strength of the 980 grade both increase with increasing chromium content at low overaging temperatures. This increase in yield and tensile strength as well as the slight decrease in uniform elongation can be explained by the suppression of polygonal ferrite and the change towards a more lath-like matrix. At high overaging temperatures, yield and tensile strength also increase with increasing chromium content in the 980 grade because the harder matrix is comprised of less pre-isothermal transformation product and because of the larger size of the retained austenite/martensite islands. In addition, the increase in the amount of retained austenite results in higher uniform elongation.

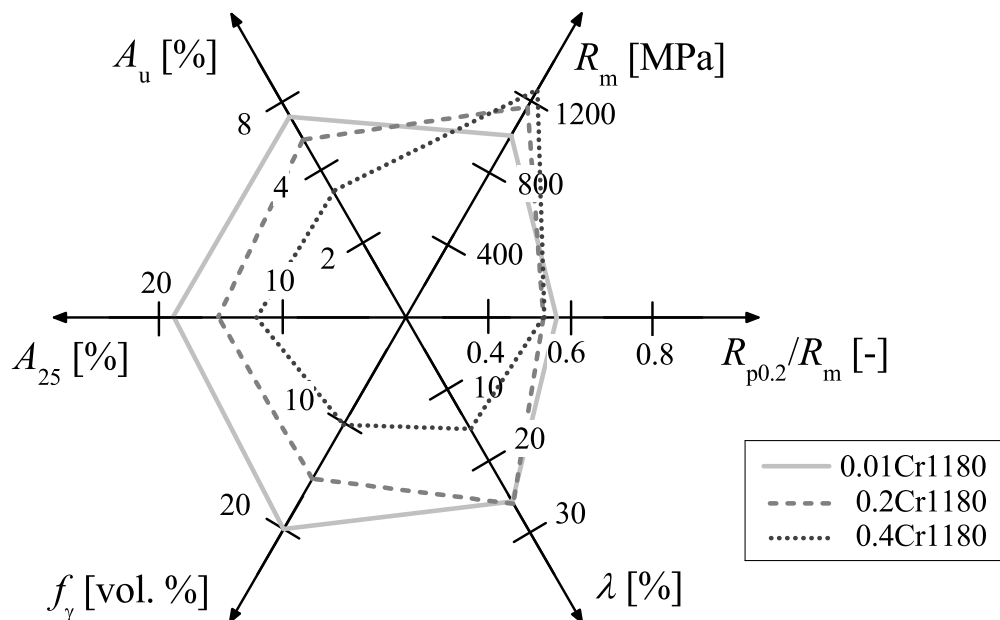
The additional carbon, manganese, and silicon in the 1180 grade result in a higher amount of retained austenite and less pre-isothermal transformation product to begin with. Therefore, the amount of retained austenite increases with increasing chromium content at low overaging temperatures (Figure 4.20). This results in a decrease of yield strength above 180s of overaging as well as an increase in uniform elongation. At high overaging temperatures, the larger size of the retained austenite/martensite islands results in a lower amount of retained austenite for higher chromium contents, similar to manganese additions. Since the much larger martensite fractions cause an increase in yield strength and significantly higher tensile strength, uniform elongation significantly decreases at high overaging temperatures due to chromium additions.

The tendencies of retained austenite and mechanical properties, in particular yield strength, are shifted to lower overaging temperatures by chromium additions to the 1180 grade as observed for phase transformation kinetics (Figure 4.20b). A similar tendency has been observed for the effect of manganese on phase transformations and mechanical properties. However, chromium is more effective in stabilizing the austenite, in particular at high overaging temperatures, which leads to larger areas of fresh martensite formed upon the final cooling. This strongly increases both yield and tensile strength for high overaging temperatures, while uniform elongation is only slightly deteriorated.

To gain further understanding about the effect of chromium additions on edge formability, the mechanical properties and amount of retained austenite discussed above were compared to yield ratio and hole expansion strain, as shown in Figure 5.15. The effect of chromium on yield ratio is negligible, whereas hole expansion is slightly enhanced by higher chromium contents for the low overaging temperature of  $350^\circ\text{C}$ . Interestingly, hole expansion strain does not correlate with yield ratio for neither overaging temperature (Figure 5.15a). This demonstrates that it is crucial to measure hole expansion strain to gain clear insight into edge formability. It is important to note that chromium additions improve uniform and total elongation as well as hole expansion strain at the same time for low overaging temperatures (Figure 5.15a). In contrast, the amount of retained



a)  $T_{oa} = 350^\circ\text{C}$



b)  $T_{oa} = 425^\circ\text{C}$

Figure 5.15: Tensile strength  $R_m$ , yield ratio  $R_{p0.2}/R_m$ , hole expansion strain  $\lambda$ , amount of retained austenite  $f_\gamma$ , uniform elongation  $A_u$ , and total elongation  $A_{25}$  of grades 0.01Cr1180, 0.2Cr1180 and 0.4Cr1180 for overaging temperatures of a)  $T_{oa} = 350^\circ\text{C}$  and b)  $T_{oa} = 425^\circ\text{C}$  ( $t_{oa} = 600\text{ s}$ ).

austenite, uniform and total elongation as well as hole expansion strain are significantly compromised by the addition of chromium at high overaging temperatures (Figure 5.15b). This can be attributed to the significant increase in the fraction of fresh martensite.

## 5.2.4 Niobium

### Niobium in the 980 grade

In terms of their size, the two populations of NbC particles that have been found in the niobium alloyed grades (Table 4.2) indicate two distinct formation situations [173]. The Thermo-Calc© TCFE6 [165] based thermodynamic calculation (Figure 5.16) reveals that NbC particles are not completely dissolved during reheating at 1180 °C in grades 0.045Nb980 and 0.09Nb980. Thus, it can be concluded that the population of large particles in these grades results from precipitates formed during casting which undergo an additional Ostwald ripening during reheating and further processing. This seems to be in contradiction to grade 0.025Nb980, for which a complete dissolution of NbC particles is predicted. However, it is well known that segregation takes place during casting, and conventional thermomechanical processing does not reduce this segregation.

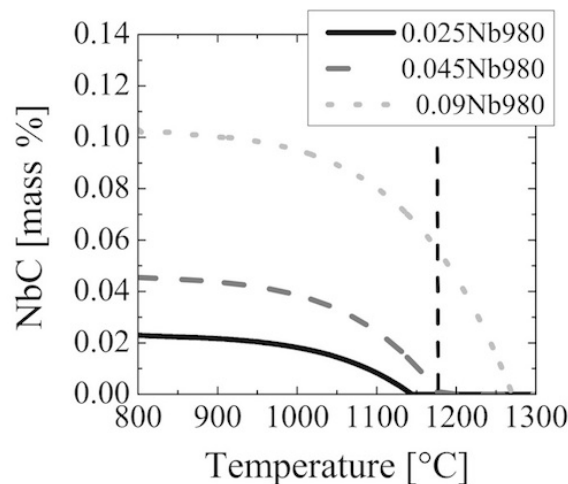


Figure 5.16: Calculated amount of NbC in thermodynamic equilibrium as a function of temperature for the grades 0.025Nb980, 0.045Nb980, and 0.09Nb980 predicted by Thermo-Calc©,  $T_{\text{rh}}$ : reheating temperature prior to hot rolling.

In order to prove segregation as a potential cause for the population of large precipitates in the grade 0.025Nb980, Scheil-Guliver calculations were carried out using the Scheil module of Thermo-Calc© TCFE6 [165] [173]. The mass fraction of niobium in the liquid and solid phase as a function of the mass fraction of solid is shown in Figure 5.17. The niobium content in the liquid and the solid phase grows exponentially with the mass fraction of solid, and the liquid phase contains more than four times as much niobium than the solid phase throughout solidification. Thus, niobium strongly segregates with a tendency to remain in the liquid phase. Segregation is not significantly reduced during reheating, so it must be expected that NbC is not dissolved in the inter-dendritic regions during reheating, even with the high niobium content in grade 0.025Nb980.

The fine particles observed in all grades are a result of precipitation during hot rolling and the slow cooling from the coiling temperature. The almost unchanged fraction of precipitates (Figure 4.25) during the annealing of the cold-rolled material is in agreement with an expected

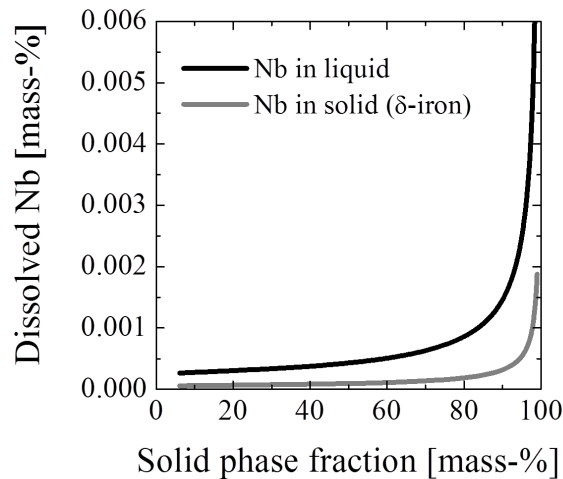


Figure 5.17: Niobium dissolved in the liquid and solid phase as a function of mass fraction of solid of the grade 0.025Nb980 according to the Scheil module of Thermo-Calc© allowing interstitial back-diffusion, i.e. interstitial atoms are allowed to redistribute in the solid phase according to thermodynamic equilibrium [173].

minor Ostwald ripening due to the low niobium content in solid solution and the low diffusivity of niobium at the low annealing temperature and short time interval.

Niobium generally refines the microstructure [173, 182, 183] (Table 4.1). There is no significant further grain refinement for the steel grades containing more than 0.025 mass % Nb. As can be concluded from Table 4.2, the addition of more than 0.025 mass % niobium does not result in the formation of a larger amount of finer precipitates (Table 4.1), which would contribute to a further grain refinement and possible precipitation strengthening. Instead, a further increase in niobium content leads to higher amounts of large precipitates, which do not change the surrounding microstructure.

As a result of grain refinement through niobium, more nucleation sites (preferably triple points of primary austenite grains) are available and lead to the accelerated pro-eutectoid ferrite and upper bainite formation of the niobium grades as opposed to the reference material (Figure 4.26a). This effect has been reported previously for microalloyed DP and conventional TRIP steels by Pichler *et al.* [107]. The quite similar transformation behaviour of niobium variants during cooling (Figure 4.26a) and overaging (Figure 4.26b) is most likely related to their similar prior austenite grain size as opposed to the niobium-free reference material.

Furthermore, the final bainitic matrix mainly comprises globular bainite as opposed to the lath-like bainite of the reference material [173] (Figure 4.22 and 4.23). This finding was confirmed by means of scanning low energy electron microscopy and electron backscatter diffraction [182, 183]. A similar observation for an addition of 0.02-0.05 mass % Nb to a 0.2 % C-1.5 % Si-1.5 % Mn TRIP-assisted bainitic steel was reported by Sugimoto *et al.* [26]. One possible explanation for the observed change in bainite morphology due to niobium addition from lath-like to globular bainite can be attributed to the pre-isothermal transformation products. Formation of ferrite and upper bainite upon cooling to IBT can cause differences in carbon distribution within the remaining austenite grains. This locally increased carbon content may influence both the bainite formation and morphology during the IBT. To clarify the validity of this explanation, counterpart experiments were conducted with the reference material without ferrite and the niobium alloyed material with pro-eutectoid ferrite. For this purpose, the reference material was cooled to overaging temperature

with a cooling rate of 30 K/s, forcing the formation of ferrite, and the niobium alloyed grade was quenched to overaging temperature with a cooling rate of 80 K/s, preventing ferrite formation. The bainite and retained austenite morphology are the same, regardless of ferrite formation. Therefore, the change in bainite and retained austenite morphology is a consequence of grain refinement, NbC precipitation or niobium in solid solution. In a work reported by Bleck *et al.* [168], it is argued that NbC preferably precipitates at the austenite grain boundaries, which influences the nucleation kinetics of bainite formation. In turn, bainite morphology can be affected by the change in nucleation kinetics.

The influence of niobium addition on bainite formation is accompanied by a markedly reduced cementite formation. This in turn results in a remarkably increased retained austenite fraction (Figure 4.27). The exact reason for these morphology changes and the decrease in the amount of precipitated cementite triggered by niobium addition remains unclear at present and requires further investigation.

The tensile strength of multiphase steel grades can be estimated by applying the rule of mixture given in Equation 2.9. Based on this relationship, the decreasing tensile strength with increasing overaging time (Figure 4.28) can be explained by the increasing fraction of bainite and the decreasing amount of martensite formed during final cooling to room temperature. Furthermore, the almost constant values for the tensile strength for overaging times larger than 200 s are in excellent agreement with the dilatometer measurements (Figure 4.26b), which show that the bainite formation saturates. The same argument holds true for the decreasing yield strength at short overaging times. For longer overaging times, a distinctive increase of the yield strength is observed. This behaviour is typical for conventional TRIP steel grades [184] and can be explained as follows: In particular for DP steel grades with hard martensite as an inclusion in a soft ferritic matrix, a low yield ratio as a result of high local stress at ferrite/martensite phase boundaries is well known. For the material in the present investigation, short overaging times result in a considerable amount of martensite formed during final cooling and therefore the observation of low yield strength is reasonable. Increasing overaging time increases the stability of the austenite and decreases the amount of martensite formed during final cooling. This in turn decreases the impact of the local stresses and therefore an increase in yield strength is observed. Moreover, an increase in the amount of bainite during overaging also contributes to the increase in yield strength.

The addition of niobium and the subsequent NbC precipitation are well known for enhancing the tensile strength resulting from precipitation strengthening and grain refinement [87, 106, 107, 168–170]. This is in apparent contradiction to the present results which clearly show a decrease in strength resulting from the addition of niobium (Figure 4.28a). For the present material, an increase in strength resulting from precipitation hardening and a lower grain size is also expected. However, the replacement of harder fine lath-like bainite by softer pro-eutectoid ferrite/upper bainite and the more globular bainitic matrix as a consequence of the niobium addition result in a decrease of strength.

Prolonged overaging times lead to an increase in the bainite fraction and therefore to enhanced carbon partitioning and austenite stabilization (Figure 4.27a). However, in particular at temperatures of 450 °C and higher, carbon intended for partitioning begins to precipitate after certain overaging times, thus resulting in a strong decrease in the amount of retained austenite. In this case, time and temperature are interchangeable, which results in accelerated partitioning and precipitation at higher temperatures (Figure 4.30). The increase in uniform and total elongation with prolonged overaging times (Figure 4.28b) can likewise be attributed to the stabilization of retained austenite due to carbon enrichment as the bainite transformation proceeds. The reduced strain-induced martensite formation at low strain levels results equivalently to conventional TRIP steels in an increasing work hardening at high strain levels (Figure 4.29) and thereby in increasing elongation values (Figure 4.28b).

The elongation of the Nb-TBF steels is significantly improved compared to the reference material as a result of a higher amount of retained austenite with the same stability behaviour [173] (Figure 4.27). This makes more sources available for the overall TRIP effect in the case of niobium microalloyed steels. In addition, the soft phase transformation product from cooling to overaging most likely contributes to enhanced elongations. The similarity of the stability behaviour of the retained austenite indicated by the almost parallel graphs is in good agreement with the XRD measurements revealing approximately identical lattice constants and thus carbon content of the retained austenite for the reference material and the niobium containing grades (Section 4.1.7).

As the overaging temperature decreases, strength increases and elongations decrease (Figure 4.30) as expected based on lath thickness decrease and microstructure change from a globular to a lath-like bainite or even tempered martensite.

The yield ratio shown in Figure 4.30 reveals two distinct regions with low values above 450 °C and high values below 425 °C. When their large scatter is disregarded, the hole expansion strains decrease more or less linearly with overaging temperature as shown in Figure 4.31. It is reasonable to study the relationship between yield ratio and hole expansion strain multiplied by tensile strength as given in Figure 5.18 for the different overaging temperatures. In general, the product of tensile strength and hole expansion strain increases almost linearly with increasing yield ratio as well as with decreasing overaging temperature within a deviation range of 5000 MPa%. However, the data density is high for the lower and the upper ends of the yield ratio range, suggesting stagnation of the yield ratio once the range of 0.6 to 0.8 is exceeded on either side. When overaging temperatures of 400 °C and below are considered, the yield ratio is in the range of 0.8 to 0.85, whereas an improvement in hole expansion strains can be achieved with lower overaging temperatures.

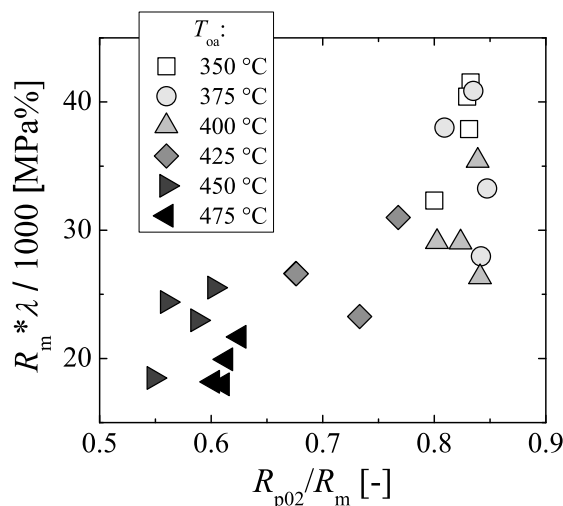


Figure 5.18: Tensile strength  $R_m$  times hole expansion strain  $\lambda$  as a function of the yield ratio for all investigated niobium variants of the 980 grade. Overaging temperatures range from 350-475 °C and overaging time is set to 600 s [173].

Finally, the hole expansion strains of the niobium variants are at the same level as those of the reference material (Figure 4.31). The fact that edge formability is unaffected by the impressive influence of niobium on mechanical properties is a key finding of the present work and provides valuable information for further development of high-strength high-ductility sheet steels.

### Niobium in the 1180 grade

In contrast to the 980 grade, the response of the 1180 grade to niobium additions is in good agreement with literature [87, 100, 106, 107, 168–170]. The tensile strength of the 980 grade decreases when soft phases such as ferrite and (upper) bainite are introduced because the grain refinement caused by niobium additions leads to significant acceleration during continuous cooling to the overaging step (Figure 4.26a). The additional carbon, manganese, and silicon in the 1180 grade, on the other hand, suffice to prevent this transformation acceleration (Figure 4.32a), so that the addition of niobium to the 1180 grade base composition does not result in the formation of pro-eutectoid ferrite and (upper) bainite during cooling as opposed to the 980 grade. Therefore, the microstructures of the niobium variants as well as the reference material of the 1180 grade is composed of isothermal transformation product, i.e. bainite, and retained austenite (Figure 4.33). This results in higher tensile strength of the niobium variants compared to the niobium-free reference material of the 1180 grade. Since the niobium grain refinement results in a more globular microstructure, irrespective of the base composition, the drop in tensile strength in the 980 grade caused by niobium additions must be related to the introduction of the softer phases during cooling to overaging temperature.

Within a range of 0.02-0.09 mass % niobium, the exact amount of niobium plays a minor role in both the 980 and 1180 grade when compared to the presence of niobium as part of the composition in the first place. When the mechanical properties and the amount of retained austenite of the 1180 grade are compared at different overaging temperatures (Figure 4.34b), the yield strength and uniform elongation of the niobium variants and the reference material show similar behaviour for most overaging time and temperature combinations, whereas the tensile strength of all niobium variants persistently lies above the tensile strength of the reference material. Thus, the influence of niobium additions on mechanical properties is independent of overaging temperature.

Consequently, the 1180 grade benefits from a significant increase in tensile strength caused by precipitation strengthening and grain refinement and without changing other properties of the steel. The product of tensile strength and total elongation as a function of yield ratio as given in Figure 5.19 assesses the steels potential with respect to strength, elongations, and yielding. At low overaging temperatures the product of tensile strength and total elongation of the 1180 grade is particularly sensitive to niobium additions. It decreases, while the yield ratio increases with increasing niobium content. It is important to note, that on average the yield ratio decreases with an increase in the product of tensile strength and total elongation. At 475 °C the yield ratio is drastically impaired by the addition of niobium for comparable values of tensile strength multiplied by total elongation. Overaging temperatures in this range, however, are not considered for industrial production because very low hole expansion values arising from a large fraction of fresh martensite in the microstructure are expected, as the low yield ratios suggest. The fact that an increase in the product of tensile strength multiplied by total elongation correlates with a decrease in yield ratio demonstrates that a material with higher combinations of strength and elongations has to be carefully evaluated, especially if a yield strength requirement has to be met. This finding is most likely a result of additional inhomogeneities in the hardness of the microstructure components of the matrix presumably introduced by changes in the amount of retained austenite. In addition, hole expansion strain can be negatively affected by a lower yield strength for the same tensile strength level. While higher amounts of retained austenite can increase the product of tensile strength and total elongation, they introduce greater hardness differences between the softer untransformed retained austenite and the harder bainitic and/or martensitic matrix. This can decrease yield strength and hole expansion strain.

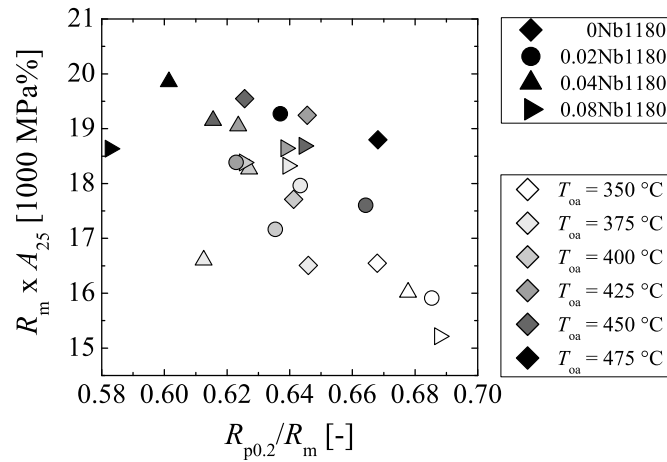


Figure 5.19: Product of tensile strength and total elongation as a function of yield ratio for various overaging temperatures and all investigated niobium variants of the 1180 grade.

## 5.3 Influence of annealing cycle on TBF and Q&P sheet steel

### 5.3.1 Quenching

#### Quench temperature

The influence of the two-step Q&P cycle on microstructure and mechanical properties as presented in this work provides insight into transformation and partitioning conditions. The evaluation of mechanical properties as a function of time at quench temperature and quench temperature itself is crucial to the industrial realization of the highly ductile advanced high-strength sheet steel grades with a minimum tensile strength of 980 and 1180 MPa. As mentioned in Section 4.2, previous research was focused on the influence of quench temperature on the amount of retained austenite [15, 16, 41, 185, 186]. Since the present contribution is driven by the interest in the industrial realization of the mentioned steel grades, emphasis is placed on edge formability, which is of importance for the forming process and may possibly also influence crash performance.

Tensile and in particular yield strength decrease, whereas the amount of retained austenite and elongations increase with increasing quench temperature (Figure 4.36). This behaviour has been reported in previous publications [187]. The hole expansion strain decreases strongly with increasing quench temperature. The sensitivity of the hole expansion strain toward changes in quench temperature is significantly higher in steel IN0.9Si1180 compared to grade IN980. The significant decrease in hole expansion strain of steel IN0.9Si1180 compared to the much slighter decrease with increasing quench temperature observed for grade IN980 occurs despite the higher overaging temperature of  $T_{oa} = 450$  °C for steel IN980 versus  $T_{oa} = 400$  °C for steel IN0.9Si1180.

Lower undercooling, i.e. lower thermodynamic driving force, results in slower transformation and a lower critical carbon content  $c_0$  causes the bainite transformation to stop at lower amounts of bainite. Therefore, higher overaging temperatures are usually associated with higher amounts of austenite prior to the final quenching. Therefore, it might seem unexpected that steel IN0.9Si1180 shows a stronger increase in size of the retained austenite/martensite islands. However, the additional carbon and manganese in steel IN0.9Si1180 thermodynamically stabilize the retained austenite and result in lower driving forces for the isothermal transformation, as both carbon and manganese lower the  $A_3$  temperature as well as  $M_s$ .

Since the retained austenite/martensite islands are larger in steel IN0.9Si1180 and the amount of retained austenite is approximately the same in both steel grades, steel IN0.9Si1180 comprises a higher amount of fresh martensite as opposed to grade IN980. The higher strength level of the matrix of steel IN0.9Si1180 compared to grade IN980 is expected to decrease the hardness difference between matrix and inclusions. Nonetheless, the additional fresh martensite might be the cause of the deteriorated hole expansion properties for higher quench temperatures in grade IN0.9Si1180, since it can promote decohesion between inclusions and matrix.

In contrast to the significant changes in hole expansion strain in particular of steel IN0.9Si1180, tensile strength and elongations show very low sensitivity to quench temperature variations in the range of  $T_q = 280^\circ\text{C}$  to  $T_q = 340^\circ\text{C}$ . This behaviour is in good agreement with the similar matrix of the microstructures for the different quench temperatures (Figure 4.35). A possible reason for the low differences in tensile strength and elongations is the enhanced tempering resistance as a result of the chromium additions of 0.3 mass % is present in both steel grades.

The extraordinarily high hole expansion strain of steel IN0.9Si1180 for a quench temperature of  $T_q = 280^\circ\text{C}$  is in good agreement with the strain-hardening behaviour of CP steel, when compared to a quench temperature of  $T_q = 340^\circ\text{C}$  and grade IN980 at both quench temperatures (Figure 4.36, 4.37, and 4.38). The high yield strength, the low strain-hardening rates in particular at higher strains, and a low plateau of the differential  $n$ -value for the quench temperature of  $T_q = 280^\circ\text{C}$  is characteristic for a CP-type strain-hardening behaviour. The microstructure of this grade is comprised of small round finely dispersed retained austenite islands embedded in a network of particularly fine and short laths (Figure 4.35d). Contrastingly, the DP-like strain-hardening behaviour of steel IN0.9Si1180 at a quench temperature of  $T_q = 340^\circ\text{C}$  and grade IN980 at quench temperatures of  $T_q = 280^\circ\text{C}$  and  $T_q = 340^\circ\text{C}$  is characterized by higher strain-hardening rates at higher strains, lower initial strain-hardening rates, and in particular high differential  $n$ -values at higher strains.

The difference between fracture strength and tensile strength correlates with the degree of necking and provides a rough estimate of a sheet steel's toughness. In principle, the greater the drop in strength from tensile to fracture strength, the higher the degree of necking and the greater the resistance against microcrack propagation. Steel IN0.9Si1180 and in particular steel IN980 both exhibit a higher difference between tensile strength and fracture strength for the lower quench temperature of  $T_q = 280^\circ\text{C}$  compared to the higher quench temperature of  $T_q = 340^\circ\text{C}$  (Figure 4.37). The lower quench temperature is expected to promote resistance against microcrack propagation in both steels.

### Time at quench temperature

A slight increase in tensile strength, a significant increase in yield strength as well as hole expansion strain with increasing time at quench temperature was observed in steel IN980 (Figure 4.40). The lower the quench temperature, the higher the amount of transformed fraction during quenching. If quenched at a rate above the critical cooling rate, only martensite forms before the quench temperature is reached. This martensite can serve as a nucleation site for bainite formation at quench and overaging temperature. A higher amount of transformed fraction during quenching also results in less fresh martensite formation during the final cooling.

As time at quench temperature proceeds, bainite transformation progresses and more carbon precipitates within and between the bainite laths in the form of finely dispersed cementite particles (Figure 4.39). Interstitial carbon increases the strength of the matrix through enhanced distortion of the bainitic or martensitic matrix. Therefore, the loss in solid solution strengthening through the reduced amount of interstitial carbon as a consequence of annealing should result in lower yield and tensile strength. In addition, finely dispersed precipitates contribute to precipitation strengthening.

The combination of reduced internal strains and enhanced precipitation strengthening potentially result in higher yield strength and hole expansion strain.

However, the most important effect on tensile and in particular on yield strength is expected to arise from the lower amount and smaller size of fresh martensite as well as retained austenite/martensite islands. A decrease in the amount and size of retained austenite and/or martensite islands results in reduced local stress concentration and postponed decohesion between the retained austenite/(martensite) inclusions and the surrounding matrix promoting yield strength and hole expansion strain.

Figure 5.20 illustrates the significant increase in the product of tensile strength and hole expansion strain with only a minor loss in uniform elongation with increasing time at quench temperature. To lower the strength of this grade originally designed for a tensile strength of 980 MPa and to enhance deep drawability, it would be useful to install a reheating booster that directly follows rapid jet cooling.

On the other hand, the results clearly indicate that prolonged quenching is highly beneficial to edge formability (Figure 4.40a). Therefore, reducing the strength level by other means, for instance by less alloying or the introduction of small amounts of polygonal ferrite or softer bainite types such as upper bainite, carbide-free bainite or granular bainite, and at the same time prolonging the time at quench temperature to benefit from superior edge formability, is an idea worth considering for the future development of this grade.

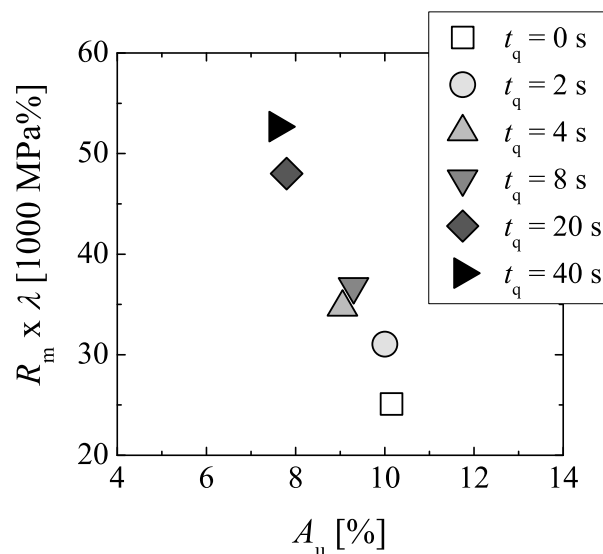


Figure 5.20: Product of tensile strength and hole expansion strain as a function of uniform elongation of two-step Q&P heat-treated sheet steel IN980 for selected times at quench temperature ( $T_q = 350^\circ\text{C}$ ,  $T_{oa} = 450^\circ\text{C}$ ,  $t_{oa} = 300\text{ s}$ ).

### 5.3.2 Impact of polygonal ferrite

The influence of polygonal ferrite is highly relevant both from a scientific standpoint and for industrial realization of the sheet steel production. As described in Section 4.2.3, the main differences in terms of microstructure and mechanical properties between classical TRIP steels with polygonal ferritic matrix and TRIP-assisted bainitic ferritic steels are well-known [13, 188, 189]. Despite

its importance, the influence of small amounts of polygonal ferrite in the microstructure has not been documented in the literature to date. The results of this section help to estimate how deviations from the annealing cycle such as changes in cooling rate or annealing temperature affect the performance of the sheet steel.

The results presented in Section 4.2.3 suggest that the effect of polygonal ferrite depends on the specific shape and location of the ferrite. A key conclusion of the present investigation, therefore, is that the influence of polygonal ferrite on hole expansion strain depends on the way the ferrite is produced. If polygonal ferrite is induced via an additional intermediate holding step, small holding times will result in the formation of small amounts of polygonal ferrite and a considerable drop in hole expansion strain, e.g. 10 % of polygonal ferrite are accompanied by a relative drop in hole expansion strain of 20 % (Figure 4.41 and 4.42).

Higher intermediate holding temperatures are even more detrimental to hole expansion strain. This is most probably due to the fact that the higher intermediate holding temperature of 625 °C results in faster diffusion, in particular carbon diffusion, outranging the lower thermodynamic driving force compared to lower overaging temperatures. However, since not much more polygonal ferrite appears in the microstructures of  $T_f = 625$  °C compared to  $T_f = 575$  °C, the reason for higher hole expansion strain at the lower holding temperature is most likely related to the fact that the hardness difference between the ferrite formed at lower holding temperatures and the rest of the microstructure is lower as compared to higher overaging temperatures.

In contrast to intermediate holding, small amounts of ferrite induced by means of intercritical annealing do not result in reduced hole expansion strains (Figure 4.43 and 4.44). Down to an annealing temperature of  $T_{an} = 810$  °C, which is clearly below austenitizing temperature  $A_3$ , yield and tensile strength decrease with annealing temperature to the same extent, so that hole expansion strain remains unaffected, even though considerable amounts of polygonal ferrite are clearly present (Figure 4.43d and 4.43e). This is an important finding, since it is now possible to lower the annealing temperature even slightly below  $A_3$  without compromising edge crack resistance. It even enables to lower the tensile strength and increase elongations, thereby enhancing formability, whilst maintaining highly favourable edge formability. This is particularly valuable for the 980 grade, as it shows rather high tensile strength. In addition, production economy benefits from lower annealing temperatures, contributing to higher cost efficiency.

Below  $T_{an} = 810$  °C the hole expansion strongly decreases in a sigmoidal manner with decreasing annealing temperature just like it does with increasing intermediate holding time. The onset of decreasing hole expansion strain might be related to the formation of polygonal ferritic bands, presumably in combination with larger retained austenite/martensite islands embedded in large regions of pure polygonal ferrite. Carbide banding is already present at higher annealing temperatures such as  $T_{an} = 820$  °C and  $T_{an} = 810$  °C and also slightly in the fully austenitized reference material of  $T_{an} = 900$  °C. However, the mixture of the polygonal ferritic and the bainitic matrix is fairly homogeneous until polygonal ferrite bands form at an annealing temperature of 800 °C and below. These ferrite bands also contain larger retained austenite/martensite islands than the (bainitic) ferritic matrix of higher annealing temperatures.

## 5.4 Failure mechanisms

Figure 4.45 suggests that the void density up to uniform elongation is negligible compared to the void density found in the post-uniform strained sample area. Based on the approach of geometrically necessary dislocations, the local stress on a particle interface increases with the square root of decreasing particle radius (Equation 2.23). Hence, the required applied strain for void nucleation is higher for particles with larger particle radius. However, Figure 4.45 shows that void nucleation in

all investigated steels occurs at approximately the same thickness strain of around 25%. Thus, the effect of changes in the particle radius described by Equation 2.23 is negligible. Void formation in this steel can be described more precisely by the approach of continuum mechanics formulated by Argon *et al.*, since in their model the maximum stress at the inclusion/matrix interface is independent of the particle radius [128, 145, 190, 191]. A possible explanation of the radius independent nucleation behaviour is the equivalent nucleation of voids in all investigated steels due to impurity inclusions such as oxides. Large and/or brittle inclusions can break during cold rolling or exhibit very low or no adhesion forces between particle and matrix.

Subsequent to the observed simultaneous initial void nucleation, the void densities are significantly higher for steels that were held at higher overaging temperatures. This is in good agreement with the expected enhanced void nucleation in the steels with more pronounced hardness difference between matrix and inclusions.

Equation 2.27 suggests that the void radius increases exponentially with applied strain. Figure 4.46 shows, however, that the average equivalent circle diameter increases approximately linearly with increasing strain. In addition, the void sizes of the various steels are very similar. These observations can both be attributed to the diverging void populations within the different steels. The higher void nucleation rate of the steels held at higher overaging temperatures appear to balance out the larger size of the initial voids. Maire *et al.* observed quasi-stagnation of the average equivalent cavity diameter in DP steels and developed a model which accounts for this behaviour [192]. The quasi-stagnation of the average equivalent cavity diameter in DP steels was shown to be due to the competition between the growth of existing cavities and the nucleation of smaller new ones [192].

The pronounced difference in void density versus the similar average void sizes confirms that void nucleation is strongly dependent on the microstructure, while the character of void growth within different microstructures is very similar with respect to growth velocity. The fact that the void density increases exponentially with decreasing distance to the fracture surface or increasing applied strain (Figure 4.45), furthermore, results in an exponentially increasing volume fraction of voids with applied strain. Thus, given the critical condition for void coalescence of Equation 2.28, the factor of the mean stress for the initiation of internal necking decays exponentially with linearly increasing applied stress.

The observation of the fracture surface of tensile tested samples confirms the results of the quantitative void formation (Figure 4.48). When the fracture surface of the tensile tested steels is compared with different base composition exposed to the same heat treatment, the dimples of the 1180 grade with 0.2 mass % carbon and 0.8 mass % silicon are more distorted and flatter than those of the 980 grade with 0.17 mass % carbon and 0.7 mass % silicon. This indicates that higher local stresses and in particular higher shear stresses were present before void coalescence in the 1180 grade with the higher carbon content compared to the 980 grade. This is in good agreement with the greater strain-hardening potential of the 1180 grade indicated by the significantly higher difference between yield and tensile strength resulting in higher tensile strength as well as elongation.

Steel 2.6Mn1180, held at a lower overaging temperature of 400 °C, clearly shows a high amount of dimples and only one population of the dimple sizes in the form of a log-normal distribution (Figure 4.48). In contrast, the lower overaging temperature of 350 °C results in numerous particularly small dimples arising from voids formed at low tensile strains and a second population of very large dimples originating from voids formed at the early stages of the plastic deformation process. Thus, it can be concluded that the nucleation of the first voids, which grow to large dimples on the fracture surface, occurs at a similar strain level. Therefore, the first voids form most likely independently of the microstructure as a result of brittle impurity inclusions such as oxides. The second population of dimples of the steel that was held at the lower overaging temperature of 350 °C exhibits a smaller size compared to the average dimple size of the steel held at 400 °C. Assuming a similar void growth rate in both steels, this indicates that the nucleation of the smaller voids occurred at higher strains.

Thus, the nucleation of voids as a result of the microstructure is postponed in the steel with a matrix of higher strength and therefore lower hardness difference between matrix and inclusion.

## 5.5 Industrial trials on 1180 MPa Q&P sheet steel

The microstructure of steel IN1.5Si1180 comprises significant amounts of polygonal ferrite (Section 4.4). As seen in Figure 4.50, for a cooling rate of 30 K/s no transformation takes place prior to  $M_s$  in IN1.5Si1180, if the steel was fully austenitized at 900 °C (Figure 4.50b). The actual cooling rate used for the industrial trials was even faster than that, i.e. 40 K/s. In addition, the  $A_{c3}$  temperature of IN1.5Si1180 is even greater than 900 °C for the investigated heating rate of 25 K/s (Figure 4.50a). Therefore, it can be concluded that the applied annealing temperature of  $T_{an} = 850$  °C results in intercritical annealing rather than full austenitization for IN1.5Si1180 as opposed to IN0.9Si1180. Thus, the polygonal ferrite found in IN1.5Si1180 is predominantly a result of intercritical annealing. In addition, the intercritically formed polygonal ferrite may serve as nucleation site for the formation of pro-eutectoid ferrite during cooling between annealing and overaging temperature. Therefore, the presence of small amounts of pro-eutectoid ferrite in IN1.5Si1180 is also possible.

Transformation kinetics during overaging shown in Figure 4.51 suggests that the indirect austenite stabilizing effect through the prevention of carbon precipitation by additional silicon in IN1.5Si1180 is more pronounced than the austenite stabilization through the higher chromium content of IN0.9Si1180. This is especially interesting when considering the deceleration of isothermal phase transformations by chromium additions, which leads to a lower final amount of isothermal transformation product in particular for higher overaging temperatures, as demonstrated in Figure 4.13 and 4.16.

In the investigated range of process parameters, i.e.  $T_{an} = 850$  °C,  $T_{oa} = 380$  °C, and  $t_{oa} \approx 460$  s, IN1.5Si1180 appears slightly more DP-like due to its higher total elongation compared to IN0.9Si1180 (Figure 4.52, Figure 4.53, and Figure 5.21). It is, therefore, the preferable grade for applications requiring high deep drawability. Interestingly, the advantage of 1% total elongation of IN0.9Si1180 in combination with hardly any difference in uniform elongation at the top end compared to IN1.5Si1180 indicates that post-uniform deformation of IN0.9Si1180 is superior to that of IN1.5Si1180 (Figure 4.52). The enhanced elongations are, on one hand, most probably a consequence of the strong austenite stabilizing effect of the high silicon in IN1.5Si1180 (Figure 4.51). On the other hand, the polygonal ferrite found in the this grade (Figure 4.49) presumably largely contributes to a softening of the matrix. It appears small enough and well embedded in the bainitic/(tempered) martensitic surrounding microstructure to circumvent negative impact on edge crack resistance. This is in good agreement with the positive effects of small amounts of ferrite on the product of tensile strength and elongation in combination with little loss in hole expansion strain, in particular if they arise from intercritical annealing, as described in Section 4.2.3.

By contrast, higher hole expansion strains of well above 50% are achieved with IN0.9Si1180 than with IN1.5Si1180, indicating improved edge formability preferable for car components with high forming radii and enhanced crash performance. The fact that, for an overaging temperature of  $T_{oa} = 380$  °C the decrease in hole expansion strain with increasing total elongation is not very pronounced, is evidence for highly favourable combinations of deep drawability and edge crack resistance of IN0.9Si1180. However, Figure 4.52 suggests that IN1.5Si1180 may possibly enable the same or even higher hole expansion strains if lower quench temperatures were applied.

Figure 5.21 shows hole expansion strain as a function of total elongation, each multiplied by tensile strength. This figure clearly illustrates that the high hole expansion strains of IN0.9Si1180 are accompanied by high tensile strength levels, which exceed the requirement of 1180 MPa by 50 to 100 MPa (Figure 4.53). It could be interesting for future developments to reduce the strength

of the steel with the aim of improving elongations without affecting the highly advanced hole expansion values. This could be achieved either by alloying, for instance through slight reductions in strengthening elements, such as carbon or chromium. To avoid undesirable side effects of changes in composition, alternatively the annealing temperature could be lowered to decrease the strength level and promote elongations by provoking small polygonal ferrite islands (see Section 4.2.4).

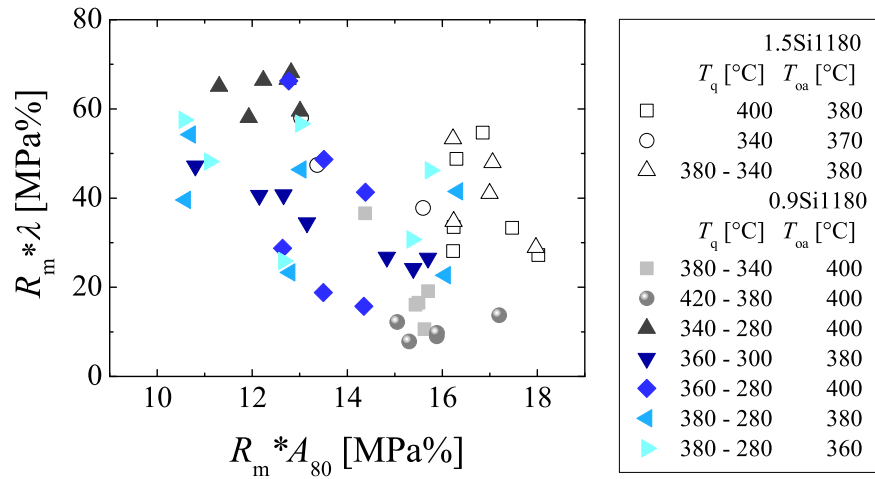


Figure 5.21: Product of tensile strength and hole expansion strain as a function of the product of tensile strength and total elongation  $A_{80}$  of several industrially produced two-step Q&P heat-treated sheet steels of composition IN1.5Si1180 and IN0.9Si1180 for various annealing cycles ( $T_{an} = 850$  °C).



## Chapter 6

# Summary

In the present work, TBF and Q&P steels designed for a tensile strength above 980 and 1180 MPa were investigated. The influence of silicon, manganese, chromium, and niobium on phase transformations, microstructure and mechanical properties of these two types of third-generation advanced high-strength steels was studied in detail. The reaction of TBF, one-step Q&P, and two-step Q&P steels to variations in heat treatment was tested regarding annealing, quenching, and overaging. A newly designed 1180 grade with reduced silicon content and its predecessor were produced on the industrial production line. The following summarizes the results and conclusions gained by the conducted investigations on TBF and Q&P sheet steel.

Silicon suppresses carbide formation, promotes the amount of retained austenite, and increases the elongation. Due to the higher carbon content and the significantly higher chromium content, these changes in silicon content are much less pronounced in the 1180 grade than in the 980 grade. A loss in yield and tensile strength with increasing silicon content is observed in the 980 grade and is caused by an acceleration of ferrite and bainite formation upon cooling to overaging temperature.

An analysis of transformation kinetics during overaging applying the Johnson-Mehl-Avrami-Kolmogorov approach revealed a deceleration of nucleation and growth of isothermal phase transformation products as a consequence of manganese additions. The bainite morphology changes from lath-like to slightly more globular as a result of the decelerated bainite formation. In particular, the deceleration of transformation kinetics and the thermodynamic stabilization of austenite by manganese additions increase amount of retained austenite and elongation at low overaging temperatures, while they increase fresh martensite fraction and tensile strength at high overaging temperatures.

According to Thermo-Calc© calculations, chromium increases the  $A_1$  temperature, while at the same time slightly decreasing the  $A_3$  temperature. Thus, the temperature window in which both ferrite and austenite are present in equilibrium is smaller for higher chromium contents. Chromium significantly shifts the isothermal phase transformation to longer holding times resulting in larger-sized and higher amounts of retained austenite/(tempered) martensite islands. As a consequence, edge crack resistance is significantly reduced at high overaging temperatures. However, chromium contributes to a reduction of carbide precipitation and promotes tempering resistance. As a consequence of the harder matrix, edge formability can be promoted by chromium additions at low overaging temperatures.

The addition of niobium results in considerable grain refinement. The much smaller grain size accelerates diffusion-controlled phase transformations, which leads to the formation of pre-isothermal transformation products in the 980 grade. The soft microstructure components significantly reduce strength and increase elongation. The niobium variants, furthermore, show higher amounts of retained austenite. The strongly reduced amount of cementite that is found in the bainite of the

niobium variants results in more carbon available for the stabilization of retained austenite. This leads to higher amounts of retained austenite with the same carbon content in the niobium-bearing alloys as compared to the reference material, resulting in significantly improved uniform and total elongation. A significant change in bainite morphology from lath-like to globular induced by the addition of niobium was observed. TEM analysis revealed that higher niobium contents only increase the size of the niobium carbides, while the number of carbides remains similar. Therefore, grain size, microstructure, bainite morphology and mechanical properties remain consistent through different niobium concentrations. As opposed to the 980 grade, strength increases with increasing niobium content in the 1180 grade as a result of both grain refinement, as described by the Hall-Petch relation, as well as precipitation hardening arising from the niobium additions. This is because, in contrast to the 980 grade, the higher carbon and manganese content of the 1180 grade suppress the formation of soft phases upon cooling to overaging temperature.

In annealing cycle trials at quench temperatures well below  $M_s$  temperature, low sensitivity of elongation and tensile strength to variations in quench temperature was found in industrially produced 980 and 1180 sheet steel. On the other hand, significantly higher hole expansion strains can be achieved with lower quench temperatures in particular for high overaging temperatures. Most probably the higher martensite fraction for a lower quench temperature helps to prevent large-sized retained austenite/(tempered) martensite islands.

Prolonged holding at quench temperature of two-step Q&P sheet steel results in enhanced precipitation of interstitial carbon, which decreases internal strains. Furthermore, higher amounts of bainite form at quench temperature and the austenite is enriched with carbon in case of longer times of quench temperature. This leads to reduced amounts of fresh martensite formed during the final cooling. The present work shows that longer times at quench temperature significantly increase yield strength, tensile strength, and in particular the hole expansion strain of Q&P steel with minor losses in amount of retained austenite and elongation. These observations on mechanical properties are in agreement with the mentioned changes in phase transformations and microstructure.

The introduction of small amounts of polygonal ferrite into the matrix was investigated by means of intercritical annealing and intermediate holding. Lower annealing temperatures as well as prolonged holding at elevated temperatures allow to achieve significantly higher amounts of retained austenite as well as uniform and total elongation. Small amounts of polygonal ferrite below 10 vol. % reduce yield and tensile strength, while the effect on hole expansion strain is negligible.

Quantitative void analysis on tensile sample cross sections of TBF/Q&P sheet steel revealed an exponential increase of the void density with increasing strain in the thickness direction. The void density, furthermore, increases with increasing overaging temperature. The average void size, by contrast, is independent of overaging temperature and shows an approximately linear increase with increasing strain in the thickness direction. Investigations on size, distribution, and shape of the dimples on the fracture surface indicated bimodal dimple population for low overaging temperatures below  $M_s$  temperature, whereas the surface of the same steel held at higher overaging temperatures showed a continuous transition between different dimple sizes of the same population. The harder matrix obtained by lower overaging temperatures possibly postpones void initiation with the exception of small hard inclusions.

Two 1180 grades, the standard grade comprising 1.5 mass% silicon and a new 1180 grade with a silicon content below 1.0 mass% and significant chromium additions, were produced on the industrial production line. At the highest industrially feasible annealing temperature, the standard grade showed small amounts of polygonal ferrite arising from intercritical annealing, while the newly designed steel was fully austenitized. Despite comparable amounts of retained austenite before plastic deformation, elongation is higher on average for the 1.5Si grade for comparable tensile strengths and hole expansion strains. While chromium significantly decelerates continuous and isothermal phase transformations, higher amounts of the additional austenite at the end of the overaging step

transform to martensite upon the final cooling. Furthermore, the reduced carbon mobility through chromium additions results in enhanced tempering resistance, less carbon enrichment of the austenite during overaging, and lower stability of the retained austenite.

In 2013, a Japanese automobile manufacturer launched a new car production series that employs a third-generation 1180 MPa AHSS [193]. European car companies are about to adopt refined 980 and 1180 TBF and Q&P sheet steels to structural car components.



# Bibliography

- [1] D. K. Matlock, J. G. Speer, *Third Generation of AHSS: Microstructure Design Concepts*, Springer (2009).
- [2] G. Speich, V. Demarest, R. Miller, “Formation of austenite during intercritical annealing of dual-phase steels”, *Metall. Trans. A* **12**, 1419–1428 (1981).
- [3] J. O. Sperle, H. Lundh, “Strength and crash resistance of structural members in high-strength dual-phase steel sheet”, *Scand. J. Metall.* **13**, 343–351 (1984).
- [4] V. F. Zackay, E. R. Parker, D. Fahr, R. Busch, “The enhancement of ductility in high-strength steels”, *Trans. Am. Soc. Met.* **60**, 252–259 (1967).
- [5] R. G. Davies, “Edge cracking in high-strength steels”, *J. Appl. Metalwork.* **2**, 293–299 (1983).
- [6] A. A. Konieczny, “On the formability behavior of advanced high strength steels”, *Steel Res. Int.* **79**, 47–54 (2008).
- [7] T. Labudde, W. Bleck, “Formability characterisation of press hardened steels”, in: M. Oldenburg, K. Steinhoff, B. Prakash, eds., *Proceedings of hot sheet metal forming of high performance steel*, 127–135, Luelå, Sweden (2009).
- [8] P. Larour, H. Pauli, T. Kurz, T. Hebesberger, “Influence of post uniform tensile and bending properties on the crash behaviour of AHSS and press-hardening steel grades”, in: IDDRG, ed., *Tools and technologies for the processing of ultrahigh strength steels*, Graz, Austria (2010).
- [9] J. G. Speer, E. De Moor, K. O. Findley, D. K. Matlock, B. C. De Cooman, D. V. Edmonds, “Analysis of microstructure evolution in quenching and partitioning automotive sheet steel”, *Metall. Mater. Trans. A* **42**, 3591–3601 (2011).
- [10] G. Frommeyer, U. Bruex, “Microstructures and mechanical properties of high-strength Fe-Mn-Al-C light-weight TRIPLEX steels”, *Steel Res. Int.* **77**, 627–633 (2006).
- [11] L. Bracke, K. Verbeken, L. Kestens, J. Penning, “Microstructure and texture evolution during cold rolling and annealing of a high Mn TWIP steel”, *Acta Mater.* **57**, 1512–1524 (2009).
- [12] C. Herrera, D. Ponge, D. Raabe, “Design of a novel Mn-based 1GPa duplex stainless TRIP steel with 60% ductility by a reduction of austenite stability”, *Acta Mater.* **59**, 4653–4664 (2011).
- [13] K.-I. Sugimoto, J. Sakaguchi, T. Iida, T. Kashima, “Stretch-flangeability of a high-strength TRIP type bainitic sheet steel”, *ISIJ Int.* **40**, 920–926 (2000).

- [14] K.-I. Sugimoto, S. Hashimoto, Y. Mukai, “Advanced formable high and ultra high strength TRIP-aided sheet steels”, in: TMS, ed., Int. Symp. on Niobium Microalloyed Sheet Steel for Automotive Applications, 285–302, Araxa, Brazil (2005).
- [15] E. De Moor, S. Lacroix, A. J. Clarke, J. Penning, J. G. Speer, “Effect of retained austenite stabilized via quench and partitioning on the strain hardening of martensitic steels”, *Metall. Mater. Trans. A* **39**, 2586–2595 (2008).
- [16] A. J. Clarke, J. G. Speer, M. K. Miller, R. E. Hackenberg, D. V. Edmonds, D. K. Matlock, F. C. Rizzo, K. D. Clarke, E. De Moor, “Carbon partitioning to austenite from martensite or bainite during the quench and partition (Q&P) process: A critical assessment”, *Acta Mater.* **56**, 16–22 (2008).
- [17] M. Mukherjee, O. N. Mohanty, S. Hashimoto, T. Hojo, K.-I. Sugimoto, “Strain-induced transformation behaviour of retained austenite and tensile properties of TRIP-aided steels with different matrix microstructure”, *ISIJ Int.* **46**, 316–324 (2006).
- [18] J. Kobayashi, D. Ina, N. Yoshikawa, K.-I. Sugimoto, “Effects of the addition of Cr, Mo and Ni on the microstructure and retained austenite characteristics of 0.2% C–Si–Mn–Nb ultrahigh-strength TRIP-aided bainitic ferrite steels”, *ISIJ Int.* **52**, 1894–1901 (2012).
- [19] S.-J. Kim, J. G. Speer, H. S. Kim, B. C. De Cooman, “Kinetics of phase transformation during Q&P processing”, in: AIST, ed., Int. Conf. on New Developments in AHSS, Orlando, FL, USA (2008).
- [20] G. A. Thomas, J. G. Speer, D. K. Matlock, “Considerations in the application of the quenching and partitioning concept to hot-rolled AHSS production”, *Iron Steel Tech.* **5**, 209–217 (2008).
- [21] E. De Moor, J. G. Speer, D. K. Matlock, J.-H. Kwak, S.-B. Lee, “Quenching and partitioning of CMnSi steels containing elevated manganese levels”, *Steel Res. Int.* **83**, 322–327 (2012).
- [22] K. Oi, C. Lux, G. R. Purdy, “A study of the influence of Mn and Ni on the kinetics of the proeutectoid ferrite reaction in steels”, *Acta Mater.* **48**, 2147–2155 (2000).
- [23] E. De Moor, D. K. Matlock, J. G. Speer, M. J. Merwin, “Austenite stabilization through manganese enrichment”, *Scr. Mater.* **64**, 185–188 (2011).
- [24] S.-J. Kim, C. G. Lee, I. Choi, S. Lee, “Effects of heat treatment and alloying elements on the microstructures and mechanical properties of 0.15 wt. pct. C transformation-induced plasticity-aided cold-rolled steel sheets”, *Metall. Mater. Trans. A* **32**, 505–514 (2001).
- [25] J. Pacyna, A. Jędrzejewska-Strach, M. Strach, “The effect of manganese and silicon on the kinetics of phase transformations during tempering - Continuous heating transformation (CHT) curves”, *J. Mater. Proc. Technol.* **64**, 311–318 (1997).
- [26] K.-I. Sugimoto, T. Muramatsu, S.-I. Hashimoto, Y. Mukai, “Formability of Nb bearing ultra high-strength TRIP-aided sheet steels”, *J. Mat. Proc. Tech.* **177**, 390–395 (2006).
- [27] K.-I. Sugimoto, M. Murata, S. Song, “Formability of Al–Nb bearing ultra high-strength TRIP-aided sheet steels with bainitic ferrite and/or martensite matrix”, *ISIJ Int.* **50**, 162–168 (2010).
- [28] D. V. Edmonds, K. He, F. C. Rizzo, B. C. De Cooman, D. K. Matlock, J. G. Speer, “Quenching and partitioning martensite - a novel steel heat treatment”, *Mater. Sci. Engng. A* **438**, 25–34 (2006).

- [29] O. Matsumura, Y. Sakuma, H. Takechi, “Enhancement of elongation by retained austenite in intercritical annealed 0.4 C-1.5 Si-0.8 Mn steel”, *Trans. Iron Steel Inst. Jpn.* **27**, 570–579 (1987).
- [30] B. C. De Cooman, L. Barbe, J. Mahieu, D. Krizan, L. Samek, M. D. Meyer, “Mechanical properties of low alloy intercritically annealed cold-rolled TRIP sheet steel containing retained austenite”, *Can. Metall. Quart.* **43**, 13–24 (2004).
- [31] T. Kobayashi, N. Wakai, W. Yagi, T. Kazino, Y. Ueda, “Effects of manganese and nickel increase on mechanical properties of TRIP steel”, *Tetsu to Hagane* **71**, 1178–1185 (1985).
- [32] M. De Meyer, D. Vanderschueren, B. C. De Cooman, “The influence of the substitution of Si by Al on the properties of cold-rolled C-Mn-Si TRIP steels”, *ISIJ Int.* **39**, 813–822 (1999).
- [33] A. Pichler, P. Stiaszny, “TRIP steel with reduced silicon content”, *Steel Res.* **70**, 459–465 (1999).
- [34] K.-I. Sugimoto, A. Nagasaka, M. Kobayashi, S. Hashimoto, “Effects of retained austenite parameters on warm stretch-flangeability in TRIP-aided dual-phase sheet steels”, *ISIJ Int.* **39**, 56–63 (1999).
- [35] K.-I. Sugimoto, T. Iida, J. Sakaguchi, T. Kashima, “Retained austenite characteristics and tensile properties in a TRIP type bainitic sheet steel”, *ISIJ Int.* **40**, 902–908 (2000).
- [36] A. T. Davenport, The crystallography of upper bainite, Steel Research Rep. on Project 12051 (1974).
- [37] J. G. Speer, A. M. Streicher, D. K. Matlock, F. Rizzo, G. Krauss, “Quenching and partitioning: a fundamentally new process to create high-strength TRIP sheet microstructures”, in: Symp. on the Thermodynamics, Kinetics, Characterization and Modeling of: Austenite Formation and Decomposition, 505–522, Chicago, IL, USA (2003).
- [38] J. G. Speer, D. K. Matlock, B. C. De Cooman, J. G. Schroth, “Carbon partitioning into austenite after martensite transformation”, *Acta Mater.* **51**, 2611–2622 (2003).
- [39] J. G. Speer, D. V. Edmonds, F. C. Rizzo, D. K. Matlock, “Partitioning of carbon from supersaturated plates of ferrite, with application to steel processing and fundamentals of the bainite transformation”, *Curr. Opin. Solid State Mater. Sci.* **8**, 219–237 (2004).
- [40] J. G. Speer, F. C. R. Assunção, D. K. Matlock, D. V. Edmonds, “The quenching and partitioning process: Background and recent progress”, *J. Mater. Res.* **8**, 417–423 (2005).
- [41] A. M. Streicher, J. G. Speer, D. K. Matlock, B. C. De Cooman, J. G. Speer, “Quenching and partitioning response of a Si-added TRIP sheet steel”, in: AIST, ed., Proceedings of the Intl. Conf. on AHSS for Automotive Applications, 51–62, Warrendale, PA, USA (2004).
- [42] E. De Moor, J. G. Speer, D. K. Matlock, J.-H. Kwak, S.-B. Lee, “Effect of carbon and manganese on the quenching and partitioning response of CMnSi steels”, *ISIJ Int.* **51**, 137–144 (2011).
- [43] G. A. Thomas, J. G. Speer, D. K. Matlock, “Quenched and partitioned microstructures produced via gleeble simulations of hot-strip mill cooling practices”, *Metall. Mater. Trans. A* **42**, 3652–3659 (2011).

- [44] R. A. Grange, H. M. Stewart, "The temperature range of martensite formation", *Trans. Am. Inst. Min. Metall. Engrs.* **167**, 467–494 (1945).
- [45] R. Grange, R. Baughman, "Hardness of tempered martensite in carbon and low-alloy steels", *Trans. Am. Soc. Met.* **48**, 165–197 (1956).
- [46] H. K. D. H. Bhadeshia, *Bainite in steels*, Inst. of Metals (1992).
- [47] P. Jacques, F. Delannay, J. Ladrière, "On the influence of interactions between phases on the mechanical stability of retained austenite in transformation-induced plasticity multiphase steels", *Metall. Mater. Trans. A* **32**, 2759–2768 (2001).
- [48] A. G. Allten, P. Payson, "The effect of silicon on the tempering of martensite", *Trans. Am. Soc. Met.* **45**, 498–532 (1953).
- [49] W. S. Owen, "The effect of silicon on the kinetics of tempering", *Trans. Am. Soc. Met.* **45**, 812–829 (1954).
- [50] R. M. Hobbs, G. W. Lorimer, N. Ridley, "Effect of Si on the microstructure of quenched and tempered medium-C steels", *J. Iron Steel Inst.* **210**, 757–764 (1972).
- [51] G. Miyamoto, J. C. Oh, K. Hono, T. Furuhashi, T. Maki, "Effect of partitioning of Mn and Si on the growth kinetics of cementite in tempered Fe-0.6 mass% C martensite", *Acta Mater.* **55**, 5027–5038 (2007).
- [52] E. Kozeschnik, H. K. D. H. Bhadeshia, "Influence of silicon on cementite precipitation in steels", *Mater. Sci. Technol.* **24**, 343–347 (2008).
- [53] J. Wang, P. J. Van Der Wolk, S. Van Der Zwaag, "On the influence of alloying elements on the bainite reaction in low-alloy steels during continuous cooling", *J. Mater. Sci.* **35**, 4393–4404 (2000).
- [54] H. K. D. H. Bhadeshia, J. Christian, "Bainite in steels", *Metall. Mater. Trans. A* **21**, 767–797 (1990).
- [55] S. M. C. van Bohemen, M. J. Santofimia, J. Sietsma, "Experimental evidence for bainite formation below  $M_s$  in Fe-0.66C", *Scr. Mater.* **58**, 488–491 (2008).
- [56] I. Yakubtsov, G. Purdy, "Analyses of transformation kinetics of carbide-free bainite above and below the athermal martensite start temperature", *Metallurgical and Materials Transactions A* **43**, 437–446 (2012).
- [57] C. García-Mateo, F. G. Caballero, H. K. D. H. Bhadeshia, "Development of hard bainite", *ISIJ Int.* **43**, 1238–1243 (2003).
- [58] C. García-Mateo, F. G. Caballero, H. K. D. H. Bhadeshia, "Low temperature bainite", *J. Phys. IV* **112**, 285–288 (2003).
- [59] E. De Moor, P. J. Gibbs, J. G. Speer, D. K. Matlock, J. G. Schroth, "Strategies for third-generation advanced high-strength steel development", *AIST Trans. Iron Steel Technol.* **7**, 132 (2010).
- [60] Y. Sakuma, O. Matsumura, H. Takechi, "Mechanical properties and retained austenite in intercritically heat-treated bainite-transformed steel and their variation with Si and Mn additions", *Metall. Mater. Trans. A* **22**, 489–498 (1991).

- [61] K.-I. Sugimoto, B. YU, Y. Mukai, S. Ikeda, “Microstructure and formability of aluminum bearing TRIP-aided steels with annealed martensite matrix”, *ISIJ Int.* **45**, 1194–1200 (2005).
- [62] A. Nagasaka, K.-I. S. Sugimoto, A. Mio, T. Hojo, K. Makii, M. Kawajiri, M. Kitayama, “Effect of yag laser cutting on stretch-flangeability of ultra high strength TRIP sheet steel with bainitic ferrite matrix”, *ISIJ Int.* **50**, 1441–1446 (2010).
- [63] E. C. Bain, Functions of the alloying elements in steel, Am. Soc. Met. (1939).
- [64] P. Jacques, E. Girault, T. Catlin, N. Geerlofs, T. Kop, S. van der Zwaag, F. Delannay, “Bainite transformation of low-carbon Mn-Si TRIP-assisted multiphase steels: influence of silicon content on cementite precipitation and austenite retention”, *Mater. Sci. Engng. A* **273**, 475–479 (1999).
- [65] F. B. Pickering, Constitution and properties of steels, VCH (1992).
- [66] A. Hultgren, K. Kuo, “La transformation isotherme de l’austénite et le partage des éléments spéciaux dans les aciers faiblement alliés.”, *Rev. Metall* **50**, 847–856 (1953).
- [67] T. Sato, T. Nishizawa, Y. Honda, “Study on carbides in practical steels by electrolytic isolation”, *Tetsu-to-Hagané* **41**, 1188–1192 (1955).
- [68] J. Wang, S. Zwaag, “Stabilization mechanisms of retained austenite in transformation-induced plasticity steel”, *Metall. Mater. Trans. A* **32**, 1527–1539 (2001).
- [69] K. Han, G. D. W. Smith, D. V. Edmonds, “Pearlite phase transformation in Si and V steel”, *Metall. Mater. Trans. A* **26**, 1617–1631 (1995).
- [70] J. Mahieu, Contribution to the Physical Metallurgy of Crash-resistant galvanized TRIP-assisted Steel for Automotive Structures, Ph.D. thesis, Ghent University, Ghent, Belgium (2004).
- [71] J. Mahieu, B. C. De Cooman, S. Claessens, “Galvanizability of high-strength steels for automotive applications”, *Metall. Mater. Trans. A* **32**, 2905–2908 (2001).
- [72] G. Lagerberg, “Carbon damping in manganese-alloyed ferrite”, *Acta Metall.* **7**, 137–139 (1959).
- [73] G. R. Purdy, Y. J. M. Brechet, “A solute drag treatment of the effects of alloying elements on the rate of the proeutectoid ferrite transformation in steels”, *Acta Metall. Mater.* **43**, 3763–3774 (1995).
- [74] G. Airey, T. Hughes, R. Mehl, “The growth of cementite particles in ferrite”, *Trans. Am. Inst. Min. Metall. Engrs.* **242** (1968).
- [75] T. Mukherjee, W. Stumpf, C. Sellars, W. Tegart, “Kinetics of coarsening of carbides in chromium steels at 700 °C”, *J. Iron Steel Inst.* **207**, 621–631 (1969).
- [76] T. Sakuma, N. Watanabe, T. Nishizawa, “The effect of alloying element on the coarsening behavior of cementite particles in ferrite”, *Trans. JIM* **21** (1980).
- [77] M. Ko, T. Sakuma, T. Nishizawa, “Effect of magnetism on the partition of alloying elements between cementite and ferrite”, *J. Jpn. Inst. Met.* **40**, 593–601 (1976).
- [78] S. Al-Salman, G. Lorimer, N. Ridley, “Pearlite growth kinetics and partitioning in a Cr- Mn eutectoid steel”, *Metall. Mater. Trans. A* **10**, 1703–1709 (1979).

- [79] S. Babu, K. Hono, T. Sakurai, “APFIM studies on martensite tempering of Fe-C-Si-Mn low alloy steel”, *Appl. Surf. Sci.* **67**, 321–327 (1993).
- [80] M. Umemoto, Z. G. Liu, K. Masuyama, K. Tsuchiya, “Influence of alloy additions on production and properties of bulk cementite”, *Scr. Mater.* **45**, 391–398 (2001).
- [81] C. Zhu, X. Y. Xiong, A. Cerezo, R. Hardwicke, G. Krauss, G. D. W. Smith, “Three-dimensional atom probe characterization of alloy element partitioning in cementite during tempering of alloy steel”, *Ultramicroscopy* **107**, 808–812 (2007).
- [82] A. Pichler, S. Traint, T. Hebesberger, P. Stiaszny, E. A. Werner, “Processing of thin sheet multiphase steel grades”, *Steel Res. Int.* **78**, 216–223 (2007).
- [83] M. J. Merwin, “Low-carbon manganese TRIP steels”, in: Trans. Tech. Publ., ed., Mater. Sci. Forum, 4327–4332 (2007).
- [84] B. Wietbrock, M. Bambach, S. Seuren, G. Hirt, “Homogenization strategy and material characterization of high-manganese TRIP and TWIP steels”, in: Mater. Sci. Forum, 3134–3139, Trans. Tech. Publ. (2010).
- [85] W. Xu, P. Rivera-Diaz-del Castillo, S. Van Der Zwaag, “Ferrite/pearlite band prevention in dual phase and TRIP steels: Model developmentf”, *ISIJ Int.* **45**, 380–387 (2005).
- [86] B. De Cooman, “Structure-properties relationship in TRIP steels containing carbide-free bainite”, *Curr. Opin. Solid State Mater. Sci.* **8**, 285–303 (2004).
- [87] S. Traint, A. Pichler, P. Stiaszny, M. Blaimschein, B. Röthler, C. Kremaszky, E. Werner, “Alloy design, processing and properties of TRIP-steels: A critical comparison”, in: AIST, ed., Int. Conf. on Advanced High-Strength Sheet Steel for Automotive Applications, 79–98, Winter Park, CO, USA (2004).
- [88] K.-I. Sugimoto, M. Murata, T. Muramatsu, Y. Mukai, “Formability of C–Si–Mn–Al–Nb–Mo ultra high-strength TRIP-aided sheet steels”, *ISIJ Int.* **47**, 1357–1362 (2007).
- [89] D. Kim, J. Speer, H. Kim, B. De Cooman, “Observation of an isothermal transformation during quenching and partitioning processing”, *Metall. Mater. Trans. A* **40**, 2048–2060 (2009).
- [90] K. M. Wu, M. Kagayama, M. Enomoto, “Kinetics of ferrite transformation in an Fe-0.28 mass % C-3 mass % Mo alloy”, *Mater. Sci. Engng. A* **343**, 143–150 (2003).
- [91] H. Aaronson, W. Reynolds Jr, G. Purdy, “Coupled-solute drag effects on ferrite formation in Fe-CX systems”, *Metallurgical and Materials Transactions A* **35**, 1187–1210 (2004).
- [92] A. Samoilov, Y. Titovets, N. Zolotarevsky, G. Hribernic, A. Pichler, “Cr influence on steel microstructure and kinetics of austenite decomposition at near-bay temperatures”, 311–320 (2005).
- [93] N. A. Razik, G. W. Lorimer, N. Ridley, “Chromium partitioning during the austenite-pearlite transformation”, *Metall. Trans. A* **7**, 209–214 (1976).
- [94] J. Chance, N. Ridley, “Chromium partitioning during isothermal transformation of a eutectoid steel”, *Metall. Trans. A* **12**, 1205–1213 (1981).
- [95] N. Ridley, M. Malik, G. Lorimer, “Partitioning and pearlite growth kinetics in an Ni–Cr eutectoid steel”, *Mater. Charact.* **25**, 125–141 (1990).

- [96] D. E. Parsons, T. F. Malis, J. D. Boyd, “Microalloying and precipitation in Cr-V rail steels”, *J. Heat Treat.* **3**, 213–219 (1984).
- [97] R. Thomson, M. K. Miller, “Carbide precipitation in martensite during the early stages of tempering Cr- and Mo-containing low alloy steels”, *Acta Mater.* **46**, 2203–2213 (1998).
- [98] J. Takahashi, K. Kawakami, M. Sugiyama, T. Tarui, “Quantitative composition analysis of spherical cementite by three-dimensional atom probe”, *Tetsu-to-Hagané* **93**, 145–149 (2007).
- [99] S. Paul, Entwicklung neuer Legierungskonzepte für höchstfeste TRIP-Stähle mit nicht-ferritischer Matrix und reduziertem Siliziumgehalt, Ph.D. thesis, Technische Universität München (2012).
- [100] A. J. DeArdo, “Niobium in modern steels”, *Int. Mater. Rev.* **48**, 371–402 (2003).
- [101] E. Orowan, “Metals and alloys”, in: *Inst. Met.*, ed., Symp. on Internal Stresses, London, England (1948).
- [102] E. O. Hall, “The deformation and ageing of mild steel: III discussion of results”, *Proc. Phys. Soc. B* **64**, 747–753 (1951).
- [103] N. J. Petch, “The cleavage strength of polycrystals”, *J. Iron Steel Inst.* **174**, 25–28 (1953).
- [104] W. Bleck, K. Hulka, K. Papamantellos, “Effect of niobium on the mechanical properties of TRIP steels”, in: *Trans. Tech. Publ.*, ed., *Mater. Sci. Forum*, 327–334 (1998).
- [105] K. Hulka, W. Bleck, K. Papamantellos, “Relationships between heat treatment conditions, microstructure and properties of niobium microalloyed TRIP steel”, in: *Iron Steel Soc.*, ed., 41 st Mechanical Working and Steel Processing Conference, 67–77, Baltimore, MD, USA (1999).
- [106] D. Krizan, B. C. De Cooman, J. Antonissen, “Retained austenite stability in the cold-rolled CMnAlSiP micro-alloyed TRIP steels”, in: *AIST*, ed., *Int. Conf. on Advanced High Strength Sheet Steel for Automotive Applications*, 205–215, Winter Park, CO, USA (2004).
- [107] A. Pichler, T. Hebesberger, S. Traint, E. Tragl, T. Kurz, C. Kremaszky, P. Tsipouridis, E. Werner, “Advanced high strength thin sheet grades: Improvement of properties by microalloying assisted microstructure control”, in: *TMS*, ed., *Int. Symp. of Niobium Microalloyed Sheet Steel for Automotive Application*, 245–273 (2006).
- [108] C. Zener, “Kinetics of the decomposition of austenite”, *Trans. Am. Inst. Min. Metall. Engrs.* **167**, 550–595 (1946).
- [109] T. Gladman, *The physical metallurgy of microalloyed steels*, Maney Pub. (1997).
- [110] M. Avrami, “Kinetics of phase change. I General theory”, *J. Chem. Phys.* **7**, 1103–1112 (1939).
- [111] A. C. Kneissl, C. I. Garcia, A. J. DeArdo, G. Tither, Z. Shouhua, “HSLA Steels: Processing, Properties and Applications”, 99–105, Warrendale, PA, USA (1992).
- [112] H. Tamehiro, M. Murata, R. Habu, M. Nagumo, “Optimum microalloying of niobium and boron in HSLA steel for thermomechanical processing”, *Trans. Iron Steel Inst. Jpn.* **27**, 120–129 (1987).
- [113] T. Gladman, “Precipitation hardening in metals”, *Mater. Sci. Technol.* **15**, 30–36 (1999).

- [114] J. Irvine, T. Baker, "Effect of rolling deformation on niobium carbide particle size distribution in low-carbon steel", *Met. Sci.* **13**, 228–237 (1979).
- [115] H. Watanabe, Y. Smith, R. Pehlke, "Precipitation kinetics of niobium carbonitride in austenite of high-strength low-alloy steels", 140–168, New York, NY, USA (1977).
- [116] G. Gottstein, *Physikalische Grundlagen der Materialkunde*, Springer-Lehrbuch, Springer-Verlag Berlin Heidelberg (2007).
- [117] G. E. Dieter, *Mechanical Metallurgy*, 3rd ed., McGraw-Hill Book Company (1986).
- [118] R. L. Fleischer, "Substitutional solution hardening", *Acta Metall.* **11**, 203–209 (1963).
- [119] R. Labusch, "A statistical theory of solid solution hardening", *Physica Status Solidi B* **41**, 659–669 (1970).
- [120] A. Suzuki, "Synthetic studies via the cross-coupling reaction of organoboron derivatives with organic halides", *Pure Appl. Chem.* **63**, 419–422 (1991).
- [121] A. Kelly, M. Fine, "The strength of an alloy-containing zones", *Acta Metall.* **5**, 365–367 (1957).
- [122] A. Ghosh, "Tensile instability and necking in materials with strain hardening and strain-rate hardening", *Acta Metall.* **25**, 1413–1424 (1977).
- [123] P. Ludwik, *Elemente der technologischen Mechanik*, J. Springer (1909).
- [124] M. F. Ashby, "The deformation of plastically non-homogeneous materials", *Philos. Mag.* **21**, 399–424 (1970).
- [125] N. Fleck, G. Muller, M. Ashby, J. Hutchinson, "Strain gradient plasticity: theory and experiment", *Acta Metall. Mater.* **42**, 475–487 (1994).
- [126] B. Karlsson, G. Linden, "Plastic deformation of ferrite-pearlite structures in steel", *Mater. Sci. Engng. A* **17**, 209–219 (1975).
- [127] H. Fischmeister, J. O. Hjalmered, B. Karlsson, G. Linden, B. Sundström; "Strength of metals & alloys (9th edn.)", in: *Inst. of Metals & Iron and Steel*, ed., Proc. 3rd Int. Conf. Strength of Metals and Alloys, Cambridge, England (1973).
- [128] H. Fischmeister, B. Karlsson, "Plastizitätseigenschaften grob-zweiphasiger Werkstoffe", *Z. Metallkd.* **68**, 311–327 (1977).
- [129] D. C. Drucker, "Thoughts on the present and future interrelation of theoretical and experimental mechanics", *Exp. Mech.* **8**, 97–106 (1968).
- [130] I. Tamura, Y. Tomota, H. Ozawa, in: *Inst. of Metals & Iron and Steel*, ed., Proc. 3rd Int. Conf. Strength of Metals and Alloys, 611, Cambridge, England (1973).
- [131] G. Reisner, E. Werner, F. Fischer, "Micromechanical modeling of martensitic transformation in random microstructures", *Int. J. Solids Struct.* **35**, 2457–2473 (1998).
- [132] F. Fischer, G. Reisner, E. Werner, K. Tanaka, G. Cailletaud, T. Antretter, "A new view on transformation induced plasticity (TRIP)", *Int. J. Plast.* **16**, 723–748 (2000).

- [133] N. Van Dijk, A. Butt, L. Zhao, J. Sietsma, S. Offerman, J. Wright, S. Van der Zwaag, “Thermal stability of retained austenite in TRIP steels studied by synchrotron X-ray diffraction during cooling”, *Acta Mater.* **53**, 5439–5447 (2005).
- [134] E. Jimenez-Melero, N. Van Dijk, L. Zhao, J. Sietsma, S. Offerman, J. Wright, S. Van der Zwaag, “Characterization of individual retained austenite grains and their stability in low-alloyed TRIP steels”, *Acta Mater.* **55**, 6713–6723 (2007).
- [135] P. Jacques, “Transformation-induced plasticity for high-strength formable steels”, *Curr. Opin. Solid State Mater. Sci.* **8**, 259–265 (2004).
- [136] S. Chatterjee, H.-S. Wang, J. R. Yang, H. K. D. H. Bhadeshia, “Mechanical stabilisation of austenite”, *Mater. Sci. Technol.* **22**, 641–644 (2006).
- [137] H. K. D. H. Bhadeshia, R. W. K. Honeycombe, *Steels: Microstructure and Properties*, Butterworth-Heinemann (2011).
- [138] A. F. L. Mark, Microstructural effects on the stability of retained austenite in transformation induced plasticity steels, Ph.D. thesis, Queen’s University (2008).
- [139] K.-I. Sugimoto, A. Kanda, R. Kikuchi, S. Hashimoto, T. Kashima, S. Ikeda, “Ductility and formability of newly developed high strength low alloy TRIP-aided sheet steels with annealed martensite matrix”, *ISIJ Int.* **42**, 910–915 (2002).
- [140] P. F. Thomason, *Ductile fracture of metals*, Pergamon Press Oxford (1990).
- [141] A. Pichler, E. Tragl, T. Kurz, E. Werner, P. Tsipouridis, A. Haglund, J. Zajac, J. M. Artimez, J. A. G. Ferreño, DP grades with improved formability, Research Fund for Coal & Steel (2009).
- [142] L. Ryde, D. Lindell, A. Pichler, J. A. G. Ferreño, Y. V. Granbom, E. Werner, A. Fillafer, R. Wesenjak, P. Tsipouridis, Micro-scale damage, tolerance of AHSS steels as function of microstructure and stress/strain state, Research Fund for Coal & Steel (2013).
- [143] L. Brown, W. Stobbs, “The work-hardening of copper-silica V. Equilibrium plastic relaxation by secondary dislocations”, *Philosophical Magazine* **34**, 351–372 (1976).
- [144] S. Goods, L. Brown, “Overview no. 1: The nucleation of cavities by plastic deformation”, *Acta Metall.* **27**, 1–15 (1979).
- [145] A. Argon, J. Im, R. Safoglu, “Cavity formation from inclusions in ductile fracture”, *Metall. Trans. A* **6**, 825–837 (1975).
- [146] J. Gurland, J. Plateau, “The mechanism of ductile rupture of metals containing inclusions”, *Trans. Am. Soc. Met.* 442–454 (1963).
- [147] R. v. Mises, “Mechanik der festen Körper im plastisch-deformablen Zustand”, *Nachrichten von der Gesellschaft der Wissenschaften zu Göttingen, Mathematisch-Physikalische Klasse* 582–592 (1913).
- [148] C. Kremaszky, J. Ocenasek, V. Espinoza, E. Werner, T. Hebesberger, A. Pichler, “Micromechanical modeling of the formability of dual-phase steels”, in: *Proceedings MS&T*, 31–42, Detroit, MI, USA (2007).

- [149] A. Bhattacharyya, G. Weng, “Theoretical calculation of the stress-strain behavior of dual-phase metals with randomly-oriented spheroidal inclusions”, *Metall. Mater. Trans. A* **27**, 2359–2365 (1996).
- [150] P. Tsipouridis, Mechanical Properties of Dual Phase Steels, Ph.D. thesis, Technische Universität München (2006).
- [151] C. Kremaszky, J. Ocenasek, V. Espinoza, P. Tsipouridis, E. Werner, T. Hebesberger, A. Pichler, “Micromechanical modeling of the formability of advanced high strength steels”, in: AIST, ed., Int. Conf. on New Developments in AHSS, 305–313, Orlando, FL, USA (2008).
- [152] A. Hiramatsu, T. Yamada, “Prediction of stress-strain curves in ferrite single structure steels”, *ISIJ Int.* 263–268 (1994).
- [153] M. Considère, Memoire sur l’emploi du fer et de l’acier dans les constructions, Dunod (1885).
- [154] J. Gurland, The measurement of grain contiguity in two-phase alloys, Division of Engineering, Brown University (1957).
- [155] J. R. Rice, D. M. Tracey, “On the ductile enlargement of voids in triaxial stress fields”, *J. Mech. Phys. Solids* **17**, 201–217 (1969).
- [156] G. Le Roy, J. Embury, G. Edwards, M. Ashby, “A model of ductile fracture based on the nucleation and growth of voids”, *Acta Metall.* **29**, 1509–1522 (1981).
- [157] R. Hill, “Discontinuity relations in mechanics of solids”, *Progress Solid Mechanics* **2**, 245–276 (1961).
- [158] P. F. Thomason, “A theory for ductile fracture by internal necking of cavities”, *J. Inst. Metals.* **96**, 360–365 (1968).
- [159] F. LePera, “Improved etching technique for the determination of percent martensite in high-strength dual-phase steels”, *Metallography* **12**, 263–268 (1979).
- [160] W. S. Rasband, ImageJ, US and National Institutes of Health and others, Bethesda, MD, USA (2009).
- [161] E. Wirthl, R. Angerer, K. Hauzenberger, “Determination of the volume amount of retained austenite in small specimens by magnetic measurements”, in: 2000 AISE Annual Convention and Exposition (2000).
- [162] E. Wirthl, A. Pichler, R. Angerer, P. Stiaszny, K. Hauzenberger, Y. F. Titovets, M. Hackl, “Determination of the volume fraction of retained austenite in small specimens by magnetic measurements”, in: Int. Conf. on TRIP-Aided High Strength Ferrous Alloys, 61–64, Ghent, Belgium (2002).
- [163] H. M. Rietveld, “Line profiles of neutron powder diffraction peaks for structure refinement”, *Acta Crystallogr.* **22**, 151–152 (1967).
- [164] H. M. Rietveld, “A profile refinement method for nuclear and magnetic structures”, *J. Appl. Cryst.* **2**, 65–71 (1969).
- [165] Thermo-Calc Software TCFE6 Steels Fe-alloys database version 6 (2010).

- [166] K. Hausmann, D. Krizan, A. Pichler, E. Werner, “TRIP-aided bainitic-ferritic sheet steel: A critical assessment of alloy design and heat treatment”, in: MS&T, ed., *Advanced Steel Metallurgy: Design, Processing, and Technological Exploitation*, 209–219, Montreal, Canada (2013).
- [167] K. Hausmann, “Cementite in ferrite from first-principles: Influence of substitutional impurities on thermodynamic stability”, Diploma Thesis, RWTH Aachen University (2011).
- [168] W. Bleck, A. Frehn, J. Ohlert, “Niobium in dual phase and TRIP steels”, in: TMS, ed., *Int. Symp. Niobium*, 727–752, Orlando, FL, USA (2001).
- [169] D. Krizan, B. C. De Cooman, “Analysis of the strain-induced martensitic transformation of retained austenite in cold-rolled micro-alloyed TRIP steel”, *Steel Res. Int.* **79**, 513–522 (2008).
- [170] S. Traint, A. Pichler, R. Sierlinger, H. Pauli, E. Werner, “Low-alloyed TRIP steels with optimized strength, forming and welding properties”, *Steel Res. Int.* **77**, 641–649 (2006).
- [171] E. Pereloma, I. Timokhina, P. Hodgson, “Transformation behaviour in thermomechanically processed C-Mn-Si TRIP steels with and without Nb”, *Mater. Sci. Engng. A* **273**, 448–452 (1999).
- [172] D. Krizan, *Structure-Property Relationships in 1 GPa Micro-Alloyed TRIP Steel*, Ph.D. thesis, Universiteit Gent (2006).
- [173] K. Hausmann, D. Krizan, K. Spiradek-Hahn, A. Pichler, E. Werner, “The influence of Nb on transformation behavior and mechanical properties of TRIP-assisted bainitic-ferritic sheet steels”, *Mater. Sci. Engng. A* **588**, 142–150 (2013).
- [174] S. Bechet, L. Beaujard, “Nouveau réactif pour la mise en évidence micrographique du grain austénitique des aciers trempés ou trempés-revenus”, *Rev. Met.* **52**, 830–836 (1955).
- [175] D. Dyson, B. Holmes, “Effect of alloying additions on the lattice parameter of austenite”, *J. Iron Steel Inst.* **208**, 469–474 (1970).
- [176] D. Koistinen, R. Marburger, “A general equation prescribing the extent of the austenite-martensite transformation in pure iron-carbon alloys and plain carbon steels”, *Acta Metall.* **7**, 59–60 (1959).
- [177] M. Oka, H. Okamoto, “Swing back in kinetics near martensite start temperature in hypereutectoid steels”, *Metall. Mater. Trans. A* **19**, 447–452 (1988).
- [178] L.-J. Zhu, D. Wu, X.-M. Zhao, “Effect of silicon content on thermodynamics of austenite decomposition in C-Si-Mn TRIP steels”, *J. Iron Steel Res. Int.* **13**, 57–73 (2006).
- [179] E. S. Davenport, E. C. Bain, “Transformation of austenite at constant subcritical temperatures”, *Trans. Am. Inst. Min. Metall. Engrs. Iron Steel Div.* **90**, 117 (1930).
- [180] J. R. Vilella, G. E. Guellich, E. C. Bain, “On naming the aggregate constituents in steel”, *Trans. Am. Soc. Met.* **24**, 225–261 (1936).
- [181] H. K. D. H. Bhadeshia, “Bainite: Overall transformation kinetics”, *J. Phys. Colloq.* **43**, 4 (1982).

- [182] Š. Mikmeková, K. Hausmann, D. Krizan, “The potentials of ultra-high vacuum scanning low-energy electron microscopy for study of multiphase steel”, in: The 2nd International Conference on Engineering and Applied Science, Tokyo, Japan (2013).
- [183] Š. Mikmeková, K. Hausmann, D. Krizan, “Microstructure characterization of AHSS by unconventional microscopy techniques”, in: 1st East-Asia Microscopy Conference, Chongqing, China (2013).
- [184] P. Jacques, F. Delannay, X. Cornet, P. Harlet, J. Ladriere, “Enhancement of the mechanical properties of a low-carbon, low-silicon steel by formation of a multiphased microstructure containing retained austenite”, *J. Metall. Mater. Trans. A* **29**, 2383–2393 (1998).
- [185] A. J. Clarke, J. G. Speer, D. K. Matlock, F. C. Rizzo, D. V. Edmonds, M. J. Santofimia, “Influence of carbon partitioning kinetics on final austenite fraction during quenching and partitioning”, *Scr. Mater.* **61**, 149–152 (2009).
- [186] A. Clarke, Carbon partitioning into austenite from martensite in a silicon-containing high-strength sheet steel, Ph.D. thesis, Colorado School of Mines, Golden, CO (2006).
- [187] A. Bachmaier, K. Hausmann, D. Krizan, A. Pichler, “Development of TBF steels with 980 MPa tensile strength for automotive applications: Microstructure and mechanical properties”, in: Int. Symp. on New Developments in AHSS, 131–139, Vail, CO (2013).
- [188] K.-I. Sugimoto, M. Murata, Y. Mukai, “Stretch-flangeability of C-Mn-Si-Al-Nb ultra high-strength TRIP-aided cold-rolled sheet steel”, in: AIST, ed., Int. Conf. on New Developments in AHSS, 57–67, Orlando, FL, USA (2008).
- [189] F. G. Caballero, S. Allain, J. Cornide, J. D. Puerta Velásquez, C. Garcia-Mateo, M. K. Miller, “Design of cold-rolled and continuous-annealed carbide-free bainitic steels for automotive application”, *Materials & Design* **49**, 667–680 (2013).
- [190] A. Argon, J. Im, “Separation of second phase particles in spheroidized 1045 steel, Cu-0.6 pct Cr alloy, and maraging steel in plastic straining”, *Metall. Trans. A* **6**, 839–851 (1975).
- [191] E. Hornbogen, G. Eggeler, E. Werner, *Werkstoffe. Aufbau und Eigenschaften von Keramik-, Metall-, Polymer- und Verbundwerkstoffen*, Springer (2012).
- [192] E. Maire, O. Bouaziz, M. D. Michiel, C. Verdu, “Initiation and growth of damage in a dual-phase steel observed by X-ray microtomography”, *Acta Mater.* **56**, 4954 – 4964 (2008).
- [193] M. Katsukura, “First use of 1180 MPa advanced high-strength steel with high formability in the new Infinity Q50”, in: Materials in Car Body Engineering, Bad Nauheim, Germany (2014).